الجمهورية الجزائرية الديمقراطية الشعبية
République Algérienne Démocratique et Populaire
Ministère de l'Enseignement Supérieur et de la Recherche Scientifique

جامعة سطيف 1 - فرحات عباس
Université Sétif 1 - Ferhat Abbas
Faculté de Technologie

THÈSE

Présentée au Département d'Électronique

Pour l'obtention du diplôme de

DOCTORAT

Domaine : Sciences et Technologie

Filière : Électronique **Option :** Instrumentation

Par

Melle. ABDELMALEK Feriel

THÉME

Étude, modélisation et réalisation expérimentale d'un système de compensation de la puissance réactive connecté à un générateur photovoltaïque

Soutenu le : 22/04/2026 devant le jury :

Semcheddine Samia	**Prof**	**Université Sétif 1 - Ferhat Abbas**	**Président**
Afghoul Hamza	**Prof**	**Université Sétif 1 - Ferhat Abbas**	**Directeur**
Feroura Hamza	**MCA**	**Université Sétif 1 - Ferhat Abbas**	**Examinateur**
Bouafassa Amar	**MCA**	**ENP Constantine**	**Examinateur**
Djellad Abdelhak	**MCA**	**ENSTI Annaba**	**Examinateur**
Krim Fateh	**Prof**	**Université Sétif 1 - Ferhat Abbas**	**Invité**

الجمهورية الجزائرية الديمقراطية الشعبية

People's Democratic Republic of Algeria

Ministry of Higher Education and Scientific Research

جامعة سطيف 1 - فرحات عباس

Setif 1 University - Ferhat ABBAS

Faculty of Technology

THESIS

Submitted to the Department of Electronics

In partial fulfillment of the requirements for the degree of

DOCTORAT

Field: Science and Technology

Specialty: Electronics **Option:** Instrumentation

By

Melle. ABDELMALEK Feriel

Entitled

Study, Modeling, and Experimental Implementation of a Reactive Power Compensation System Connected to a Photovoltaic Generator

Defended on: 22/04/2026 before the jury:

Semcheddine Samia	**Prof**	**Setif 1 University - Ferhat ABBAS**	**President**
Afghoul Hamza	**Prof**	**Setif 1 University - Ferhat ABBAS**	**Supervisor**
Feroura Hamza	**MCA**	**Setif 1 University - Ferhat ABBAS**	**Examiner**
Bouafassa Amar	**MCA**	**ENP Constantine**	**Examiner**
Djellad Abdelhak	**MCA**	**ENSTI Annaba**	**Examiner**
Krim Fateh	**Prof**	**Setif 1 University - Ferhat ABBAS**	**Guest**

Acknowledgements

First and foremost, I praise Almighty Allah, the Most Merciful, for granting me health, knowledge, patience, and the strength required to complete this thesis.

I would like to express my deepest gratitude to my supervisor, **Dr. Hamza AFGHOUL**, for his guidance, advice, and continuous support throughout this research. I also thank him for his encouragement, patience, and kindness during all stages of this work. I express here my sincere respect and profound appreciation for his support.

I am deeply grateful to my co-supervisor, **Prof. Fateh KRIM** (Professor at the University of Ferhat Abbas Sétif-1), for entrusting me with and guiding this project.

I am grateful to the members of the examination committee for accepting to evaluate this doctoral work. I would like to thank **Prof. Samia Semcheddine** (University of Ferhat Abbas Sétif-1) for accepting to chair the jury, **Dr. Hamza Feroura** (University of Ferhat Abbas Sétif-1) **Dr. Djellad Abdelhak** (ENSTI Annaba), and **Dr. Bouafassa Amar** (ENP Constantine) for evaluating this manuscript.

I would like to express my appreciation to the members of the LEPCI laboratory, as well as to all colleagues and researchers who supported and encouraged me throughout this academic journey.

My sincere thanks also go to **Mr. Djallal Eddine Zabia** (University of Biskra) for his valuable assistance during the experimental work and for his help with the setup and operation of the experimental test bench.

Finally, I express my gratitude to the Dean of the Faculty of Technology, the Head of the Department of Electronics, and the Director of LEPCI laboratory at the University of Ferhat Abbas Sétif-1 for granting me access to laboratory facilities and for their continuous support.

Dedication

By the will and grace of Almighty God, this work has been accomplished. Every effort, outcome, and achievement presented in this thesis is made possible through His guidance and support.

﴿وَمَا تَوْفِيقِي إِلَّا بِاللَّهِ عَلَيْهِ تَوَكَّلْتُ وَإِلَيْهِ أُنِيبُ﴾

سورة هود، الآية 88

To the readers of this thesis, with the hope that this work may be of benefit.

To my beloved parents, for their guidance, prayers, and unwavering support.

To my brothers and sisters, for their encouragement and constant presence.

To all those who contributed to my education and learning.

To my friends, for the shared moments and sincere support throughout this journey.

List of Symbols

i_{sa}, i_{sb}, i_{sc}	Source currents of phases a, b, and c
v_{sa}, v_{sb}, v_{sc}	Grid voltages
i_{La}, i_{Lb}, i_{Lc}	Load currents
i_{fa}, i_{fb}, i_{fc}	Filter output currents
v_{α}, v_{β}	Grid voltages in the αβ frame
R_f, L_f	Resistance and inductance of the filter
S_{α}, S_{β}	Equivalent switching functions in the αβ frame
S_a, S_b, S_c	Switching signals of the inverter
i_{α}, i_{β}	Source current components in $\alpha\beta$ stationary frame
V_{dc}	DC-link voltage
V_{dcref}	Reference DC-link voltage
C_{dc}	DC-link capacitor
$R_{L,}$ L_L	Resistive and inductance load
$P_{ref,}$ Q_{ref}	Reference active and reactive power
P	Instantaneous active power
Q	Instantaneous reactive power
S	Instantaneous apparent power
D	Instantaneous distortion power
I_{PV}	PV array output current
V_{MPP}	Voltage at maximum power point
I_{MPP}	Current at maximum power point
P_{mpp}	Power at maximum power point
V_{oc}	Open-circuit voltage
I_{sc}	Short-circuit current
q	Electron charge
k	Boltzmann constant
T	Cell temperature
G	Solar irradiance
T_T	Tracking Time

List of Acronyms

AC	Alternating Current
ANN	Artificial Neural Networks
APF	Active Power Filter
CCM	Continuous Conduction Mode
CSI	Current Source Inverter
DC	Direct Current
DCC	Direct Current Control
DDM	Double Diode Model
DER	Distributed Energy Resources
DSC	Dynamic Shading Conditions
DPC	Direct Power Control
FLC	Fuzzy Logic Controller
FOPI	Fractional Order Proportional Integral
FOPI-AW	Fractional Order Proportional Integral- Anti-Windup
FPA	Flower Pollination Algorithm
GCPV	Grid Connected Photovoltaic
GCPV-SAPF	Grid Connected Photovoltaic-Shunt Active Power Filter
GMPP	Global Maximum Power Point
GWO	Grey Wolf Optimization
GWEO	Grey Wolf Equilibrium Optimizer
GWO-PSO	Grey Wolf Optimization- Particle Swarm Optimization
HC	Hill Climbing
HPF	Hybrid Power Filter
IEEE	Institute of Electrical and Electronics Engineers
IGBT	Insulated Gate Bipolar Transistor
IM	Ideal Model
INC	Incremental Conductance
LMPP	Local Maximum Power Point
LUT	Lookup Table

MOAs	Metaheuristic Optimization Algorithms
MPP	Maximum Power Point
MPPT	Maximum Power Point Tracking
OCA	Oustaloup Continuous Approximation
P&O	Perturb and Observe
PCC	Point of Common Coupling
PF	Power Factor
PI	Proportional Integral
PLL	Phase Locked Loop
PSC	Partial Shading Conditions
PSO	Particle Swarm Optimization
PQ	Power Quality
P-DPC	Predictive-Direct Power Control
PPF	Passive Power Filters
PV	Photovoltaic
P–V	Power–Voltage
PWM	Pulse Width Modulation
RMS	Root Mean Square
SAPF	Shunt Active Power Filter
SDM	Single Diode Model
SEAPF	Series Active Power Filter
STC	Standard Test Conditions
THD	Total Harmonic Distortion
THDi	Total Harmonic Distortion of Current
THDv	Total Harmonic Distortion of Voltage
UIC	Uniform Irradiance Conditions
UPQC	Unified Power Quality Conditioner
VSI	Voltage Source Inverter
WOA	Whale Optimization Algorithm
ZOA	Zebra Optimization Algorithm

Table of Contents

General Introduction

Chapter 1: Literature Review on Photovoltaic Systems, Power Quality Issues, and Harmonic Mitigation Techniques

Chapter 2: Modeling of the Grid-Connected Photovoltaic System with SAPF

Chapter 3: Development of Metaheuristic and Hybrid Optimization Algorithms for Photovoltaic MPPT Enhancement

Chapter 4: Advanced Control and Regulation Techniques for Shunt Active Power Filters

Chapter 5: Experimental Implementation and Performance Evaluation of the Grid-Tied PV system with SAPF

List of Figures

List of Tables

I. Research background

The energy environment across the globe is undergoing profound changes, influenced by the urgent need to mitigate environmental degradation and reduce dependence on fossil fuels [1]. Growing concerns over climate change, the rise in greenhouse gas emissions, coupled with the diminishing availability of non-renewable energy resources, has prompted governments, industries, and research institutions to promote clean and sustainable energy alternatives. Among these, solar photovoltaic (PV) among various solutions, energy has surfaced as a particularly promising renewable technologies due to its abundance, modularity, and capability of direct electricity generation without moving parts or harmful emissions [2].

PV systems have evolved from small-scale, standalone applications to large-scale, grid connected PV (GCPV), playing an increasingly vital role in modern power networks. The integration of PV generation into electrical grids contributes to the decarbonization of energy production [3]. It supports the development of smart grids, where distributed energy resources (DERs) enhance reliability and efficiency. However, despite their advantages, GCPV systems introduce several operational challenges related to power quality (PQ), stability, and grid compliance, especially when integrated in large numbers within distribution networks [4].

The intermittent and nonlinear characteristics of solar irradiance and temperature cause frequent power fluctuations, voltage instability, and dynamic disturbances. Additionally, the widespread use of power electronic converters, essential for energy conversion, control, and grid synchronization, introduces harmonic distortions that can deteriorate the overall PQ [5]. The coexistence of nonlinear loads, unbalanced conditions, and distributed renewable sources makes harmonic mitigation and reactive power compensation indispensable for maintaining grid standards such as IEEE 519 and IEC 61000-3-2 [6].

To address these challenges, Shunt active power filters (SAPFs) have been widely adopted as practical solutions for mitigating harmonics and compensating reactive power within distribution networks. When integrated with PV systems, SAPFs not only enhance PQ but also facilitate efficient utilization of generated energy, increasing the general stability and reliability of the network. This configuration, known as GCPV with SAPF (GCPV–SAPF) system, allows bidirectional energy exchange, enabling the PV unit to inject active power into the grid while the SAPF mitigates current distortions and maintains a unity power factor (PF) operation [7].

In parallel, maximum power point tracking (MPPT) techniques play a vital role in ensuring that photovoltaic (PV) arrays operate at their optimal power point under varying environmental conditions.

Conventional algorithms, such as Perturb and Observe (P&O) and Incremental Conductance (INC) [8], are simple to implement but often exhibit limited performance, particularly under partial shading conditions (PSCs).

Intelligent approaches, including fuzzy logic control (FLC) and artificial neural networks (ANNs), have been employed to handle nonlinearities and uncertainties in PV systems; however, they generally involve high computational complexity and substantial memory requirements, which may restrict real-time implementation.

Consequently, metaheuristic optimization algorithms (MOAs), inspired by natural and biological processes, have gained increasing attention due to their simpler structure, reduced computational burden, and strong global search capability. Algorithms such as particle swarm optimization (PSO), grey wolf optimization (GWO), whale optimization algorithm (WOA), and their hybrid variants have demonstrated improved robustness and reliable global maximum power point (GMPP) tracking under complex and PSCs, overcoming the limitations of conventional MPPT methods that tend to converge to local maxima [9].

Moreover, the control of SAPFs requires precise regulation of DC-link voltage (V_{dc}) and instantaneous power exchange with the grid. Conventional Proportional-Integral (PI) controllers, while simple to implement, often fail to deliver satisfactory dynamic performance, particularly during transient conditions or nonlinear disturbances [10].

To overcome these limitations, advanced control techniques such as Fractional-Order PI (FOPI) control [11], Backstepping control (BC), and Sliding Mode Control (SMC) have been developed [12]. These methods offer faster response, improved robustness, and enhanced harmonic compensation capability compared to classical control approaches.

The combination of these technologies—metaheuristic MPPT optimization, advanced SAPF control, and real-time implementation—forms the foundation of this thesis. The proposed system aims to enhance both energy extraction and power quality, enabling the GCPV–SAPF system to operate efficiently under diverse environmental and grid conditions.

II. Problem statement

Despite the significant progress in PV integration and active power filtering technologies, several persistent challenges continue to limit the optimal performance of GCPV–SAPF systems. These challenges can be broadly categorized into three main areas: energy extraction efficiency, power quality management, and system control robustness.

1. MPPT under PSCs:

Among the most critical issues affecting PV system efficiency is the accurate and stable tracking of the MPP, particularly under PSCs. Shading, which can result from environmental factors such as passing clouds, dust accumulation, or nearby obstacles, leads to the appearance of multiple local maxima on the P–V curve. Under these conditions, conventional MPPT algorithms, such as P&O and INC, often converge to local maxima instead of the global optimum [13].

This behavior causes a significant reduction in harvested energy and deteriorates overall system efficiency. Furthermore, under dynamically changing irradiance, these conventional algorithms often exhibit slow response, poor adaptability, and increased oscillations around the operating point, which can result in frequent power fluctuations and instability in the V_{dc}.

2. Power quality deterioration in GCPV–SAPF system operation:

In GCPV–SAPF systems, the interaction between the PV converter, nonlinear loads, and grid interface contributes to deterioration in PQ. The presence of nonlinear loads generates current harmonics and reactive power components, which distort the grid current waveform and reduce the system's overall power factor (PF) [2].

Additionally, the switching behavior of power electronic converters introduces high-frequency harmonics that can propagate into the grid, violating established PQ standards such as IEEE 519. These distortions may also cause overheating in electrical equipment, malfunctioning of sensitive loads, and increased losses in transmission lines [3].

Although passive filtering solutions can mitigate some harmonic components, they are limited by bulky components, fixed compensation characteristics, and potential resonance issues. Maintaining high power quality under dynamic grid and load variations remains a persistent challenge that requires precise and adaptive control of the active power filtering stage.

3. Limitations of conventional control strategies:

Conventional control strategies employed in GCPV–SAPF systems, including PI-based regulators, classical direct power control (DPC), and direct current control (DCC) methods, exhibit several inherent limitations when applied to highly nonlinear and dynamic operating environments. PI controllers, commonly used for DC-link voltage regulation, rely on fixed control parameters, which makes them sensitive to parameter variations, system nonlinearities, and external disturbances. As a result, they often suffer from poor transient performance, overshoot, and slow recovery under rapidly changing operating conditions [14].

Likewise, classical DPC and DCC approaches, which typically depend on predefined switching tables or hysteresis-based control mechanisms, are associated with variable switching frequency, increased power and current ripples, and limited robustness under grid disturbances. These drawbacks lead to fluctuations in instantaneous active and reactive powers (P and Q), degraded current waveforms, and increased total harmonic distortion (THD). Consequently, ensuring stable operation, accurate power control, and low harmonic distortion under dynamic grid and load conditions remains a critical challenge.

4. Real-time implementation and validation:

A large portion of the existing research on GCPV–SAPF systems remains confined to simulation-based validation. While simulations provide valuable insights into control behavior, they often neglect practical issues such as sensor noise, computational delays, switching nonlinearities, and hardware constraints, which can significantly affect the real-time performance and stability of the proposed control strategies.

Real-time implementation and validation are essential to bridge the gap between theoretical models and practical applications. Without experimental verification, the accuracy, robustness, and efficiency of control techniques under hardware constraints, sensor noise, and computational delays cannot be reliably guaranteed. Furthermore, limited real-time validation restricts proper assessment of system performance with respect to international grid standards, thereby limiting the practical feasibility of advanced control approaches for large-scale deployment.

In summary, the main challenges in GCPV–SAPF systems can be outlined as follows:

- The inability of conventional MPPT algorithms to effectively track the global maximum power point (GMPP) under partial shading and dynamic irradiance conditions.
- Degradation of PQ due to harmonics, reactive power imbalance, and switching-induced distortions.
- Limited adaptability and robustness of classical control strategies under nonlinear and time-varying operating conditions.
- Lack of comprehensive real-time experimental validation for advanced control and filtering strategies.

Addressing these unresolved issues is essential for improving energy extraction efficiency, enhancing PQ, and ensuring stable and reliable operation of modern GCPV–SAPF systems.

III. Objectives of the thesis

The overarching aim of this research is to develop, optimize, and experimentally validate an intelligent and robust control framework for a GCPV–SAPF system. The proposed framework aims to achieve maximum energy extraction, superior power quality, and enhanced dynamic performance under both standard and disturbed operating conditions.

This thesis seeks to bridge the gap to experimental validation by integrating metaheuristic optimization, advanced control techniques, and real-time implementation into a unified GCPV–SAPF system.

- **Objective 1: Comprehensive review and identification of research gaps**

The first objective of this research was to conduct an extensive literature review on photovoltaic (PV) systems, PQ issues, and harmonic mitigation techniques. This review involved a critical analysis of existing MPPT algorithms, converter control approaches, and active filtering strategies.

The study revealed that conventional MPPT algorithms such as P&O and INC often fail under PSCs due to their inability to escape local maxima on the P–V curve. Likewise, classical control schemes, such as DPC and conventional PI regulators, tend to suffer from variable switching frequencies, high power ripples, and limited adaptability to nonlinear and time-varying systems.

These findings highlighted significant research gaps in terms of global optimization capability, control robustness, and real-time experimental validation. Addressing these limitations motivated the development of the advanced hybrid optimization and control solutions presented in this thesis.

- **Objective 2: Modeling of the GCPV-SAPF system**

The second objective was to develop a comprehensive mathematical model of the GCPV–SAPF system. The model incorporated detailed representations of the PV array, DC–DC and DC–AC converters, and grid interface.

To support laboratory experimentation, an implicit electrical model of the PV array was developed to reproduce its dynamic behavior in real time. This model was implemented as a PV emulator using a Lookup Table (LUT)– based approach that generates the corresponding voltage–current (V–I) characteristics under varying irradiance conditions.

The developed emulator enabled flexible, repeatable, and safe testing of the proposed control and optimization algorithms without relying on physical PV panels. It also provided a controlled environment for evaluating system performance under different shading patterns and environmental variations.

- **Objective 3: Development of advanced MPPT algorithms using metaheuristic optimization**

The third objective was to design and compare advanced MPPT algorithms based on metaheuristic optimization to overcome the limitations of conventional techniques under PSC and dynamic irradiance conditions. These algorithms were developed to enhance tracking accuracy, minimize steady-state oscillations, and accelerate convergence toward the GMPP.

The following optimization methods were implemented and analyzed:

- Zebra Optimization Algorithm (ZOA)
- Grey Wolf Equilibrium Optimizer (GWEO)
- Hybrid GWO–PSO algorithm

- **Objective 4: Design of advanced control strategies for SAPF and DC-link regulation**

The fourth objective of this thesis was to design advanced control strategies for the SAPF to ensure improved power quality and dynamic stability. The P-DPC method was implemented to enhance both transient and steady-state performance of the SAPF. This control approach is designed to estimate instantaneous power variations and select the optimal switching state to regulate active and reactive powers (*P* and *Q*), aiming to maintain a fixed switching frequency, minimize THD, and provide faster transient responses compared with conventional DPC methods.

To further improve DC-link voltage regulation and robustness, a Fractional-Order PI (FOPI) controller with an anti-windup mechanism was designed. This controller offers superior tuning flexibility and adaptability to nonlinear operating conditions compared with classical integer-order PI regulators, thus ensuring stable operation under fluctuating grid and load scenarios.

➢ **Objective 5: Optimization of controller parameters using metaheuristic algorithms**

The fifth objective of this thesis was to optimize the controller parameters to achieve superior transient and steady-state performance. Manual tuning of controller parameters is often inefficient, time-consuming, and prone to inaccuracies. Therefore, the ZOA was employed to automatically tune the parameters of the FOPI-AW controller within the P-DPC framework.
The tuning process was formulated as a multi-objective optimization problem, aiming to:

- Minimize DC-link voltage overshoot,
- Reduce THD of the supply current,
- Minimize steady-state voltage error in the DC-link regulation loop, and
- Enhance transient response, stability, and robustness under varying operating conditions.

➢ **Objective 6: Experimental implementation and performance validation**

The final objective of this thesis was to carry out the real-time experimental implementation and validation of the proposed GCPV–SAPF system using a dSPACE DS1104 platform. A laboratory-scale prototype was developed to evaluate the proposed optimization and control strategies under standard test conditions (STC), partial shading conditions (PSCs), and dynamic shading conditions (DSCs), as well as under nonlinear and time-varying loading conditions.

A programmable PV emulator, based on the developed lookup table (LUT) model, was employed to reproduce realistic PV behavior under different irradiance profiles. In addition, a high-precision power analyzer was used for real-time measurement and monitoring of the system variables.

The experimental evaluation focused on key performance indicators, including:

- Global MPPT efficiency and convergence speed,
- DC-Link voltage stability,
- THD of grid current,
- Reactive power compensation and power factor improvement,
- Dynamic performance under transient operating conditions.

IV. Structure of the thesis

The organization of this thesis consists of five core chapters. Chapter 1 provides a comprehensive literature review on photovoltaic (PV) systems, power quality issues, and harmonic mitigation techniques, setting the foundation for the research. Chapter 2 presents the detailed modeling of the GCPV–SAPF system, capturing its dynamic behavior and interactions with the grid. In Chapter 3, metaheuristic and hybrid optimization algorithms are developed to enhance MPPT performance for PV systems. Chapter 4 focuses on advanced control and regulation techniques for SAPF, ensuring improved power quality and system stability. Finally, Chapter 5 presents the experimental implementation and performance evaluation of the GCPV-SAPF, validating the proposed methods under real operating conditions. This structure ensures a logical progression from theory and modeling to algorithm development, control design, and practical validation.

Chapter 1:

Literature Review on Photovoltaic Systems, Power Quality Issues, and Harmonic Mitigation Techniques

1.1 Introduction

With the continuous increase in global energy demand and the growing interest in sustainable solutions, photovoltaic (PV) systems have emerged as one of the most attractive and widespread renewable energy sources (RESs) due to their high efficiency in generating clean and environmentally friendly energy. However, with this widespread deployment, whether in grid-connected or stand-alone applications, modern electrical power grids face increasing technical challenges related to efficiency, stability, and power quality (PQ).

One of the most critical challenges is PQ degradation, where nonlinear loads and the use of power electronic converters in PV systems lead to complex issues such as harmonic distortions, voltage fluctuations, frequency variations, and power factor (PF) deterioration. These disturbances not only reduce the efficiency of electrical systems but also affect grid reliability and shorten equipment lifespan, which has led to the establishment of international standards such as IEEE Std 519 and IEC 61000 to ensure compliance with PQ requirements.

To address these challenges, a variety of filtering techniques have been developed, including passive power filters (PPFs) for their simplicity and low cost, active power filters (APFs) for efficient dynamic compensation, and hybrid power filters (HPFs) that combine the advantages of both techniques to achieve superior performance.

This chapter provides a comprehensive review of the principles and technologies of PV systems, analyzes the PQ challenges faced by modern electrical grids, and discusses mitigation strategies ranging from conventional filtering techniques to advanced methods. Furthermore, it paves the way for a deeper understanding of modern trends in designing effective compensation systems aimed at ensuring grid stability and achieving high PQ.

1.2 Photovoltaic systems: principles and technologies

Over the last several decades, the world's demand for electricity, primarily sourced from consumption of fossil fuels, including natural gas, oil, and coal, has been rising steadily [1]. However, burning these resources releases harmful byproducts that exacerbate problems such as global warming and air pollution, which are detrimental to both ecosystems and human life [13]. Due to these issues, an increasing number of people are becoming interested in RES, with solar photovoltaic (PV) technology emerging as a leading solution [8].

The term "photovoltaic" originates from the Greek words “photo,” which means light, and “voltaic,” referring to electricity [15]. Photovoltaic (PV) technology involves the direct conversion of solar radiation into electrical energy using semiconductor materials, a process known as the photovoltaic effect [9]. This phenomenon was first discovered in 1839 by Antoine Becquerel, the grandfather of Henri Becquerel, who later discovered radioactivity in 1896 [15].

PV systems are a long-term and effective way to address the growing need for electricity. Because they have no moving parts, they are highly reliable and require minimal maintenance. Additionally, they produce no noise and require only sunlight to power generation. The solar cell, typically built from silicon-based materials, is the most crucial component of a PV system. These cells are assembled into modules, which can then be combined into larger arrays to meet various power demands [16].

The Global Solar Energy Council (GSEC) and the European Photovoltaic Industry Association (EPIA) have conducted recent statistical analyses that show the worldwide photovoltaic (PV) capacity has been growing steadily and significantly [1,17]. According to recent data, the global installed PV capacity expanded from about 8 GW in 2007 to approximately 515 GW by 2018, and continued its rapid growth to exceed 2,240 GW by the end of 2024, as illustrates in Figure 1.1. Projections suggest that global PV capacity could approach 2,500 GW by 2025 [18].

Notably, the year 2024 marked a record-breaking milestone, with 602 GW of new PV capacity added worldwide [18]. This rapid acceleration in deployment can be attributed to several key factors: the continuous reduction in the cost of PV modules, improvements in system efficiency, and favorable regulatory policies under international agreements, such as the Kyoto Protocol [1]. These developments underscore the crucial role of solar PV technology in driving the global transition toward clean and sustainable energy sources.

Furthermore, PV systems offer flexibility in scale and application. They can be easily configured as small, low-power systems for individual use or as large, high-power installations for utility-scale generation, often at lower costs compared to other renewable technologies [17]. Based on their integration with the electrical grid, PV systems are generally categorized into two main types: stand-alone (off-grid) systems and grid-connected systems.

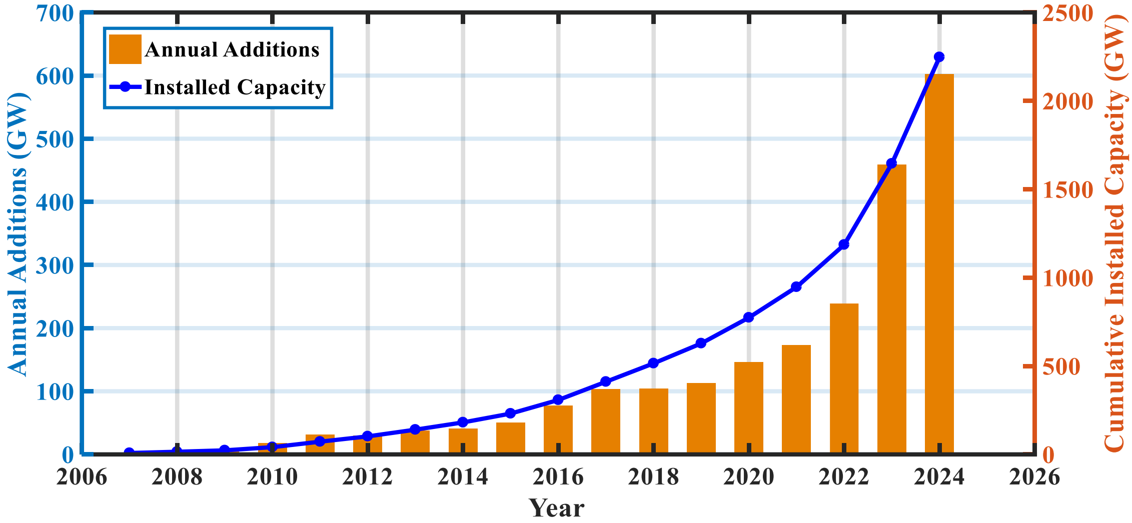

Figure 1.1: Global installed solar PV capacity and annual additions (2007–2024) [17]

There are two basic types of photovoltaic systems: stand-alone (off-grid) systems and grid-connected (on-grid) systems [2]. In grid-connected systems, the PV array is connected directly to the public energy grid. The electricity generated by the PV modules is converted into alternating current (AC) using power electronic devices, primarily inverters, and then fed into the utility grid. These systems typically incorporate components such as filters and control units to ensure efficient and stable integration [19].

GCPV systems can be further divided into distributed generation and centralized power systems. Distributed systems are installed to supply electricity either to local consumers connected to the grid or directly to the grid itself. Centralized systems, on the other hand, are generally implemented at a larger scale with the primary goal of reducing greenhouse gas emissions from conventional, fossil-fuel-based energy sources [1].

In contrast, stand-alone PV systems operate independently of the utility grid and rely on energy storage units, such as batteries, to ensure a continuous and reliable power supply during periods of low solar irradiance or nighttime operation [19]. These systems are typically deployed in remote or isolated areas where grid connection is unavailable or economically impractical. In such configurations, the PV generator supplies either DC loads directly or AC loads through a power conditioning unit. Stand-alone PV systems are commonly applied in small-scale applications, including rural electrification, telecommunications, and solar-powered water pumping systems [17].

1.2.1 Overview of Off-grid photovoltaic systems: design, uses, and benefits

Stand-alone PV systems, often known as off-grid systems, are intended to operate independently of the public electrical grid. These systems are often set up to fulfil specified DC and/or AC power requirements [20]. A typical stand-alone PV system consists of major components such as solar panel arrays, power electronic converters, and energy storage devices. These elements collectively facilitate the conversion of solar energy into electrical power, which is then used either to supply electrical loads directly or to charge storage systems [1].

Stand-alone PV systems are a practical and cost-effective solution for supplying electricity in areas where grid connectivity is either unavailable or economically impractical, such as distant or rural areas. These systems have numerous uses, including solar home systems (SHS), domestic water pumping (DWP), livestock watering (LW), small-scale irrigation (SSI), and aquaculture (fish farming) [17].

Stand-alone PV systems have several advantages, including a long operating lifespan, the ability to provide continuous electricity to the load during solar hours, and low long-term maintenance requirements. These advantages make them a dependable and sustainable solution for decentralized power generation, as shown in Figure 1.2 [53].

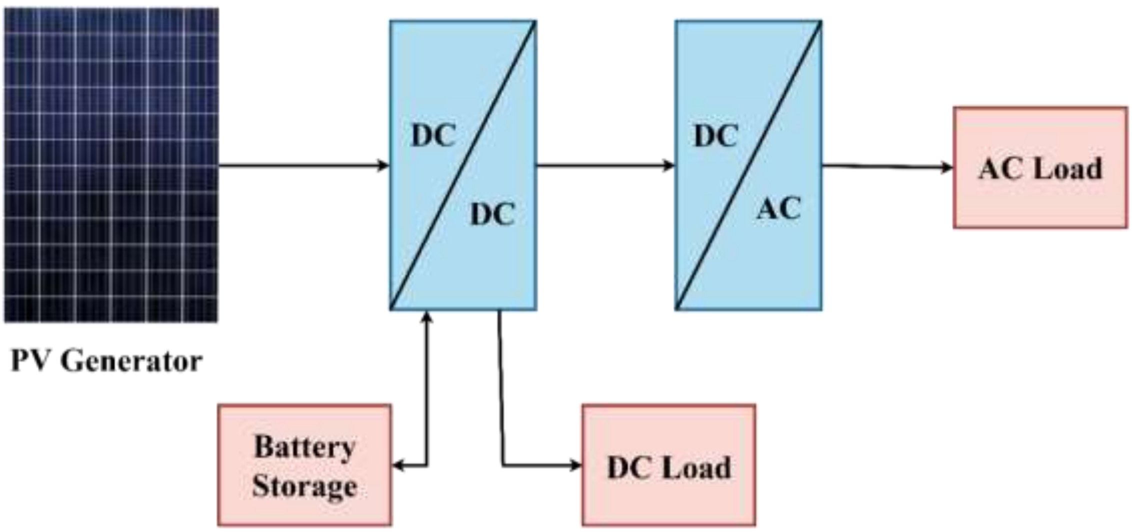

Figure 1.2: General configuration of a stand-alone photovoltaic (PV) system

1.2.2 Overview of grid-connected photovoltaic systems

The goal of GCPV systems is to inject the electricity generated by PV arrays into the public power grid. These systems are frequently connected to local distribution networks and are used in homes, businesses, and factories. They may considerably boost a country's overall energy production and are becoming increasingly important in today's modern power systems [1,21].

GCPV systems usually include more than one step of energy conversion, which is typically done using power electronic converters [19]. These stages are in charge of extracting maximum energy from the PV array and injecting it into the grid in a way that works. These systems contribute to decreasing reliance on fossil fuels and mitigating greenhouse gas emissions by providing power directly to consumers who are linked to the grid or in massive amounts to help the system [1,22].

Within grid-connected systems, the inverter serves as the primary component. It converts the DC from the PV modules into AC compatible with the utility grid. However, since inverters switch semiconductor devices at high frequencies, they also cause significant harmonic distortion [23].

To ensure safe, efficient, and standard-compliant operation, the integration of distributed energy resources (DERs), such as PV systems, into the grid is subject to various international standards. Among the most widely referenced are those established by the International Electrotechnical Commission (IEC) and the Institute of Electrical and Electronics Engineers (IEEE) [17,1].

Key operational parameters are defined to guarantee compliance with these standards, including:

- THD
- DC current injection limits
- Galvanic isolation requirements
- Anti-islanding protection
- Counter-voltage thresholds
- Frequency range constraints

This section provides a brief overview of the most relevant standards for GCPV systems, particularly IEC 61727 and IEEE 1547-2003. Additionally, Table 1.1 summarizes the key technical requirements outlined in these standards based on the aforementioned criteria [24].

Table 1.1: Summary of key technical standards and operating limits for grid-connected power systems

Criteria	IEC 61727	IEEE 1547-2003
THD	≤ 5% of rated current	≤ 5% of rated current (individual ≤ 3%)
DC current injection	≤ 1% of rated output current	≤ 0.5% of rated output current
Frequency range	49 – 51 Hz (for 50 Hz systems)	59.3 – 60.5 Hz (for 60 Hz systems)
Voltage range	85% – 110% of nominal grid voltage	88% – 110% of nominal grid voltage
Power Factor	≥ 0.9 lagging at rated power	Near unity unless required otherwise
Galvanic isolation	Required for transformerless inverters	Strongly recommended for personnel protection
Anti-islanding protection	Mandatory (disconnection within 2 seconds)	Mandatory (disconnection within 2 seconds)
Response to grid faults	Must disconnect within 2 seconds	Must disconnect within 2 seconds
Reconnection Delay	At least 180 seconds after grid restoration	5 minutes (adjustable)
Voltage Flicker	Should not exceed 3%	Minimal flicker required

1.2.2.1 Topological structures of grid-connected PV systems

The progress of power electronics has significantly improved the efficiency of using photovoltaic (PV) energy, making it possible to produce electricity at a high rate and deliver it straight to the utility grid. As a result, GCPV systems are now the most popular kind on the PV market. This popularity is primarily attributed to their cost-effectiveness, minimal maintenance requirements, and the fact that they do not require energy storage devices [22,17].

The primary electrical components of a GCPV system include PV arrays, power electronic converters (inverters), and grid filters. Among these, the power electronic stage plays a crucial role in both maximizing the energy extracted from the PV arrays and ensuring that the injected power meets grid quality standards in terms of voltage, frequency, and harmonic content [1].

GCPV system architectures are typically categorized according to the number of energy conversion stages into two main categories:

- Single-stage systems are those where a single power converter handles energy conversion and grid interfacing [17].
- Double-stage systems, which use separate converters for MPPT and grid synchronization and injection [17].

These two configurations form the basis for most modern power electronic topologies used in GCPV applications.

1.2.2.1.1 Topology of single-stage grid-integrated PV systems

A single-stage GCPV system operates with only one power conversion stage, typically a DC-AC inverter, which performs all critical control tasks, as shown in Figure 1.3. These include MPPT, regulation of output current and voltage, and compliance with grid connection, protection, and stability requirements [17]. The use of a single conversion stage offers significant advantages, such as reduced system weight, size, and cost. However, the simplicity of this topology limits its ability to optimize performance across all functions, particularly when balancing efficiency, dynamic control, and grid synchronization.

For effective implementation of this configuration, the input voltage of the inverter (PV output voltage) must exceed the peak grid voltage to enable proper energy injection into the grid.

This requirement can be fulfilled using one of the following approaches:

- Inserting a step-up transformer after the inverter to enable operation with a lower PV array voltage while still achieving the required grid voltage [1].
- Connecting a large number of PV modules in series to generate a PV array with a sufficiently high DC voltage that directly meets or exceeds the grid voltage requirements [22].

Both solutions are widely used in practice; nevertheless, each has limitations. The installation of a DC-DC converter increases the system's complexity, weight, and expense while also contributing to significant power losses [19]. Alternatively, connecting a large number of PV modules in series causes problems like:

- The risk of hot spots under PSCs,
- Safety concerns related to high-voltage operation,

- An increased likelihood of leakage currents due to parasitic capacitance between the PV panels and ground.

Moreover, both methods require sophisticated control strategies that integrate MPPT functionality with inverter control, increasing the overall control system complexity [1].

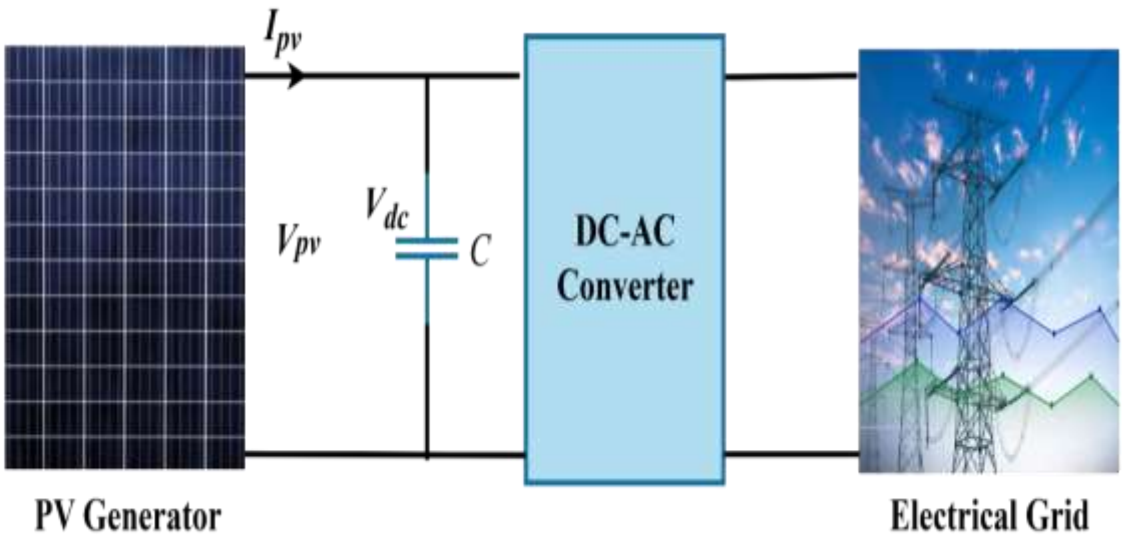

Figure 1.3: Configuration of a single-stage GCPV system

1.2.2.1.2 Topology of dual-stage grid-integrated PV systems

In a dual-stage (two-stage) GCPV system, energy conversion is divided into two distinct stages, as illustrated in Figure 1.4. The first stage typically consists of a DC-DC converter, which is responsible for boosting the PV array voltage and performing MPPT to ensure optimal energy extraction from the solar modules. The second stage involves a DC-AC inverter, which converts the regulated DC voltage into AC and injects the extracted power into the grid. This stage also controls the V_{dc} and regulates the grid current to comply with grid standards [2].

Compared to single-stage systems, the weight, size, and cost of the two-stage configuration are generally higher, owing to the presence of additional components and circuitry. This also leads to increased power losses within the conversion chain due to the multiple energy transformation stages [1].

Despite these drawbacks, two-stage systems are widely implemented because they offer several operational advantages. By decoupling the MPPT and grid current injection functions into two separate converters, the control design becomes more flexible and easier to manage. This architecture also enables the V_{dc} to be maintained above the grid's peak voltage, regardless of the specific PV array configuration or the level of solar irradiance and power generation [22]. As a result, two-stage systems are highly effective in maximizing energy harvesting and ensuring robust grid integration under varying operating conditions.

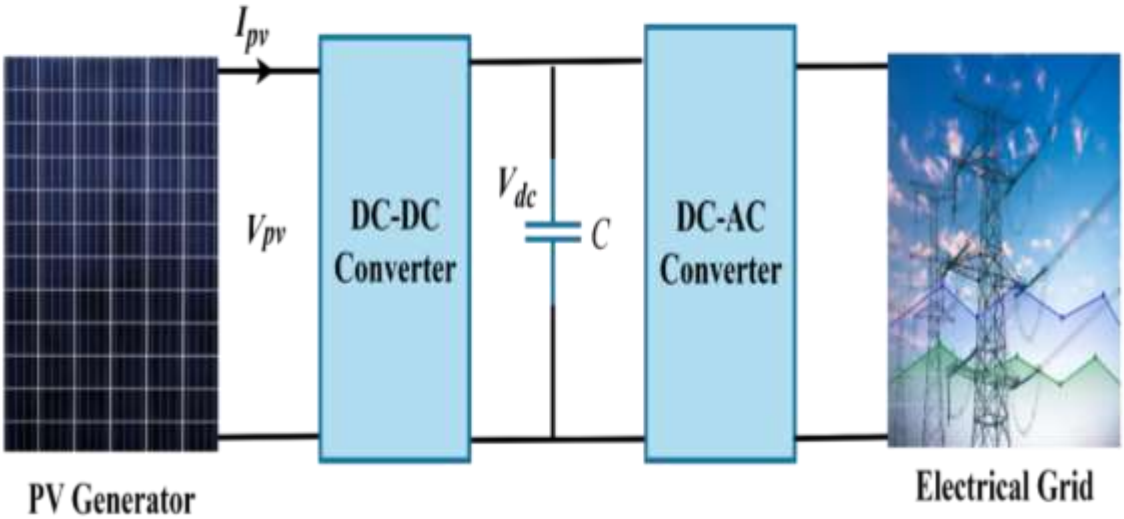

Figure 1.4: Configuration of a dual-stage GCPV system

1.2.3 Topologies of PV system

Various GCPV system topologies have been developed using both single-stage and two-stage configurations, especially for medium- and high-power applications. A key component of these systems is the inverter, which converts the DC output of the PV panels into AC that is synchronized with the grid. At present, three main inverter topologies are commonly used in PV power plants to provide efficient energy conversion: central inverters, string inverters, and multi-string inverters. Among these, multi-string configurations and central inverters combined with multiple MPPT controllers are the most widely employed solutions [25].

In centralized inverter systems, numerous photovoltaic (PV) modules are interconnected in series and parallel to form a large solar array, which is linked to the electrical grid via a single central inverter, as shown in Figure 1.5(a). This configuration is widely adopted due to its cost-effectiveness and ease of inverter maintenance. However, it also has notable limitations, such as lower reliability, since a failure in the central inverter causes the entire PV system to stop operating. Moreover, energy losses may arise from a mismatch between PV modules and partial shading, due to the use of a single MPPT mechanism, which can reduce the overall efficiency of power generation.

In string inverter configurations, several photovoltaic (PV) modules are connected in series to form individual strings, each associated with its own DC-AC converter, as illustrated in Figure 1.5(b). This topology enhances system reliability and efficiency since each string can independently track its MPP, thereby minimizing the adverse effects of partial shading. Moreover, the modular nature of the string architecture allows for easy system expansion by adding more strings to increase the total power capacity. However, this configuration is typically more expensive due to the higher number of inverters required [1,26].

In the multi-string inverter architecture, each photovoltaic string is paired with its own DC-DC converter, which performs MPPT and boosts the voltage level. These individual converters are connected to a single centralized DC-AC inverter via a shared DC bus, as depicted in Figure 1.5(c). This configuration merges the strengths of both string and centralized systems. It enhances energy output by allowing each string to operate independently at its optimal power point, while also reducing overall system cost through the use of a single inverter. However, this approach has slightly lower reliability than the string topology and introduces additional energy losses due to the presence of multiple DC-DC converters [1,17,22].

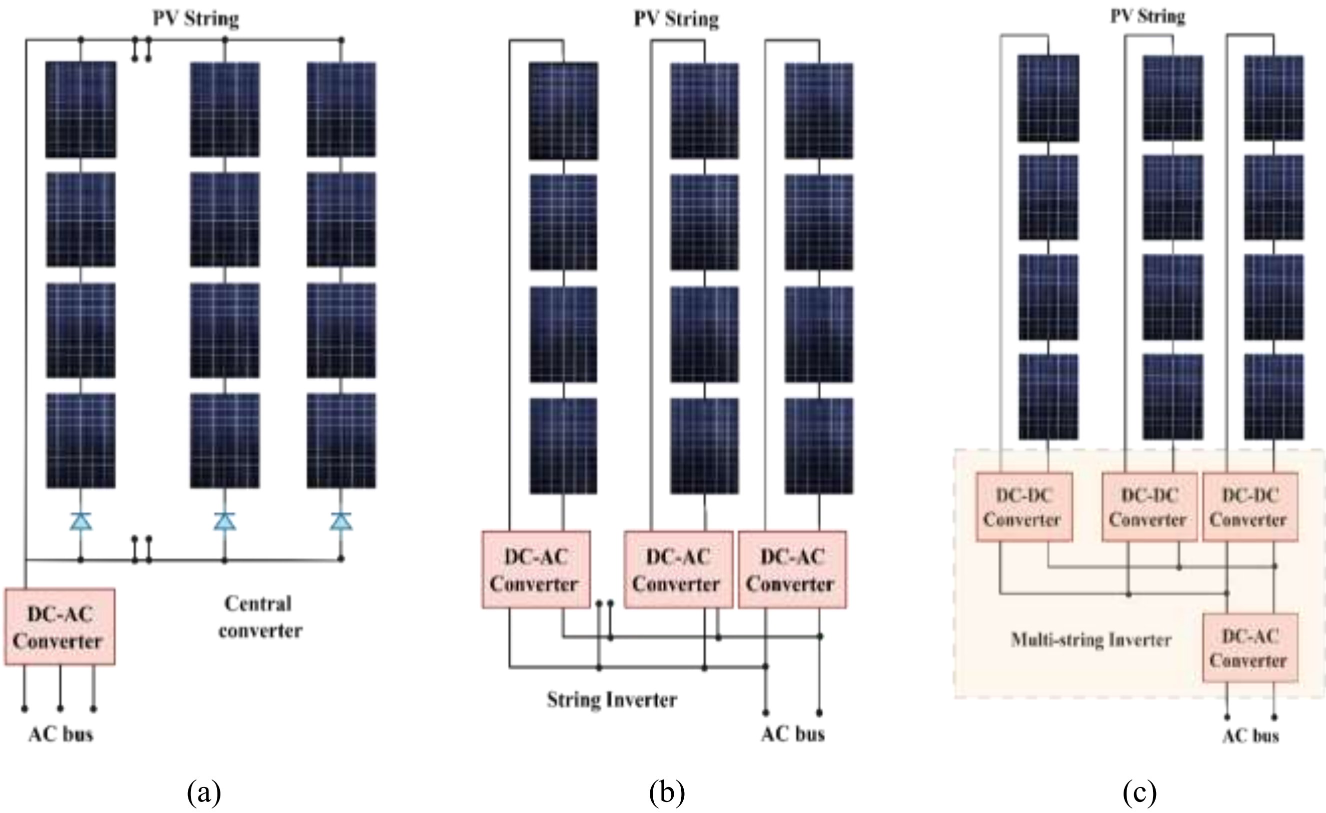

Figure 1.5: Topologies of GCPV systems: a) Central inverter configuration; b) String inverter configuration; c) Multi-string inverter configuration

1.3 Power quality issues in electrical networks

PQ denotes the capability of an electrical power system to deliver a clean, stable, and undistorted supply within defined standards for voltage, frequency, and waveform. These parameters must remain within acceptable limits to ensure the efficient and reliable performance of electrical equipment [24]. In a typical three-phase system, the critical characteristics include sinusoidal waveform, consistent frequency, and equal voltage amplitude across all phases. Poor PQ can significantly affect system performance, leading to decreased equipment efficiency, shortened lifespan, higher maintenance costs, operational failures, and safety concerns [22].

In the context of an idealized three-phase system, the three voltages are sinusoidal, equal in magnitude, and shifted by 120° (2π/3 rad) in phase. Any deviation from this ideal condition is classified as a power quality disturbance. Common disturbances include:

- Voltage sags and swells, usually triggered by faults, heavy load variations, or capacitor switching;
- Voltage interruption, either short- or long-duration, caused by faults, switching failures, protection actions, or external factors;
- Voltage imbalance, when three-phase voltages deviate in amplitude or phase (from 120°), typically caused by asymmetrical faults, unequal phase loads, or transformer and system issues;
- Voltage flicker, caused by load variations or equipment failures, leading to disturbances in electrical devices;
- Voltage frequency variation, resulting from rapid load changes;
- Harmonics, which are waveform distortions caused by the presence of higher-order frequency components whose values are integer multiples of the fundamental frequency [5].

PQ is an important challenge in electrical power generation and distribution systems. The extensive usage of power electronic gadgets typically makes this worse. These devices add harmonics to the system since they do not behave linearly [5]. This causes problems, including distortion in current and voltage waveforms and a lower PF. High levels of harmonics may mess with voice communication systems. These harmonics may cause joule losses, noise, and mechanical vibrations as they travel back to the power source via transmission lines. Also, they may make the voltage profile worse at various places on the network [24,27].

1.3.1 Harmonics in power systems: issues and effects

Nonlinear loads, especially those caused by power electronic converters, make power quality much worse by adding more harmonic pollution to the distribution network. This high harmonic content may cause equipment linked to the grid to stop working [24]. As a result, the problem has received significant attention, and many are working to develop ways to reduce or eliminate harmonic distortion. Many electrical loads linked to distribution systems, particularly those considered polluting, use reactive power and create imbalanced, unstable currents. The initial effect of this behavior is that generators, transformers, and transmission lines lose some of their ability to transmit and generate active power [27]. The second effect is voltage distortion or even voltage collapse if the coil resistance is very low. These nonlinear loads create current harmonics that spread across the electrical network, making the voltage profile even more distorted at many locations in the grid [1]. Harmonics are sinusoidal components at integer multiples of the fundamental frequency that combine with the main waveform to produce distortion. Figure 1.6 shows a distorted current waveform decomposed into its fundamental (50 Hz) and higher-order harmonics (3rd, 5th, 7th, and 9th), which are commonly caused by nonlinear loads. These harmonics degrade PQ, increase losses, and can damage sensitive equipment. The combined effect of these harmonic components forms the overall distorted signal [28].

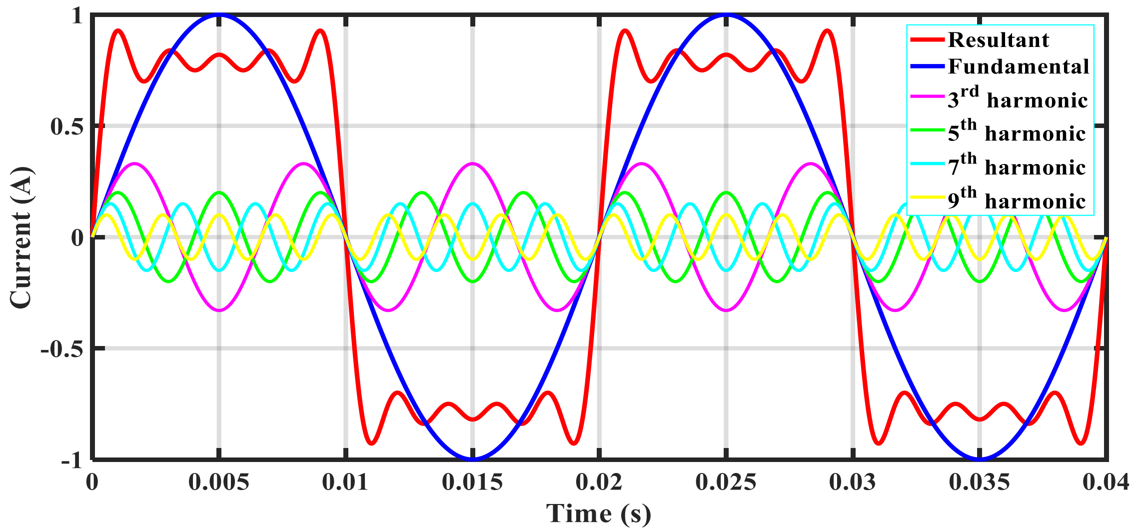

Figure 1.6: Example of a distorted sinusoidal waveform along with its fundamental component and selected harmonic components

Harmonics in electrical grids are mainly generated by nonlinear loads. These loads draw current in a way that is not proportional to the voltage supplied, which changes the fundamental waveform. Inverters, rectifiers, triacs, and diodes are all examples of static power conversion devices that are often employed in systems for controlling speed and power.

In homes, standard electrical devices like TVs, computers, fluorescent lights, and air conditioners that may change speed are also key generators of harmonics [28]. Electric arc furnaces, induction heating systems, and adjustable-speed motors may all cause much harmonic distortion in industrial settings, especially when they are under much stress [22,27]. Also, RES like wind and solar plants that use power electronic converters can exacerbate harmonics. Also, several physical factors, such as ferromagnetic resonance, magnetic core saturation, and asynchronous resonance, may make harmonics stronger. These distortions lower the quality of electricity and have several harmful effects:

- Decrease in power factor due to the presence of reactive power in the electrical network.
- Overheating of conductors, cables, capacitors, and rotating machines caused by additional copper and iron losses.
- Errors and inaccuracies in measurement devices.
- Heating and degradation of transformer insulation.
- Electromagnetic interference with communication networks due to coupling between power and telecom systems, leading to noise issues.
- Resonance between transformer inductance and cable capacitance can align with harmonic frequencies, causing significant amplification and potential equipment damage.
- Disturbance of control systems, such as thyristor switching errors during voltage zero-crossing.
- Audible noise is generated in transformers and inductors due to harmonic effects [24].

1.3.1.1 Harmonic characterization

Accurately analyzing the behavior of harmonics in a system is essential for precisely measuring harmonic voltages and currents [27]. Various criteria can be used to assess these disturbances, the most commonly employed being the nth-order harmonic rate, the THD, the power factor (PF), and the crest factor (CF).

A. Total Harmonics Distortion (THD)

THD is a common and important way to measure harmonic distortion in voltage or current. It makes it easier to systematically and fairly compare the quality of power systems. It measures how much a signal deviates from a perfect sine wave because of the harmonics [22]. THD is defined as the square root of the sum of the mean-squared values of all harmonic components, divided by the mean-squared value of the fundamental component. *THDv* stands for voltage distortion, while *THDi* stands for current distortion [27]. Equations (1.1 and 1.2) defines both quantities:

$$THDv(\%) = \frac{\sqrt{\sum_{h=2}^{\infty} V_h^2}}{V_1} * 100 \tag{1.1}$$

$$THDi(\%) = \frac{\sqrt{\sum_{h=2}^{\infty} I_h^2}}{I_1} * 100 \tag{1.2}$$

B. Crest Factor (CF)

The CF of a signal is expressed as the ratio of its peak current or voltage to its root mean square (RMS) value. For voltages or currents that are purely sinusoidal, the CF is 2. For signals that are not sinusoidal, it might be more or less than 2. In the case of highly distorted waveforms, the CF can reach values up to 5 [27]. Equation (1.3) shows it.

$$CF = \frac{X_{\max}}{X_{RMS}} \tag{1.3}$$

C. Power Factor (PF)

PF is mathematically represented as the ratio of the active power (*P*) delivered to the load to the apparent power (*S*). It reflects how efficiently electrical energy is converted into practical work. PF is not merely the cosine of the phase angle between voltage and current; it is also referred to as the distortion factor (DF) and coincides with PF only in the case of linear loads supplied with purely sinusoidal voltages and currents [24,27]. A low PF results in inefficient device operation [22]. For a sinusoidal signal, the PF is expressed as:

$$PF = \frac{P}{S}$$
$$PF = \frac{P}{\sqrt{P^2 + Q^2}} \tag{1.4}$$

The S is expressed as:

$$S = V_{RMS}.I_{RMS}$$
$$\mathrm{S} = V_{RMS}\cdot\sqrt{\frac{1}{T}\int_0^T i^2 dt} \tag{1.5}$$

The P and Q are defined by the following expressions:

$$P = 3V_1 I_1 \cos\varphi_1 \tag{1.6}$$

$$Q = 3V_1 I_1 \sin\varphi_1 \tag{1.7}$$

Where, V_1 and I_1 represent RMS phase voltage and current of the fundamental harmonic.

In the presence of harmonics, an additional component known as the distortion power (D) arises. This power is given by the following relation:

$$D = V_{RMS}\cdot\sqrt{\sum_{n=2}^{\alpha} I_{Ln}{}^2} \tag{1.8}$$

The S can then be expressed as follows:

$$S = \sqrt{P^2 + Q^2 + D^2} \tag{1.9}$$

Therefore, the PF is given by the following expression:

$$PF = \frac{P}{\sqrt{P^2 + Q^2 + D^2}} \tag{1.10}$$

1.3.1.2 Standard regulations for limiting current and voltage harmonics

Various international organizations and institutions have developed documents aimed at regulating electrical power quality for both consumers and distributors, while also guiding suppliers and users on proper connection of electrical equipment [1].

These documents include:

- Guidelines offering detailed explanations and practical solutions.
- Recommendations suggesting preferred methods and practices.

- Formal, legally binding standards established between producers, consumers, and government authorities to ensure proper and efficient electricity generation and consumption

The primary objectives of these documents are to minimize harmonic disturbances, standardize terminology and procedures, and promote compatibility between producers and consumers, thereby maintaining stable and reliable power quality.

The Institute of Electrical and Electronics Engineers (IEEE) provide practical guidelines and standards for controlling harmonics and compensating for reactive power in static transformers in electric power systems. This standard applies to both power providers and end users, and it covers all power ratings. It establishes limitations on harmonics depending on the ratio of the short-circuit current at the grid connection point to the base load current.

IEEE Std-519—Standard for harmonic control in electric power systems is an important resource in the subject of power quality [24,29]. It provides instructions for how to design power systems so that power sources and loads may interact with each other in the right way. The IEEE 519-1992 version sets the highest levels of distortion that may be tolerated in an electrical system. For most circumstances, the THD should not be more than 5%, and for systems running at voltages of 69 kV or more, it should not be more than 3%. Tables 1.2 and 1.3 present the allowable limits for odd-order harmonic current distortion (THD%) at the point of common coupling (PCC), categorized according to the system voltage level and the ratio of short-circuit current to load current [22,30].

Table 1.2: Allowable voltage distortion levels

Voltage level at PCC	Individual voltage distortion (%)	Total voltage distortion THD (%)
Up to 69 kV	3.0	5.0
From 69.001 kV to 161 kV	1.5	2.5
Above 161 kV	1.0	1.5

Table 1.3: Summary of maximum allowable harmonic current distortion by system voltage level and short-circuit ratio includes limits for odd-order harmonics and THD as specified by IEEE 519-1992

System voltage level	I_{SC}/I_L	h < 11	11 ≤ h < 17	17 ≤ h < 23	23 ≤ h < 35	h ≥ 35	THD%
Distribution (120 V - 69 kV)	< 20	4.0	2.0	1.5	0.6	0.3	5.0
	20 – 50	7.0	3.5	2.5	1.0	0.5	8.0
	50 – 100	10.0	4.5	4.0	1.5	0.7	12.0
	100 –1000	12.0	5.5	5.0	2.0	1.0	15.0
	> 1000	15.0	7.0	6.0	2.5	1.4	20.0
Sub-transmission (69.001 kV – 161kV)	< 20	2.0	1.0	0.75	0.3	0.15	2.5
	20 – 50	3.5	1.75	1.25	0.5	0.25	4.0
	50 – 100	5.0	2.25	2.0	0.75	0.35	6.0
	100 –1000	6.0	2.75	2.5	1.0	0.5	7.5
	> 1000	7.5	3.5	3.0	1.25	0.7	10.0
Transmission (> 161 kV)	< 50	2.0	1.0	0.75	0.3	0.15	2.5
	≥ 50	3.0	1.5	1.15	0.45	0.22	3.75

Where, I_{SC} is the available short-circuit current at PCC, and I_L is the maximum load current of the user.

1.4 Mitigation strategies for harmonic disturbances in electrical systems

There are several ways to make up for reactive power in electrical networks to improve the PF, reduce losses, and keep the voltage stable. One way to do this is to use sinusoidal current absorption, which tries to make the current drawn seem like a pure sinusoidal waveform with a PF of 1 [24]. This is typically achieved using PWM. Smoothing inductors are also used to reduce higher-order harmonics by raising impedance at higher frequencies. Using filters to eliminate harmonics is one of the best ways to improve power quality [27]. The filter operates by injecting a compensatory current that cancels out the load current's harmonic components, as shown in Figure 1.7.

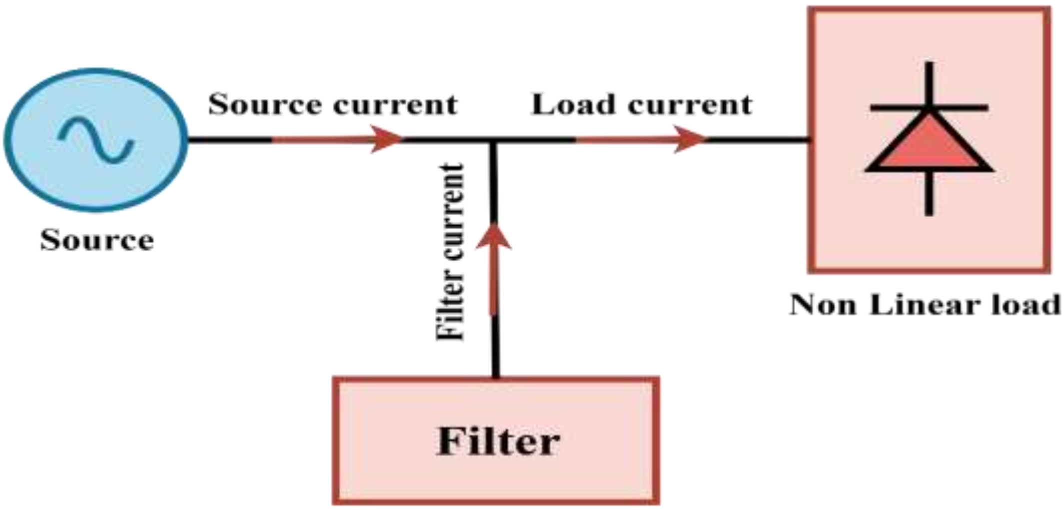

Figure 1.7: Basic operation of a filter

Filters can generally be classified into three main categories: active power filters (APFs), passive power filters (PPFs), and hybrid power filters (HPFs). Each category includes specific subtypes, as illustrated in Figure 1.8.

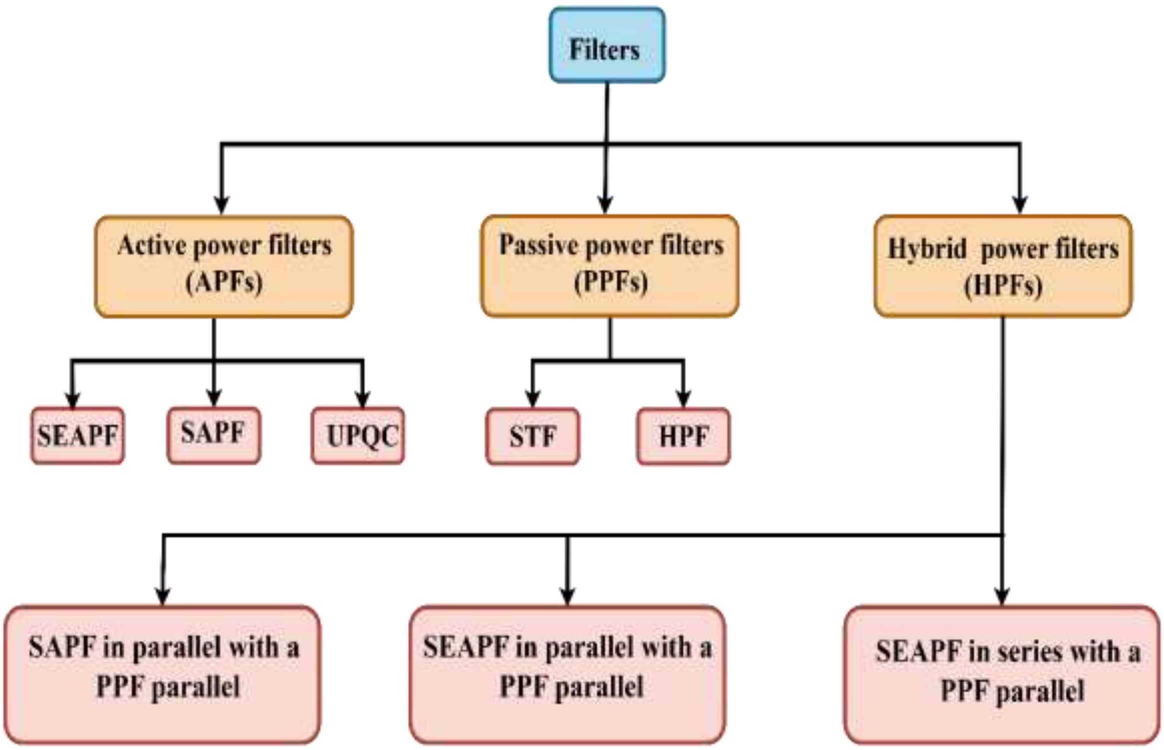

Figure 1.8: Filters classification

1.4.1 Passive power filters (PPFs)

PPFs are a traditional yet effective way to reduce harmonic distortion and address the long-standing problem of parallel resonance. They function by changing the impedance of the network in a specific area, which changes the flow of harmonic currents and lowers the voltage of harmonic currents [22]. These filters are made up of passive parts like capacitors, inductors, and resistors. They not only reduce harmonics but may also provide reactive power compensation. However, their performance depends a lot on the impedance of the system. Figure 1.9 illustrates the types of passive filters and their various configurations [15].

Among passive filters, the single-tuned filter (STF) is an LC-type passive filter that is regarded for its simplicity and its ease of combination with other ways to reduce harmonics. It has a low impedance at a specific harmonic frequency, which lets harmonic currents flow through it easily and reduces distortion in the system. To enhance the PF at the fundamental frequency, it is important to choose the correct value for the capacitor [15].

High-pass filters (HPFs), on the other hand, are designed to get higher-order harmonics. They are available in different configurations: first, second, and third order. The second-order high-pass filter (HPF) is the most commonly used type because it strikes the best balance between ease of use and filtering power. The third-order HPF is more effective at reducing harmonics. However, it is not often used in low-voltage applications since it is more complicated, costs more, and offers no practical advantage in these cases [15,27]. As summarized in Table 1.4, the main advantages and disadvantages of PPFs are compared to highlight their performance characteristics and inherent limitations.

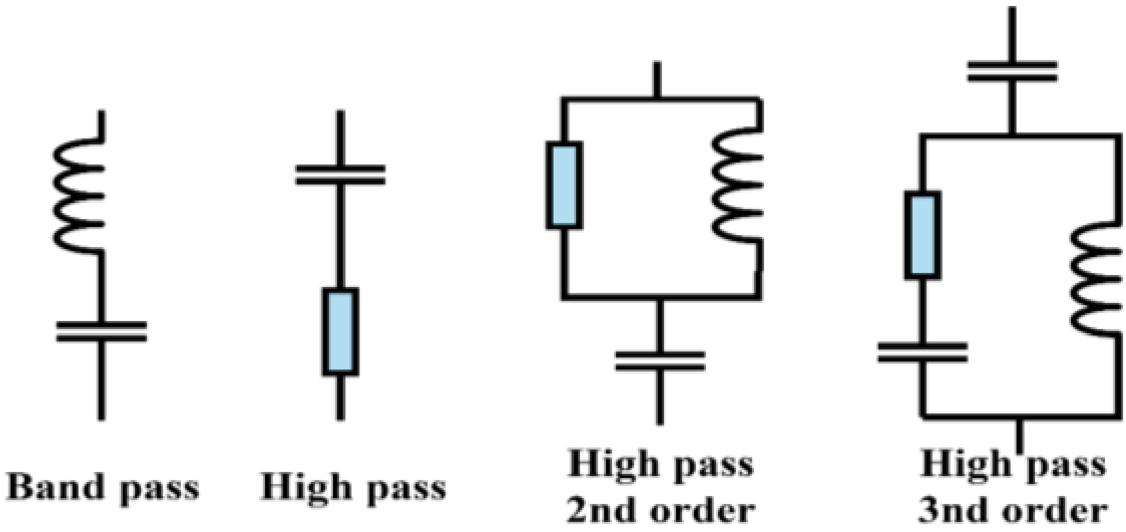

Figure 1.9: Configurations of PPFs

Table 1.4: Comparison of advantages and disadvantages of PPFs

	Aspect	Description
Advantages	Simple design	Straightforward structure, easy to implement without complex control strategies
	Low cost	Economical in both initial investment and operation
	Efficient performance	Effective in harmonic mitigation under stable operating conditions
	Easy integration	Can be easily integrated into industrial power systems
Disadvantages	Dependent on network impedance	Filtering performance is highly sensitive to the grid impedance
	Lack of adaptability	Cannot respond to load variations or component aging (e.g., heating, drift)
	Resonance issues	Risk of harmonic amplification due to resonance with the network
	Harmonic circulation	Identical-rank filters on the same network can cause harmful harmonic currents
	Requires detailed study	Proper design needs accurate grid parameters, which are not always available
	Bulky equipment	May require large components, especially for high-power applications
	Limited performance at low THD	Achieving low THD increases cost and complexity

1.4.2 Actives power filters (APFs)

To address the limitations of passive filters, power engineers have developed dynamic and adaptive solutions to enhance power quality. The APF is a well-known example that is being used increasingly in modern power systems. APFs were first developed in the 1970s [24]. They operate by employing a VSI to provide compensatory currents or voltages based on the grid's configuration. APFs maintain sinusoidal grid voltage and current waveforms by creating harmonic components that are the same size but out of phase with those generated by nonlinear loads, often achieving a unity PF [15].

The fundamental operating principle is the use of power electronics to make current components that cancel the harmonic distortions that nonlinear loads create. APFs can do more than reduce harmonics; they can also offer reactive power compensation, load balancing, voltage regulation, and neutral current management. APFs can be classified in several ways, including:

- **By Power System Type:**
  - Single-phase APFs—for low-power uses and home networks.
  - Three-phase APFs are for industrial and commercial applications that need more power.
- **By Connection Method:**
  - Shunt APFs — connected in parallel with the load. Their primary purpose is to fix the power factor and reduce current harmonics.
  - Series APFs — linked in series with the supply line and are used to get rid of voltage harmonics, sags, and swells.
  - Hybrid(series–shunt)) APFs— combine both types of APFs to deal with complicated power quality and harmonic problems.
- **By kind of converter:**
  - Voltage Source Inverter (VSI) – the most common kind since, it responds quickly to changes and has a high level of control.
  - Current Source Inverter (CSI) - not as prevalent; primarily used in specific industrial settings.

The best APF setup depends on the kind of harmonic distortion (voltage or current) and the operational requirements of the network [22,24,27].

1.4.2.1 Shunt active power filter (SAPF)

SAPF functions as a controlled current source, injecting harmonic components equal in magnitude but opposite in phase (180° phase shift) to those generated by the load. This process effectively cancels the load current harmonics, resulting in a sinusoidal source current and phase with the grid voltage. The SAPF is suitable for a wide range of load types and also improves the power factor. Structurally, it typically consists of a VSI and an inductive output filter, as illustrated in Figure 1.10 (a). The VSI-based SAPF configuration is currently the most widely used due to its well-established topology and simplicity of implementation [22,24].

1.4.2.2 Series active power filter (SEAPF)

SEAPF is an advanced solution to improve power quality, especially by mitigating voltage distortions. It is connected in series with the load and uses a controlled VSI to provide a compensatory voltage via a coupling transformer [27]. Its primary job is to protect the load from harmonics and distortions that come from the grid while making up for voltage drops, rises, and imbalances. This guarantees a perfect sinusoidal voltage waveform at the connecting point, which is excellent for sensitive loads. However, the SEAPF has limited capability in compensating harmonic currents and requires a highly efficient protection system to withstand short-circuit conditions, which adds complexity to its design and practical implementation [22]. A schematic diagram of the SEAPF is shown in Figure 1.10(b).

1.4.2.3 Unified power quality conditioner (UPQC)

UPQC is an advanced integrated device designed to enhance electrical PQ. It combines a SEAPF and a SAPF that are linked via a shared DC bus. This configuration makes it possible to fix various PQ issues at the same time, such as voltage dips, surges, and imbalances, as well as current and voltage harmonics. The series filter compensates for voltage problems, while the shunt filter eliminates current harmonics and provides reactive power compensation. UPQC is a fantastic way to improve power quality since it works well and can be used in various applications [22,27]. However, it needs more complex control techniques and costs more to install than regular active filters, which might make it harder for businesses to use on a large scale. Figure 1.10(c) shows how UPQC is built.

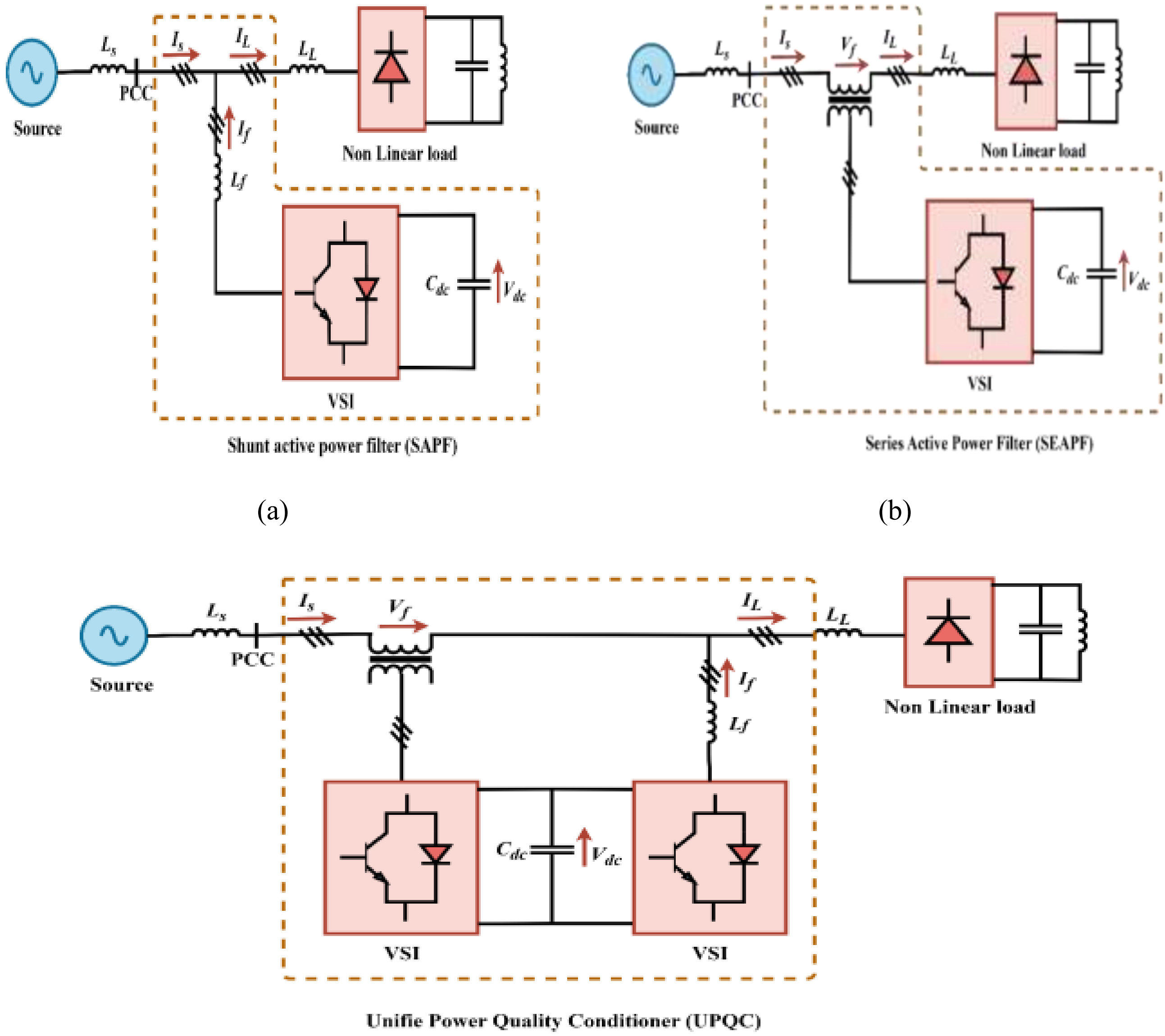

(c)

Figure 1.10: Topologies of active filters: a) SAPF, b) SEAPF, and c) UPQC

1.4.3 Hybrid power filters (HPFs)

HPFs are practical solutions to improve power quality since they combine the best features of both active and passive filters into a single configuration. Several arrangements are possible, the most common being:

- An APF connected in parallel with a PPF,
- An APF linked in series with a PPF, or

- A series-connected APF followed by a parallel PPF.

This combination allows for compensation across a broader range of harmonic frequencies. The PPF focuses on specific low-order harmonics, while the APF deals with the rest of the harmonic spectrum. This kind of integration makes system parts smaller, improves the overall system performance, and addresses the problems that PPFs have when circumstances change [22,24]. Figure 1.11 illustrates each of these filter configurations.

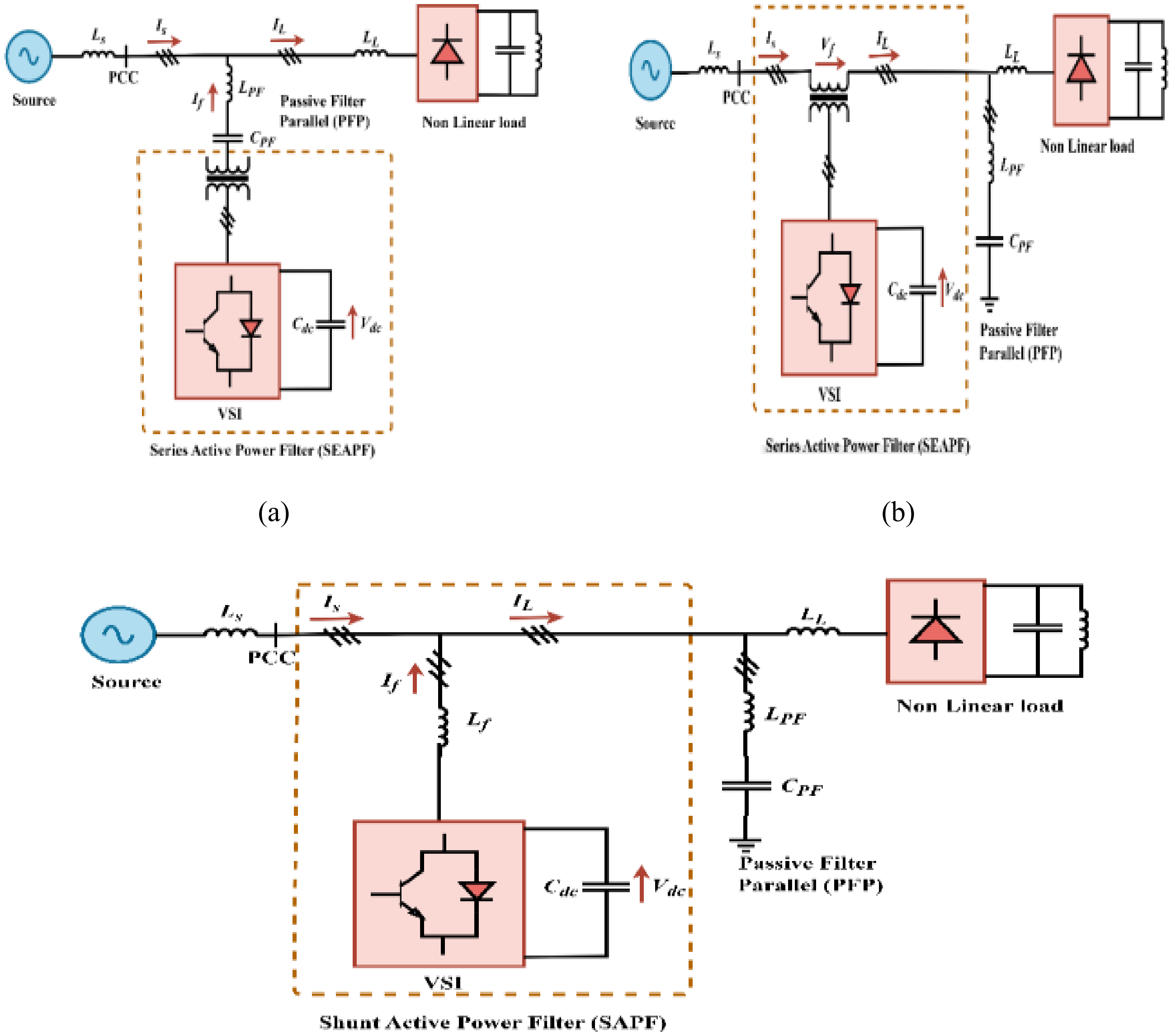

(a) (b)

(c)

Figure 1.11: Representative topologies of hybrid active power filters: a) series SEAPF combined with PPF, b) parallel SEAPF combined with PPF, and c) parallel SAPF combined with PPF

As illustrated in Table 1.5, the advantages and disadvantages of APFs are outlined to emphasize their operational capabilities and limitations.

Table 1.5: Advantages and disadvantages of APFs

Advantages of APFs	Disadvantages of APFs
A single filter can eliminate a wide range of unwanted harmonics	High initial cost limits their use in small-scale industrial applications
No resonance issues, enhancing power system stability	Higher power losses due to switching and semiconductor components
Capable of adapting to nonlinear and varying loads	Difficult to build high-power APFs with wide bandwidth and low losses
Fast dynamic response and wide compensation bandwidth	Requires complex control systems and real-time signal processing
Consumes negligible active power aside from internal component losses	The overall system cost remains higher compared to passive filters
Smaller physical size compared to bulky passive filter systems	Limited deployment due to investment and maintenance costs

1.5 Shunt active power filters (SAPFs): Structure and control strategies

In electrical power systems, SAPFs are widely employed to compensate for reactive power and eliminate current harmonics. Gyugyi and Strycula first introduced the concept of this type of filter in 1976 [22,27]. Recently, SAPF technology has been extensively studied and applied to mitigate harmonic currents generated by non-linear loads connected to electrical networks.

A SAPF consists of a multilevel inverter (MLI) connected in parallel with a non-linear load. The inverter injects a compensating current of the same magnitude but opposite phase to that of the harmonic current produced by the load, thereby cancelling it [22].

A VSI connected in parallel with the supply network through a low-pass filter (LF) at its output is the most common way to improve PQ. The main aspects of the general structure are:

- Voltage source
- R–L load bridge with diodes
- Multilevel inverter representing the SAPF

Figure 1.12 illustrates the schematic diagram of a SAPF. To generate control signals for the VSI, two basic functional blocks are required (Figure 1.13):

1. **Power Stage:**
    - A voltage source with switches that can be controlled (e.g., IGBT or GTO) and diodes that are anti-parallel.
    - Energy storage circuit, usually a DC-link capacitor.
    - A coupling filter reduces switching harmonics [22].
2. **Control Stage:**
    - DC-link voltage regulator keeps the reference value stable.
    - Control signals generation for inverter switches, which is frequently done with multilevel PWM.
    - System for synchronizing grids that usually uses Phase-Locked Loop (PLL) technology.

The control technique is just as important as the physical structure when it comes to making sure that reactive power is compensated for and harmonics are reduced [22,27]. Different control methods have been devised, each with its own rules, accuracy, and speed of response to changes:

- **Direct Power Control (DPC):** This method controls both active and reactive power directly by choosing the right inverter voltage vectors. It doesn't need a standard PWM stage. It has a simple math structure and a fast dynamic reaction.
- **Predictive Direct Power Control (PDPC):** An improved version of DPC that employs a predictive system model to choose the best voltage vectors, which makes control more accurate and cuts down on power ripples.
- **Direct Current Control (DCC):** This is all about directly controlling the reference compensating current that the filter will inject. It is one of the most common ways to do things because it is easy to use and works well with harmonic extraction methods.
- **Other methods:** These include PWM-based systems, linear controllers (PI, FOPI), fuzzy logic control, adaptive control, and hybrid methods that use more than one strategy to improve performance in different operating situations.

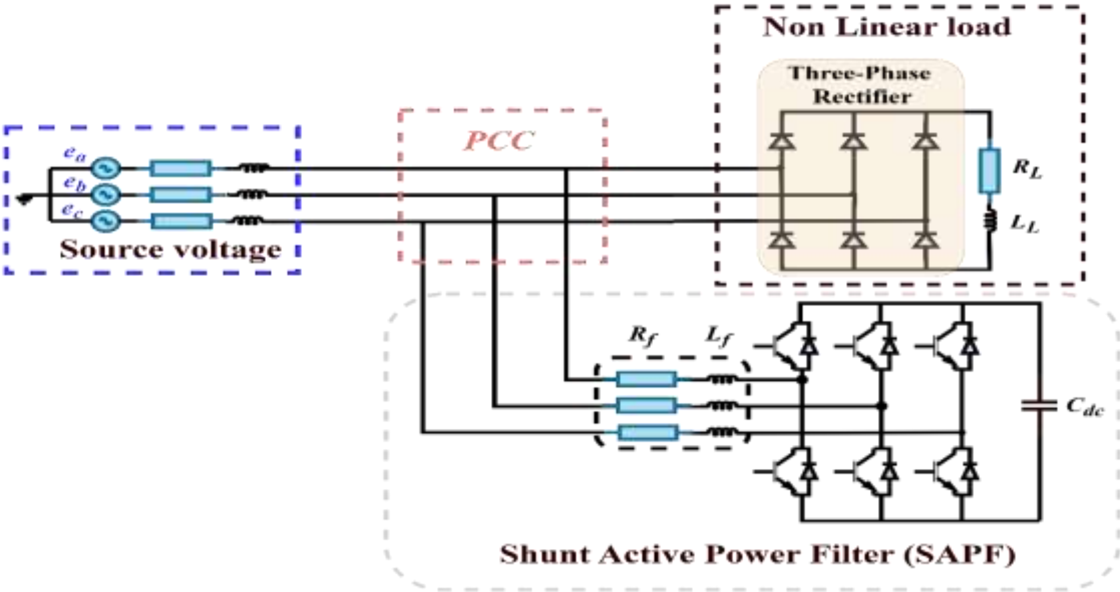

Figure 1.12: Structural Representation of a SAPF

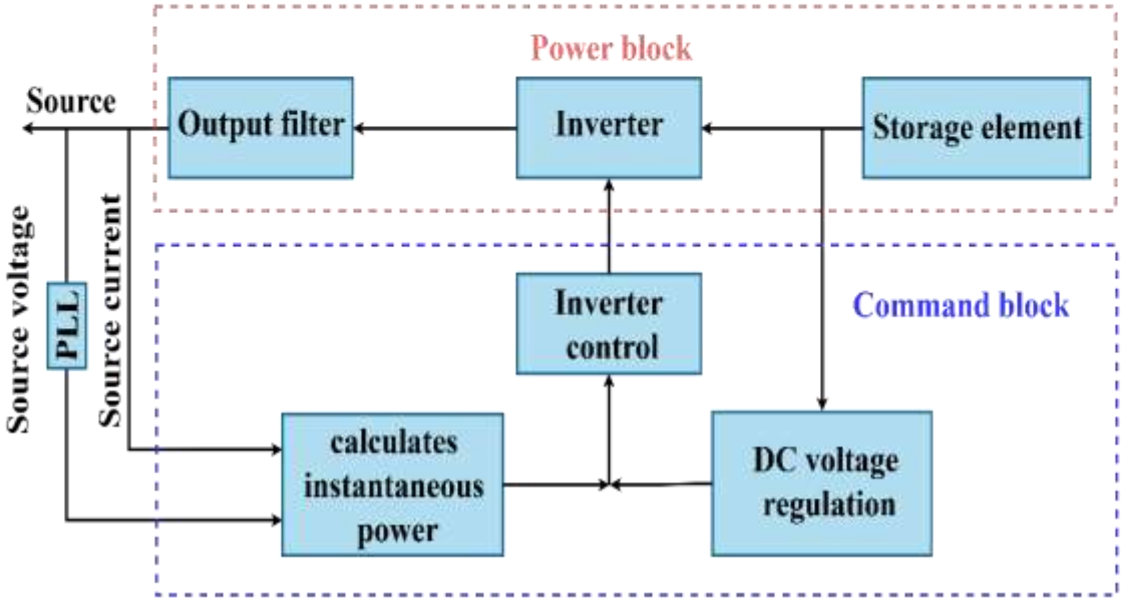

Figure 1.13: General structure and parameters of APFs

1.6 Conclusion

In this first chapter, we presented a comprehensive study of photovoltaic (PV) systems and the challenges associated with power quality in modern electrical networks. We began by highlighting the growing importance of PV energy and its integration in both stand-alone and grid-connected configurations, which play a significant role in meeting the global demand for clean and sustainable energy. However, the integration of PV systems also introduces several power quality issues due to the widespread use of nonlinear loads and power electronic converters. These issues manifest as harmonic distortions, voltage fluctuations, frequency deviations, and reduced power factor, which negatively impact the efficiency, stability, and reliability of electrical systems.

To address these challenges, we explored various compensation techniques. Conventional solutions, such as PPFs, were presented for their simplicity and low cost but showed limitations in dynamic environments. APFs were then discussed for their superior dynamic performance and effective compensation of a wide range of disturbances. Furthermore, HPFs were introduced as an optimized approach combining the advantages of both passive and active filtering, offering improved overall performance for power quality enhancement.

In addition, the chapter examined the classification and topologies of PV systems and provided an overview of SAPFs, including their structure and control strategies, highlighting their significant role in power quality improvement in GCPV systems.

Overall, this chapter establishes a solid foundation for the remainder of this thesis by introducing the fundamental concepts, key challenges, and state-of-the-art solutions related to PV integration and power quality enhancement. It also underscores the importance of advanced control techniques in achieving efficient, stable, and reliable operation of future energy system

Chapter 2:

Modeling of the Grid-Connected Photovoltaic System with SAPF

2.1 Introduction

The integration of photovoltaic (PV) systems into electrical grids has become a key solution for sustainable energy generation. However, the intermittent nature of solar irradiance and the nonlinear characteristics of PV modules necessitate accurate system modeling to enable reliable performance prediction and effective control design. A grid-connected photovoltaic (GCPV) system generally comprises a PV generator, power electronic converters, and a grid interface, all of which must be described using appropriate mathematical models for accurate analysis and simulation.

In this chapter, the studied GCPV–SAPF system is modeled. The system adopts a two-stage power conversion architecture consisting of a DC–DC boost converter, which regulates the PV output voltage and performs MPPT, and a three-phase voltage source inverter (VSI). The VSI is responsible for injecting the extracted PV power into the grid while simultaneously operating as a SAPF to mitigate current harmonics and compensate reactive power generated by nonlinear loads.

The chapter begins with the analytical modeling of the PV array using the single-diode equivalent circuit. The influence of irradiance, temperature, and series/parallel connections on PV performance is discussed, along with the effects of partial shading. An implicit PV model, in which the terminal voltage is numerically determined from the imposed current, is then developed to ensure compatibility with the emulator. In addition, a Lookup Table (LUT)-based approach is employed, where the P–V and I–V characteristics under different operating conditions are tabulated and used for fast and accurate system-level simulations in MATLAB-Simulink. This hybrid modeling strategy, combining analytical and LUT-based models, ensures both high accuracy and computational efficiency.

Subsequently, the models of the boost converter, inverter, and SAPF are presented, together with the sizing of their key electrical components. Finally, it should be noted that while this chapter focuses on system modeling, the design and operation of the MPPT controller for the boost converter and the SAPF controller for the inverter will be presented in detail in the following chapters.

2.2 Studied grid-tied PV system with SAPF

The studied GCPV–SAPF system is designed to ensure effective renewable energy integration while simultaneously improving power quality through the use of a SAPF. Figure 2.1 shows the general configuration of the proposed system, highlighting the interaction between its main components and their combined role in power injection, mitigation of harmonic distortion and compensation of reactive power.

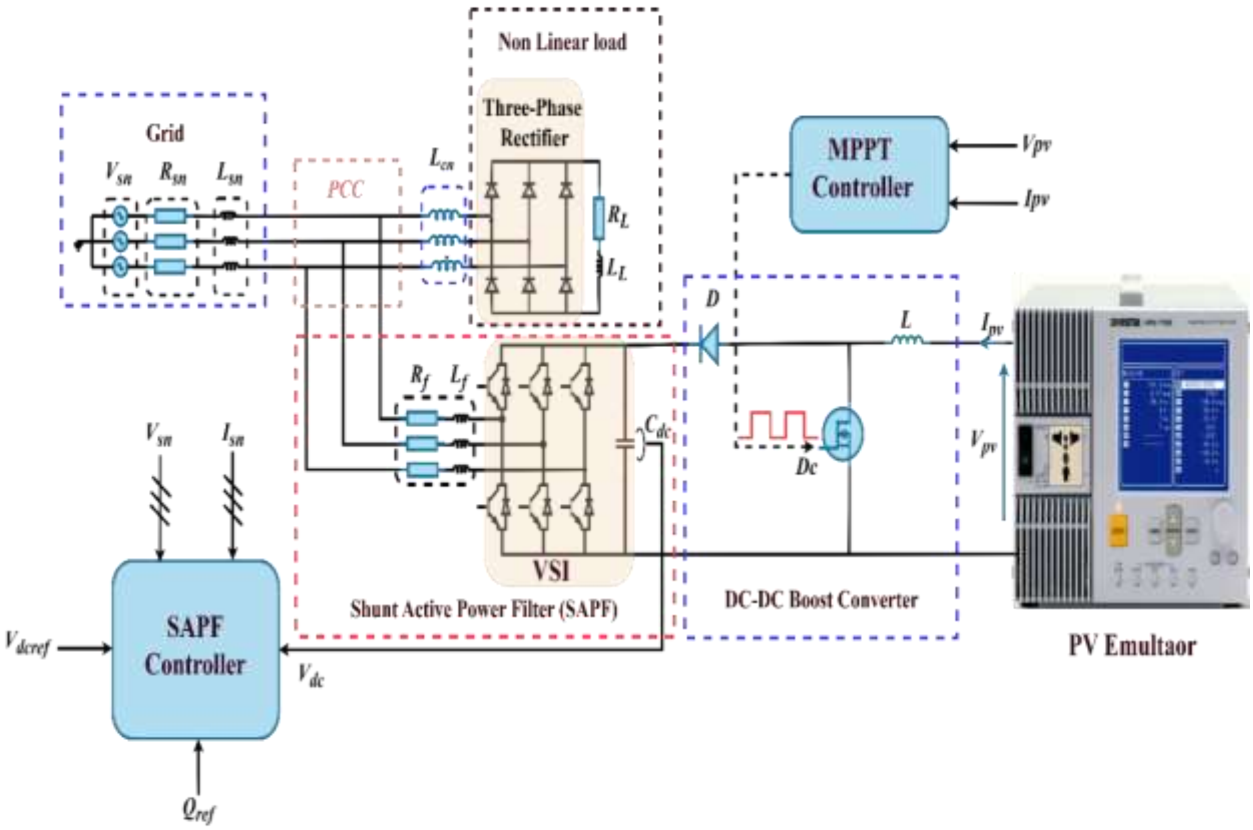

Figure 2.1: Schematic representation of the investigated GCPV–SAPF system

The studied system operates in parallel with a three-phase utility grid, which provides both synchronization and backup power when solar generation is insufficient. To emulate realistic operating conditions, a nonlinear load is connected; such loads (three-phase rectifiers) introduce current harmonics and reactive power demand, which result in voltage distortion and reduced efficiency.

The PV generator, represented either by a real PV array or a PV emulator, produces DC power. This power is conditioned by a DC–DC boost converter, which is equipped with a MPPT algorithm. The converter regulates the DC voltage and ensures maximum energy extraction under varying irradiance conditions.

At the core of the system lies the three-phase VSI. This inverter performs a dual function:

1. Grid integration – converting the regulated DC power into synchronized three-phase AC and injecting it into the utility grid.
2. Power quality enhancement – operating as a SAPF to generate compensating currents that cancel harmonic and reactive components drawn by the nonlinear load.

By combining renewable energy generation with active power conditioning in a single structure, the proposed configuration not only increases the system's efficiency but also ensures adherence to international power quality standards (such as IEEE 519). To achieve these objectives, the system incorporates two main controllers:

- an MPPT controller, which guarantees maximum power extraction from the PV generator, and
- an SAPF controller, which drives the VSI to mitigate harmonics and compensate reactive power.

The detailed operation of these controllers will be discussed in the next chapters.

2.3 Analytical modeling of PV arrays

To understand how electricity is made in a PV-based power production system, you need to know the basic principles behind photovoltaic (PV) energy. The PV cell is the fundamental component of a PV array. It is made of semiconductor materials that can absorb sunlight. These materials release photons that excite electrons, resulting in an electric current [8,31]. Figure 2.2 shows how individual PV cells are joined to make PV modules and how numerous modules are integrated to make a PV array. The system achieves the correct voltage and current levels through the series–parallel interconnection of PV modules.

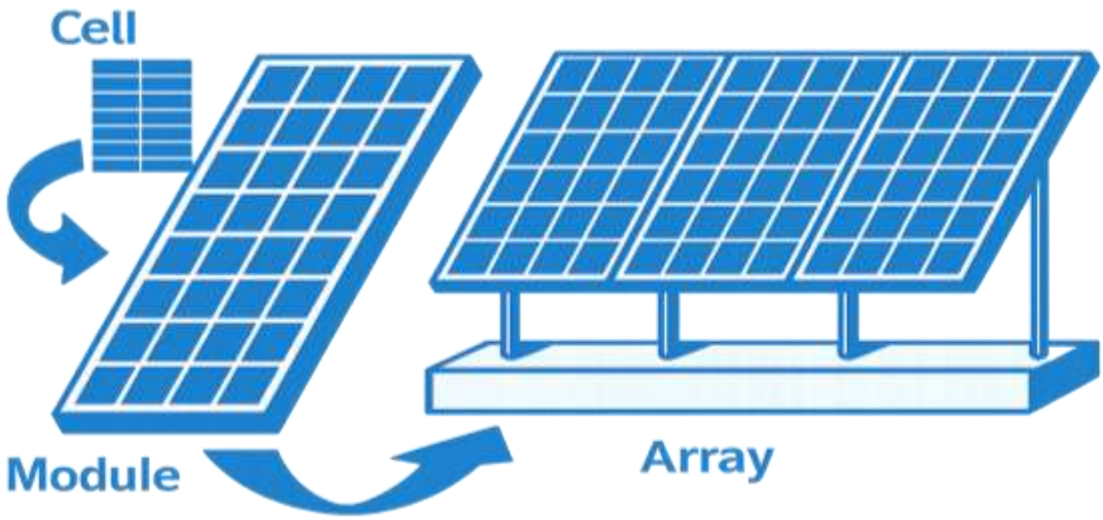

Figure 2.2: Schematic representation of a photovoltaic (PV) array system showing the interconnection of PV cells, modules, and arrays

2.3.1 Equivalent circuit modeling of a PV array

When modeling a photovoltaic (PV) power generator, it is crucial to employ a circuit that accurately represents how a PV cell behaves. Several mathematical models have been proposed in the literature to describe the I-V relationship of PV cells, which exhibit nonlinear electrical features [9]. The primary differences between these models lie in their mathematical formulation and the number of parameters used to describe the PV module.

Among the most commonly used models are:

- **Ideal model (IM):** This is the simplest way to depict a PV cell. Figure 2.3 in the square red illustrates that it features a photocurrent source (I_{ph}) and a diode (D), both of which are connected in parallel [32]. It assumes that there are no resistive losses and is generally used for basic theoretical research.

- **Double-diode model (DDM):** The DDM provides a more reliable representation of PV cell behavior, especially in low irradiance conditions [32]. As depicted in Figure 2.3, it consists of a photocurrent source (I_{ph}), two diodes, a shunt resistance (R_{sh}), and a series resistance (R_s). While this model enhances accuracy, it requires solving more complex equations and involves additional parameters.

- **Single-diode model (SDM):** This is the most popular model used in PV system simulations because it is both simple and accurate [32]. Figure 2.3 depicts its equivalent circuit, which is made up of:

  - A photocurrent source (I_{ph}) that depicts the current that irradiation from the sun makes.
  - A diode (D) models the charge recombination phenomena.
  - A shunt resistance (R_{sh}) represents leakage currents within the cell.
  - A series resistance (R_s) accounts for resistive losses in the semiconductor material and electrical contacts.

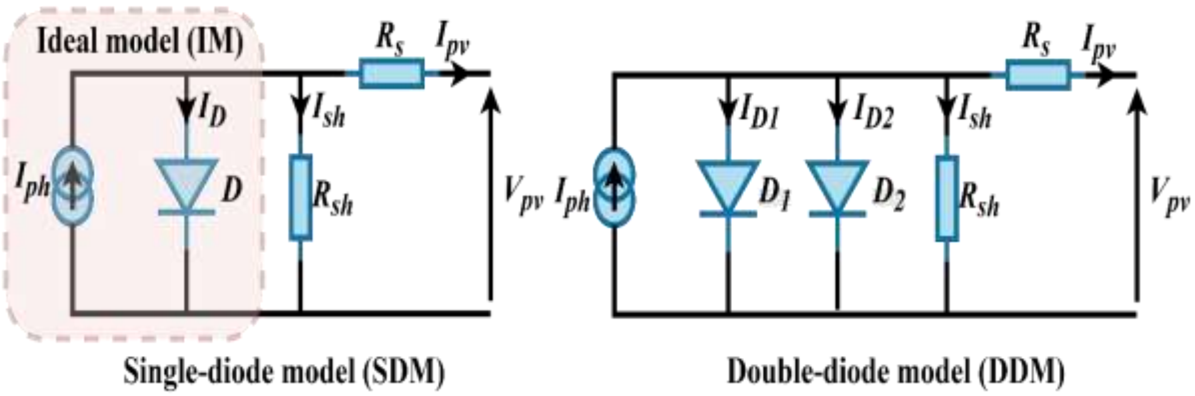

Figure 2.3: Equivalent circuit of a photovoltaic (PV) cell illustrating the IM, SDM, and DDM

2.3.2 Mathematical modeling of a single-diode PV cell

A PV module contains numerous PV cells, which are connected in series or parallel. A PV array is composed of several modules that are arranged together [32,9]. The voltage and current measured at the terminals of a PV cell are denoted as V_{pv} and I_{pv}, respectively.

As illustrated in Figure 2.3, the I–V equation of a photovoltaic cell is obtained from the corresponding equivalent circuit, where:

$$I_{pv} = I_{ph} - I_0.[\exp(\frac{V_{pv} + R_s.I_{pv}}{A.U_T}) - 1] - (\frac{V_{pv} + R_s.I_{pv}}{R_{sh}}) \tag{2.1}$$

In which U_T corresponds to the thermal voltage potential given by:

$$U_T = \frac{kT}{Q} \tag{2.2}$$

While, k represents the Boltzmann constant ($k = 1.38 * 10^{-23}$ J.K^{-1}), T is the temperature, and Q the electron charge($Q = 1.9^{*}10^{-19}$ C).

A solar cell's photocurrent (I_{ph}) is influenced by numerous material properties. Nevertheless, it can be reasonably approximated with sufficient accuracy as being linearly dependent on irradiance and temperature, as indicated in Equation (2.3).

$$I_{ph} = \frac{G}{G_r}[I_{sc,r} + K_0.(T - T_r)] \tag{2.3}$$

Whereas , $I_{sc,r}$ is the cell's short-circuit current under reference conditions (Standard Test Conditions (STC)), G denotes the solar irradiation (W/m^2), indicates the reference irradiation ($G_r = 1000$ W/m^2), K_0 is the current's coefficient of variation as a function of temperature, T_r is the reference temperature($298^{\circ}\mathrm{K}(25^{\circ}\mathrm{C})$), and T represents the cell temperature.

In contrast, the cell's saturation current fluctuates with temperature, as seen below:

$$I_0 = I_{0,r}(\frac{T}{T_r})^{\frac{3}{A}} \exp(\frac{Q.E_g}{K.A})(\frac{1}{T_r} - \frac{1}{T}) \tag{2.4}$$

Where, $I_{0,r}$ refers to the cell's reverse saturation current measured at reference conditions, and E_g indicates the energy of the semiconductor's band gap, expressed in eV:

$$I_{0,r} = \frac{I_{sc,r}}{\left(\exp\frac{Q.V_{oc,r}}{A.K.T_r} - 1\right)} \tag{2.5}$$

Where, $V_{oc,r}$ denotes the cell's open-circuit voltage under reference conditions, and A is the ideality factor.

2.3.2.1 Performance characteristics of a PV module

A single photovoltaic (PV) cell does not produce enough power for most energy uses. To overcome this limitation, several PV cells are connected in series or in parallel to form a PV module that can provide the required power. STC are usually used to test PV modules. In STC, the temperature of the cells is kept at 25 *°C* and the solar irradiation is set to 1000 W/m^2.

A PV module can be modeled as an equivalent current source whose output is directly influenced by G and T. The I–V and P–V characteristics reveal that the MPP varies over time, depending on the weather conditions, particularly the amount of sunlight and temperature. As a result, PV power systems utilize MPPT algorithms to adjust the duty cycle (D_c) of the DC-DC converter in real-time, ensuring that the maximum energy is extracted and the PV system operates more efficiently overall [27,32].

Assuming that all cells in a PV module are the same and work under the same temperature and irradiance, the module output current (I_{pv}) can be stated like this:

$$I_{pv} = N_p.I_{ph} - N_p.I_0.\left[\exp\left(\frac{V_{pv} + \left(\frac{N_s}{N_p}\right)R_s.I_{pv}}{N_s A U_T}\right) - 1\right] - \left(\frac{V_{pv} + \left(\frac{N_s}{N_p}\right)R_s.I_{pv}}{\left(\frac{N_s}{N_p}\right)R_{sh}}\right) \tag{2.6}$$

Where, N_s , N_p indicates series and parallel number of cells, respectively.

In solar photovoltaic (PV) systems, different types of PV modules are designed to meet the requirements of various applications. The electrical performance parameters of a PV module are typically defined under STC. In this study, the detailed electrical specifications of the selected PV module are presented in Table 2.1.

Table 2.1: Electrical parameters of the PV array under STC

PV array parameters	Values
Maximum Power $P_{mpp}(W)$	58.494
Voltage at MPP $V_{mpp}(V)$	9.066
Current at MPP $I_{mpp}(A)$	6.5
Open-circuit voltage $V_{oc}(V)$	11.89
Short-circuit current $I_{sc}(A)$	7.2
Temperature coefficient of $V_{oc}(\%/deg.C)$	-0.35602
Temperature coefficient of I_{sc} $(\%/deg.C)$	0.07

Figure 2.4 illustrates the I–V and P–V curves of the studied PV module under STC. The P–V curve clearly shows a single power peak, which corresponds to the MPP. Three key operating points can be identified from these curves:

- I_{SC}: corresponds to the point where the output voltage is zero and represents the maximum current the cell can deliver.
- V_{oc}: occurs when the output current is zero and represents the maximum voltage the cell can produce.
- MPP: represents the optimal operating point at which the PV module delivers the maximum extractable power.

These operating points are fundamental for assessing the performance of PV modules and play a crucial role in the design and implementation of MPPT algorithms to ensure efficient solar energy utilization. Furthermore, the voltage and current at the MPP, denoted as V_{mpp} and I_{mpp}, define the optimal operating conditions under which the PV module operates at peak efficiency. These parameters are particularly important in MPPT algorithm development, as they serve as reference values for the control system to regulate the operating point of the PV generator under varying environmental and operating conditions.

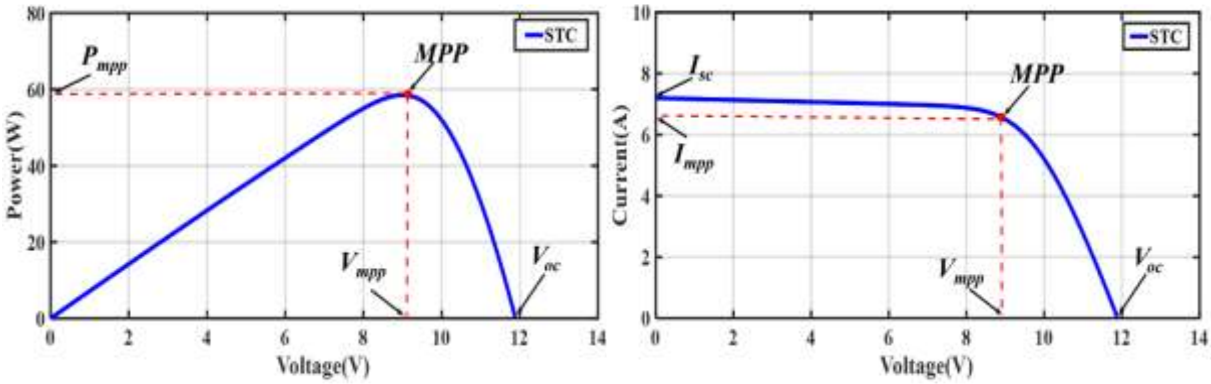

(a) (b)

Figure 2.4: PV module characteristic curves under STCs: a) P–V curves and b) I–V curves

2.3.2.2 Influence of solar irradiance and temperature on PV module behavior

To analyze the influence of G and T on the performance of the PV module, the I–V and P–V characteristics are examined, as they reflect the electrical behavior of the PV module under varying operating conditions. When T is kept constant and G increases, I_{sc} rises almost linearly, resulting in a higher output current of the module and, consequently, an increase in the maximum power (P_{mpp}). Conversely, when the T increases while maintaining constant irradiance, V_{oc} decreases noticeably, whereas the I_{sc} remains nearly unchanged. As a result, the maximum output power of the PV module declines [22]. Figure 2.5 illustrates the strong correlation between the module current and G, indicating that the MPP shifts upward as irradiance increases. On the other hand, Figure 2.6 shows that variations in T have a relatively less pronounced effect on the MPP, especially considering that T fluctuations throughout the day are generally modest.

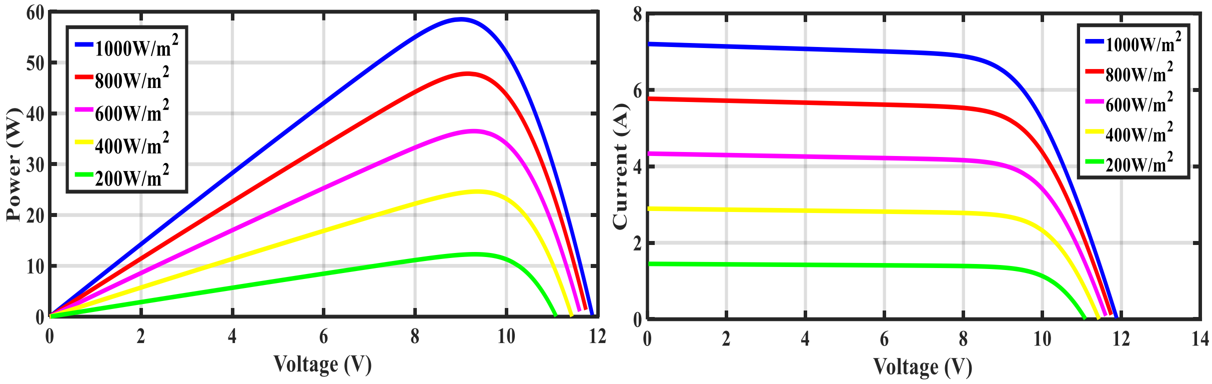

(a) (b)

Figure 2.5: Influence of solar irradiance on the P–V and I-V characteristics of the PV module: a) P-V curves and b) I-V curves

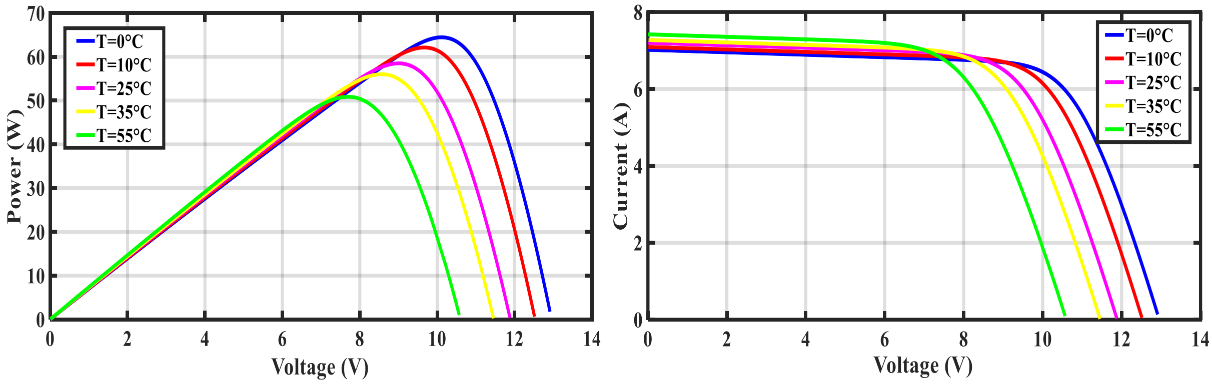

(a) (b)

Figure 2.6: Influence of temperature on the P–V and I–V characteristics of the PV module: a) P-V curves and b) I-V curves

2.3.2.3 Influence of series and parallel connections on PV module behavior

PV modules can be interconnected in series, parallel, or a combined series-parallel arrangement to achieve the desired voltage and current levels. The complete set of connected modules is referred to as a PV array [32]. In a series connection (N_s), the total voltage of the array is equal to the sum of the voltages of the individual modules. At the same time, the current remains constant and equal to that of a single module, as illustrated in Figure 2.7. In a parallel connection (N_p), the configuration aims to increase the total current of the array, making it equal to the sum of the currents of all modules. At the same time, the voltage remains unchanged and equal to that of a single module, as shown in Figure 2.8. For applications requiring both high voltage and high current, a mixed (series-parallel) configuration is adopted. This setup combines the benefits of both series and parallel connections to meet the high-power demands of the system, as depicted in Figure 2.9.

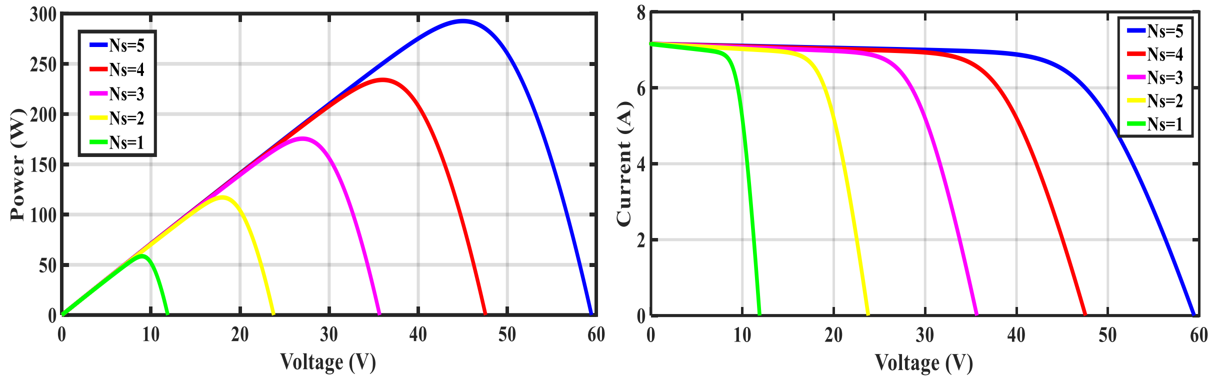

(a) (b)

Figure 2.7: Influence of series connection: a) P-V curves and b) I-V curves

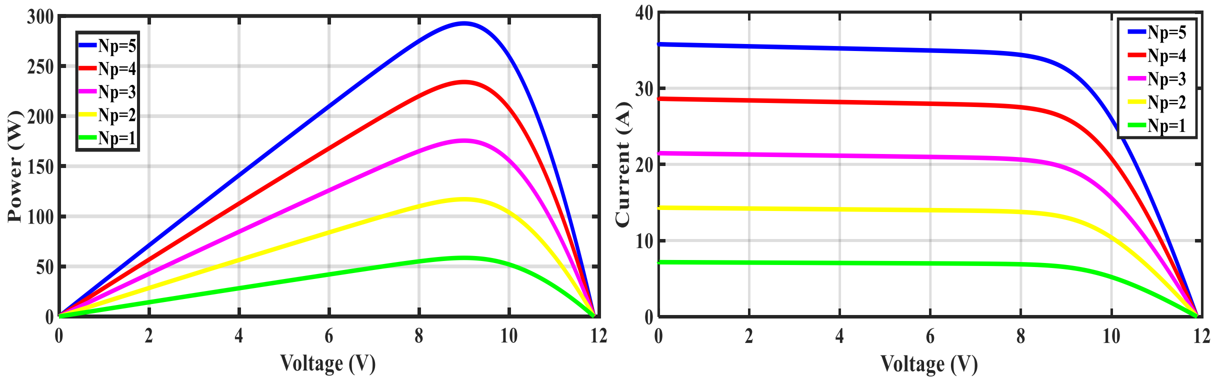

(a) (b)

Figure 2.8: Influence of parallel connection: a) P-V curves and b) I-V curves

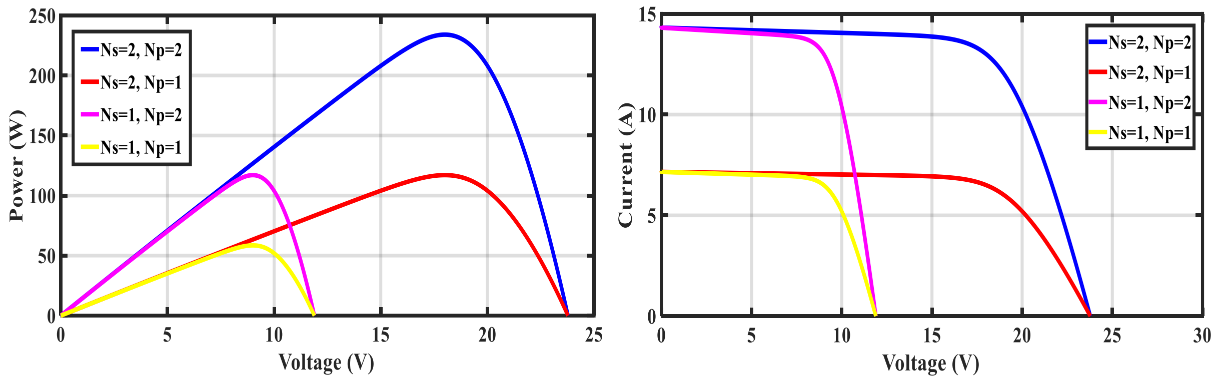

(a) (b)

Figure 2.9: Influence of mixed connection: a) P-V curves and b) I-V curves

2.3.2.4 Effect of partial shading on PV array performance

Due to the inherently low efficiency of photovoltaic (PV) systems, it is crucial to operate them consistently at their MPP to maximize energy extraction. To achieve this, PV modules are typically interconnected in series and parallel configurations [33]. However, environmental factors such as clouds, dust, or foliage can cause partial shading, as illustrated in Figure 2.10, leading to non-uniform solar irradiance across the PV array.

Under PSCs, the current generated by shaded cells drops significantly, while unshaded cells continue producing higher currents. This mismatch forces shaded cells to dissipate excess power as heat, which can lead to the hot spot effect [34]. To mitigate this issue, bypass diodes are integrated into PV modules to protect them and maintain efficient energy harvesting. When one or more modules become shaded, their current output decreases, creating an imbalance with the unshaded modules. As shown in Figure 2.11, bypass diodes connected in anti-parallel with each module provide an alternative path for current flow. During shading, the affected module's diode becomes forward-biased, allowing the current to bypass module [35]. This prevents overheating and cell degradation while ensuring that the remaining modules continue to operate efficiently, thereby improving system reliability and overall performance.

However, incorporating bypass diodes introduces nonlinearities into the P–V characteristics of the PV system, resulting in multiple peaks on the power curve. As shown in Figure 2.12, the curve displays several local maximum power points (LMPPs) in addition to a single global maximum power point (GMPP). This creates a significant challenge for conventional MPPT algorithms like P&O and INC, which often become trapped at LMPPs and fail to locate the true GMPP [9]. To address this limitation, advanced MPPT techniques based on intelligent metaheuristic algorithms are employed. These methods are capable of efficiently exploring the complex search space, accurately identifying the GMPP, and thereby maximizing overall energy extraction [36].

(a)

(b)

(c)

Figure 2.10: Common causes of partial shading in photovoltaic systems: a) Clouds, b) Tree shade, c) Dust accumulation

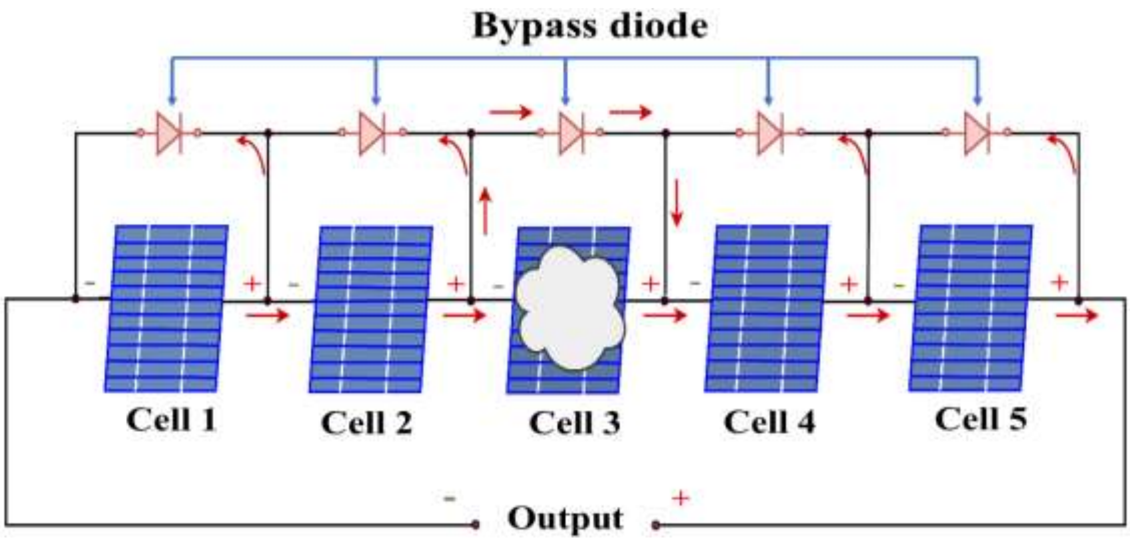

Figure 2.11: Protecting solar panels with bypass diodes in photovoltaic junction boxes

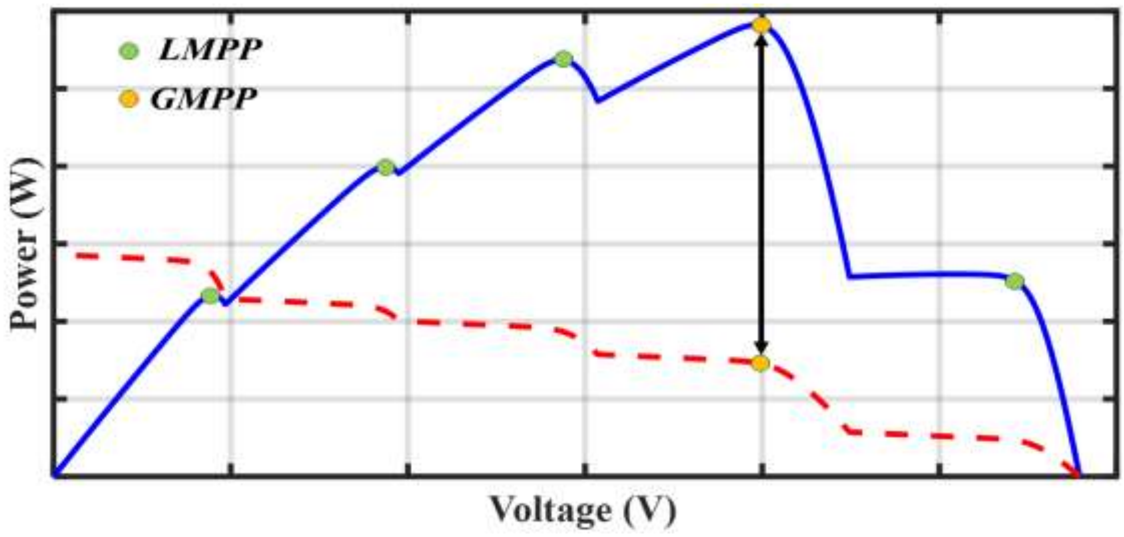

Figure 2.12: P–V and I–V characteristics of a PV system under PSC showing multiple LMPPs and a single GMPP

2.4 Implicit PV system modeling for emulator applications

A real photovoltaic (PV) generator is inherently modeled as a current-source device, where the output current is mainly governed by solar irradiance, while the terminal voltage remains constrained by the nonlinear I–V characteristics of the PV module. However, the laboratory emulator employed in this work operates as a voltage-source system (as will be discussed in the final chapter). Therefore, to ensure compatibility between the PV model and the emulator, the conventional formulation of the PV model must be reformulated.

Instead of directly computing the PV current as a function of voltage, the proposed approach determines the terminal voltage for an imposed current value using a nonlinear numerical formulation. This approach enables direct interfacing with the voltage-source emulator while preserving the nonlinear electrical behavior of the real PV generator.

The proposed formulation is based on the classical single-diode model (SDM) previously introduced. The SDM leads to a nonlinear implicit equation in which the terminal voltage appears both linearly and within an exponential term. Owing to this nonlinear structure, obtaining a fully explicit analytical expression of the voltage is difficult without introducing significant approximations.

To address this limitation, the PV model is formulated as a nonlinear algebraic equation derived from Kirchhoff's current law:

$$N_p.I_{ph} - N_p.I_0.\left[\exp\left(\frac{V_{pv} + \left(\frac{N_s}{N_p}\right)R_s.I_{pv}}{N_s A U_T}\right) - 1\right] - \left(\frac{V_{pv} + \left(\frac{N_s}{N_p}\right)R_s.I_{pv}}{\left(\frac{N_s}{N_p}\right)R_{sh}}\right) - I_{pv} = 0 \tag{2.7}$$

In this formulation, the PV voltage (V_{pv}) is treated as an unknown variable, whereas the current (I_{pv}) is imposed as an input. The nonlinear equation is solved numerically using an algebraic solver block in Simulink, which computes the voltage corresponding to each current value under varying irradiance conditions.

Figure 2.13 illustrates the Simulink-based implementation of the proposed PV model. The model represents the five PV modules used in this study, where irradiance and current are applied as external inputs, while the corresponding terminal voltage is obtained numerically from the implicit nonlinear formulation. The resulting I–V characteristic shown on the right reflects the nonlinear behavior of the PV generator under STC.

This numerical modeling approach ensures full compatibility with the voltage-source emulator used in the experimental setup while accurately preserving the physical characteristics of the PV system. Furthermore, it provides a reliable framework for validating power electronic converters and advanced control algorithms.

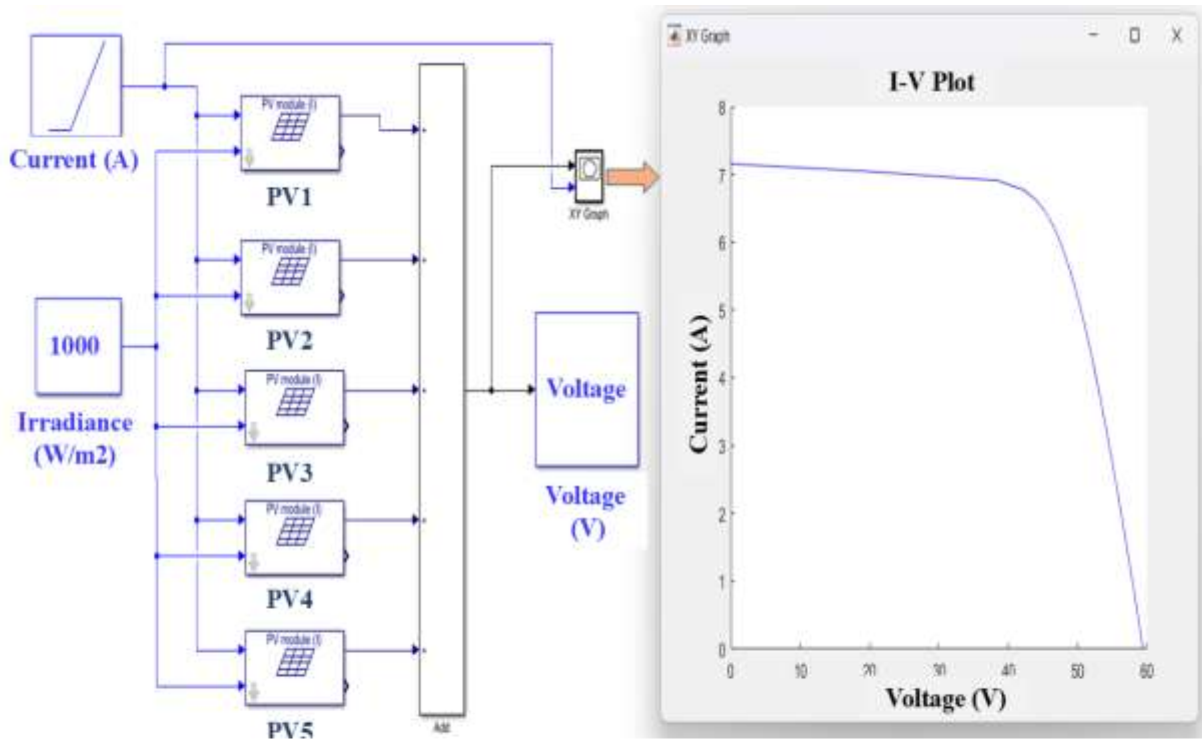

Figure 2.13: Simulink implementation of the implicit PV model

2.5 Modeling of a PV system using the lookup table method

In conventional photovoltaic (PV) system modeling, the algebraic loop problem often arises due to the strong interdependence between voltage, current, and power, which leads to iterative cycles and complicates the determination of the MPP. This issue stems from the intensive mathematical modeling of conventional PV arrays, which requires numerous interdependent calculations. Specifically, the loop occurs when there is mutual dependence between variables: the value of one variable depends on another, which in turn is influenced by the first. This circular dependency leads to repetitive computational cycles that can hinder both convergence and accuracy of the model.

To overcome this limitation, the Lookup Table (LUT) method has been introduced as an efficient alternative. This approach relies on pre-stored datasets of voltage, current, and power obtained either experimentally or through detailed simulations under different irradiance and temperature conditions. These datasets are imported into MATLAB/Simulink, where cubic interpolation is applied to generate smooth three-dimensional (3D) surfaces of the I–V characteristics.

Mathematically, the LUT model can be expressed as:

$$LUT(I_{pv}, G) \rightarrow V_{pv} \tag{2.8}$$

Where I_{pv} is the PV current, V_{pv} is the PV voltage, and G is the solar irradiance. The function $f(\cdot)$ is not derived analytically but is instead obtained from experimental or simulated datasets stored in the LUT.

The LUT-based block then maps irradiance and current inputs to voltage outputs, enabling accurate reproduction of PV array behavior without solving complex nonlinear equations. Figure 2.14 illustrates the cubic interpolation plot: Figure 2.14(a) shows the I–V characteristics under various irradiance levels (600, 800, and 1000 W/m²), while Figure 2.14(b) presents the response under different PSCs (PSC-1, PSC-2, PSC-3). The deformation of the I–V surfaces clearly demonstrate the LUT method's ability to capture nonlinear variations in operating scenarios. By avoiding algebraic loops and reducing computational burden, the LUT method ensures faster and more reliable PV system simulations, Rendering it especially suitable for real-time MPPT applications.

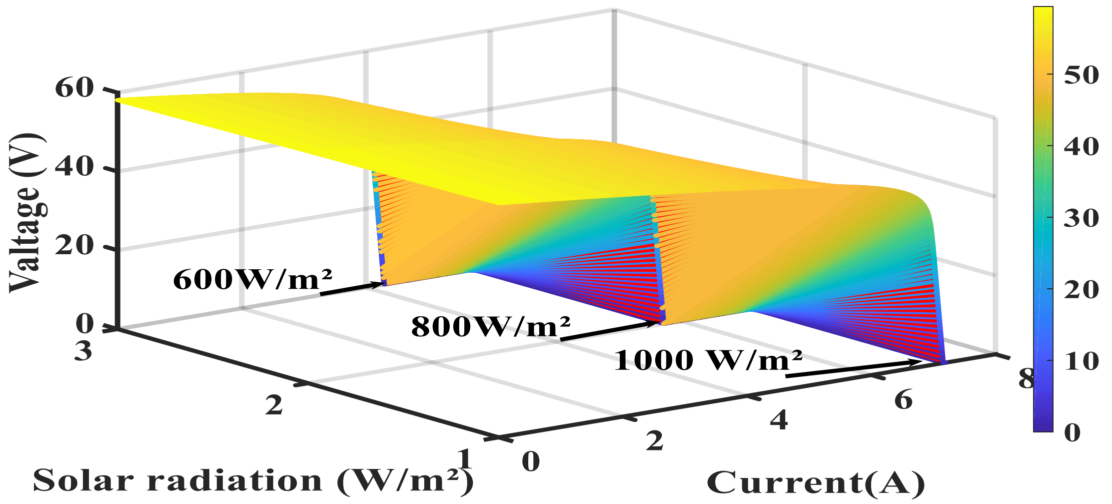

(a)

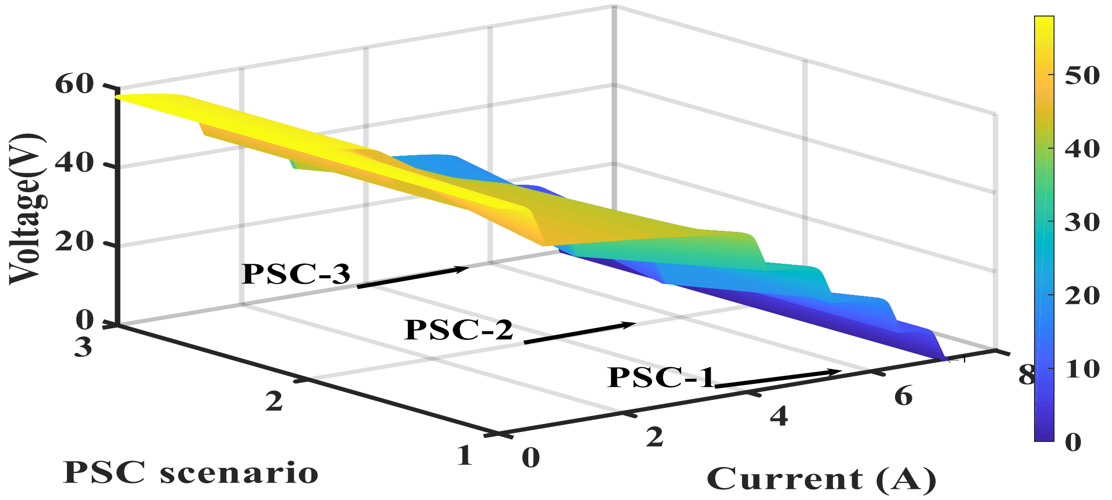

(b)

Figure 2.14: Three-dimensional representation of LUT breakpoints data — a) I–V characteristics under different irradiance levels, and b) I–V characteristics under various PSCs

Compared to the conventional five-parameter diode-based PV model, which requires solving nonlinear exponential equations and is computationally intensive, the LUT method provides a data-driven and faster alternative. While the five-parameter model offers deeper physical insight into the PV cell behavior, the LUT method prioritizes computational efficiency and robustness under dynamic conditions, making it more practical for real-time control and MPPT strategies.

To further illustrate the process, Figure 2.15 presents a flowchart of the LUT method for PV system modeling in Simulink. It outlines the main steps, starting from the environmental and electrical inputs (irradiance and current), to the pre-stored datasets imported from measurement or simulation, followed by the interpolation block that generates 3D surfaces, and finally the lookup block in Simulink that maps the inputs to voltage and power outputs. This visual representation highlights the efficiency of the LUT method in avoiding algebraic loops and reducing computational complexity, making it particularly well-suited for real-time MPPT applications.

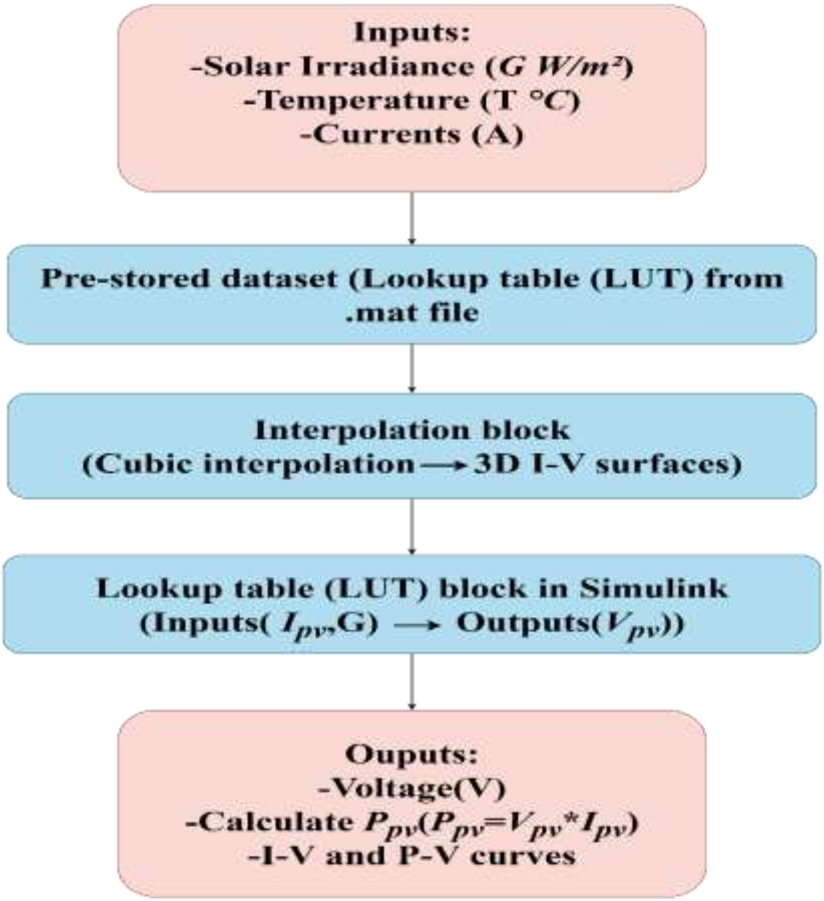

Figure 2.15: Flowchart of the lookup table method for PV system modeling in Simulink

2.6 Modeling of the DC-DC boost converter

The DC-DC boost converter, also known as a step-up chopper, is widely used in photovoltaic (PV) systems to increase the output voltage of the PV array and ensure optimal operation at the MPP [1,32]. It is highly preferred due to its simplicity, robustness, and ensuring a continuous input current, thereby making it appropriate for efficient power conversion in renewable energy applications [22,27]. The boost converter consists mainly of an electronic switch T (typically a MOSFET), a diode (D), an inductor (L), and a capacitor (C). Its operation is controlled through a PWM signal with a fixed switching period (T_s) and a variable duty cycle (D_c). The basic schematic of the boost converter is illustrated in Figure 2.16.

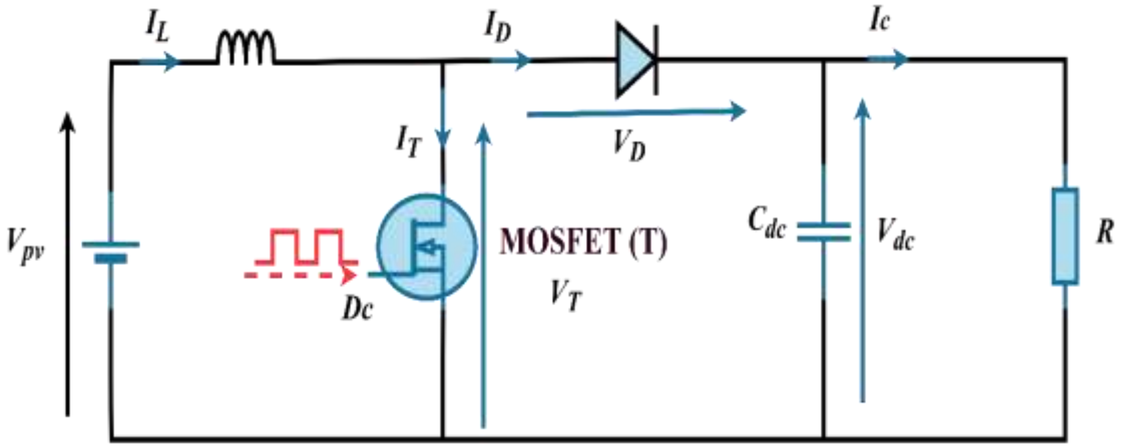

Figure 2.16: Basic diagram of a DC-DC boost converter

In continuous conduction mode (CCM), which is the most relevant operating mode for PV applications, the converter works in two states:

- ON-State ($0 \rightarrow D_cT_s$) (Figure 2.17(a)): When the switch (T) is closed, the inductor (L) stores energy from the input source. During the reverse-biased phase of the diode (D), the current in the inductor increases linearly., isolating the load from the source.

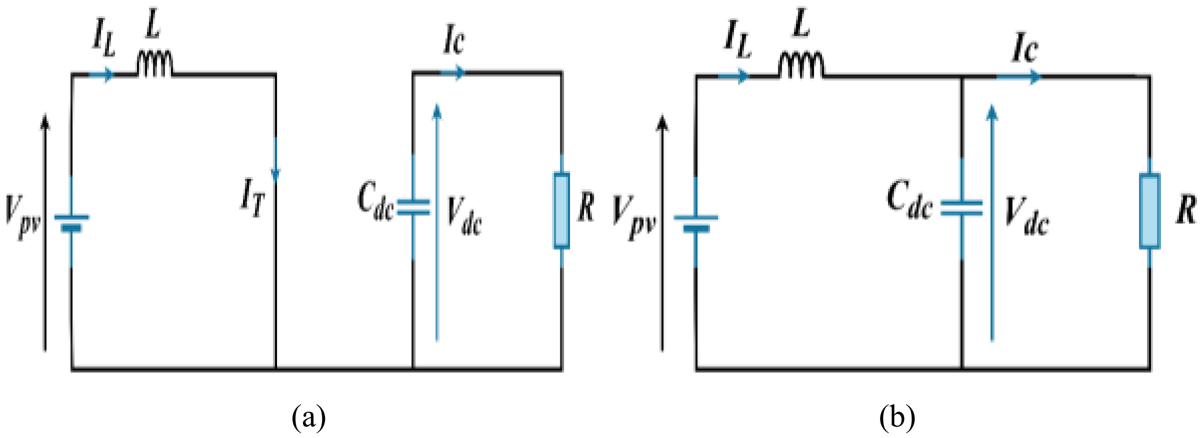

Figure 2.17: Equivalent circuits of the boost converter

During this operating interval, the inductor current (I_L) and the output voltage (V_{dc}) can be formulated using the following equation:

$$\begin{cases} \dfrac{dI_L}{dt} = \dfrac{1}{L} V_{pv} \\ \dfrac{dV_{dc}}{dt} = -\dfrac{V_{dc}}{RC} \end{cases} \tag{2.9}$$

- OFF-State ($D_cT_s \rightarrow T_s$) (Figure 2.17(b)): When the switch (T) opens, the inductor (L) opposes the sudden decrease in current and releases its stored energy through the diode (D) into the load. The combination of the source voltage and the induced inductor voltage results in an V_{dc} greater than the V_{pv}.

In this operating mode, I_L and V_{dc} are expressed by the following equations:

$$\begin{cases} \dfrac{dI_L}{dt} = \dfrac{1}{L}(V_{pv} - V_{dc}) \\ \dfrac{dV_{dc}}{dt} = \dfrac{1}{C}(I_L - \dfrac{V_{dc}}{R}) \end{cases} \tag{2.10}$$

The waveform diagram in Figure 2.18 illustrates the variation of I_L, switch current (I_T), diode current (I_D), and corresponding voltages during the switching cycle. I_L rises during the ON-state and decreases during the OFF-state, while the voltages across the switch and diode exhibit complementary behaviors.

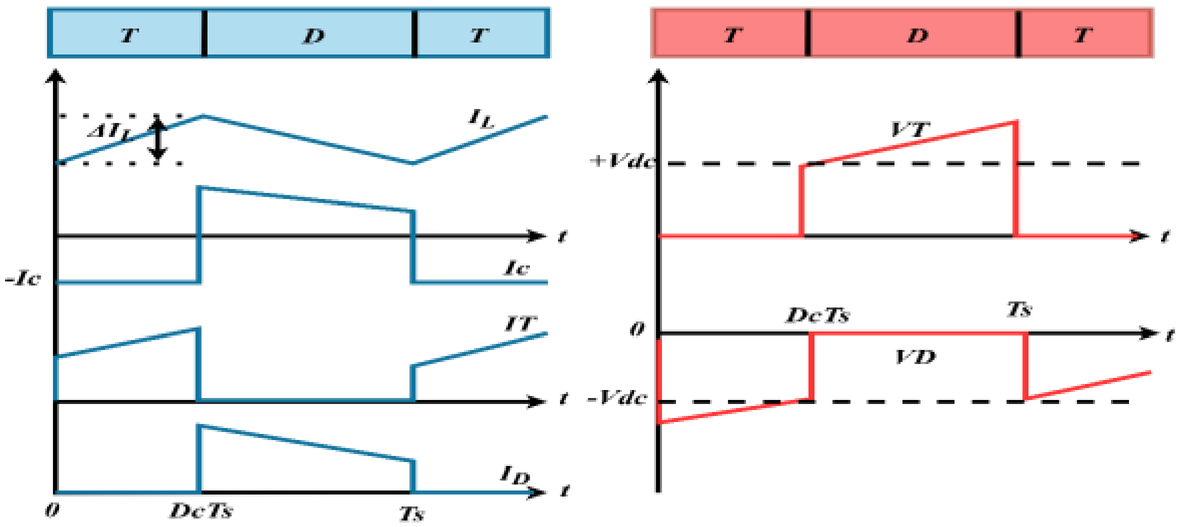

Figure 2.18: Waveforms of boost converter currents and voltages

At the end of the first period, I_L increases by:

$$\Delta I_{Lon} = \int_0^{D_cT_s} I_L \mathrm{d}t = \int_0^{D_cT_s} \frac{V_{pv}}{L} \mathrm{d}t \tag{2.11}$$

ΔI_{Lon} denotes the I_L ripple corresponding to the interval during which the switch (T) remains in the ON state.

$$\Delta I_{Lon} = \frac{V_{pv} D_c T_s}{L} \tag{2.12}$$

Therefore, the change in the I_L during the second interval can be expressed as:

$$\Delta \mathrm{I}_{Loff} = \int_{D_c T_s}^{T_s} I_L \mathrm{d}t = \int_{D_c T_s}^{T_s} \frac{V_{pv} - V_{dc}}{L} \mathrm{d}t \tag{2.13}$$

$\Delta \mathrm{I}_{Loff}$ denotes the variation (ripple) of the I_L during the interval when the switch (T) is open.

$$\Delta \mathrm{I}_{Loff} = \frac{(V_{pv} - V_{dc})(1 - D_c)T_s}{L} \tag{2.14}$$

Assuming that the converter operates in steady-state conditions, the energy stored in each component remains the same at the beginning and at the end of each switching cycle [32]. Consequently, the I_L will also be identical at the start and end of every switching cycle. This can therefore be expressed as follows:

$$\Delta \mathrm{I}_{Lon} + \Delta \mathrm{I}_{Loff} = 0 \tag{2.15}$$

So:

$$\frac{(V_{pv})D_c T_s}{L} + \left[\frac{(V_{pv} - V_{dc})(1 - D_c)T_s}{L} \right] = 0 \tag{2.16}$$

It follows that:

$$V_{dc} = \frac{V_{pv}}{1 - D_c} \tag{2.17}$$

Where:

- V_{pv}: Photovoltaic (PV) voltage or boost converter input voltage (V).
- V_{dc}: Boost converter output voltage (V).
- D_c: Duty cycle of the boost converter, considered as an input control variable.

2.7 DC-AC inverter model

A DC-AC inverter is a crucial component in GCPV power systems. Its primary function is to convert the harvested PV power from DC into AC synchronized with the grid frequency, while also controlling the power flow between the DC-DC boost converter and the utility grid by regulating the current injected into the grid [1].

In this thesis, a two-level VSI topology is employed due to its simplicity, robustness, and efficiency. The inverter primary circuit consists of six power switches, each composed of an insulated gate bipolar transistor (IGBT) connected in parallel with a free-wheeling diode, which ensures bidirectional current flow while providing unidirectional voltage blocking capability, as illustrated in Figure 2.19. The switches are controlled using PWM techniques to synthesize three-phase quasi-sinusoidal output voltages suitable for grid integration [22,27].

To prevent short-circuiting of the DC-link, the two switches in each leg of the inverter are operated in a complementary manner, meaning that when the upper switch is ON, the corresponding lower switch must be OFF, and vice versa [10,13].

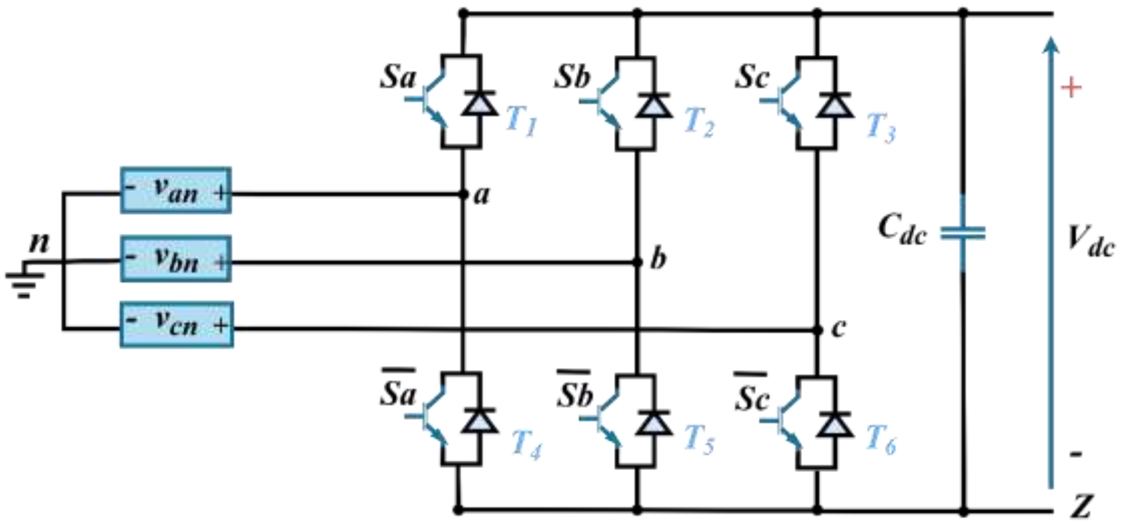

Figure 2.19: Configuration of a three-phase two-level inverter

The output voltage of the inverter, shown in Figure 2.19, can assume two distinct levels depending on the DC source voltage and the switching states of the inverter transistors. As presented in Table 2.2, the inverter has eight possible switching states, two of which produce zero AC line voltage at the output. The control of the two switches on the same leg is complementary: when one switch is turned ON, the other is turned OFF [27]. The control defines the state of each switch signal, S_a, S_b, and S_c, as follows:

$$Sa = \begin{cases} 1 & T_1 \; closed \; and \; T_4 \; open \\ 0 & T_1 \; open \; and \; T_4 \; closed \end{cases} \tag{2.18}$$

$$Sb = \begin{cases} 1 & T_2 \; closed \; and \; T_5 \; open \\ 0 & T_2 \; open \; and \; T_5 \; closed \end{cases} \tag{2.19}$$

$$Sc = \begin{cases} 1 & T_3 \; closed \; and \; T_6 \; open \\ 0 & T_3 \; open \; and \; T_6 \; closed \end{cases} \tag{2.20}$$

Table 2.2: Switching states of a three-phase inverter

State	*Sa*	*Sb*	*Sc*	V_{ab}	V_{bc}	V_{ca}
0	0	0	0	0	0	0
1	0	0	1	0	$-V_{dc}$	$+V_{dc}$
2	0	1	0	$-V_{dc}$	$+V_{dc}$	0
3	0	1	1	$-V_{dc}$	0	$+V_{dc}$
4	1	0	0	$+V_{dc}$	0	$-V_{dc}$
5	1	0	1	$+V_{dc}$	$-V_{dc}$	0
6	1	1	0	0	$+V_{dc}$	$-V_{dc}$
7	1	1	1	0	0	0

The phase-to-neutral voltages of the inverter (v_{aZ}, v_{bZ}, v_{cZ}) are related to the DC-link voltage (V_{dc}) and the switching states (S_a, S_b, and S_c) of the inverter as follows:

$$\begin{cases} V_{aZ} = V_{dc} S_a, \\ V_{bZ} = V_{dc} S_b, \\ V_{cZ} = V_{dc} S_c. \end{cases} \tag{2.21}$$

In the case of a balanced three-phase system, the sum of the inverter phase voltages and currents is zero:

$$v_{an} + v_{bn} + v_{cn} = 0 \tag{2.22}$$

$$i_{an} + i_{bn} + i_{cn} = 0 \tag{2.23}$$

Where (v_{an}, v_{bn} , and v_{cn}) and (i_{an}, i_{bn} , and i_{cn}) are the output phase voltages and current of the inverter.

Considering the switches and diodes to be ideal, the three composite voltages (v_{ab}, v_{bc}, v_{ca}) of the inverter can be defined by:

$$\begin{cases} v_{ab} = v_{aZ} - v_{bZ} \\ v_{bc} = v_{bZ} - v_{cZ} \\ v_{ca} = v_{cZ} - v_{aZ} \end{cases} \tag{2.24}$$

By replacing Equation (2.21) with Equation (2.24), the following expression is derived:

$$\begin{cases} V_{ab} = v_{aZ} - v_{bZ} = V_{dc}(S_a - S_b), \\ V_{bc} = v_{bZ} - v_{cZ} = V_{dc}(S_b - S_c), \\ V_{ca} = v_{cZ} - v_{Z} = V_{dc}(S_c - S_a). \end{cases} \tag{2.25}$$

Here, v_{aZ}, v_{bZ}, v_{bZ} represent the phase-to-neutral voltages of the inverter, where point "Z" is considered as the reference.

The phase voltages of the inverter are related to the neutral voltage (v_{nZ}) of the load through the following relations:

$$\begin{cases} v_{aZ} = v_{an} - v_{nZ} \\ v_{bZ} = v_{bn} - v_{nZ} \\ v_{cZ} = v_{cn} - v_{nZ} \end{cases} \tag{2.26}$$

Where, v_{nZ} represents the neutral point voltage of the load, measured with respect to point “Z”. By substituting Equation (2.22) into Equation (2.26), the neutral voltage can be derived as:

$$v_{nZ} = \frac{1}{3}(v_{aZ} + v_{bZ} + v_{cZ}) \tag{2.27}$$

By inserting Equation (2.27) into Equation (2.26), the following expression is derived:

$$\begin{cases} v_{an} = \frac{1}{3}(2v_{aZ} - v_{bZ} - v_{cZ}) \\ v_{bn} = \frac{1}{3}(2v_{bZ} - v_{aZ} - v_{cZ}) \\ v_{cn} = \frac{1}{3}(2v_{cZ} - v_{aZ} - v_{bZ}) \end{cases} \tag{2.28}$$

By substituting Equation (2.21) into Equation (2.28), the inverter phase voltages can be expressed in matrix form:

$$\begin{pmatrix} v_{an} \\ v_{bn} \\ v_{cn} \end{pmatrix} = \frac{V_{dc}}{3} \begin{bmatrix} 2 & -1 & -1 \\ -1 & 2 & -1 \\ -1 & -1 & 2 \end{bmatrix} . \begin{bmatrix} S_a \\ S_b \\ S_c \end{bmatrix} \tag{2.29}$$

Where:

- S_a, S_b, and $S_c \in \{0,1\}$: inverter switching signals,
- V_{dc}: DC-link voltage at the input of the inverter.

2.8 Modeling of the SAPF

The inverter is connected to the PCC through a Class R–L filter, which is specifically designed to suppress switching transients and reduce PWM harmonics before they propagate into the grid. By effectively attenuating the high-frequency components generated by the inverter, the filter prevents their interference with the grid’s fundamental frequency [22,24]. Consequently, it enhances the current quality at the PCC. It ensures that the entire system complies with photovoltaic (PV) grid interconnection standards and relevant regulatory requirements, as illustrated in Figure 2.20.

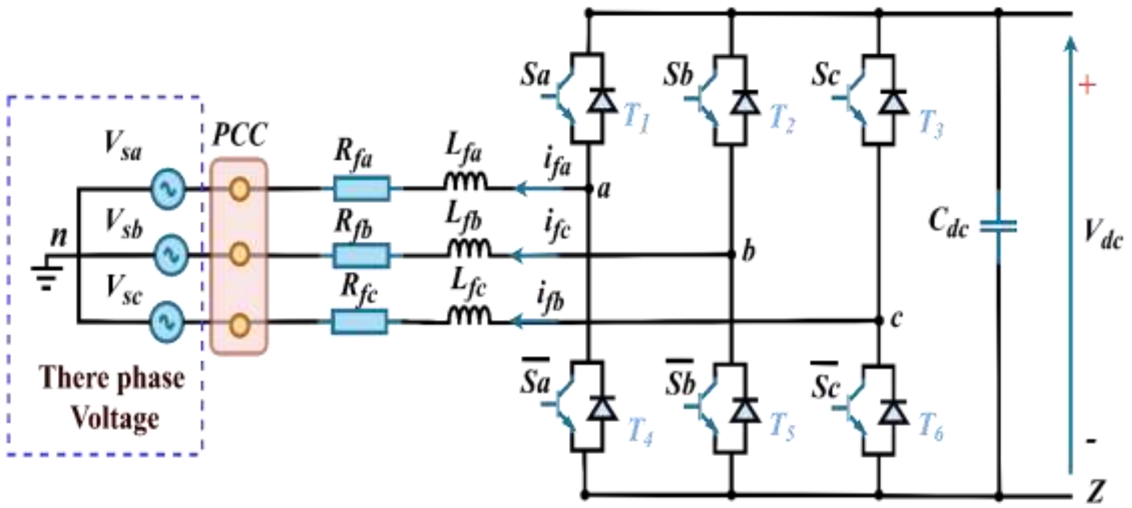

Figure 2.20: Structure of the two-level voltage inverter operating in SAPF mode

In power systems, loads represent the components that consume and transform electrical energy. The amount of power drawn from the network is determined by the nature and characteristics of these loads. Hence, an accurate load representation is essential to describe precisely the interaction between the load and the inverter [22].

In this work, the electrical grid is modeled as an ideal, balanced three-phase voltage source. Its instantaneous phase voltages can be written in matrix form as:

$$\begin{bmatrix} v_{sa}(t) \\ v_{sb}(t) \\ v_{sc}(t) \end{bmatrix} = V_{\max} \begin{bmatrix} \sin(\omega t) \\ \sin(\omega t - \frac{2\pi}{3}) \\ \sin(\omega t + \frac{2\pi}{3}) \end{bmatrix} \tag{2.30}$$

Where:

- $v_{sa}(t), v_{sb}(t)$, and $v_{sc}(t)$: are the instantaneous three-phase grid voltages (V),
- V_{max}: is the max amplitude of the phase voltage (V),
- ω : is the angular frequency of the grid supply (rad/s).

For each phase of the SAPF, applying Kirchhoff's Voltage Law (KVL) yields the following equation describing the relationship between the converter output voltage, filter components, and the grid voltage:

$$v_{sn} = V_{fn} - V_{Lfn} - V_{Rfn} = V_{fn} - L_f \frac{dI_{fn}}{dt} - R_f I_{fn}, \qquad n = a,b,c \tag{2.31}$$

Where:

- $n=a, b, c$: denotes the three-phase indices,
- V_{fn}: inverter output voltage of phase n,
- L_f: filter inductance,
- R_f: filter resistance,
- I_{fn}: filter current of phase n.

Thus, the equations are formulated as follows:

$$\begin{cases} v_{sa} = V_{fa} - V_{Lfa} - V_{Rfa} = V_{fa} - L_f \dfrac{di_{fa}}{dt} - R_f i_{fa} \\ v_{sb} = V_{fb} - V_{Lfb} - V_{Rfb} = V_{fb} - L_f \dfrac{di_{fb}}{dt} - R_f i_{fb} \\ v_{sc} = V_{fc} - V_{Lfc} - V_{Rfc} = V_{fc} - L_f \dfrac{di_{fc}}{dt} - R_f i_{fc} \end{cases} \Leftrightarrow L_f \frac{d}{dt}\begin{bmatrix} i_{fa} \\ i_{fb} \\ i_{fc} \end{bmatrix} = -R_f \begin{bmatrix} i_{fa} \\ i_{fb} \\ i_{fc} \end{bmatrix} + \begin{bmatrix} v_{fa} \\ v_{fb} \\ v_{fc} \end{bmatrix} - \begin{bmatrix} v_{sa} \\ v_{sb} \\ v_{sc} \end{bmatrix} \tag{2.32}$$

The state equation of the V_{dc} can be expressed in terms of the switching functions as follows:

$$C_{dc} \frac{dV_{dc}}{dt} = S_a i_{fa} + S_b i_{fb} + S_c i_{fc} \tag{2.33}$$

The system of equations that governs the operation of the SAPF in the three-phase reference frame can be represented as follows:

$$\begin{cases} L_f \dfrac{di_{fa}}{dt} = -R_f i_{fa} + v_{fa} - v_{sa} \\ L_f \dfrac{di_{fb}}{dt} = -R_f i_{fb} + v_{fb} - v_{sb} \\ L_f \dfrac{di_{fc}}{dt} = -R_f i_{fc} + v_{fc} - v_{sc} \\ C_{dc} \dfrac{dV_{dc}}{dt} = S_a i_{fa} + S_b i_{fb} + S_c i_{fc} \end{cases} \tag{2.34}$$

By applying the Park transformation to the system described by Equation (2.34), the model of the SAPF can be expressed in the rotating dq reference frame as follows:

$$\begin{cases} L_f \dfrac{di_{fd}}{dt} = -R_f i_{fd} - L_f \omega i_{fq} + v_{fd} - v_d \\ L_f \dfrac{di_{fq}}{dt} = -R_f i_{fq} - L_f \omega i_{fd} + v_{fq} - v_q \\ C_{dc} \dfrac{dV_{dc}}{dt} = S_d i_{fd} + S_q i_{fq} \end{cases} \tag{2.35}$$

Where:

- i_{fd}, i_{fq} : filter current components in the dq frame,
- v_{fq}, v_{fd} : inverter output voltages in the dq frame,
- v_q, v_d : grid voltage components in the dq frame,
- R_f, L_f : resistance and inductance of the filter,
- ω : angular frequency of the synchronous frame (grid frequency),
- C_{dc}: DC-link capacitor,
- S_d, S_q: equivalent switching functions in the dq frame.

The modeling of the SAPF in the stationary reference frame αβ can be obtained by applying the Concordia transformation to the system given by Equation (2.36):

$$\begin{cases} L_f \dfrac{di_{f\alpha}}{dt} = -R_f i_{f\alpha} + v_{f\alpha} - v_\alpha \\ L_f \dfrac{di_{f\beta}}{dt} = -R_f i_{f\beta} + v_{f\beta} - v_\beta \\ C_{dc} \dfrac{dV_{dc}}{dt} = S_\alpha i_{f\alpha} + S_\beta i_{f\beta} \end{cases} \tag{2.36}$$

Where:

- $i_{f\alpha}, i_{f\beta}$: filter current components in the stationary αβ frame,
- $v_{f\alpha}, v_{f\beta}$: inverter output voltages in the αβ frame,
- v_α, v_β : grid voltages in the αβ frame,
- S_α, S_β: equivalent switching functions in the αβ frame.

2.9 Sizing of a grid-tied PV system with SAPF

To ensure the reliable and efficient operation of the GCPV–SAPF system, the appropriate sizing of both passive and active components is crucial. The correct selection of elements, such as the boost inductor (L), DC-link capacitor (C_{dc}), and inverter-side filter inductors (L_{fn}), directly affects the system's dynamic response, voltage stability, harmonic suppression, and overall efficiency. Oversizing may lead to unnecessary cost, volume, and power losses, while under-sizing can cause excessive ripple, instability, and poor power quality. Therefore, before proceeding with the detailed component design, the general methodology for system sizing is presented. In the following subsections, the design of the L, C_{dc}, and L_{fn} will be discussed step by step, based on analytical formulations and design constraints.

2.9.1 Determination of the boost inductor value

The boost inductor (L (mH)) is a key element in the DC–DC converter, as it determines the current ripple and directly influences system efficiency and stability. In most practical cases, the inductor value is specified by the manufacturer in the datasheet for the targeted application. However, it can also be estimated analytically without relying on datasheet values, using the following expression [1]:

$$L = \frac{V_{pv}}{\Delta \mathrm{I}_L \cdot f_s} \cdot \left(\frac{V_{dc} - V_{pv}}{V_{dc}} \right) \tag{2.37}$$

Where the inductor ripple current $\Delta \mathrm{I}_L$ is defined as:

$$\Delta \mathrm{I}_L = \varepsilon_i \cdot I_{sc} \cdot \left(\frac{V_{dc}}{V_{pv}} \right) \tag{2.38}$$

With:

- ε_i: ripple factor, typically 20–40% of the I_{sc},
- I_{sc} : maximum current generated by the PV array (A),
- f_s: switching frequency of the boost converter (KHz).

These equations provide a practical way to size the boost inductor, ensuring that the converter operates efficiently while maintaining acceptable ripple levels in the inductor current.

2.9.2 Determination of the DC-link capacitor size

A key role of the C_{dc} is to stabilizing the V_{dc} and ensuring smooth power transfer between the PV generator and the grid. To enable effective grid integration, the DC-link reference (V_{dcref}) voltage must be regulated to a value greater than the grid peak voltage. This V_{dcref} is estimated as [24,27]:

$$V_{dcref} = \mu \cdot \sqrt{3} V_{\max}, \text{ where } \mu > 1 \tag{2.39}$$

Where, μ is a safety factor greater than unity to guarantee continuous power injection into the grid. Once the V_{dc} is defined, the C_{dc} can be sized using [27]:

$$C_{dc} = \frac{P_{pv}}{4\pi F V_{dcref} \Delta V} \tag{2.40}$$

With parameters defined as:

- ΔV: is amplitude of the DC-link voltage ripple, typically set to 10% of V_{max},
- F: Grid frequency (typically 50),
- V_{dcref}: is reference DC-link voltage (V).

This equation ensures that the capacitor is properly sized to limit the DC voltage ripple within acceptable levels, thus maintaining stable operation of the inverter and improving overall power quality.

➢ **Design Guidelines:**

- The factor μ is generally chosen between 1.1 and 1.2, ensuring that V_{dcref} always remains above the grid peak voltage while avoiding excessive stress on the inverter switches.
- The voltage ripple ΔV should remain below 10% of Vmax to maintain stable inverter operation and limit harmonics injected into the grid.
- A higher capacitance reduces voltage ripple but increases cost, volume, and inrush current at startup. Therefore, a trade-off must be considered between performance and practicality.

This design approach guarantees that the capacitor maintains a stable DC bus, minimizes voltage fluctuations, and supports reliable operation of the inverter and SAPF.

2.9.3 Sizing of the inverter-side inductor

The inverter-side inductor L_f is a key element of the L-filter, ensuring that the switching harmonics produced by the inverter are sufficiently attenuated before injecting current into the grid. The inductor value can be estimated as [1]:

$$L_f = \frac{\sqrt{3} \cdot m \cdot V_{dc}}{12 \cdot h \cdot f_s \cdot \Delta I_{Lf}} \tag{2.41}$$

Where:

- L_{fn}: is the inverter-side inductor (mH),
- h: is the overloading factor, typically set to 1.2,
- m: is the modulation index, selected within the range 0.5–1,
- ΔI_{Lf}: is the current ripple, usually fixed at 5% of the rated current.

➢ **Design considerations:**

- The choice of modulation index m influences both the inductor size and the harmonic spectrum; values close to 1 maximize DC-link utilization but increase harmonic distortion.
- The ripple current ΔI_{Lf} should be limited to 3–5% of the rated current to balance harmonic reduction and inductor size.
- A larger inductance improves filtering but results in higher cost, size, and losses. Conversely, too small an inductance may cause excessive current ripple and THD.
- The resistance R_f of the inductor must be considered in practice, as it introduces power losses and reduces efficiency.

This sizing method ensures that the inverter output current remains within grid standards for harmonic distortion, while maintaining acceptable inductor dimensions and efficiency.

2.10 Conclusion

In this chapter, a comprehensive modeling framework of the studied GCPV system with a SAPF has been developed. The modeling process began with the analytical representation of the PV array using the SDM, where the influence of irradiance, temperature, series/parallel configurations, and partial shading on the PV characteristics was examined.

To ensure compatibility with the voltage-source emulator used in the experimental implementation, an implicit PV model was adopted, where the terminal voltage is obtained numerically from the imposed current. In addition, a Lookup Table (LUT)-based modeling method was introduced, allowing accurate reproduction of PV characteristics while avoiding algebraic loops and reducing computational complexity in MATLAB/Simulink simulations.

The subsequent sections presented the modeling of the DC–DC boost converter, the DC–AC VSI, and the SAPF, along with the sizing of their associated passive components. Together, these models form the foundation of the two-stage GCPV system considered in this work, ensuring both efficient energy conversion and power quality enhancement.

The detailed controllers governing the boost converter (MPPT controller) and the inverter (SAPF controller) are not addressed in this chapter, since the focus here was on system modeling. Their design, control strategies, and performance evaluation will be thoroughly discussed in the next chapter.

Chapter 3:

Development of Metaheuristic and Hybrid Optimization Algorithms for Photovoltaic MPPT Enhancement

3.1 Introduction

The efficiency and reliability of photovoltaic (PV) systems are fundamentally determined by their ability to continuously operate at the MPP under diverse and dynamically changing environmental conditions. Variations in solar irradiance and temperature introduce strong nonlinearities into I–V and P–V characteristics of PV modules, resulting in a continuously shifting MPP. Consequently, effective MPPT algorithms are crucial to ensure optimal energy harvesting and system stability, particularly in real-time applications and under PSCs.

Over the past decades, a wide range of MPPT techniques have been proposed, evolving from conventional methods—such as P&O and INC—to intelligent and optimization-based algorithms inspired by nature and swarm behavior. While classical approaches are appreciated for their simplicity and ease of implementation, they often exhibit slow dynamic response, steady-state oscillations around the MPP, and degraded tracking performance when subjected to rapidly fluctuating irradiance or PSCs. These limitations have motivated the exploration of more adaptive and computationally efficient algorithms capable of achieving global optimization in complex and nonlinear search spaces.

In this context, soft computing and metaheuristic optimization techniques have emerged as powerful alternatives, offering robustness, flexibility, and improved convergence toward the GMPP. These algorithms—modeled after natural phenomena such as animal behavior, social intelligence, and physical processes—are inherently capable of balancing exploration and exploitation during the search for optimal operating conditions. Their stochastic nature allows them to escape local optima and adapt to the nonlinear power characteristics of PV systems.

This chapter presents a comprehensive investigation of advanced and hybrid optimization-based MPPT techniques aimed at enhancing the performance of PV systems. Several newly developed and improved algorithms are proposed, including the ZOA based on P–V characteristics, the GWEO algorithm, a hybrid and GWO–PSO approach. Each of these methods is specifically designed to improve the tracking accuracy, minimize steady-state oscillations, and accelerate convergence toward the GMPP, particularly under challenging environmental scenarios such as partial shading or abrupt irradiance variations.

To validate their effectiveness, the proposed algorithms are compared against several well-established MPPT techniques, including Equilibrium Optimization (EO), Particle Swarm Optimization (PSO), Flower Pollinate Algorithm (FPA), Whale Optimization Algorithm (WOA), and Grey Wolef Optimization (GWO). The comparative analysis focuses on key performance metrics such as tracking efficiency, response speed, convergence stability, and robustness under dynamic conditions.

The theoretical formulations, algorithmic mechanisms, and integration frameworks discussed in this chapter form the foundation for the practical implementation and performance evaluation of these methods. By combining adaptive exploration–exploitation strategies and intelligent control, the proposed optimization-based MPPT algorithms aim to advance the efficiency and stability of PV systems.

3.2 MPPT Methods

To ensure the efficient utilization of photovoltaic (PV) energy, a wide range of MPPT methods have been proposed and extensively investigated in the scientific literature. These techniques are designed to continuously adjust the operating point of a PV system so that it delivers the maximum available power under varying environmental conditions. Depending on their level of complexity, sensor requirements, convergence speed, and implementation cost, MPPT methods can generally be grouped into three main categories: traditional methods, soft computing and intelligent techniques, and metaheuristic algorithms.

3.2.1 Conventional MPPT Methods

Conventional MPPT methods represent the oldest and most widely applied approaches in photovoltaic (PV) systems. Their simplicity, low cost, and suitability for real-time applications make them highly attractive for practical use. These methods typically rely on straightforward electrical measurements, such as current, voltage, or conductance, to determine the operating point of the PV array and adjust it toward the MPP. While they perform effectively under steady environmental conditions, their efficiency often decreases in the presence of rapid variations in solar irradiance or temperature, where tracking speed and accuracy become critical. Despite these limitations, their ease of implementation and minimal hardware requirements have ensured their continued adoption in both stand-alone and GCPV systems.

Among the most common techniques, the P&O method relies on introducing small voltage perturbations and evaluating the resulting power changes based on past and present operating conditions. Its popularity is attributed to its simplicity, reduced measurement requirements, and straightforward feedback structure; however, its efficiency is limited by the trade-off between oscillations around the MPP and the tracking speed [39]. Conversely, the Incremental Conductance (INC) method determines the MPP by analyzing the derivative of power with respect to voltage, combining both conductance and incremental conductance [40]. While INC avoids the tracking direction ambiguity often found in the conventional Perturb and Observe (P&O) algorithm, it still faces similar limitations under rapidly changing environmental conditions. Both techniques are fundamentally classified as Hill Climbing (HC) methods [41]. Specifically, the HC approach updates the operating point of the P–V curve by directly adjusting the duty cycle of the DC–DC converter, whereas P&O typically perturbs the reference voltage or current. Despite these operational differences, these conventional methods generally perform well under Uniform Irradiation Conditions (UIC), where the PV power curve exhibits a single, unique MPP [8].

3.2.2 Soft computing and intelligent MPPT methods

Soft computing and intelligent MPPT methods have been increasingly adopted in recent years to overcome the limitations of conventional techniques, especially under fast-changing environmental conditions and partial shading scenarios. These approaches rely on advanced computational intelligence to handle nonlinearities, uncertainties, and stochastic variations in PV systems more effectively. Unlike traditional methods, which depend mainly on direct electrical measurements, intelligent techniques use adaptive models and learning capabilities to enhance tracking accuracy, reduce steady-state oscillations, and improve overall system efficiency. Academics have therefore turned to soft computing approaches such as fuzzy logic controllers (FLC) and artificial neural networks (ANN), which have demonstrated significant improvements in MPPT performance and reliability. However, these methods restrict their usage in real-time PSC applications, even if they have advantages, since they rely on past information of the PV model and require significant processing resources [42,43].

3.2.3 Metaheuristic MPPT methods

Metaheuristic MPPT methods have emerged as a promising alternative to overcome the limitations of both conventional and intelligent techniques, particularly under dynamic conditions and partial shading. Unlike traditional approaches, metaheuristics do not require prior system knowledge, detailed PV models, or extensive parameter tuning; instead, they treat the MPPT task as a black-box optimization problem where the PV power is the objective function and the duty cycle is the decision variable [44]. The search process is typically divided into two main stages: exploration, where the algorithm broadly investigates the search space to identify multiple potential optimal regions, and exploitation, where the focus shifts to refining the most promising regions until convergence toward the MPP is achieved [9]. In practice, these methods begin with an initial population of candidate solutions, which are iteratively improved by updating their search trajectories based on past results and shared information among candidates. The optimization continues until a maximum number of iterations is reached or a convergence condition is satisfied [45].

Due to their adaptability and robustness, MOAs have gained increasing popularity in engineering applications, as they demonstrate a strong capability to avoid local optima while efficiently converging toward global solutions in complex and nonlinear optimization problems such as MPPT. As illustrated in Figure 3.1, metaheuristic algorithms can be classified into several categories: evolutionary algorithms inspired by natural selection, swarm-based algorithms modeled on collective animal behavior, physics-inspired algorithms derived from physical laws, human-inspired algorithms reflecting social and cognitive behaviors, bio-inspired algorithms replicating animal survival strategies, and other algorithms that combine mathematical or hybrid approaches [46]. Each category offers specific strengths and trade-offs in terms of convergence speed, robustness, and implementation complexity, making metaheuristics a versatile and powerful tool for MPPT [47].

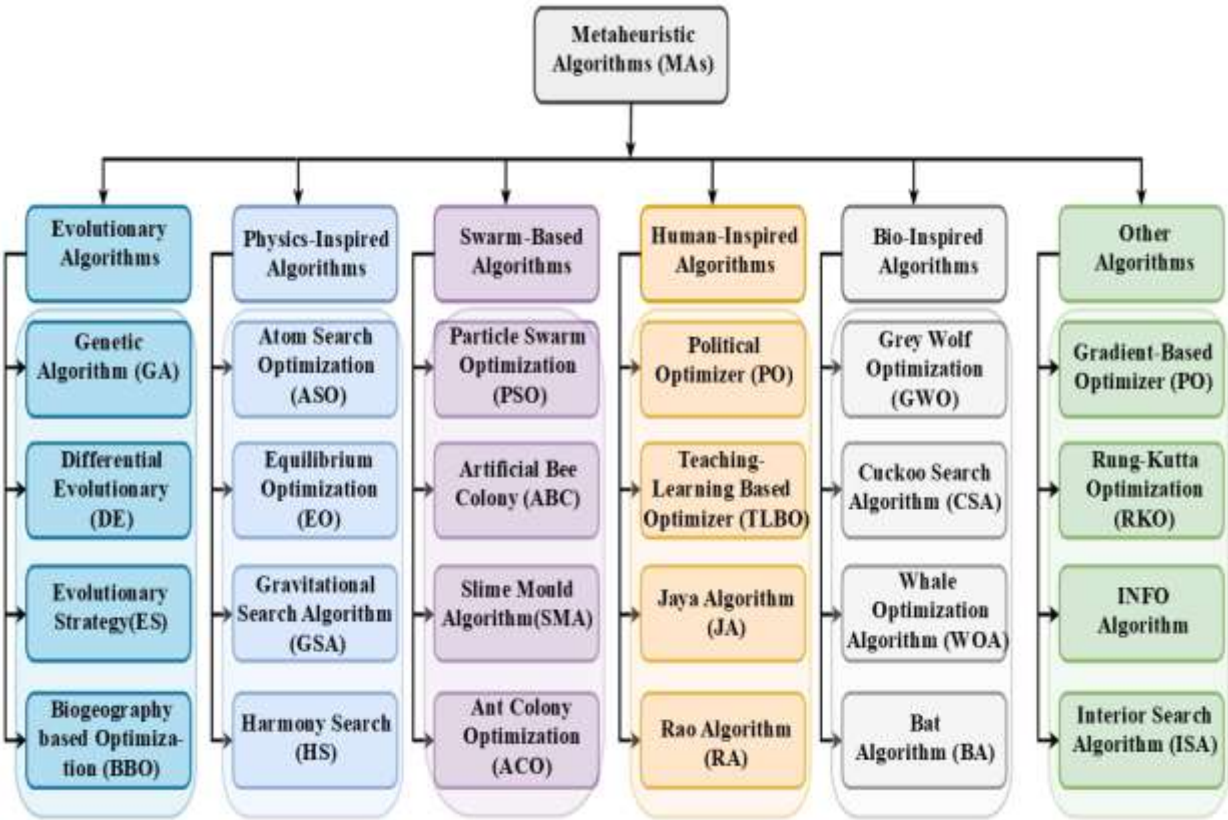

Figure 3.1: Comprehensive categorization of MOAs

3.3 Proposed MOAs for MPPT

In this thesis, several recently developed metaheuristic algorithms, as well as hybrid variants, have been implemented and analyzed for MPPT applications under dynamic and partial shading conditions. These algorithms were chosen for their strong optimization potential, their ability to escape local maxima, and their relatively simple implementation compared to traditional methods. Among them are the ZOA, GWEO, and the hybrid GWO-PSO. We specifically focused on their application in solar energy systems connected to the electrical grid and conducted a detailed comparison with several well-established metaheuristic methods. In the following sections, we will discuss each algorithm in detail and demonstrate how they can be effectively applied to achieve reliable and efficient MPPT performance.

3.3.1 Proposed ZOA for MPPT

MOAs are widely applied to search for optimal solutions within a given space, making them particularly suitable for determining the MPP on a PV power curve. In this thesis, the ZOA is applied to a GCPV system integrated with a SAPF to improve power extraction while maintaining high power quality. ZOA, inspired by the cooperative foraging and defense behavior of zebras, provides strong global search capability, high efficiency, and ease of implementation [48]. In this algorithm, each zebra represents a candidate solution defined by the duty cycle of the DC–DC boost converter, and its position in the search space corresponds to a potential operating point of the PV system. The zebra population is iteratively updated to converge toward the global MPP. Mathematically, the entire population is expressed as a matrix of candidate solutions, which evolve through exploration and exploitation until the optimal duty cycle (D_c) is reached [9]. By integrating the ZOA-based MPPT with the SAPF control structure, the proposed system ensures maximum utilization of PV energy while simultaneously maintaining high power quality in the grid. The zebra population can be represented mathematically by the following matrix [48].

$$D_c = \begin{bmatrix} D_{c1} \\ \vdots \\ D_{ci} \\ \vdots \\ D_{cN} \end{bmatrix}_{N\times m} = \begin{bmatrix} D_{c1,1} & \cdots & D_{c1,j} & \cdots & D_{c1,m} \\ \vdots & \ddots & \vdots & \ddots & \vdots \\ D_{ci,1} & \cdots & D_{ci,j} & \cdots & D_{ci,m} \\ \vdots & \ddots & \vdots & \ddots & \vdots \\ D_{cN,1} & \cdots & D_{cN,j} & \cdots & D_{cN,m} \end{bmatrix}_{N\times m} \tag{3.1}$$

In this formulation, D_c denotes the overall population matrix of zebras (duty cycle), where each row corresponds to a candidate solution. D_{ci} represents i_{th} zebra within the population, while $D_{ci,j}$ refers to the value of j_{th} decision variable proposed by i_{th} zebra. N defines the total number of zebras, i.e., the population size, and m specifies the number of decision variables that characterize the optimization problem.

In the context of MPPT for a GCPV-SAPF system, the decision variable is the duty cycle of the DC–DC boost converter, which directly governs the PV system’s operating point. This mathematical representation therefore enables the ZOA to search systematically for the optimal D_c, ensuring convergence toward the global MPP even under partial shading or rapidly changing conditions.

The value of the objective function is determined by evaluating the proposed decision variable values associated with each zebra in the population. In the MPPT framework, this corresponds to computing both the PV power for the duty cycle values suggested by each zebra and the quality of power injected into the grid.

The obtained objective function values are expressed in vector form as follows:

$$P = \begin{bmatrix} P_{pv}(D_{c1}) \\ \vdots \\ P_{pv}(D_{ci}) \\ \vdots \\ P_{pv}(D_{cN}) \end{bmatrix}_{N\times 1} \tag{3.2}$$

Where, P denotes the vector of objective-function values to be maximized, and $D_{c1}, D_{ci}, ...D_{cN}$ are the candidate duty cycles generated by the population of N zebras. Each element $P_{pv}(D_{ci})$ is the PV power corresponding to the duty cycle D_{ci} proposed by the i_{th} zebra. Since both zebra positions (candidate duty cycles) and their objective values are updated at every iteration, identifying the best solution in each cycle is essential. ZOA exploits the natural behaviors of zebras, primarily foraging and defense, to guide this search.

During the foraging stage (first phase), population members are updated according to simulated zebra movement rules, allowing candidates to move toward promising regions of the search space progressively. The zebra with the best performance at a given iteration is designated the "zebra pioneer (PZ)", and its position attracts and steers the rest of the population toward improved solutions. The mathematical update rules that describe the zebras' location changes during the foraging stage are given in Equations (3.3) and (3.4).

$$D_{ci}^{new,P1} = D_{ci,j} + r \cdot (PZ_j - I \cdot D_{ci,j}) \tag{3.3}$$

Where:

- $r \in [0,1]$ is a uniform random number,
- $I = round(1 + rand) \in \{1,2\}$, where rand is a random number in the interval [0,1].

The candidate duty cycle is accepted only if it improves the fitness:

$$D_{ci} = \begin{cases} D_{ci}^{new,P1}, & P_{pv}\left(D_{ci}^{new,P1}\right) < P_{pv}(D_{ci}); \\ D_{ci}, & else, \end{cases} \tag{3.4}$$

In the first foraging phase of the ZOA-based MPPT process, the operating states of the zebras are updated according to their foraging strategy. Here, $D_{ci}^{new,P1}$ denotes the updated duty cycle proposed by the i_{th} zebra, while $D_{ci,j}^{new,P1}$ represents its value in the j_{th} decision dimension within the search space. The corresponding PV power obtained at this state is expressed as the objective function value $P_{pv}\left(D_{ci}^{new,P1}\right)$. Among all candidates, the zebra with the best performance, referred to as PZ, is identified, and its position in each dimension, PZ_j, serves as a reference to guide the rest of the population. This mechanism enables the algorithm to progressively direct the duty cycle updates of the boost converter toward the MPP.

In the second phase, known as the defense stage, the ZOA updates zebra positions by simulating natural defense strategies against predators. Two behaviors are modeled: escape (S1) (exploitation phase) in Equation (3.5) represents where zebras flee from threats such as lions, and group defense (S2) (exploration phase) in Equation (3.5), where they coordinate to disorient predators like cheetahs or wild dogs. These strategies enhance population diversity, preventing premature convergence and improving the algorithm's ability to locate the global MPP under varying conditions.

During this stage, a newly generated zebra position (candidate duty cycle) is accepted only if it provides a higher PV power compared to its previous state. This acceptance criterion ensures that the MPPT process steadily progresses toward better operating points on the PV curve. The condition governing this update is mathematically formulated in Equation (3.6).

$$D_{ci}^{new,P2} = \begin{cases} S_1 : D_{ci,j} + R\cdot(2r-1)\cdot(1-\dfrac{t}{T})\cdot D_{ci,j}, & Ps \le 0.5; \\ S_2 : D_{ci,j} + r\cdot(AZ_j - I\cdot D_{ci,j}), & else, \end{cases} \tag{3.5}$$

$$D_{ci} = \begin{cases} D_{ci}^{new,P2}, & P_{pv}\left(D_{ci}^{new,P2}\right) < P_{pv}(D_{ci}); \\ D_{ci}, & else, \end{cases} \tag{3.6}$$

In this stage, $D_{ci}^{new,P2}$ represents the updated position of the i_{th} zebra, while $D_{ci,j}^{new,P2}$ denotes its value in the j_{th} dimension. The corresponding objective function value (PV power) is expressed as $P_{pv}\left(D_{ci}^{new,P2}\right)$. The parameter t is the current iteration, and T is the maximum number of iterations. A small constant $R = 0.01$ is introduced, while Ps defines the probability of selecting between the two defense strategies within the range [0,1]. Here, PZ refers to the attacked zebra, and PZ_j indicates its value in the j_{th} dimension.

The overall procedure of the ZOA applied as an MPPT method is summarized in Figure 3.2.

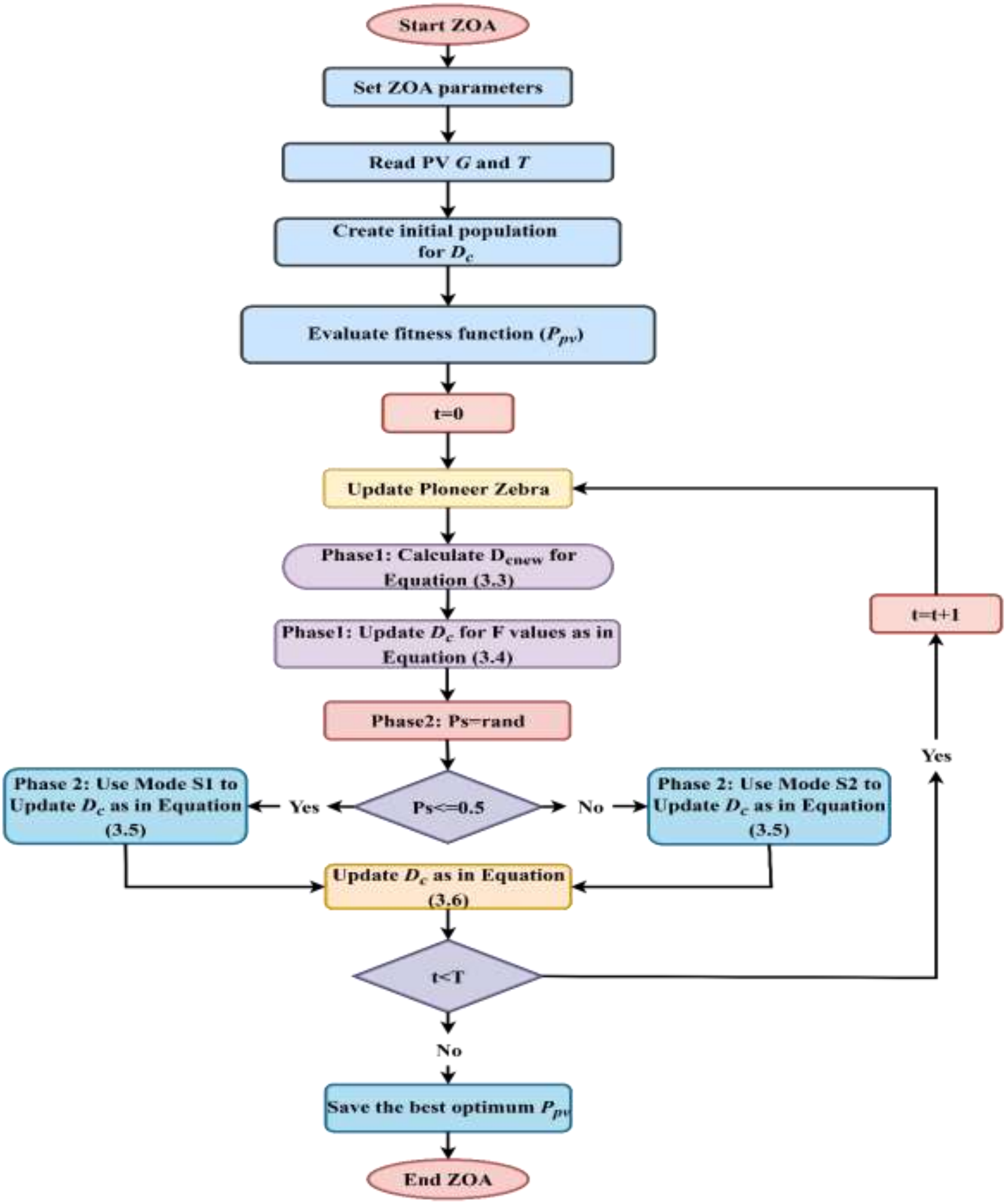

Figure 3.2: Flowchart of ZOA

3.3.2 Proposed GWEO for MPPT

As highlighted earlier, MOAs are designed to perform an extensive search for optimal solutions within a defined search space, much like identifying the MPP on the nonlinear PV power curve. GWEO is a recently developed hybrid algorithm that combines the updating mechanisms of GWO and EO. By leveraging the strengths of both approaches, GWEO enhances convergence speed, reduces computational complexity, and improves tracking performance under dynamic conditions. This makes it highly effective in addressing the MPP search challenge. By integrating the GWEO-based MPPT algorithm with the SAPF control structure, the proposed system achieves optimal utilization of PV energy while maintaining superior power quality at the grid interface. In the following, we will examine each method, GWO and EO, to identify their individual advantages and strengths before analyzing the hybrid GWEO approach [14].

3.3.2.1 GWO for MPPT

GWO is a nature-inspired metaheuristic that models the leadership hierarchy and cooperative hunting strategy of grey wolves. For the MPPT problem, GWO naturally maps to duty cycle search: each wolf represents a candidate duty cycle for the DC–DC converter, and the fitness of each candidate is evaluated by the PV power (P_{pv}) (the objective to maximize). The population is ranked at every iteration, and the three best solutions are labelled α (best), β (second best), and δ (third best). The remaining wolves ω represent the rest of the possible solutions [8,49].

GWO balances exploration and exploitation via coefficient vectors that regulate the wolves' movement toward the prey (here, the global MPP). The hunting process is modelled in three steps: (1) encircling the prey, (2) hunting (guided by α, β, δ), and (3) attacking (convergence). When applied to MPPT, the algorithm iteratively updates duty-cycle candidates, evaluates P_{pv} for each candidate, and replaces candidates when improvements are found. The algorithm terminates when the maximum number of iterations is reached or a convergence criterion is satisfied, and the best duty cycle found corresponds to the estimated MPP [50].

Equations (3.7)–(3.9) define how GWO updates candidate duty cycles for MPPT by following the best three solutions (α, β, δ). The coefficients A and C control exploration and exploitation, ensuring balance in the search. This mechanism allows GWO to track the global MPP efficiently, even under PSC.

$$\begin{cases} D_{c1} = D_{\alpha} - A_1 . \left| C_1 . D_{\alpha} - D_{ci}^{t} \right| \\ D_{c2} = D_{\beta} - A_2 . \left| C_1 . D_{\beta} - D_{ci}^{t} \right| \\ D_{c3} = D_{\delta} - A_3 . \left| C_1 . D_{\delta} - D_{ci}^{t} \right| \end{cases} \tag{3.7}$$

$$D_{ci}^{t+1} = \frac{D_{c1} + D_{c2} + D_{c3}}{3} \tag{3.8}$$

You can get the vectors A and C by:

$$\begin{cases} A = 2a.r_1 - a \\ C = 2r_2 \end{cases} \tag{3.9}$$

In the GWO-based MPPT process, the updated duty cycle $D_{c_i}^{t+1}$ is constrained within the allowable range [L, U] to ensure feasible converter operation. The corresponding PV power is then evaluated, and the new duty cycle is accepted if $P_{pv}\left(D_{c_i}^{t+1}\right) > P_{pv}\left(D_{c_i}^{t}\right)$; Otherwise, the previous duty cycle is maintained. At the end of each iteration, the α, β and δ wolves are reassigned as the top three solutions based on their power values, guiding the search toward the global MPP [51].

Here, D_{c1}, D_{c2}, and D_{c3} denote the distance vectors between the candidate duty cycle $D_{c_i}^{t}$ and the best search agents, i.e., D_α, D_β ,and D_δ, corresponding to the α, β, and δ wolves. These distances are scaled by the random coefficients A_1, A_2, A_3 and C_1, C_2, C_3, which control the trade-off between exploration and exploitation. This mechanism directs the population toward the optimal duty cycle, thereby ensuring reliable convergence to the global MPP.

The convergence factors are calculated as described in Equation (3.10), and their values decrease linearly from 2 to 0 over the course of iterations, thereby ensuring a smooth transition from exploration to exploitation in the search for the global MPP.

$$a = 2\left(1 - \frac{t}{T}\right) \tag{3.10}$$

Where, t denotes the current iteration number, and T represents the maximum number of iterations.

The overall procedure of the GWO applied as an MPPT method is summarized in Figure 3.3.

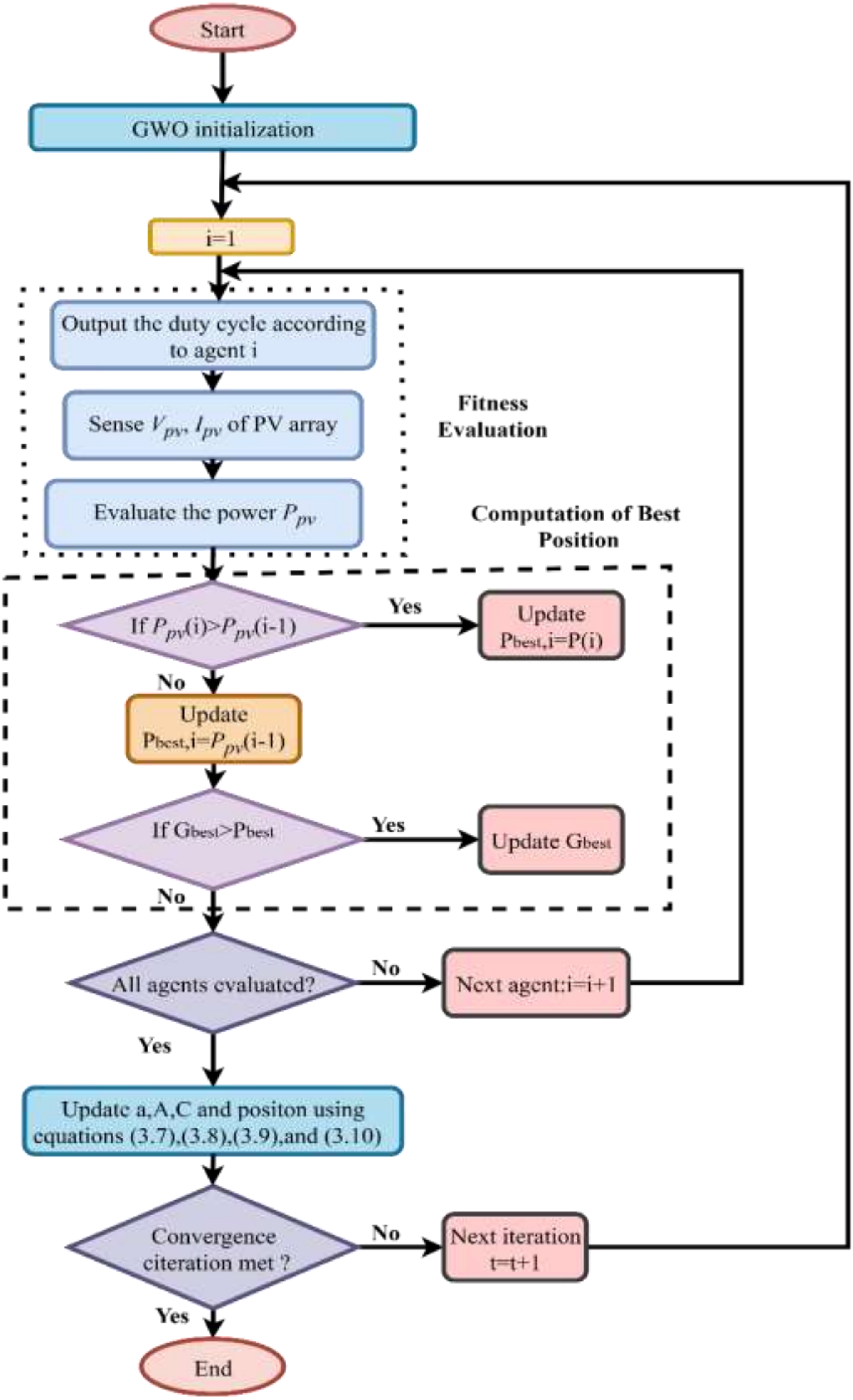

Figure 3.3. Flowchart of GWO method.

3.3.2.2 EO for MPPT

EO proposed by Faramarzi et al. [52], is a metaheuristic inspired by the concept of volumetric mass balance, where the rate of mass variation is expressed as the difference between inflow and outflow, resulting in the final mass [53,14]. For MPPT applications, each particle in EO corresponds to a possible duty cycle, and its concentration determines the search position within the PV operating range. The particles attempt to move toward equilibrium states, which represent the optimal power points, by following randomly selected equilibrium positions within the search domain. In this context, concentration reflects the PV operating condition, and the algorithm gradually drives particles toward the MPP [14].

The algorithm's main objective is to achieve equilibrium, which represents the global MPP. To strengthen both exploration and exploitation, EO selects four of the best-performing duty cycles along with one additional candidate. These five, known as equilibrium candidates, improve the balance between global search and local refinement. Their average is also considered in the exploitation phase to enhance convergence toward the global MPP [14]. The candidates are finally combined to form the equilibrium set, given by:

$$\begin{cases} D_{ceq}^{t} \in \{D_{ceq1}, D_{ceq2}, D_{ceq3}, D_{ceq4}, D_{ceq,ave}\} \\ D = D_{c} - D_{ceq}^{t} \\ D_{c}^{t+1} = D_{ceq}^{t} - D.F + \dfrac{G_{\alpha}}{\lambda_{\alpha}}.(1 - F_{\alpha}) \end{cases} \tag{3.11}$$

Where, $D_{ceq1}, D_{ceq2}, D_{ceq3}, D_{ceq4}$ represent the control variables corresponding to the four best-fit individuals in the current generation, while $D_{ceq,ave}$ denotes their average value. D_{c} is randomly selected from these candidates. In the context of MPPT, these variables correspond to duty cycle candidates that guide the search toward the MPP.

In the EO-based MPPT, the duty cycle update relies on the equilibrium candidates defined in Equation (3.11). At each iteration, the new position of a particle (duty cycle) is determined by randomly selecting one of the best four equilibrium points or their average, ensuring equal probability across the options. The difference vector D expresses the deviation between the current solution and the chosen equilibrium state.

The update process is further influenced by two control terms:

- F defined in Equation (3.12), which introduces an exponential component with random variation to balance exploration and exploitation.
- G expressed in Equation (3.13), which adds an adaptive correction term guided by the global control parameter *GCP*.

The parameter λ is a uniformly distributed random vector in [0,1], and l (Equation (3.14)) ensures gradual convergence by decreasing with iterations. Together, these factors enable EO to effectively guide particles (duty cycles) toward the MPP.

$$F = 2\text{sign}\left(r - 0.5\right).\left(e^{l\lambda} - 1\right) \tag{3.12}$$

$$\begin{cases} G = G_0.F \\ G_0 = GCP.[D_{ceq}^t - \lambda.D] \\ GCP = \begin{cases} 0.5r_1 & r_2 \geq GP \\ 0 & r_2 < GP \end{cases} \end{cases} \tag{3.13}$$

r is a random vector with a uniform distribution over the unit interval. r_1 and r_2 are random values with a uniform distribution within the unit interval.

$$l = \left(1 - \frac{t}{T}\right)^{\frac{t}{T}} \tag{3.14}$$

The overall procedure of the EO applied as an MPPT method is summarized in Figure 3.4.

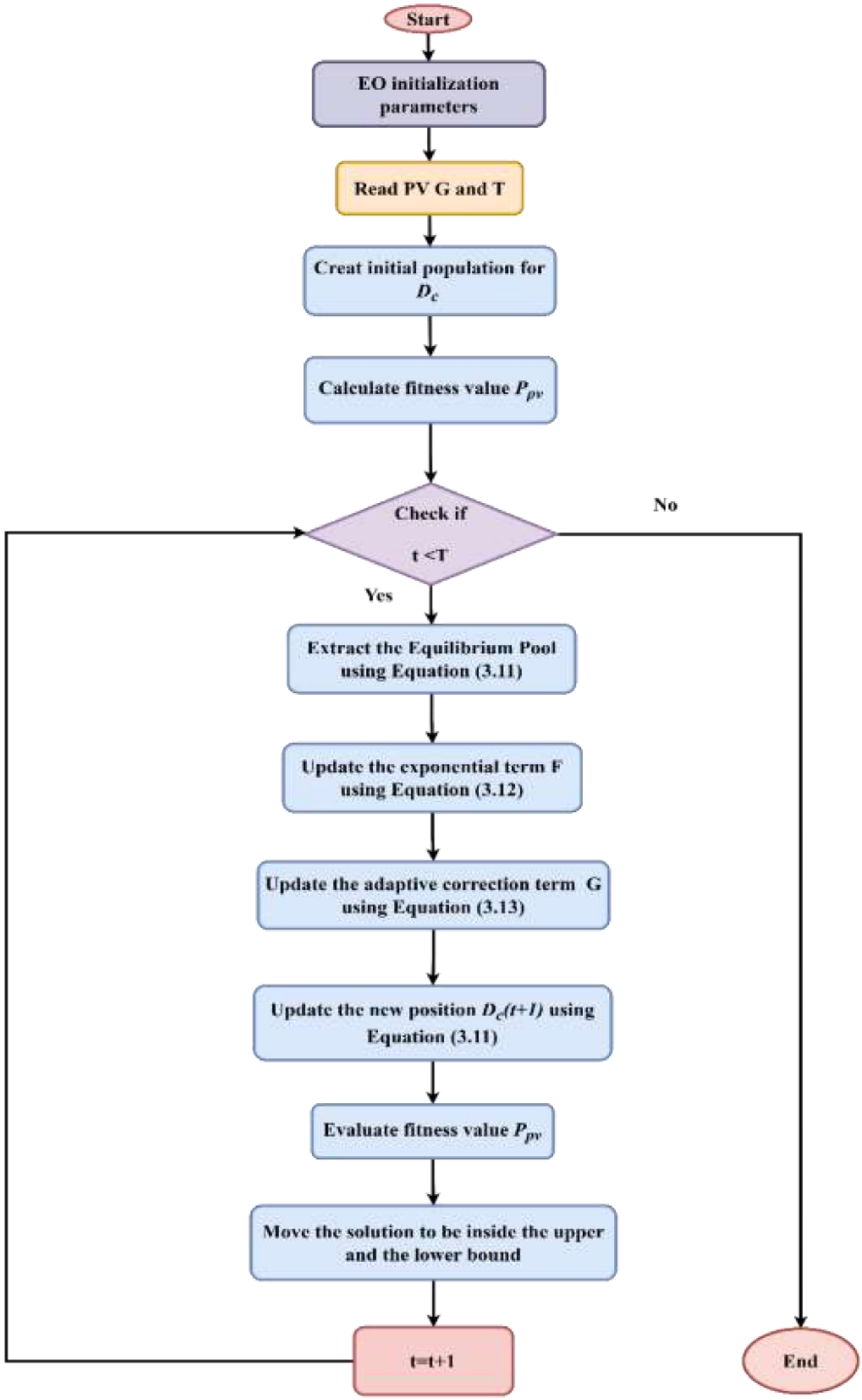

Figure 3.4: Flowchart of EO method

3.3.2.3 Hybrid GWEO approach

Building on the comparison between the updating mechanism of GWO and EO, a hybrid GWEO algorithm is developed for MPPT in grid-connected photovoltaic (PV) systems. This method is designed to effectively address the challenge of optimizing power extraction under UICs, and PSCs [14].

The improved updating mechanism of GWEO overcomes the inherent shortcomings of both GWO and EO. Specifically, in GWO, the random vector components are generated within the range [−2,2], whereas in EO, this range is reduced to [−1.2642,1.2642] [54]. The narrower search domain of EO may restrict exploration and thus reduce tracking efficiency. Moreover, GWO does not incorporate a random perturbation factor, which increases the likelihood of premature convergence to a local optimum, preventing accurate identification of the global MPP.

To mitigate these issues, the proposed GWEO algorithm integrates the updating operators of GWO and EO, as expressed in Equations (3.7)– (3.8) and (3.11). The corresponding update rules (Equations (3.15)– (3.17)) define how the positions of the wolves, representing candidate operating points of the PV system, are adapted in each iteration. The update is guided by the three best wolves (α, β, and δ), while additional stochastic perturbations are introduced to enhance the balance between exploration and exploitation.

This hybrid updating strategy strengthens the ability of the algorithm to avoid local traps, ensuring more reliable convergence toward the true MPP. Consequently, the GWEO-based MPPT achieves superior performance in tracking maximum power output under diverse irradiance and temperature conditions. The overall algorithmic structure of GWEO is illustrated in Figure 3.5, which presents the pseudo-code of the proposed method.

The formula for the population updating approach is as follows:

$$\begin{cases} D_\alpha = \left| C_1 . D_\alpha - D_{ci}^t \right| \\ D_\beta = \left| C_1 . D_\beta - D_{ci}^t \right| \\ D_\delta = \left| C_1 . D_\delta - D_{ci}^t \right| \end{cases} \tag{3.15}$$

$$\begin{cases} D_{c1} = D_\alpha - A_1.D_\alpha + \dfrac{G_\alpha}{\lambda_\alpha}.(1-F_\alpha) \\ D_{c2} = D_\beta - A_2.D_\beta + \dfrac{G_\beta}{\lambda_s}.(1-F_\beta) \\ D_{c3} = D_\delta - A_3.D_\delta + \dfrac{G_\delta}{\lambda_\delta}.(1-F_\delta) \end{cases} \tag{3.16}$$

$$D_{ci}^{t+1} = \frac{D_{c1} + D_{c2} + D_{c3}}{3} \tag{3.17}$$

Input:

- Population size (N), Maximum number of iterations (T), Control parameters of GWO and EO ($a, A, C, \lambda, F, G, \ldots$ etc.), Search space boundaries (Ub , Lb)

Initialization:

- Initialize the population of wolves $D_c(i)$, where i = 1, 2, ..., N $i = 1, 2, \ldots, N$
- Set iteration counter $t = 0$

Begin:

while $(t<T)$:

- Evaluate the fitness of each wolf
- Identify the positions of α , β , and δ (best, second-best, and third-best wolves)
- Generate random vectors λ, F, G

For each $t = 1$ to T:

- Update the control parameter 'a' (decreases linearly from 2 to 0)

End for

For each wolf $D_c(i)$:

- Update coefficients A, C using Equation (3.9)

End for

- Calculate the distances to the best wolves using Equation (3.16)
- Calculate disturbance based on EO using Equation (3.17)
- Update the position of the wolf using Equation (3.18)
- Evaluate the fitness of the updated population
- Update the positions of α , β , and δ wolves

End while

Output:

- Best solution found (D_α)

end

Figure 3.5: Pseudo-code of GWEO

3.3.3 Proposed GWO-PSO for MPPT

The recently developed hybrid approach, GWO-PSO, integrates the strengths of the GWO and PSO to improve both exploration and exploitation in the search for optimal solutions. The primary objective of this hybrid strategy is to prevent premature convergence and enhance accuracy in identifying the global optimum, particularly in complex and multimodal search spaces. By combining the complementary characteristics of GWO and PSO, the method achieves a balance between local optimization and global exploration, thereby improving overall performance across various optimization problems. In this section, each method is examined separately, with GWO discussed in the previous part (proposed GWEO approach), followed by PSO.

3.3.3.1 PSO for MPPT

PSO is a MOAs technique inspired by the social behavior of birds. It employs a population-based search strategy in which potential solutions are modeled as particles moving through the search space. Each particle has a position (x) and a velocity (v), which define its movement in terms of direction, distance, and step size [55].

In the context of MPPT, the particle position corresponds to the duty cycle of the DC–DC converter, while the fitness function is the PV power of the PV system. Each particle retains memory of its best-obtained position (P_{best}) and shares information with the swarm about the global best (G_{best}), which represents the global MPP identified so far [56].

PSO is particularly attractive for MPPT because of its simplicity, fast convergence, and minimal parameter tuning. The algorithm balances exploration (searching a wide range of duty cycles to avoid local maxima) with exploitation (refining the search around promising global MPP candidates).

The velocity and position updates are governed by:

$$v_i^{t+1} = \omega . v_i^t + r_1 c_1 (P_{best,i}^t - d_i^t) + r_1 c_1 (G_{best,i}^t - D_{ci}^t) \tag{3.17}$$

$$D_{ci}^{t+1} = D_{ci}^t + v_i^{t+1} \tag{3.18}$$

In PSO-based MPPT, the position of each particle corresponds to the duty cycle of the DC–DC converter, while its velocity governs the step size and direction of adjustment. The velocity update equation incorporates several key parameters: the inertia weight (ω) that controls the influence of the previous velocity, the cognitive coefficient (c_1) that emphasizes the particle's own best position (P_{best}), and the social coefficient (c_2) that directs the search toward the global best solution (G_{best}). Random factors (r_1, $r_2 \in [0,1]$) are included to introduce stochasticity and enhance exploration. Specifically, for particle i at iteration t, D_{ci}^t denotes its duty cycle, v_i^t its velocity, P_{best},i its personal best duty cycle, and G_{best} the best duty cycle identified by the entire swarm, corresponding to the GMPP. Through this iterative mechanism, PSO continuously updates duty cycles and successfully tracks the GMPP, even under UICs and PSCs. The operational structure of the proposed PSO algorithm is depicted in Figure 3.6.

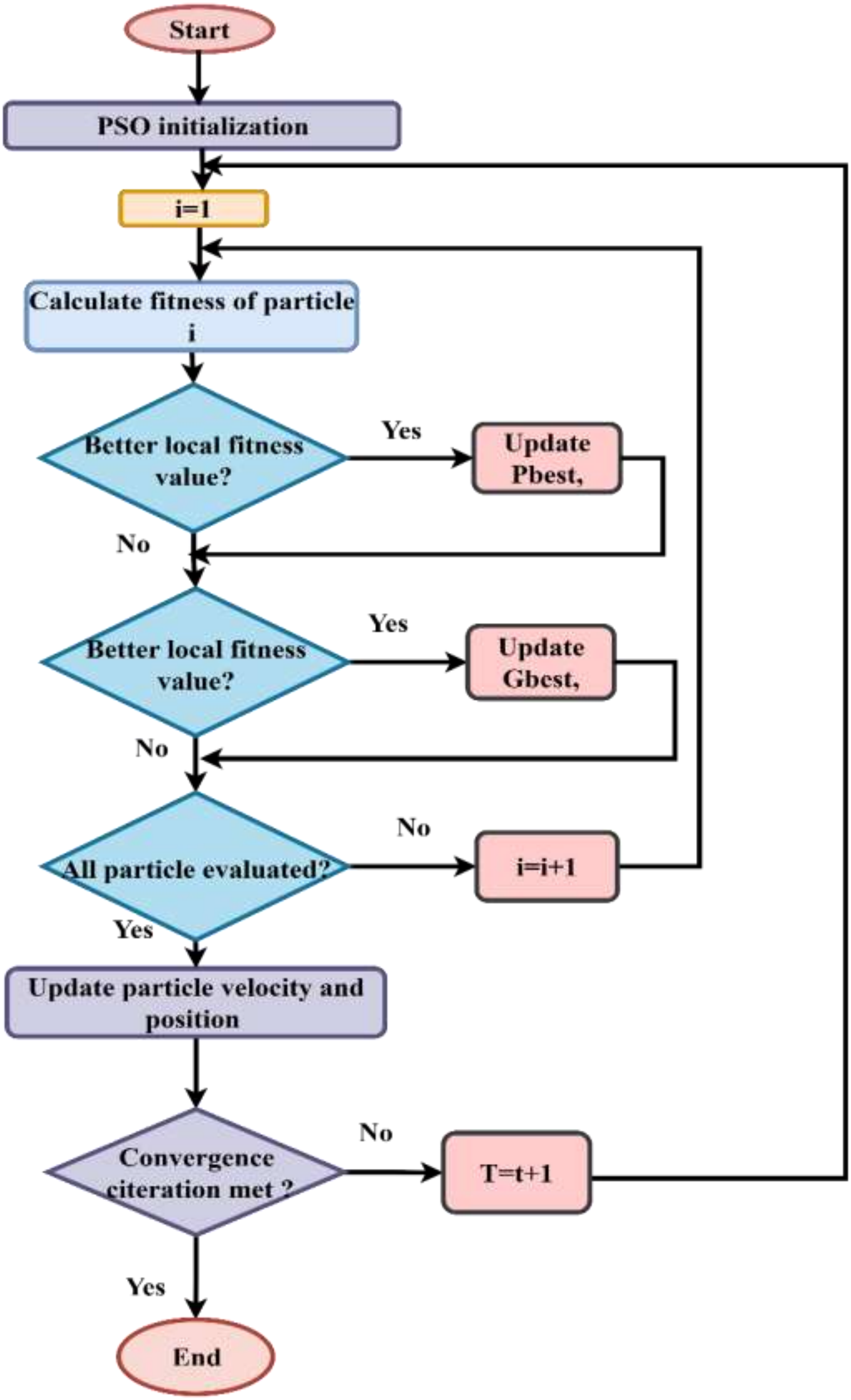

Figure 3.6: PSO MPPT flowchart

3.3.3.2 GWO-PSO approach

The hybrid GWO-PSO approach is designed to leverage the complementary advantages of the GWO and PSO in MPPT applications. While GWO provides an effective mechanism for exploitation by mimicking the leadership hierarchy and hunting strategy of grey wolves, PSO introduces a velocity-based update rule that enhances exploration and prevents premature convergence [57].

In the hybrid model, the GWO component relies on three key agents: (α, β, δ), which represent the best solutions identified so far. These wolves guide the rest of the population (ω wolves), coordinating their movements and steering the search process. The GWO mathematical model updates the positions of all search agents according to their relative attraction to α, β, δ, thereby achieving a balance between exploration and exploitation [55].

The PSO component complements this by adjusting each agent's velocity based on its previous velocity and its attraction toward both its personal best position and the global best position D_{c1}, D_{c2} and D_{c3}. The velocity and position updates are given by Equations (3.19) and (3.20), respectively. The velocity equation governs the step size and direction of the particle's movement, while the position equation updates the particle's location according to its newly calculated velocity [56].

- **Velocity update:**

$$v_i^{t+1} = \omega \cdot v_i^t + c_1 \cdot r_1 \cdot (D_{c1} - D_{ci}) + c_2 \cdot r_2 \cdot (D_{c2} - D_{ci}) + c_3 \cdot r_3 \cdot (D_{c3} - D_{ci}) \tag{3.19}$$

- **Position update:**

$$D_{ci}^{t+1} = D_{ci}^t + v_i^{t+1} \tag{3.20}$$

This equation adjusts each agent's position based on the newly estimated velocity. The hybrid method achieves the best balance of exploration and exploitation by combining GWO's exploitation-driven technique with PSO's velocity-based exploration. The algorithmic framework of the proposed GWO-PSO method is summarized in Figure 3.7.

Input:

- Set the initial parameters of the GWO–PSO algorithm;

Initialize:

$t = 1$

- Generate an initial population of search agents D_{ci} (i = 1, 2, ..., N);
- Initialize parameters a, A, and C;
- Initialize velocity Vi for each search agent;
- Calculate the fitness value of each search grey wolf;
- Identify D_{α}, D_{β}, and D_{δ} as the best, second-best, and third-best solutions;

While $t \leq T$ do

For i = 1 to N do

- Update the velocity of the current search grey wolf using Equation (3.19);
- Update the position of the current search grey wolf using Equation (3.20);

End for

- Update parameters a, A, and C
- Calculate the fitness values of all search grey wolves;
- Update D_{α}, D_{β}, and D_{δ};

$t = t + 1$

End while

- Return D_{α} (best solution);

Output:

- Display the optimum solution corresponding to D_{α};

Figure 3.7: Pseudo-code of GWO-PSO

3.4 Comparative Study Between Various MPPT Techniques

MOAs play a vital role in global MPP tracking under PSCs. To validate the effectiveness of the proposed hybrid approaches, a comparative study was conducted with several well-established MPPT methods. Specifically, the WOA and FPA were implemented under the same test conditions, alongside the previously discussed GWO and PSO techniques. Now, we will study the methods that were compared with it, which are WOA, FPA, and the others mentioned previously. These comparisons allow for a fair evaluation of performance in terms of tracking accuracy, speed of convergence, and robustness against environmental fluctuations. By benchmarking the proposed method against WOA and FPA, as well as GWO and PSO, the study highlights the improvements achieved in terms of efficiency and reliability in global MPP tracking.

3.4.1 FPA for MPPT

The FPA, first introduced by Xin-She Yang in 2012, is inspired by the natural pollination process of flowering plants. In the context of MPPT, the algorithm mimics this biological mechanism to efficiently search for the GMPP under PSCs [58,59].

FPA begins with a set of candidate duty cycles, called *pollen grains*, which represent possible operating points of the PV system. Each grain is evaluated through the DC-DC converter, where the corresponding PV power is calculated. The pollen grain with the highest extracted power is considered the best solution (P_{best}).

At each iteration, a switching probability parameter (p, typically set to 0.8) determines whether the pollination is local (exploitation) or global (exploration):

- Local pollination is modeled by Equation (3.21), where pollen grains interact within a neighborhood to refine the search around promising solutions.
- Global pollination is represented by Equation (3.22), where Lévy flights introduce randomness and allow the algorithm to escape local optima, improving the chance of locating the true GMPP.

New pollen grains (duty cycles) are generated and evaluated in every cycle. The global best solution (G_{best}), corresponding to the duty cycle yielding the maximum PV power, is updated iteratively. This process ensures that the PV system consistently converges to the optimal duty cycle, maximizing power extraction.

The general FPA update equations are expressed as:

$$D_{ci}^{t+1} = D_{ci}^{t} + \varepsilon(D_{ck}^{t} - D_{ci}^{t}) \tag{3.21}$$

$$D_{ci}^{t+1} = D_{ci}^{t} + \gamma \mathrm{L}(\lambda)(\mathrm{G}_{best} - D_{ci}^{t}) \tag{3.22}$$

Where:

- D_{ci}^{t} : represents the duty cycle of pollen grain i at iteration t.

- G_{best} : represents the current global best duty cycle, corresponding to the GMPP.
- γ : represents the step size scaling factor.
- $L(\lambda)$: represents the Lévy flight distribution used for global pollination.
- $\varepsilon \in [0,1]$: represents a random number controlling the local pollination process.
- D_{ck}^{t} : represents randomly selected duty cycles from the population.

Through this mechanism, FPA balances exploration and exploitation, ensuring reliable and efficient MPPT performance, even under partial shading and dynamic weather conditions. Figure 3.8 shows a flowchart of the FPA's step-by-step approach. This image depicts how the FPA goes through its iterative processes, from pollen production to selecting the best solution.

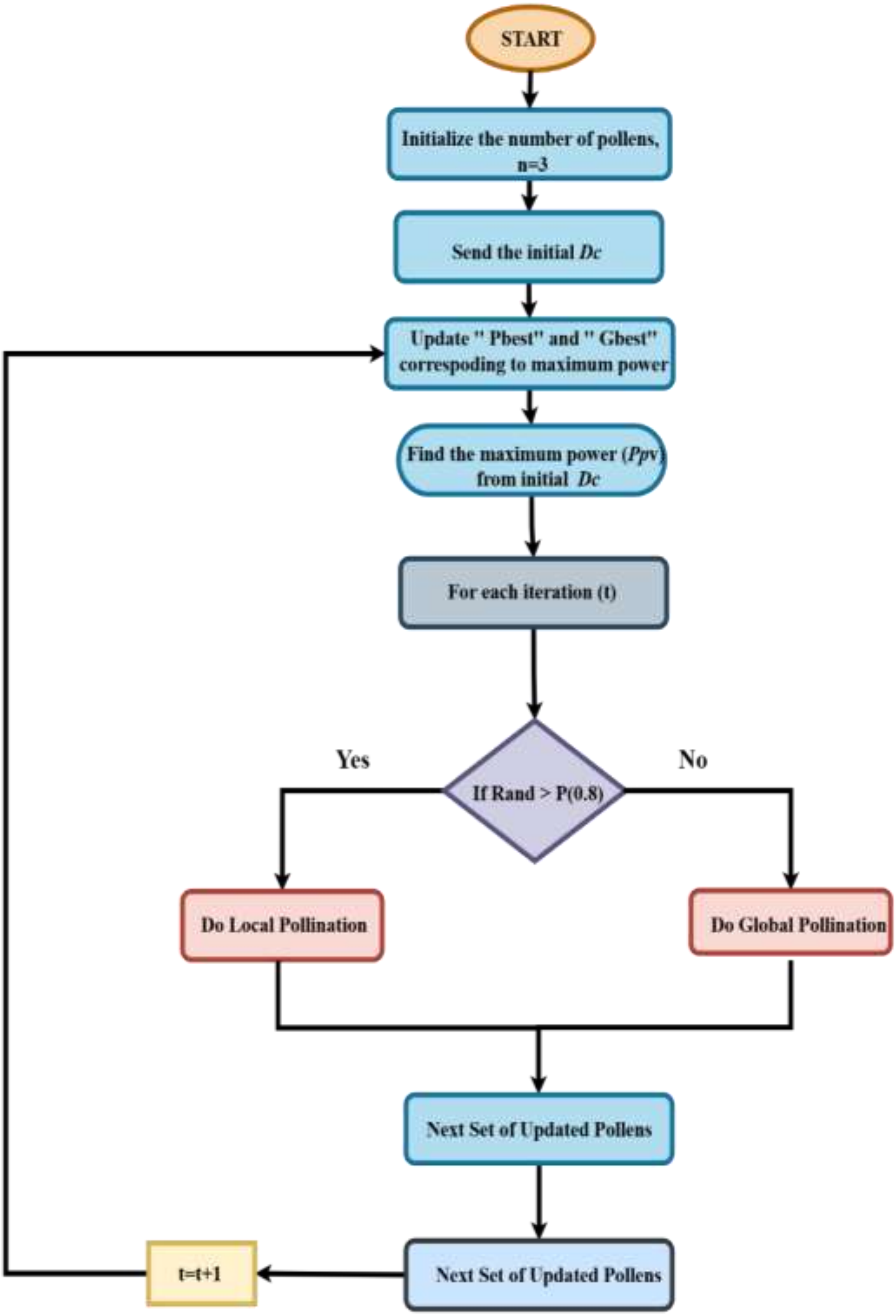

Figure 3.8: Flowchart of FPA method

3.4.2 WOA for MPPT

The WOA, introduced by Mirjalili in 2016, is inspired by the unique bubble-net hunting strategy of humpback whales. This intelligent behavior involves surrounding prey and attacking it through spiral and shrinking encircling movements. When adapted for MPPT in photovoltaic (PV) systems, WOA simulates this cooperative hunting process to dynamically locate GMPP under fluctuating environmental conditions [62]. At each iteration, the algorithm updates the position of each whale (candidate duty cycle) relative to the best-known position $D_c^*(t)$, representing the highest power point obtained so far. The encircling mechanism is modeled as:

$$D = C.D_c^*(t) - D_c(t) \tag{3.23}$$

$$D_c(t+1) = D_c^*(t) - A.D \tag{3.24}$$

The coefficient vectors A and C are defined as:

$$\begin{cases} A = 2a \cdot r - a, \\ a = 2\left(1 - \dfrac{t}{T}\right), \\ C = 2r. \end{cases} \tag{3.25}$$

with a linearly decreasing from 2 to 0 and r a random vector in [0, 1]. These adaptive coefficients allow WOA to control the balance between exploration and exploitation during the search process. When |A|<1, the search agents move closer to the current best solution (exploitation), while |A|>1 promotes exploration by directing the agents away from the best position to investigate new regions of the search space [60].

To simulate the bubble-net attacking phase, the whales simultaneously perform both spiral and shrinking encircling motions with equal probability. This stage can be expressed as:

$$D_c(t+1) = \begin{cases} D_c^*(t) - A.D & if \;\; p < 0.5 \\ D^*.e^{bl}.\cos(2\pi l) + D_c^*(t) & if \;\; p > 0.5 \end{cases} \tag{3.26}$$

where b is a constant defining the spiral shape, and l is a random number in [–1, 1], and p is a random number in [0,1]. The algorithm randomly switches between the encircling and spiral equations with a 50% probability, ensuring both convergence and diversity of the search [61]. Furthermore, the exploration phase of WOA, analogous to whales searching for new prey, is achieved by updating positions with respect to randomly selected individuals rather than the current best, following:

$$D = C.D_{crand}(t) - D_c(t) \tag{3.27}$$

$$D_c(t+1) = D_{crand}(t) - A.D \tag{3.28}$$

This mechanism allows WOA to maintain global search ability and avoid premature convergence to local maxima. Figure 3.9 outlines the algorithmic structure of the proposed WOA method.

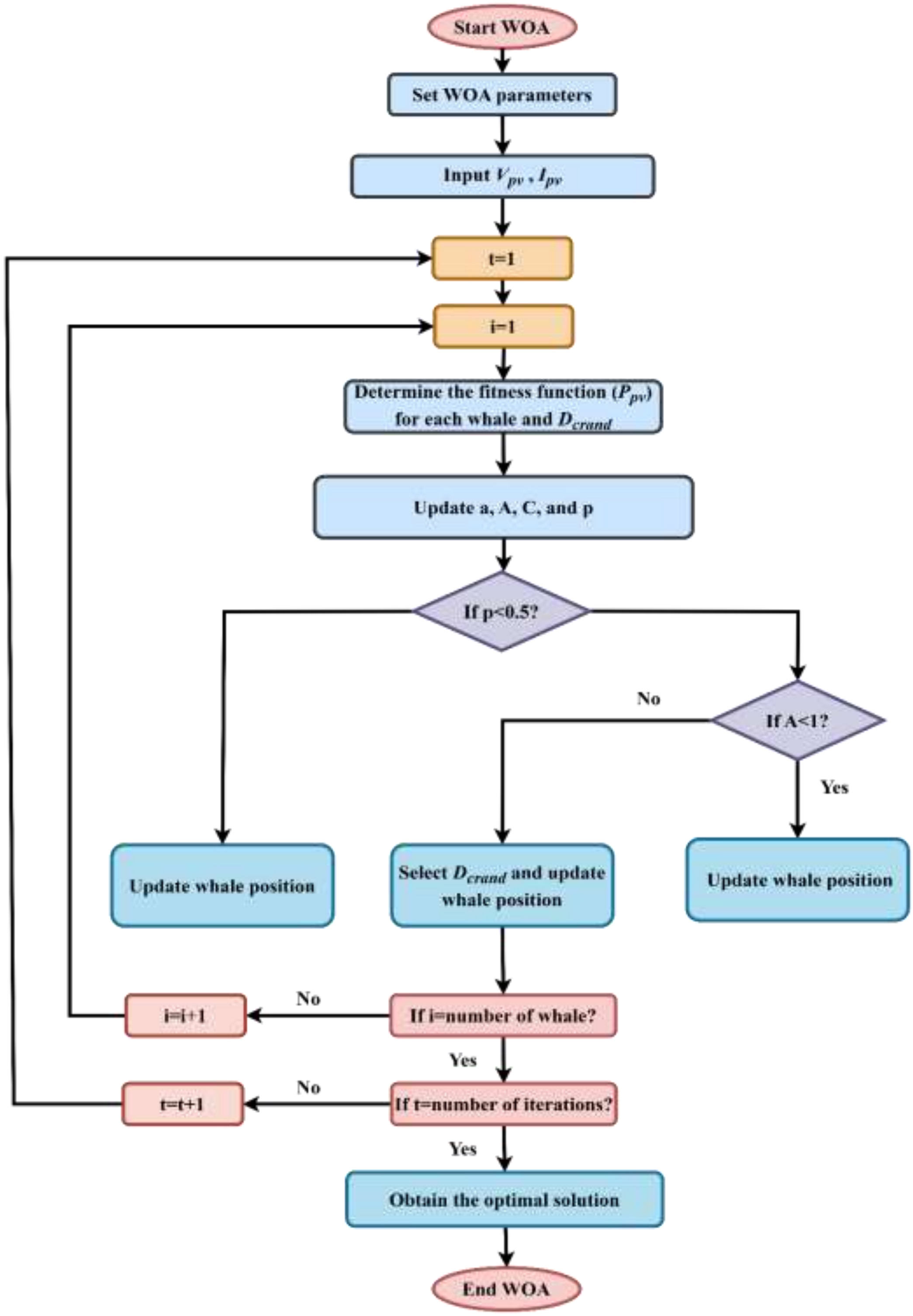

Figure 3.9: Flowchart of WOA

3.5 Conclusion

This chapter presented an in-depth analysis of MPPT techniques, encompassing both conventional algorithms and advanced intelligent optimization methods. The discussion began with an overview of traditional MPPT techniques, outlining their operational principles, advantages, and limitations. To overcome these constraints, soft computing and metaheuristic optimization methods were introduced as more adaptive and efficient alternatives, capable of ensuring faster dynamic response and improved tracking precision.

Within this thesis, several optimization-based MPPT techniques were investigated for their effectiveness in controlling the D_c of DC–DC converters and enhancing the overall power extraction efficiency of PV systems. Building upon this foundation, a series of novel and hybrid optimization algorithms were proposed, including ZOA for MPPT, GWEO, and hybrid GWO-PSO. Each of these proposed methods was developed to improve the balance between exploration and exploitation, reduce steady-state oscillations, and accelerate convergence toward the global MPP, particularly under PSCs and rapidly changing environmental conditions.

To evaluate the effectiveness of the proposed strategies, they were compared with several well-established algorithms, including WOA, FPA, PSO, and GWO. This comparative framework allows for a comprehensive assessment of performance improvements achieved through the newly developed techniques.

The theoretical and algorithmic developments presented in this chapter form the conceptual and mathematical foundation for the implementation and validation of the proposed MPPT methods. The five chapter will present the experimental verification and comparative performance analysis to assess their accuracy, robustness, and computational efficiency in real-time in GCPV systems.

Chapter 4:

Advanced Control and Regulation Techniques for Shunt Active Power Filters

4.1 Introduction

In this chapter, the main objective is to enhance the internal structures of current control techniques in order to improve filter performance in terms of harmonic mitigation, reactive power compensation, and power factor correction. To achieve these objectives, SAPF topology is selected, as it offers several advantages over other configurations reported in the literature.

This chapter focuses on the improvement and development of control strategies applied to SAPF systems. Various control techniques are investigated, starting with the conventional direct power control (DPC) method, followed by the predictive direct power control (P-DPC) approach, which represents an advanced evolution based on predictive modeling.

In addition, several controller structures are examined, including the conventional proportional-integral (PI) controller, the PI controller with anti-windup (PI-AW) compensation, and their fractional-order extensions, namely the fractional-order PI (FOPI) and fractional-order PI anti-windup (FOPI-AW) controllers. Their performances are evaluated under dynamic and nonlinear operating conditions.

Although conventional controllers can provide satisfactory performance under steady-state operating conditions (PI) and improved performance under dynamic operating conditions (FOPI), their effectiveness remains limited when dealing with parameter variations, nonlinearities, and grid disturbances. To overcome these limitations, this chapter proposes an advanced optimization-based control approach employing the ZOA to optimally tune the parameters of fractional-order (FO) controllers.

The proposed optimization framework aims to enhance system stability, dynamic response, and overall power quality by minimizing a multi-objective cost function. This cost function incorporates key performance indicators such as DC-link voltage (V_{dc}) overshoot, steady-state error, and THD of the supply current (I_s). Using this framework, the ZOA algorithm efficiently determines the optimal controller parameters, including proportional gain(k_p), and integral gain (k_i), anti-windup coefficients (G_a), and fractional integration order (α), thereby ensuring superior control performance under various grid and load conditions.

The remainder of this chapter is organized as follows:

- **Section 1** reviews the control techniques applied to SAPF systems.
- **Section 2** presents the control principles and mathematical formulations of the conventional PI and FOPI controllers.
- **Section 3** introduces the ZOA-based optimization procedure and its application in controller tuning.
- **Section 4** describes the Oustaloup Continuous Approximation (OCA) method used to implement the fractional-order operators.
- **Section 5** discusses the phase-locked loop (PLL), which is essential for grid synchronization.
- **Finally**, this chapter presents simulation results and performance analyses demonstrating the significant improvements achieved in V_{dc} regulation, harmonic mitigation, and overall SAPF stability using the proposed ZOA-optimized control strategy.

4.2 SAPFs control strategies

SAPFs are widely acknowledged as one of the most effective technologies for compensating current harmonics and enhancing power quality in electrical networks containing nonlinear loads. Over time, numerous control strategies have been proposed to achieve precise harmonic mitigation, rapid transient response, and stable performance under different grid conditions.

These strategies can generally be grouped into several categories:

- Current control–based methods, such as hysteresis control (HC) and direct current control (DCC), which are simple and easy to implement but often exhibit drawbacks like variable switching frequency or slower transient performance [27].
- Voltage-oriented control (VOC) techniques, which operate in the synchronous reference frame and enable accurate control but require multiple coordinate transformations [1].

- DPC techniques, which act directly on instantaneous power components, thus removing the need for separate current controllers or modulation stages [24,27].
- P-DPC approaches anticipate the future behavior of the system using a mathematical model to determine the optimal switching state for achieving the desired power control objectives [22].

Among these, P-DPC has gained significant attention as a highly efficient approach. By integrating the predictive modeling framework with the principles of DPC, P-DPC minimizes a predefined cost function based on instantaneous active and reactive power errors. Compared with conventional DPC, this method achieves higher control precision, faster dynamic performance, and superior harmonic suppression, while preserving a relatively simple implementation structure.

Table 4.1: Comparison of SAPFs control strategies

Control Strategy	Main principle	Advantages	Limitations	Typical applications
HC	Maintains the actual current within a hysteresis band around the reference.	Simple structure, fast dynamic response, high robustness.	Variable switching frequency, increased switching losses, EMI issues.	Low- and medium-power SAPFs where simplicity is prioritized.
DCC	Directly controls the inverter current using a reference-tracking approach with PWM modulation.	Fixed switching frequency, better harmonic compensation compared to hysteresis control.	Slower transient response, requires accurate current sensors.	Industrial SAPFs requiring moderate precision.
VOC	Uses Park transformation (d–q frame) synchronized with the grid voltage to control active and reactive power	High accuracy, decoupled control of power components, steady performance.	Complex transformations, sensitive to parameter variations.	Grid-connected systems and high-performance SAPFs.

	through current regulation			
DPC	Directly regulates instantaneous active and reactive power without current loops.	Fast dynamic response, no modulation stage, simple implementation.	High power ripple, variable switching frequency.	Real-time control applications with fast dynamics, such as grid-connected converters and SAPFs.
P-DPC	Combines predictive modeling with DPC to minimize power errors using a cost function.	High precision, fast convergence, reduced ripple, robust under dynamic conditions.	Moderate computational complexity, sensitive to modeling errors.	Modern SAPFs requiring superior power quality and fast response.

Based on this comparison, P-DPC method demonstrates the most balanced compromise between implementation simplicity, robustness, and enhanced power quality. Consequently, this thesis adopts P-DPC as the main control strategy for the proposed SAPF system. In the following sections, the classical DPC method is first analyzed to establish its operating principles and limitations, after which the predictive DPC (P-DPC) approach is introduced and developed in detail.

4.2.1 DPC technique

DPC approach emphasizes managing active and reactive powers (P and Q) differently than the DTC (Direct Torque Control) method, which uses electromagnetic torque and stator flux capacitance. They should be used for DPC, according to Noguchi [62]. Choosing the right switch state from a predetermined switch table is the key to DPC [63]. More efficient power control can be attained by managing the DC bus voltage by setting the Q to zero. The first entry in the switch table comprises power states produced by individual hysteresis controllers, and the second entry comprises 30 segment details that are calculated using the grid voltage angle. In advance of comparing the P and Q of the network with their corresponding reference powers (P_{ref} and Q_{ref}), network currents ($I_{ph-a,b,c}$) and voltages ($V_{ph-a,b,c}$) must be measured [22]. To establish an appropriate power reference (P_{ref}) and control the V_{dc} to align it around the desired reference (V_{dcref}), the suggested controller integrates into the external voltage regulation loop. Figure 4.1 shows how the DPC-based control platform is configured.

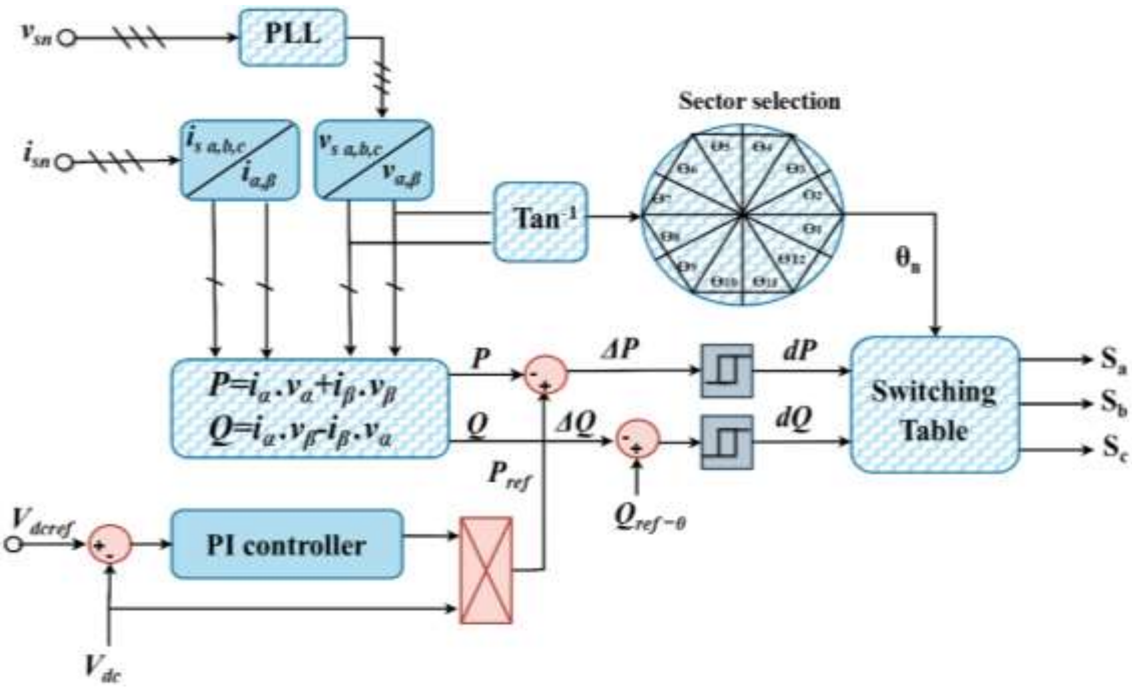

Figure 4.1: DPC configuration for SAPF

P and Q are calculated using the following expressions:

$$\begin{cases} P = i_\alpha . v_\alpha + i_\beta . v_\beta \\ Q = i_\alpha . v_\beta - i_\beta . v_\alpha \end{cases} \tag{4.1}$$

P and Q errors (ΔP, ΔQ) are given by the following expression:

$$\begin{cases} \Delta P = P_{ref} - P \\ \Delta Q = Q_{ref} - Q \end{cases} \tag{4.2}$$

The phase angle of the grid voltage vector is converted into a digital signal, as expressed in Equation (4.3). To accurately determine this phase position, the voltage components V_α and V_β are computed by transforming the three-phase supply voltages from the (a, b, c) reference frame into the stationary (α, β) reference frame, as illustrated in Figure 4.2.

$$\theta_n = \arctan\left(\frac{V_\alpha}{V_\beta}\right)$$
$$(n-2)\frac{\pi}{6} \le \theta_n \le (n-1)\frac{\pi}{6}, \quad n = 1,2,\ldots 12 \tag{4.3}$$

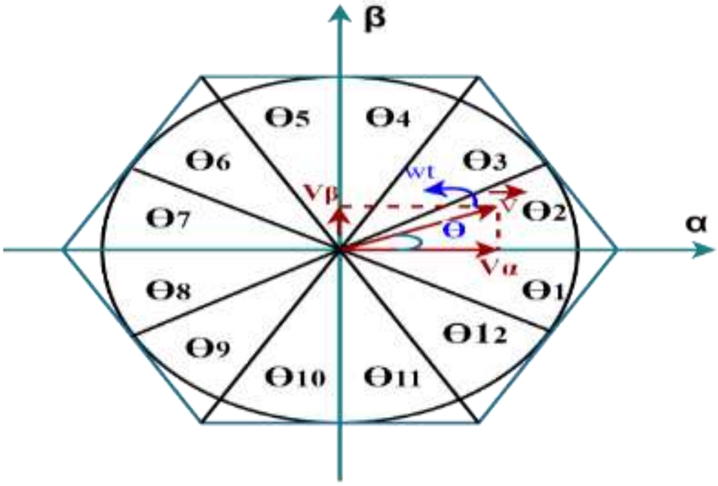

Figure 4.2: Representation of the six sectors with fixed coordinates in the *α-β* plane

Depending on the position of the grid voltage phase angle θ_n and the instantaneous errors ΔP and ΔQ, the converter determines the appropriate switching states to regulate the system's power flow. As illustrated in Table 4.2 [24,22], the twelve-sector switching table serves as the core decision-making mechanism or "brain" of the DPC strategy. This table maps the sector position of the voltage vector in the *α–β* plane and the polarity of the power errors to the optimal switching states, *Sa*, *Sb*, and *Sc*. By continuously updating these states based on the instantaneous operating conditions, the DPC ensures fast dynamic response, accurate power regulation, and adequate harmonic compensation in the SAPFs system.

Table 4.2: Switching table of DPC

dP	dQ	θ_1	θ_2	θ_3	θ_4	θ_5	θ_6	θ_7	θ_8	θ_9	θ_{10}	θ_{11}	θ_{12}
1	0	v_6	v_7	v_1	v_0	v_2	v_7	v_3	v_0	v_4	v_7	v_5	v_0
0	0	v_7	v_7	v_0	v_0	v_7	v_7	v_0	v_0	v_7	v_7	v_0	v_0
0	0	v_6	v_1	v_1	v_2	v_2	v_3	v_3	v_4	v_4	v_5	v_5	v_6
0	1	v_1	v_2	v_2	v_3	v_3	v_4	v_4	v_5	v_5	v_6	v_6	v_1

v_1(100), v_2(110), v_3(010), v_4(011), v_5(001), v_6(101), v_0(000), v_7(111).

4.2.2 P-DPC method

In recent years, P-DPC has emerged as an advanced and efficient control strategy in the field of power electronics, particularly for SAPF applications [22]. This approach is founded on the principle of model-based predictive control, where a mathematical model of the electrical system is used to predict the future values of P and Q corresponding to all possible voltage vectors generated by the VSI [1,64].

At each sampling instant, the predicted power values are compared with their respective reference values through a cost function, which quantifies the error between the desired and predicted outputs. The control algorithm then selects the optimal voltage vector that minimizes this cost function, thereby ensuring that the inverter generates the most appropriate compensation current to correct THD and Q.

The P-DPC technique offers several advantages over classical DPC, including a faster dynamic response, reduced steady-state error, and enhanced power quality. It can also be implemented using either fixed or variable switching frequency, providing flexibility to adapt to various system requirements and design constraints. Furthermore, to ensure V_{dc} stability, the predictive control loop is often complemented by a PI regulator, which maintains a balanced power exchange between the DC and AC sides of the converter [22,64].

Figure 4.3 presents the general structure of the predictive power control strategy, where the controller continuously evaluates switching states to generate compensating currents that effectively eliminate current harmonics and maintain a stable grid voltage.

Since the three-phase source voltages are assumed to remain constant during a single sampling interval Ts, their discrete evolution between two successive sampling instants can be expressed as follows:

$$\begin{cases} v_\alpha(k+1) = v_\alpha(k) \\ v_\beta(k+1) = v_\beta(k) \end{cases} \tag{4.4}$$

By combining Equations (4.1 and 4.4), the P and Q at the next sampling instant can be expressed as:

$$\begin{bmatrix} P(k+1) \\ Q(k+1) \end{bmatrix} = \begin{bmatrix} v_\alpha(k) & v_\beta(k) \\ v_\beta(k) & -v_\alpha(k) \end{bmatrix} \begin{bmatrix} i_\alpha(k+1) \\ i_\beta(k+1) \end{bmatrix} \tag{4.5}$$

Accordingly, the variation of active and reactive powers between two successive sampling instants can be written as:

$$\begin{bmatrix} P(k+1)-P(k) \\ Q(k+1)-Q(k) \end{bmatrix} = \begin{bmatrix} v_\alpha(k) & v_\beta(k) \\ v_\beta(k) & -v_\alpha(k) \end{bmatrix} \begin{bmatrix} i_\alpha(k+1)-i_\alpha(k) \\ i_\beta(k+1)-i_\beta(k) \end{bmatrix} \tag{4.6}$$

Referring to Equation (4.1), the differential equations of the SAPF in the (α, β) stationary reference frame are expressed as:

$$L_f \frac{d}{dt}\begin{bmatrix} i_\alpha \\ i_\beta \end{bmatrix} = \begin{bmatrix} v_\alpha - v_{f\alpha} \\ v_\beta - v_{f\beta} \end{bmatrix} - R_f \begin{bmatrix} i_\alpha \\ i_\beta \end{bmatrix} \tag{4.7}$$

Neglecting the series resistance R_f, this relationship can be simplified to:

$$\frac{d}{dt}\begin{bmatrix} i_\alpha \\ i_\beta \end{bmatrix} = \frac{1}{L_f}\begin{bmatrix} v_\alpha - v_{f\alpha} \\ v_\beta - v_{f\beta} \end{bmatrix} \tag{4.8}$$

By discretizing (Equation (4.7)) over one sampling period T_s, the current vector variation between two sampling instants k and $k+1$ is given by:

$$\begin{bmatrix} i_\alpha(k+1) \\ i_\beta(k+1) \end{bmatrix} = \begin{bmatrix} i_\alpha(k) \\ i_\beta(k) \end{bmatrix} + \frac{T_s}{L_f}\left(\begin{bmatrix} v_\alpha(k) \\ v_\beta(k) \end{bmatrix} - \begin{bmatrix} v_{f\alpha}(k) \\ v_{f\beta}(k) \end{bmatrix} \right) \tag{4.9}$$

Substituting (Equation (4.9)) into (Equation (4.6)) yields the predictive model of the SAPF based on instantaneous active and reactive powers:

$$\begin{bmatrix} P(k+1)-P(k) \\ Q(k+1)-Q(k) \end{bmatrix} = \frac{T_s}{L_f}\begin{bmatrix} v_\alpha(k) & v_\beta(k) \\ v_\beta(k) & -v_\alpha(k) \end{bmatrix} \left(\begin{bmatrix} v_\alpha(k) \\ v_\beta(k) \end{bmatrix} - \begin{bmatrix} v_{f\alpha}(k) \\ v_{f\beta}(k) \end{bmatrix} \right) \tag{4.10}$$

From (Equation (4.10)), it is evident that the coupling inductance L_f and T_s are the only parameters directly involved in the predictive model of the SAPF.

The reference prediction stage plays a vital role in any predictive control strategy, as it directly influences the computation of the control variables at each sampling instant. In the case of P-DPC method, the predictive controller requires the reference values of the instantaneous active and reactive powers, denoted as $P_{ref}(k+1)$ and $Q_{ref}(k+1)$, respectively.

P_{ref} is obtained from the output of the V_{dc} regulator, ensuring that the V_{dc} remains at its desired level. In contrast, the reactive power reference Q_{ref} is generally set to zero in order to maintain a unity PF.

Therefore, the predicted reference powers can be expressed as:

$$\begin{cases} \mathrm{P}_{ref}(k+1) = 2\cdot \mathrm{P}_{ref}(k) - \mathrm{P}_{ref}(k-1) \\ Q_{ref}(k+1) = Q_{ref}(k) \end{cases} \tag{4.11}$$

Finally, the optimal switching state of the inverter is selected by minimizing the cost function G, which represents the quadratic error between the predicted and reference powers:

$$G=\left(P_{ref}(k+1)-P_i(k+1)\right)^2+\left(Q_{ref}(k+1)-Q_i(k+1)\right)^2 \quad i=0,....6 \tag{4.12}$$

With:

$$\begin{cases} \Delta P_{ref}(k)=P_{ref}(k+1)-P(k) \\ \Delta Q_{ref}(k)=Q_{ref}(k+1)-Q(k) \end{cases} \tag{4.13}$$

This minimization process ensures that the inverter produces the appropriate voltage vector that drives the instantaneous powers toward their reference values, thereby enhancing the dynamic response and power quality of the system [22].

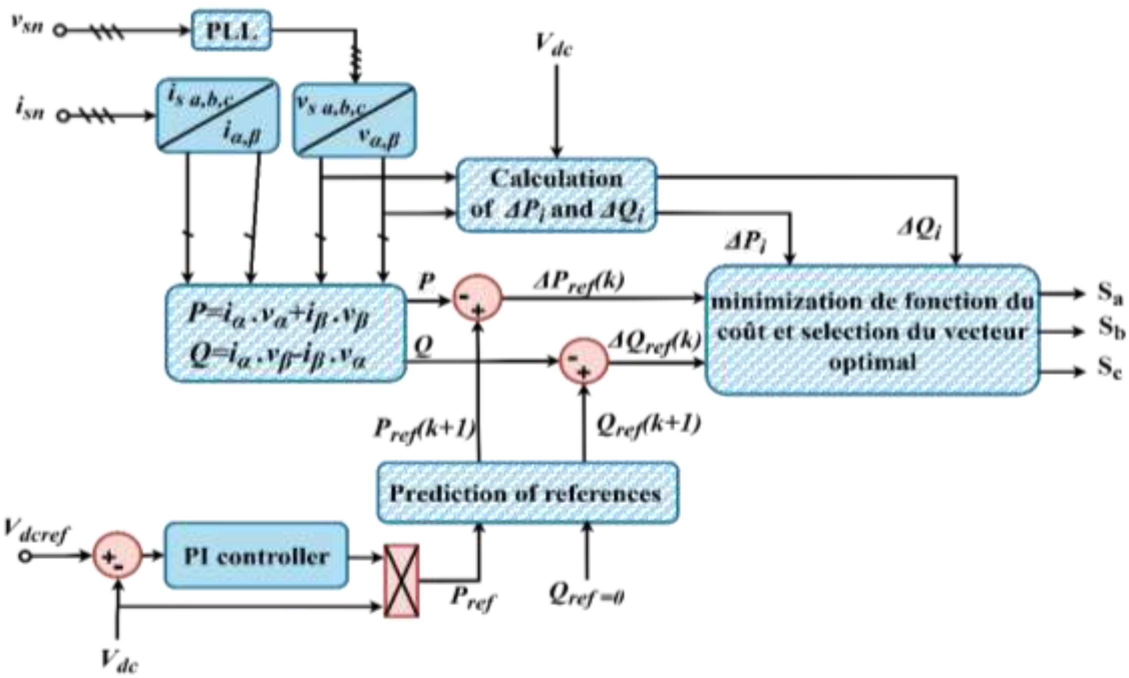

Figure 4.3: P-DPC control strategy structure

4.3 DC bus controller design

Effective regulation of the V_{dc} in a SAPF system is crucial for ensuring stable, efficient, and reliable operation. The C_{dc} serves as the primary energy storage element, supplying the instantaneous active power required to compensate for load current harmonics and reactive components [65]. Any fluctuation in the V_{dc} directly impacts the inverter's ability to generate accurate compensating currents, thereby deteriorating overall system performance and power quality [66].

To overcome this issue, the V_{dc} voltage-control loop generates the required reference signal for the P-DPC strategy, while maintaining V_{dc} at its predefined reference level under varying load and operating conditions.

This thesis evaluates multiple conventional integer-order controllers, including PI and PI-AW. Likewise, fractional-order (FO) PI regulators are investigated, including FOPI and FOPI-AW, together with the proposed FOPI-AW controller optimally tuned using the ZOA (FOPI-AW-ZOA).

Although MOAs have been applied in SAPF control design to improve transient performance, only a limited number of studies have addressed the optimal tuning of FOPI controllers for V_{dc} regulation, especially using advanced MOAs such as the ZOA optimizer in GCPV with SAPF system operating environments. This research gap highlights the need for a robust hybrid tuning framework capable of achieving fast transient response, minimal overshoot, and high steady-state regulation accuracy simultaneously.

Accordingly, this section first analyzes the behavior of the conventional integer-order controllers. The assessment is then extended to the fractional-order controllers, which are comparatively evaluated against the proposed ZOA-tuned FOPI-AW-ZOA controller to validate performance improvements across both dynamic and steady-state operating modes.

4.3.1 Conventional PI controller design

The closed-loop configuration of the V_{dc} regulation in SAPF is depicted in Figure 4.4. In this control structure, the actual V_{dc} is continuously monitored and compared with its reference value (V_{dcref}). The resulting error signal is processed by a PI controller, which generates the control output (I_{smax}). This output is multiplied by the instantaneous V_{dc} to determine the reference active power (P_{ref}) required for maintaining voltage stability [27]. Through this closed-loop regulation, the V_{dc} is effectively maintained around its desired reference, ensuring a stable power balance between the inverter and the grid. Consequently, the SAPF achieves improved dynamic performance and steady-state stability. The overall system transfer function is expressed in Equation (4.14), while Equation (4.15) defines the transfer function of the PI controller used in the DC bus regulation loop.

$$P(s) = \frac{1}{C_{dc}.s} \tag{4.14}$$

$$C_c(s) = k_{pc} + \frac{k_{ic}}{s} \tag{4.15}$$

Where:

k_{pc}: proportional gain,

k_{ic}: integral gain.

Figure 4.5 illustrates the detailed structure of V_{dc} regulation loop, whose mathematical representation is expressed in Equation (4.16).

$$G(s)=\frac{V_{dc}}{V_{dcref}}=\frac{\frac{k_{pc}}{C_{dc}}+\frac{k_{ic}}{C_{dc}}}{s^2+\frac{k_{pc}}{C_{dc}}s+\frac{k_{ic}}{C_{dc}}} \tag{4.16}$$

By simplifying Equation (4.16), the system's transfer function can be reduced to a second-order expression, as presented in Equation (4.17).

$$G(s)=\frac{V_{dc}}{V_{dcref}}=\frac{2\xi\omega_n s+\omega_n^2}{s^2+2\xi\omega_n s+\omega_n^2} \tag{4.17}$$

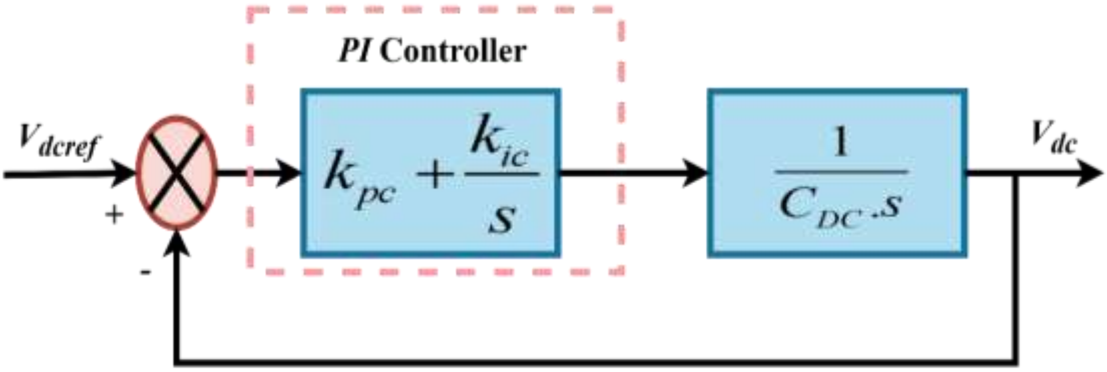

Figure 4.4: PI controller-based DC bus architecture

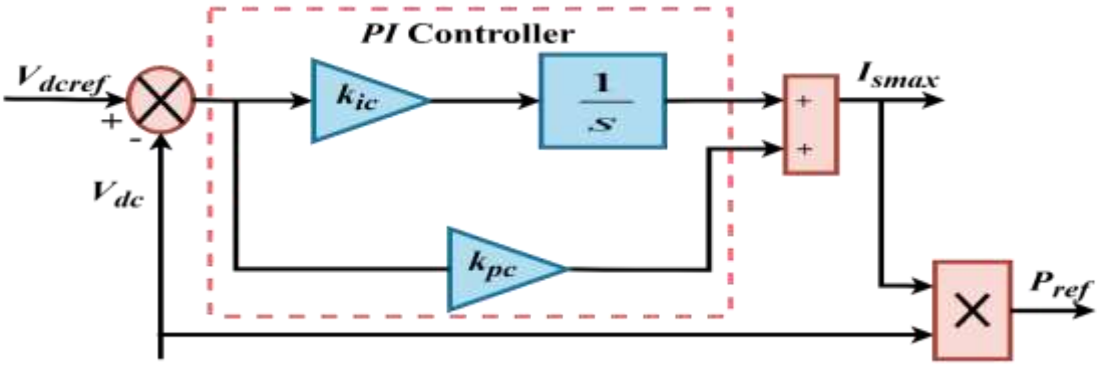

Figure 4.5: Structure of the PI controller integrated to the P-DPC algorithm

The Gains k_{pc} and k_{ic} are given by the identification of Equation (4.18) and (4.19). They are given by the following expression:

$$k_{pc}=2.\xi.\omega_n.C_{dc} \tag{4.18}$$

$$k_{ic} = C_{dc}.\omega_n^{\ 2} \tag{4.19}$$

Here, ω_n denotes the natural angular frequency and ξ the damping factor of the system.

The parameters were selected as ω_n=2π×10 and ξ=0.7 to ensure a fast and well-damped dynamic response.

4.3.2 Conventional PI-AW controller

The conventional PI controller regulates the V_{dc} by integrating the error between the actual capacitor voltage and its reference value. However, under large transient conditions, the integral term may accumulate excessively, causing the controller output to saturate and leading to instability or sluggish recovery, a phenomenon known as integrator windup [27].

To mitigate this problem, an anti-windup structure is introduced, as shown in Figure 4.6. This configuration prevents the integrator from accumulating large errors when the actuator (inverter) output saturates, thereby enhancing the system's dynamic performance and maintaining the V_{dc} within acceptable limits during transients. The anti-windup mechanism effectively limits the control signal and ensures a smoother and faster restoration of V_{dcref} [14].

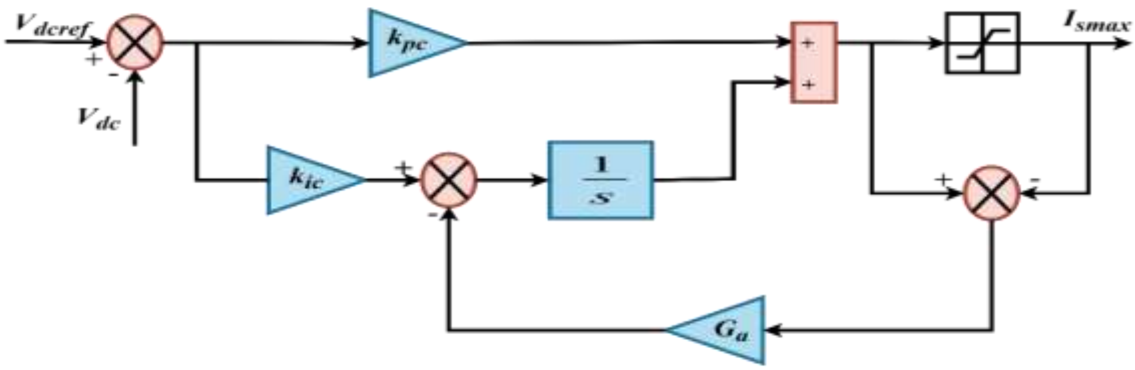

Figure 4.6: PI-AW controller implemented in both simulation and practical experiments

4.3.3 Conventional FOPI controller analysis

Designing an effective controller for industrial processes and power systems is essential to ensure stability, robustness, and high dynamic performance [67]. However, conventional integer-order controllers, including the widely used PI regulator, often exhibit limitations in transient response, overshoot suppression, and steady-state accuracy, especially under nonlinear behavior, parameter uncertainties, and time-varying operating conditions.

To mitigate these shortcomings, the FOPI controller has emerged as an advanced control solution, as depicts in Figure 4.7. By extending the integral operator from an integer order to a fractional order, the controller gains an additional tuning degree of freedom, enabling more precise shaping of both proportional and integral actions. This added flexibility improves the compromise between dynamic response speed and steady-state precision, enhances system damping, and reinforces robustness against disturbances and parametric variations [68,69].

The mathematical formulation of the FOPI controller can be expressed as:

$$C_c(s) = k_p + \frac{k_i}{s^{\alpha}} \tag{4.20}$$

Where, k_p and k_i are the proportional and integral gains, respectively.

When:

$$\begin{cases} \alpha = 1 & \text{Conventional PI} \\ \alpha \in]0,1[& \text{FOPI} \end{cases} \tag{4.21}$$

Both FOPI controller is incorporated into the P-DPC framework to enhance V_{dc} regulation in the SAPF system. By shifting from integer-order to fractional-order control, the system achieves a faster transient response, and lower voltage overshoot [14].

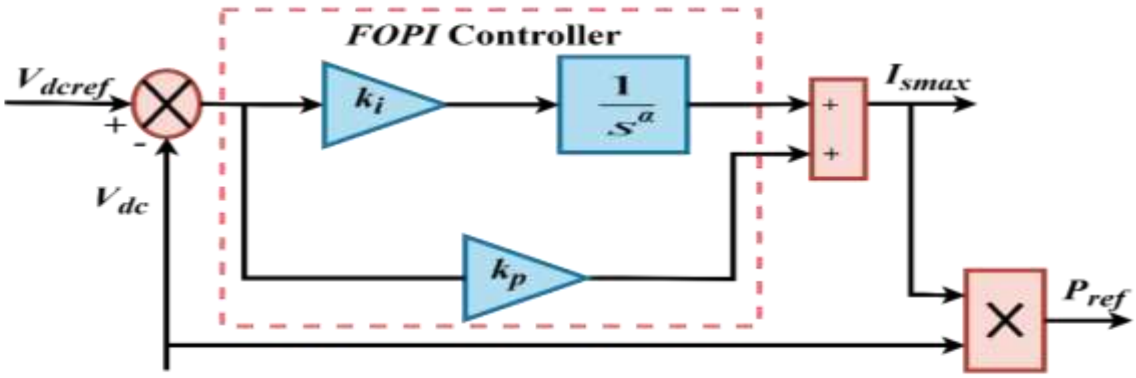

Figure 4.7: Structure of the FOPI controller integrated to the P-DPC algorithm

To further improve controller robustness under nonlinear transients and V_{dc} saturation, the controller is extended by incorporating an anti-windup (AW) configuration. The FOPI-AW regulator structures are illustrated in Figure 4.8. The controller is integrated into the P-DPC control framework for three-phase SAPF applications, where the AW mechanism prevents integral windup and preserves effective control action even under significant disturbances.

Overall, the introduction of FO control into the SAPF voltage regulation loop significantly enhances system stability, robustness, and dynamic adaptability, making the FOPI controller superior alternatives to conventional integer-order designs [69]. The following section presents the conventional procedure for calculating the FOPI controller parameters, including k_p, k_i, and α, providing a systematic foundation for the subsequent design and analysis.

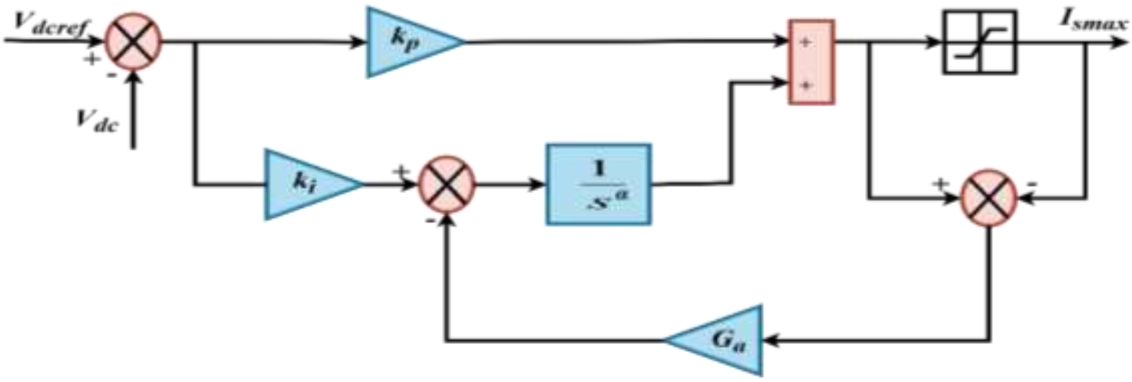

Figure 4.8: FOPI-AW controller implemented in both simulation and practical experiments

4.3.3.1 Parameters calculation

Tuning controller parameters is essential to achieving robustness, stability, and optimal performance in control systems. The parameters of the FOPI controller, k_p, k_i, and α are determined based on frequency domain specifications using the analytical design method [14,27].

The specifications for design include phase margin (ϕ_m), gain Margin, and robustness to gain variations. The closed-loop configuration of the FOPI controller used for V_{dc} regulation is presented in Figure 4.9.

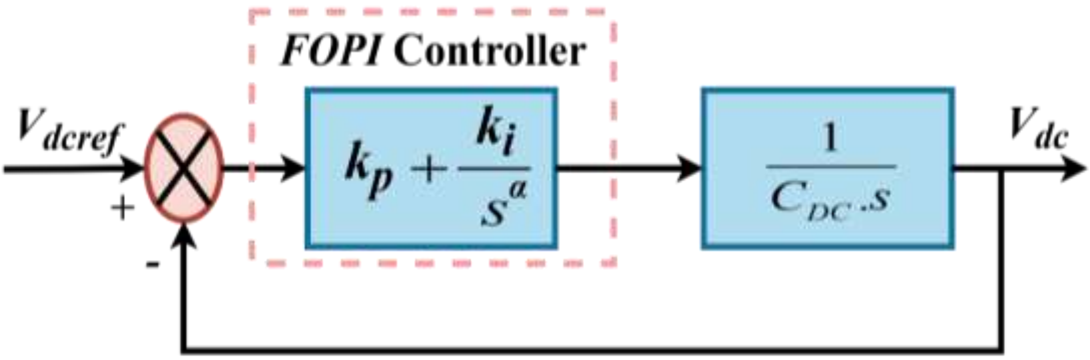

Figure 4.9: Closed-loop control of the DC voltage using an FOPI controller

The FOPI controller's transfer function $C(s)$ assumes a certain crossover frequency ω_c and desired ϕ_m. Using the basic concepts of crossover frequency and ϕ_m, the following mathematical requirements are derived:

A. Phase margin (ϕ_m)

ϕ_m is a crucial indicator of system resilience since it directly influences the system's damping properties [27]. It also determines a control system's stability margin and influences its transient responsiveness.

The open-loop phase margin $G(j\omega)$ may be expressed mathematically using the following equation:

$$arg[plant + controller]_{\omega_c} = \phi_m - \pi \tag{4.22}$$

Where, ω_c represents the crossover frequency, the frequency at which the magnitude of $G(j\omega)$ equals unity (0 dB).

By introducing the expressions for the transfer functions, we can formulate the following equations:

$$arg[C(s).P(s)]_{\omega_c} = \phi_m - \pi \tag{4.23}$$

When replacing $P(s)$ and $C(s)$, we obtain the following equation:

$$arg\left[\left(k_p + \frac{k_i}{s^\alpha}\right).\left(\frac{1}{C_{dc}.\omega}\right)\right] = \phi_m - \pi \tag{4.24}$$

At ω_c, replacing Laplace operator s with $j\omega_c$ to describe the transfer function of the FOPI controller as:

$$arg\left[\left(k_p + \frac{k_i}{(j\omega_c)^\alpha}\right).\left(\frac{1}{C_{dc}.(j\omega_c)}\right)\right] = \phi_m - \pi \tag{4.25}$$

Using the definition of the complex number argument and applying the ϕ_m constraint, the following equation is obtained:

$$arg\left(k_p + \frac{k_i}{(j\omega_c)^\alpha}\right) + \arg\left(\frac{1}{C_{dc}.(j\omega_c)}\right) = \phi_m - \pi \tag{4.26}$$

Taking:

$$\begin{cases} (j\omega_c)^{-\alpha} = \left(\omega_c e^{j\frac{\pi}{2}}\right)^{-\alpha} = \omega_c^{-\alpha}\left[\cos\left(-\alpha\frac{\pi}{2}\right) + j\sin\left(-\alpha\frac{\pi}{2}\right)\right] \\ \cos\left(-\alpha\frac{\pi}{2}\right) = \cos\left(\alpha\frac{\pi}{2}\right), \sin\left(-\alpha\frac{\pi}{2}\right) = -\sin\left(\alpha\frac{\pi}{2}\right) \end{cases} \tag{4.27}$$

By substituting Equation (4.26) into Equation (4.27), we derive the following equation:

$$arg\left(k_p + k_i\omega_c^{-\alpha}\left[\cos\left(\alpha\frac{\pi}{2}\right) + j\sin\left(\alpha\frac{\pi}{2}\right)\right]\right) + \arg\left(\frac{1}{C_{dc}.(j\omega_c)}\right) = \phi_m - \pi \tag{4.28}$$

So:

$$\arctan\left(\frac{-k_i\omega_c^{-\alpha}\sin\left(\alpha\frac{\pi}{2}\right)}{k_p + k_i\omega_c^{-\alpha}\cos\left(\alpha\frac{\pi}{2}\right)}\right) - \frac{\pi}{2} = \phi_m - \pi \tag{4.29}$$

From Equation (4.29), the relationship between k_p, k_i, and α can be formulated as follows:

$$k_i = \frac{-k_p\tan(\phi_m - \pi)}{\omega_c^{-\alpha}\sin\left(\alpha\frac{\pi}{2}\right) + \omega_c^{-\alpha}\cos\left(\alpha\frac{\pi}{2}\right).\tan(\phi_m - \pi)} \tag{4.30}$$

B. Robustness to gain variation

The gain variation robustness specification ensures that the phase remains nearly constant around ω_c, enhancing system stability and robustness against internal disturbances like parameter variations [14]. This specification is mathematically defined as:

$$\frac{d(arg[C(s).P(s)])}{d\omega}\Big|_{\omega_c} = 0 \tag{4.31}$$

By applying the $G(j\omega)$, we can derive the following equation:

$$\frac{d\left[-\arctan\left(\frac{k_i\omega_c^{-\alpha}\sin\left(\alpha\frac{\pi}{2}\right)}{k_p + k_i\omega_c^{-\alpha}\cos\left(\alpha\frac{\pi}{2}\right)}\right) - \frac{\pi}{2}\right]}{d\omega}\Big|_{\omega_c} = 0 \tag{4.32}$$

By differentiating Equation (4.32), we obtain:

$$\frac{-\dfrac{\alpha k_i\omega^{-\alpha-1}\sin\dfrac{\alpha\pi}{2}(k_p+k_i\omega^{-\alpha}\cos\dfrac{\alpha\pi}{2})+k_i^2\alpha\omega^{-2\alpha-1}\sin\dfrac{\alpha\pi}{2}\cos\dfrac{\alpha\pi}{2}}{(k_p+k_i\omega^{-\alpha}\cos\dfrac{\alpha\pi}{2})^2}}{1+\left(\dfrac{-k_i\omega_c^{-\alpha}\sin\left(\alpha\dfrac{\pi}{2}\right)}{k_p+k_i\omega_c^{-\alpha}\cos\left(\alpha\dfrac{\pi}{2}\right)}\right)^2}=0 \tag{4.33}$$

By simplifying Equation (4.33), we obtain the following result.

$$-\frac{\alpha k_i\omega^{-\alpha-1}\sin(\frac{\alpha\pi}{2})(k_p+2k_i\omega^{-\alpha}\cos(\frac{\alpha\pi}{2}))}{(k_p+k_i\omega^{-\alpha}\cos(\frac{\alpha\pi}{2}))^2+(-k_i\omega^{-\alpha}\sin(\frac{\alpha\pi}{2}))^2}=0. \tag{4.34}$$

Since the denominator is always positive, the Equation (4.34) is satisfied when the numerator is set to zero:

$$\alpha k_i\omega_c^{-\alpha-1}\sin(\frac{\alpha\pi}{2})(k_p+2k_i\omega_c^{-\alpha}\cos(\frac{\alpha\pi}{2}))=0 \tag{4.35}$$

By solving Equation (4.35), we establish the relationship between k_p, k_i, and α:

$$k_p=-2k_i\omega_c^{-\alpha}\cos(\frac{\alpha\pi}{2}) \tag{4.36}$$

C. Gain Margin

This specification defines the stability margin of the controlled system and plays a crucial role in designing FO controllers [14]. By enforcing the ω_c constraint (6) and applying the modulus definition of a complex number, the following equation is derived:

$$|C(j\omega).P(j\omega)|_{\omega_c}=1 \tag{4.37}$$

When replacing $P(s)$ and $C(s)$, we obtain the following equation:

$$\left|\left(k_p+k_i\omega_c^{-\alpha}\left[\cos\left(\alpha\frac{\pi}{2}\right)+j\sin\left(-\alpha\frac{\pi}{2}\right)\right]\right).\left(\frac{1}{C_{dc}.(j\omega_c)}\right)\right|=1 \tag{4.38}$$

Which gives:

$$\frac{1}{C_{dc}.\omega_c}\sqrt{\left(k_p+k_i\omega_c^{-\alpha}\cos\frac{\alpha\pi}{2}\right)^2+\left(k_i\omega_c^{-\alpha}\sin\frac{\alpha\pi}{2}\right)^2}=1 \tag{4.39}$$

From Equation (4.39), the relationship between k_p, k_i, and α can be formulated as follows:

$$k_p = \sqrt{\omega_c^2 . C_{dc}^2 - k_i^2 \omega_c^{-2\alpha} \sin \frac{\alpha\pi}{2}} - k_i \omega_c^{-\alpha} \cos \frac{\alpha\pi}{2} \tag{4.40}$$

4.4 Proposed ZOA for tuning FOPI-AW controller

The FOPI-AW controller is adopted in this study to ensure accurate and robust regulation of the V_{dc} in the SAPF system. However, the performance of FO controllers strongly depends on proper parameter tuning. When conventional tuning methods are used, the controller becomes sensitive to nonlinearities, parameter uncertainties, and rapid variations in grid and load conditions, which may degrade both dynamic and steady-state performance.

To address these challenges, MOAs are employed to optimally tune the controller parameters, namely the k_p, k_i, G_a, and α. These parameters have a direct impact on system stability, transient response, and steady-state accuracy.

Although FO controllers are well recognized for their superior dynamic performance and robustness, they may suffer from steady-state inaccuracies if their parameters are not carefully selected. In some reported studies, this issue has been addressed by introducing switching strategies between different controllers, where one controller operates in the dynamic regime and another is activated in the steady-state regime [10].

A multi-objective cost function is formulated to simultaneously account for both dynamic and steady-state performance indices. This formulation enables the FO controller to maintain its dynamic advantages while significantly improving steady-state performance.

Based on the comparative studies conducted in the previous chapter, the ZOA is selected for this tuning task due to its strong global search capability and fast convergence. ZOA is applied to optimally tune the FOPI-AW controller integrated within the P-DPC control structure.

The proposed ZOA, inspired by the cooperative foraging and defense behavior of zebras, provides strong global search capability, high efficiency, and ease of implementation [70]. It employs a population of candidate solutions, combined with social behavior–inspired operators, to efficiently explore and exploit the solution space [70]. The fundamental principles and mathematical formulation of ZOA were presented in detail in the previous chapter. In this section, only the implementation procedure for the optimal tuning of the FOPI-AW controller is described, without repeating the complete set of equations.

4.4.1 Initialization

The ZOA efficiently identifies a suitable search space using a population of candidate solutions. Its nature-inspired mechanisms, characterized by features such as global optimization capability, high efficiency, ease of implementation, good scalability, and broad applicability, enable an effective balance between exploration and exploitation of the solution space [70]. MOAs of this type are generally considered efficient and reliable in practical applications. The primary objective of the optimization is to minimize a multi-objective cost function representing the overall control performance of the SAPF system. This cost function integrates several key performance indices, including:

- Reduction of V_{dc} overshoot,
- Elimination of instantaneous THD of the supply current (THDi),
- Improvement of the V_{dc} control loop using the lowest steady-state error (e(t)) [65].

The objectives of this work make the ZOA particularly suitable for multi-objective optimization in efficient energy filtering applications. Here, it is employed to optimally tune the parameters of the FOPI-AW controller, aiming to improve both dynamic and steady-state performance. As reported in previous studies, FO controllers provide excellent performance in dynamic regimes, offering fast response and enhanced robustness, but they may show limitations in steady-state accuracy. By optimizing the controller parameters using ZOA, the approach effectively combines the advantages of fractional-order dynamics with improved steady-state behavior.

4.4.2 Optimization objectives

ZOA seeks the optimal parameters by minimizing a suitable objective function for the FOPI-AW controller, defined as follows:

Minimize:

$$J = f(k_p, k_i, \alpha, G_a) \tag{4.41}$$

This formulation ensures that ZOA algorithm independently determines the optimal parameters for the proposed controller, thereby minimizing the overall system cost function while focusing on V_{dc} regulation, THD reduction, and transient performance enhancement. The tuning process is carried out offline, where the FOPI-AW controller parameters are optimized prior to real-time implementation.

Within the ZOA framework, each zebra represents a candidate solution in the optimization population. Inspired by the social behavior of zebras in nature, particularly their collective movement and defensive strategies, the algorithm models an effective balance between exploration and exploitation of the search space. Mathematically, each zebra is represented by a position vector whose elements correspond to the decision variables of the FOPI-AW controller, including k_p, k_i, G_a, and α.

During the iterative optimization process, the fitness of each zebra is evaluated based on the defined multi-objective cost function. Through successive updates of the population, ZOA progressively converges toward the optimal solution. Upon completion of the optimization process, the algorithm identifies the optimal set of FOPI-AW controller parameters that ensures improved dynamic response, minimized V_{dc} deviation, reduced harmonic distortion, and enhanced overall power quality.

4.4.3 Performance indices

To minimize the V_{dc} error during both transient and steady-state conditions, the Integral of Time Squared Error (ITSE) index is adopted [65]:

$$ITSE = \int_0^{t_f} te^2(t)dt \tag{4.42}$$

Where: $e(t) = V_{dcref}(t) - V_{dc}(t)$ the instantaneous voltage error.

The ITSE criterion is selected because it penalizes errors that persist over time, thereby improving the dynamic response, reducing oscillations, and accelerating the settling process.

This performance criterion penalizes larger errors occurring at later stages, thereby promoting faster convergence and smoother dynamic performance.

The V_{dc} overshoot (D) is calculated as:

$$D = \frac{V_{dc,max} - V_{dc,final}}{V_{dc,final}} \times 100 \tag{4.43}$$

Where, $V_{dc,\,max}$ is the maximum transient voltage, and $V_{dc,\,final}$ is the steady-state voltage.
To evaluate the power quality, the THD of the source current (I_s) is also included in the objective function:

$$THD_i = \frac{\sqrt{\sum_{n=2}^{\infty} I_{sn}^2}}{I_{s1}} \times 100 \tag{4.44}$$

Where, I_{sn} and I_{s1} are the RMS values of the n^{th} harmonic and the fundamental components of the source current, respectively.

These indices (*ITSE*, *D*, and *THDi*) together form the primary evaluation criteria used to quantify controller performance.

4.4.4 Multi-objective cost function

Each performance index is associated with a weighting factor (α_i) to determine its contribution to the total cost function [7]:

$$\sum_{i=1}^{3}\alpha_i = 1 \tag{4.45}$$

The overall multi-objective cost function is then expressed as:

$$J = \alpha_1(ITSE) + \alpha_2(D) + \alpha_3(THD_i) \tag{4.46}$$

Based on sensitivity analysis, the weighting coefficients are selected as:

$$\alpha_1 = 0.6, \quad \alpha_2 = 0.3, \quad \alpha_3 = 0.1$$

Here, J represents the fitness function to be minimized.

$$lb \leq x_j \leq ub, \quad \mathrm{j} = 1, 2, \ldots, dim \tag{4.47}$$

In this context, J is the fitness (objective) function to be minimized, x_j represents the decision vector, and dim signifies the problem dimensions. The parameters lb and ub define the lower and upper limits, respectively [70], Table 4.3 summarizes and provides examples of the ZOA algorithm's configuration parameters for the proposed controller considered in this study.

Table 4.3: Parameter settings of the ZOA algorithm for proposed controller

Parameters	values
Dim	4
Number of iterations (t)	100
Number of search agents (N_p)	20
Upper bounds (ub)	[100 100 1 10000]
Lower bounds (lb)	[0.001 0.001 0.1 100]

4.4.5 Population initialization

Similar to other MOAs, the ZOA starts by generating an initial population of candidate solutions, referred to as zebras, which act as search agents within the solution space. These zebras are randomly initialized within the predefined lower and upper bounds (ub , lb) of the decision variables to ensure sufficient diversity at the beginning of the optimization process. For a population size of N_p zebras, each defined by dim decision parameters, Equation (4.48) is used to construct the population matrix containing the decision-variable vectors of all zebras. This matrix represents the initial search space of the optimization process and provides a diverse set of feasible candidate solutions [70].

Accordingly, the complete initial population matrix can be expressed as follows:

$$X_n = \begin{bmatrix} x_1^1 & x_2^1 & \cdots & x_{dim}^1 \\ x_1^2 & x_2^2 & \cdots & x_{dim}^2 \\ \vdots & \vdots & \ddots & \vdots \\ x_1^{N_p} & x_2^{N_p} & \cdots & x_{dim}^{N_p} \end{bmatrix}_{N_p \times dim} \tag{4.48}$$

4.4.6 Algorithm setup

The ZOA employed in this section follows the same structural framework and operational principles introduced in Chapter 3 for MPPT in PV system. Since the fundamental concepts and mathematical formulation of the algorithm have already been detailed, they are not reiterated here for brevity. In this study, ZOA is adapted to a different optimization task, namely the tuning of the FOPI-AW controller used for V_{dc} regulation in the SAPF control system. While the computational workflow of the algorithm remains unchanged, the decision variables and objective function are redefined to meet the dynamic and steady-state requirements of the voltage control loop. Each zebra represents a candidate solution composed of a specific set of FOPI-AW controller parameters, including k_p, k_i, α, and G_a. The optimization process seeks the parameter set that ensures improved V_{dc} regulation, fast transient response, minimal overshoot, reduced steady-state error, and lower current harmonic distortion under varying operating conditions. The ZOA operates iteratively through two complementary behavior-inspired phases:

- **Phase 1: Foraging behavior**
  - Promotes exploration of the solution space.
  - Zebras investigate different regions to maintain population diversity, prevent premature convergence, and escape local minima.

- **Phase 2: Defense strategies against predators**
  - Focuses on refining and improving candidate solutions through social behavior-inspired mechanisms.
  - The applied strategy is determined by a random threshold $Ps \in [0,1]$:

✓ **Strategy 1: Against lion (Exploitation phase)**

- Intensifies the search around the most promising solutions to improve accuracy and convergence.

✓ **Strategy 2: Against other predators (Exploration phase)**

- Encourages exploration of less-visited regions of the search space, helping the algorithm escape local optima and avoid stagnation.

Overall, although ZOA retains the same computational backbone used in the MPPT application, its optimization targets are redefined to independently tune the FOPI–AW controller parameters, leading to enhanced V_{dc} regulation and improved power quality in the GCPV with SAPF system. The complete optimization procedure and corresponding pseudo-code is presented in Figure 4.10.

Start ZOA

Input:

• GCPV system integrated with SAPF parameters

• Controller type: P-DPC-based FOPI-AW

• ZOA parameters: N_p, T, [lb, ub] for (k_p, k_i, α, G_a)

Initialization:

• Generate initial zebra population ($i = 1 \ldots N_p$) [k_p, k_i, α, G_a] within bounds [lb, ub]

• Evaluate objective function J for each zebra

• Identify the pioneer zebra PZ (best solution)

Main Optimization Loop:

For t = 1: T do

- Update pioneer zebra (PZ)

For i = 1: N_p do

% Phase 1: Foraging behavior (Exploration)

- Compute new position of zebra i using Equation (3.3)
- Update zebra position using Equation (3.4)

% Phase 2: Defense Strategies Against Predators

- Generate random number Ps ∈ [0, 1]

If Ps < 0.5, Ps=rand

% Strategy S1: Defense against lion (Exploitation)

- Update zebra position using Equation (3.5) – S1

Else

% Strategy S2: Defense against other predators (Exploration)

- Update zebra position using Equation (3.5) – S2

End if

- Update zebra position using Equation (3.6)
- Apply boundary constraints [*lb*, *ub*]
- Evaluate objective function *J*

End for

- Update pioneer zebra (best solution)

End for

Output:

• Optimal FOPI-AW parameters: (k_p*, k_i*, α*, G_a*)

• Apply optimized gains to the GCPV-SAPF system

• Analyze V_{dc} regulation, transient response (*Tr*), Overshoot (*D*), and THD

End ZOA

Figure 4.10: ZOA-Based tuning of FOPI-AW controller

4.5 Oustaloup continuous approximation (OCA)

Various techniques have been employed to approximate the term $s^{-\alpha}$, encompassing methods such as the predictor-corrector approach [71], analytical and numerical calculation of the inverse Laplace transformation [72], representation through state-space representation [73], and OCA [74]. OCA method, in particular, is widely utilized to approximate the FOPI controller with Laplace transfer functions [14]. Oustaloup has outlined an approximation algorithm suitable when a frequency band of interest is defined by $[\omega_b, \omega_h]$. In this case, the term s^{α} can be substituted using Equation (4.49).

$$s^{\alpha} = \prod_{k=-N}^{N} \frac{s+\omega_k'}{s+\omega_k} \tag{4.49}$$

The model proposed by Oustaloup for approximating the term s^{α} is expounded in [27], where s denotes a Laplace transform variable, and α is a real number confined within the range of [–1, 1]. When α resides between 0 and 1, s^{α} is referred to as an FO differentiator;

conversely, when α lies between [-1, 0], it takes on the role of an FO integrator. The TF for the term s^{α} is formulated as presented in Equation (4.50):

$$H(s) = K\left(\frac{\omega_b}{\omega_h}\right)^{\alpha} \prod_{k=-N}^{N} \frac{1+\frac{s}{\omega_k^{'}}}{1+\frac{s}{\omega_k}} \tag{4.50}$$

The filter's poles, zeros, and gain can be calculated as,

$$\omega_k^{'} = \omega_b \left(\frac{\omega_h}{\omega_b}\right)^{\frac{k+N+\frac{1}{2}(1-\alpha)}{2N+1}}, \omega_k = \omega_b \left(\frac{\omega_h}{\omega_b}\right)^{\frac{k+N+\frac{1}{2}(1+\alpha)}{2N+1}} \text{ and } K = \omega_h^{\alpha}$$

Where, $\omega_k^{'}$: are the zeros, ω_k: the poles of order k, and 2N + 1 the actual order of the approximation function [14].

Equation (4.50) can be equivalently expressed as Equation (4.51).

$$S^{-\alpha} = K\frac{(s-Z_0)(s-Z_1)(s-Z_2)(s-Z_3)(s-Z_4)(s-Z_5)(s-Z_6)}{(s-P_0)(s-P_1)(s-P_2)(s-P_3)(s-P_4)(s-P_5)(s-P_6)} \tag{4.51}$$

The parameters required for optimizing the term $s^{-\alpha}$ using OCA method are provided in Table 4.4.

Table 4.4: OCA parameters

Notation	Parameter	Basic Value
ω_h	Upper cutoff frequency	$10^{-2} rad/s$
ω_b	Lower cutoff frequency	$10^{4} rad/s$
N	Filter order	3

4.6 Phase-Locked Loop (PLL)

The PLL is a closed-loop control system designed to synchronize the phase and frequency of an internal signal with that of an external reference, such as the grid voltage in power systems. It continuously monitors the phase difference between the grid voltage and the output of its internal Voltage-Controlled Oscillator (VCO). This phase error is processed by a PI controller (loop filter), which generates a control signal that adjusts the frequency of the VCO. As the loop operates, the PLL dynamically minimizes the phase error, ensuring that the internal signal becomes locked in both phase and frequency with the grid voltage. In three-phase systems, the grid voltages are typically transformed into the *dq* reference frame using the Park transformation, as illustrated in Figure 4.11, which simplifies phase detection by isolating the quadrature component Vq. When $Vq = 0$, perfect synchronization is achieved. This enables the accurate detection of the grid angle and frequency, which are crucial for grid-connected systems, such as PV inverters and SAPFs [1,22,27].

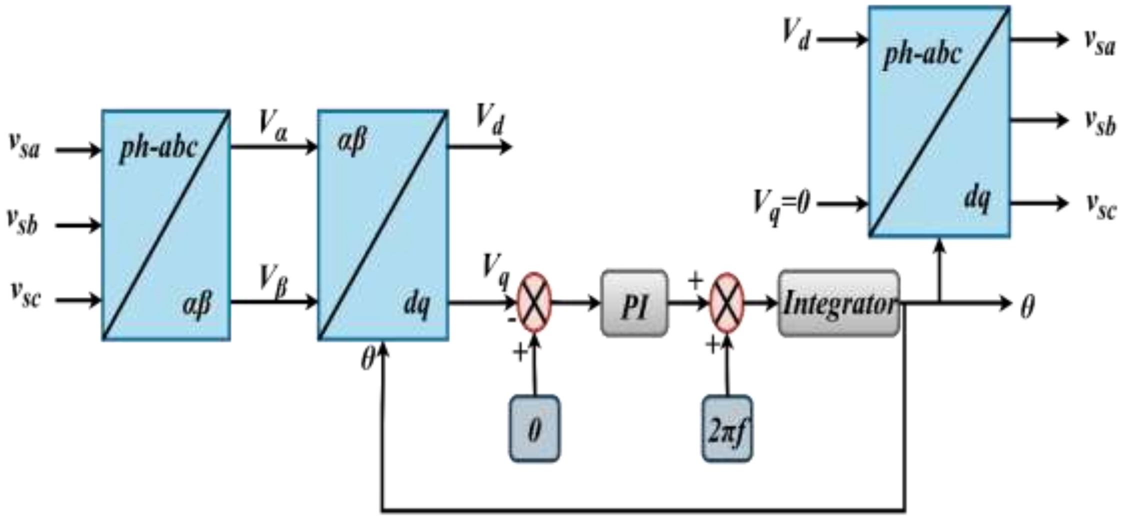

Figure 4.11: Block diagram of the three-phase PLL system

4.7 Simulation results for controllers

This section presents a simulation-based comparative assessment of DC-link voltage (V_{dc}) controllers in a GCPV system with a SAPF. The SAPF operates using the P-DPC strategy to improve power quality, while the ZOA is employed exclusively in the MPPT loop to track the GMPP under a single shading scenario. Controller performance is evaluated based on V_{dc} stability during SAPF injection, PV injection with MPPT search, and load variations occurring during both SAPF and PV injection. All system and PV parameters are kept consistent with the experimental conditions and are summarized in Table 4.5, while the PV electrical characteristics and specifications were previously defined in Chapter 2. The test sequence includes SAPF activation with nonlinear load variations, PV injection, MPPT operation under shading conditions, and additional nonlinear load changes. The obtained results enable the selection of the most suitable controller for real-time implementation based on voltage regulation, ripple minimization, dynamic response, disturbance rejection, and efficient PV power transfer.

Table 4.5: Electrical parameters of simulation setup.

Parameters	Values
Grid RMS voltage (V_{sn})	13 V
C_{dc}	2200 μF
R_L	5 Ω
L, L_f	8.5 mH
R_f	0.1 Ω
T_s	47 μs
V_{dcref}	92 V

The simulation results, indexed from Figure 4.12 to Figure 4.22, represent the dynamic and steady-state responses of all evaluated V_{dc} regulators, including the proposed optimized controller. The regulation performance was assessed over multiple operating intervals to monitor controller behavior under varying conditions and system disturbances. Initially, the time span from 0 to 0.5 s corresponds to system operation before activating the SAPF, reflecting the uncompensated V_{dc} condition. The interval from 0.5 to 5 s incorporates a load step change at 3 s, introduced to assess the transient response time (T_r), V_{dc} overshoot (D), and each controller's capability to reject load-induced disturbances.

At 5 s, the PV inverter starts injecting the MPPT-tracked current into the grid, marking the activation of the optimization-assisted MPPT tracking stage. Finally, at 8 s, an additional load variation is applied to evaluate controller robustness and stability under abrupt changes in the PV injection profile. These segmented operating regions enable a clear and comprehensive comparative interpretation of controller performance across SAPF compensation, MPPT power injection, and disturbance-driven mode transitions, validating the effectiveness of the proposed control approach.

Figures 4.12 and 4.13 present the simulated performance of the V_{dc} PI regulator in a GCPV system with a SAPF. Figure 4.12 shows that V_{dc} stabilizes with a noticeable overshoot and persistent ripple, indicating relatively slow transient regulation and sensitivity to changes in operating mode. The THD spectrum in Figure 4.13 confirms that harmonic distortion is substantially reduced after SAPF activation, with THD = 2.58% during SAPF injection, demonstrating effective filtering. The THD peak of 17.52% observed during PV injection corresponds to a I_s value close to zero and inverted, meaning that the actual distortion amplitude is almost negligible despite the high calculated value.

During the SAPF injection stage, the PI regulator reaches regulation in $Tr_1 = 0.58$ s with $D_1 = 21.30\%$, followed by stabilization at $Tr_2 = 0.49$ s with $D_2 = 1.37\%$ after a load change. In the PV injection stage, V_{dc} settles at $Tr_3 = 1.711$ s with $D_3 = 7.43\%$. During load variation under active PV-MPPT injection, the controller responds with $Tr_4 = 0.20$ s and $D_4 = 0.26\%$.

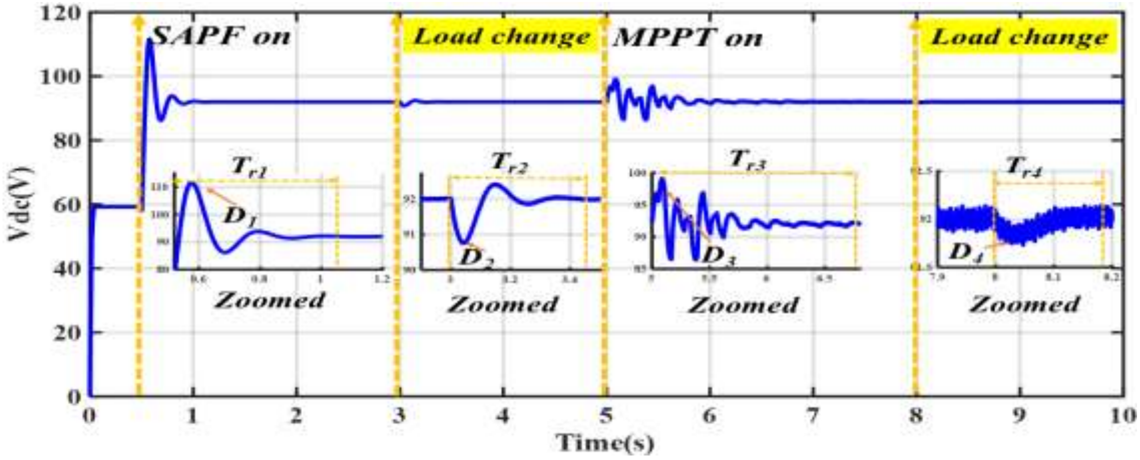

Figure 4.12: Simulation results of V_{dc} response in a GCPV system with SAPF using a conventional PI regulator across test scenarios

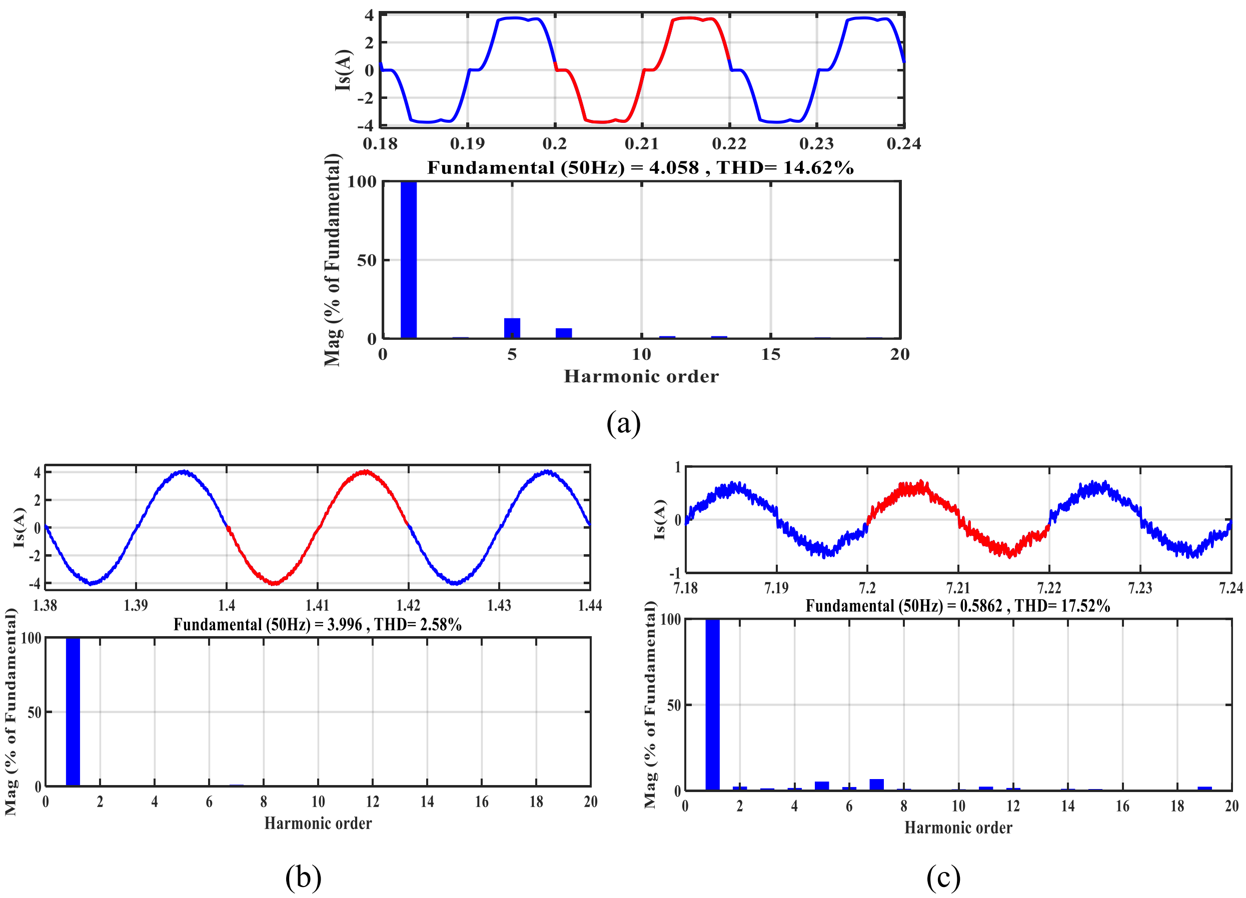

Figure 4.13: Assessment of grid current THD under the conventional PI controller: a) before SAPF, b) with SAPF, and c) with PV injection

Figures 4.14 and 4.15 illustrate the simulated performance of the conventional PI-AW regulator in the GCPV system with SAPF integration. Figure 4.14 shows improved V_{dc} regulation compared to the classical PI controller, with reduced overshoot and better voltage stability during transient transitions, although a slight ripple persists. Figure 4.15 demonstrates effective harmonic compensation, achieving a THD = 2.56% during SAPF operation, while the THD reaches about 17% during PV injection mode.

During SAPF injection, the PI-AW regulator reaches regulation faster than the conventional PI, stabilizing at Tr_1 = 0.28 s with D_1 = 9.67%, and subsequently converging at Tr_2 = 0.203 s with D_2 = 0.70% after a load change. This reflects enhanced robustness and improved rejection of dynamic disturbances. In the PV injection stage, V_{dc} maintains stable regulation, settling at Tr_3 = 1.153 s with D_3 = 3.43%. During load variation under active PV injection, the PI-AW controller preserves tight dynamic voltage containment, responding at Tr_4 = 0.172 s with D_4 = 0.18%.

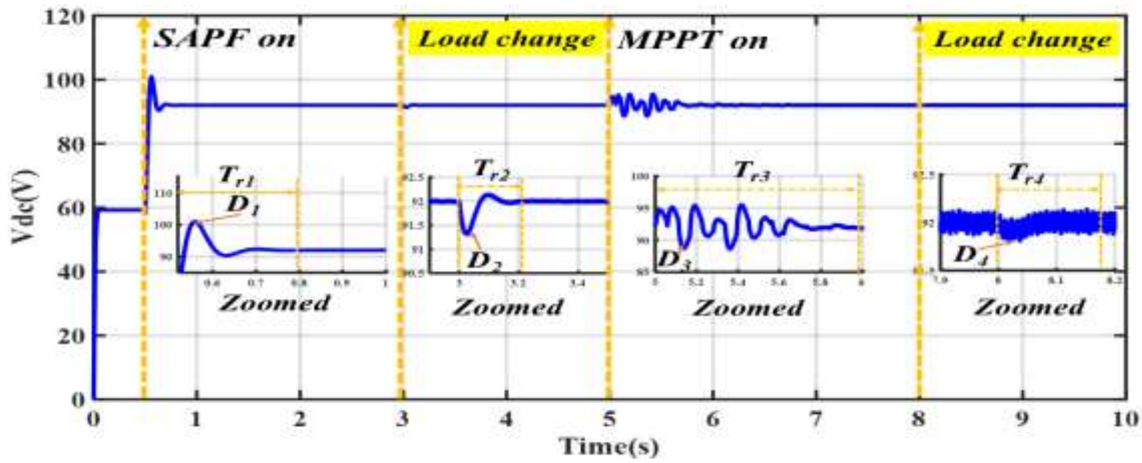

Figure 4.14: Simulation results of V_{dc} response in a GCPV system with SAPF using a conventional PI-AW regulator across test scenarios

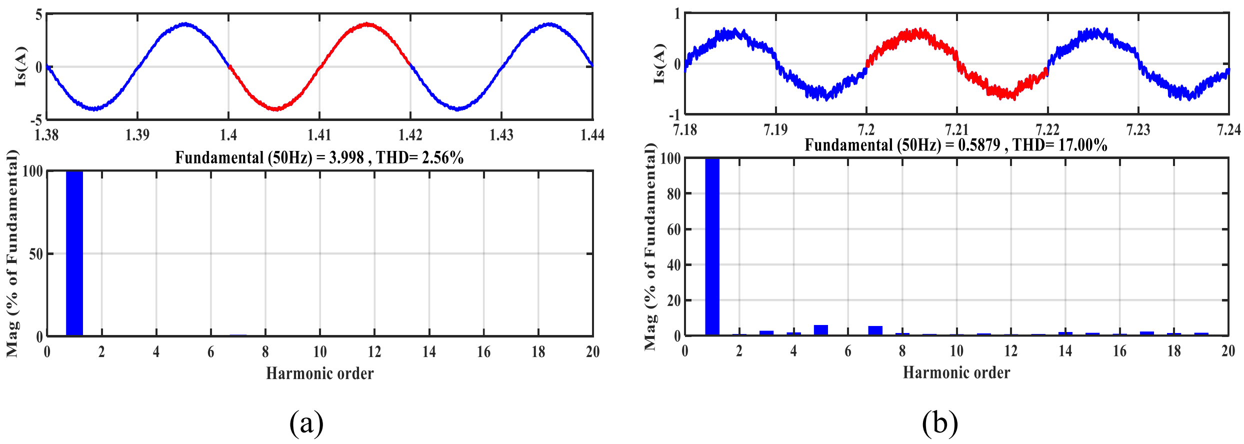

Figure 4.15: Assessment of grid current THD under the conventional PI-AW controller: a) with SAPF, and b) with PV injection

Figures 4.16 and 4.17 present the simulation results of the V_{dc} regulator based on FOPI controller in the GCPV system integrated with a SAPF. As illustrated in Figure 4.16, the FOPI controller demonstrates smoother transient responses compared to the conventional PI controller, exhibiting reduced overshoot, enhanced damping, and significantly lower voltage ripple during operational mode transitions. The THD spectrum in Figure 4.17 confirms effective harmonic mitigation when the SAPF compensation, achieving THD = 3.45% during SAPF current injection. A THD = 27.48% is observed during PV injection.

During SAPF injection, the FOPI controller stabilizes with a T_{r1}=0.15 s and a D_1=3.73%, then converges to steady-state regulation at T_{r2}=0.125 s with D_2=0.54 following a load change, highlighting improved disturbance rejection and damping capability. During PV injection, the V_{dc} maintains tight dynamic containment, settling at T_{r3}=0.956 s with D_3=2.2. Under varying load conditions during PV injection, the FOPI controller preserves stable voltage performance, responding a T_{r4}=0.179 s with D_4=0.14%.

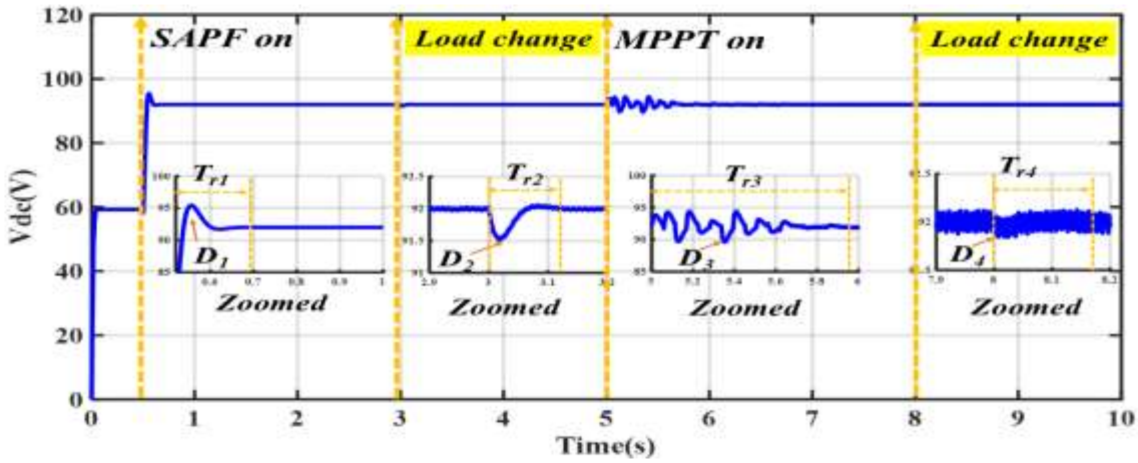

Figure 4.16: Simulation results of V_{dc} response in a GCPV system with SAPF using a conventional FOPI regulator across test scenarios

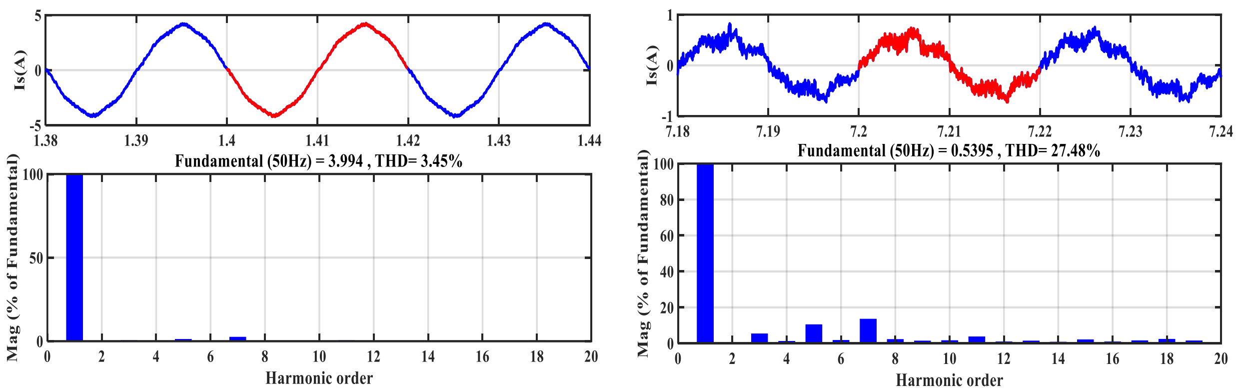

(a) (b)

Figure 4.17: Assessment of grid current THD under the conventional FOPI controller: a) with SAPF, and b) with PV injection

Figures 4.18 and 4.19 show that the FOPI-AW controller improves V_{dc} regulation in the GCPV–SAPF system by reducing overshoot, speeding up settling time, and enhancing damping during mode transitions. It also provides effective harmonic compensation, achieving a THD =3.34% during SAPF injection, while a higher THD =24.92% occurs during PV injection.

During SAPF injection, the FOPI-AW controller stabilizes rapidly, exhibiting a transient response of Tr_1 = 0.14 s with a D_1 = 2.5%, and subsequently reaching steady-state regulation at Tr_2 = 0.122 s with D_2 = 0.42% following load changes. These results indicate superior disturbance rejection and enhanced damping capability. In the PV injection stage, V_{dc} remains well-contained, settling at T_{r3} = 0.909 s with a D_3 = 2.17%. Furthermore, under load variation during active PV injection, the FOPI-AW controller preserves strong dynamic voltage containment, maintaining a T_{r4} = 0.097 with a D_4 = 0.14%, which confirms robust stability across both transient and steady-state conditions.

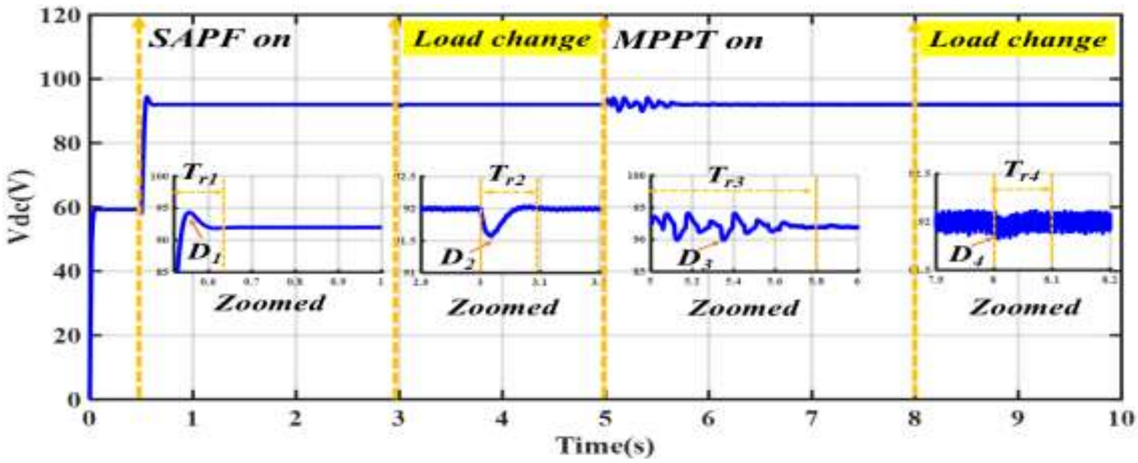

Figure 4.18: Simulation results of V_{dc} response in a GCPV system with SAPF using a conventional FOPI-AW regulator across test scenarios

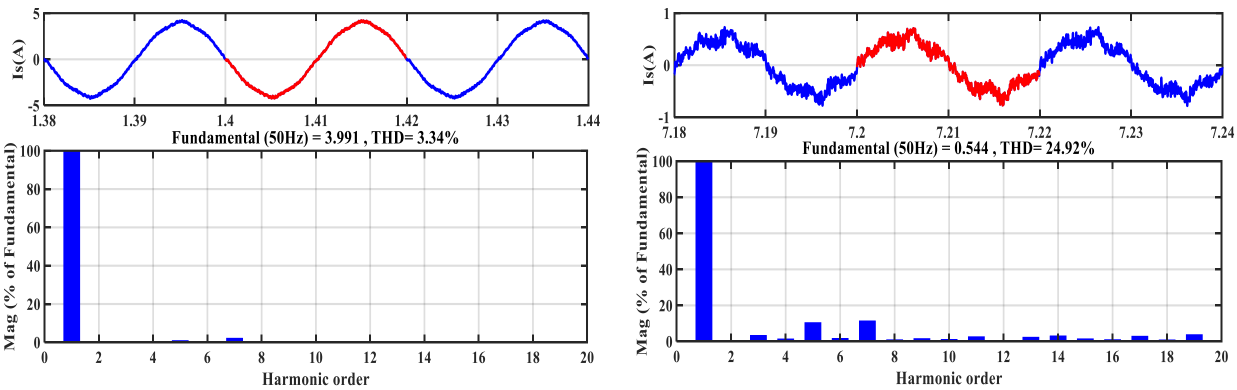

(a) (b)

Figure 4.19: Assessment of grid current THD under the conventional FOPI-AW controller: a) with SAPF, and b) with PV injection

Figures 4.20 and 4.21 further present the simulated performance of the proposed FOPI-AW controller for V_{dc} regulation in the GCPV system operating in parallel with a SAPF. As depicted in Figure 4.20, the proposed FOPI-AW achieves the most refined transient behavior among all tested regulators, combining minimal overshoot, superior damping, and very low V_{dc} ripple during transitions between SAPF compensation and PV injection modes. The THD spectrum in Figure 4.21 confirms the improved harmonic behavior of the system, where the proposed FOPI-AW-ZOA reaches THD = 2.01% under SAPF injection and THD = 16.98% during PV injection instants. Although the THD ratio rises in the latter case due to the nearly zero amplitude of the PV-MPPT current aligned in phase with the grid voltage, the actual harmonic magnitude remains practically insignificant.

During SAPF injection, the proposed FOPI–AW exhibits fast stabilization of V_{dc} with T_{r1} =0.035s and a nearly null deviation D_1=0%. After load variation, steady-state regulation is achieved at T_{r2}=0.038s with a limited deviation of D_2=0.19%, indicating strong disturbance rejection and enhanced damping.

Under PV injection mode, V_{dc} converges to its reference within T_{r3}=0.82s while maintaining acceptable dynamic behavior with D_3=1.14%. When PV injection remains active during additional load variations, voltage regulation is preserved with a rapid response of T_{r4}=0.016s and a negligible deviation of D_4=0.1%. These results confirm the robustness of the proposed FOPI-AW under both dynamic and steady-state operating conditions.

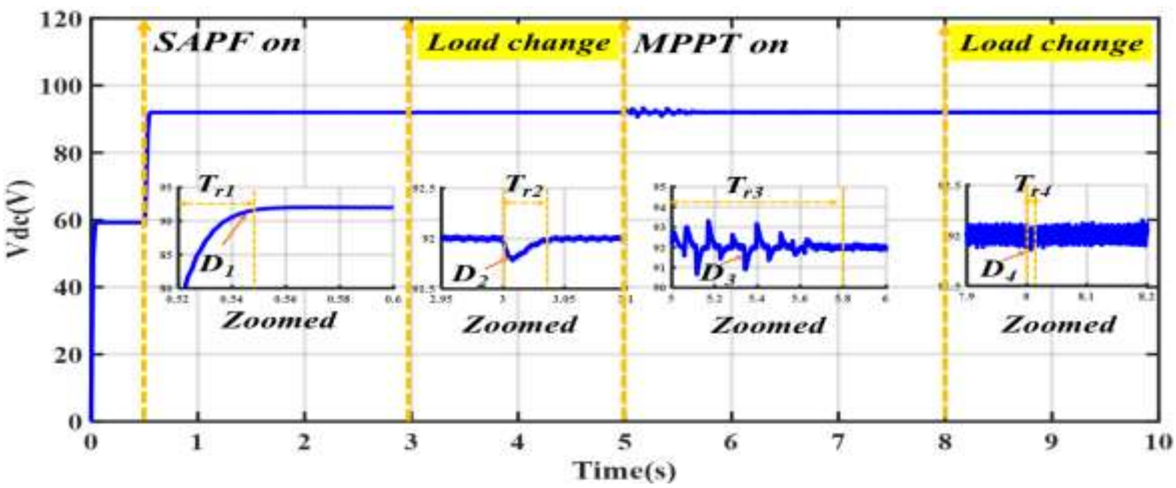

Figure 4.20: Simulation results of V_{dc} response in a GCPV system with SAPF using a Proposed FOPI regulator across test scenarios

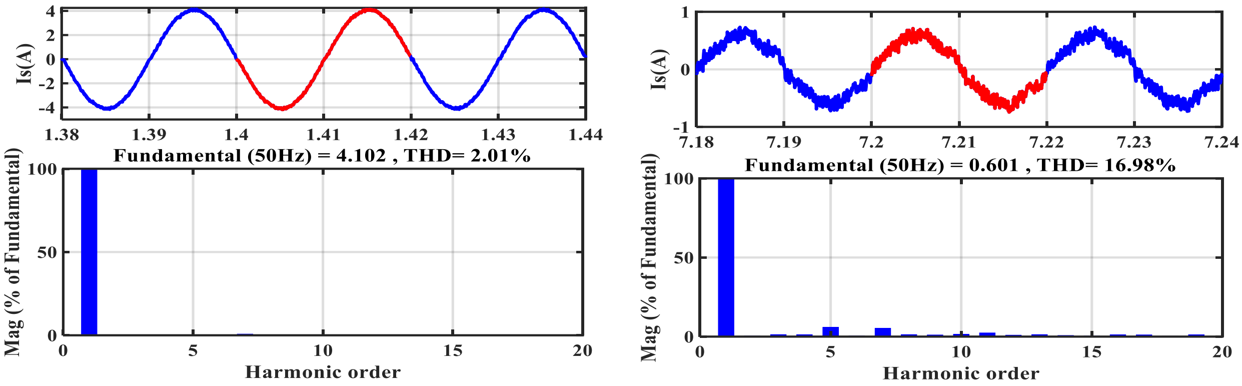

(a) (b)

Figure 4.21: Assessment of grid current THD under the Proposed FOPI controller: a) with SAPF, and b) with PV injection

Figure 4.22 provides a global comparative view of the V_{dc} regulation performance using all tested controllers operating within the GCPV system with SAPF compensation. The figure clearly highlights the behavioral differences between regulators during both operating modes. As previously established, conventional PI-based controllers present acceptable static regulation under steady-state conditions; however, their dynamic responses remain limited, exhibiting noticeable overshoot, slower settling, and higher voltage ripple. In contrast, FOPI, FOPI-AW show improved dynamic damping but still lack optimal steady-state containment.

The proposed FOPI-AW-ZOA controller achieves strong voltage containment in steady-state operation while delivering a highly damped and well-shaped dynamic response under transient conditions. The controller was developed using an optimized objective function specifically formulated to minimize THD, overshoot, and response time, resulting in a smoother V_{dc} profile, near-zero overshoots, and the lowest harmonic distortion level among all evaluated controllers, as confirmed in Table 4.6.

The validation outcomes presented substantiate the effectiveness of this design strategy, demonstrating that the proposed FOPI-AW-ZOA regulator provides the most balanced trade-off between static stability and dynamic damping. This confirms its robustness during SAPF injection, PV injection, and abrupt nonlinear load variations, making it the most suitable candidate for practical implementation in SAPF-assisted GCPV systems

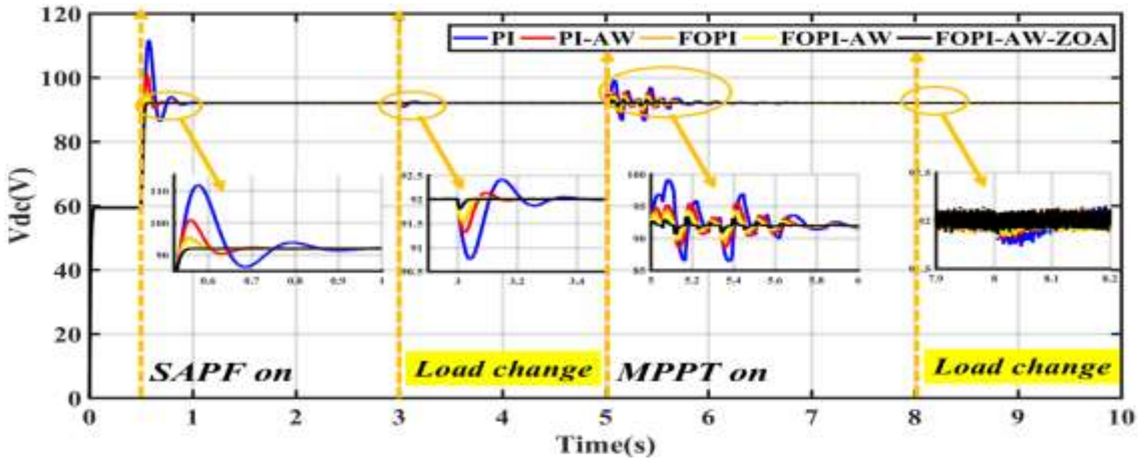

Figure 4.22: Comparative analysis of simulation results for the V_{dc} response in a GCPV system with SAPF using different regulators across the test scenarios

Table 4.6: Simulation comparison of proposed FOPI-AW and other techniques in steady state and dynamic State

Techniques	Steady State		Dynamic State							
	THD (%)		Time response (*Tr* (s))				D (%)			
			Inject SAPF		Inject PV		Inject SAPF		Inject PV	
	Inject SAPF	Inject PV	T_{r1}	T_{r2}	T_T	T_{r3}	D_1	D_2	D_3	D_4
PI	2.58	17.52	0.58	0.49	1.711	0.2	21.30	1.37	7.43	0.26
PI-AW	2.56	17	0.28	0.203	1.153	0.172	9.67	0.7	3.43	0.18
FOPI	3.45	27.48	0.15	0.125	0.956	0.179	3.73	0.54	2.2	0.14
FOPI-AW	3.34	24.92	0.14	0.1222	0.909	0.097	2.5	0.42	2.17	014
FOPI-AW-ZOA	2.01	16.98	0.035	0.038	0.82	0.016	0	0.19	1.14	0.1

4.8 Conclusion

This chapter investigated advanced control strategies for SAPF systems aimed at improving power quality through harmonic mitigation, reactive power compensation, and power factor correction. Conventional DPC and P-DPC methods were analyzed, followed by the evaluation of PI classical and FOPI controllers. While FOPI controllers enhanced dynamic performance, an optimization-based approach using the ZOA was proposed to achieve optimal parameter tuning. By minimizing a multi-objective cost function that accounts for V_{dc} regulation and current harmonic distortion, the proposed ZOA-optimized FOPI-AW controller demonstrated superior stability, robustness, and overall SAPF performance. These results establish a strong basis for the experimental validation presented in the next chapter.

Chapter 5:

Experimental Implementation and Performance Evaluation of the Grid-Tied PV system with SAPF

5.1 Introduction

The previous chapters presented the theoretical development and design of the proposed GCPV-SAPF system. Advanced control and optimization techniques were investigated to enhance both the energy extraction from the PV subsystem and the power quality of the grid-connected system. This chapter focuses on the experimental validation of these proposed control strategies through a real-time implementation on a laboratory prototype.

The main objective of this chapter is to verify the performance and feasibility of the integrated GCPV-SAPF system under realistic operating conditions. The experimental setup was designed to reproduce practical scenarios, allowing for the assessment of the system's capability to maintain stable V_{dc}, mitigate current harmonics, compensate reactive power, and efficiently extract maximum power from the PV array under varying environmental conditions. The results presented here serve as the foundation for confirming the accuracy and robustness of the developed control architecture introduced in previous chapters.

The control and optimization algorithms were implemented using the dSPACE DS1104 real-time control platform, which provides an efficient interface between MATLAB/Simulink models and the physical system. This configuration enables precise signal acquisition, PWM generation, and real-time control of the power converter units. The experimental validation process is structured to evaluate the effectiveness of the proposed algorithms, namely ZOA, and GWEO, and to compare their performance with established metaheuristics such as PSO, GWO, WOA, and FPA.

To ensure comprehensive evaluation, a systematic testing protocol was adopted, considering both steady-state and dynamic responses under multiple irradiance scenarios: STC, PSCs, and DSC. Each test aims to analyze how effectively the proposed system responds to changes in solar radiation, load variations, and grid disturbances. Performance indicators such as THD, Power Factor (PF), MPPT efficiency, tracking time (T_T), and V_{dc} stability are measured and compared across the different control strategies.

This chapter is organized as follows:

- **Section 1** introduces the architecture and setup of the experimental bench used for the validation.
- **Section 2** describes the control system implementation on the dSPACE DS1104 platform.
- **Section 3** presents the testing protocol adopted to assess the system's performance under various operating scenarios.
- **Section 4** provides detailed experimental results and analysis under STC, PSC, and DSC, highlighting the system's dynamic response and the efficiency of the proposed algorithms.
- Finally, **Section 5** summarizes the key findings and discusses the experimental validation of the proposed methods in comparison to conventional techniques.

5.2 Description of the laboratory test bench

In the previous chapters, a comprehensive overview of the GCPV-SAPF system was presented. This system ensures efficient integration of renewable energy while simultaneously enhancing power quality through the implementation of a SAPF, as illustrated in Figure 2.1 of Chapter 2. Chapter 2 detailed the overall system configuration, emphasizing the interaction between its main components and their roles in energy injection, harmonic mitigation, and reactive power compensation. Chapter 3 focused on the development of metaheuristic and hybrid optimization algorithms to improve MPPT in PV systems, while Chapter 4 introduced advanced control and regulation strategies for the SAPF to further improve dynamic and steady-state performance.

To validate the proposed control and optimization strategies, an experimental test bench was developed and implemented using a dSPACE 1104 real-time control platform at the LEPCI Laboratory, University of Setif-1, Algeria. This setup allows real-time testing and verification of both the photovoltaic (PV) subsystem and the SAPF under various operating conditions, including STCs, PSCs, and load variations. The experimental configuration, illustrated in Figure 5.1, mainly consists of a low-voltage three-phase grid, a nonlinear (polluting) load, a three-phase VSI, a DC–DC converter for PV power control, and a PV emulator that reproduces the electrical behavior of solar panels.

The complete test bench integrates two control subsystems, each managed by a dSPACE 1104 board, one dedicated to the PV generation unit and the other to the SAPF. Although these subsystems operate under separate control architectures, they are electrically coupled through the common DC-link capacitor (C_{dc}), which enables energy exchange and maintains voltage stability across the entire setup. PV emulator reproduces the electrical characteristics of PV arrays under different irradiance and temperature conditions, ensuring repeatable and controllable experimental scenarios. The DC–DC converter regulates the PV output voltage and transfers energy to the DC link, while the MPPT algorithm implemented on the dSPACE board ensures maximum energy extraction. The three-phase voltage inverter, acting as the SAPF, injects compensating currents into the grid to suppress harmonics and improve the PF. The filter inductances provide current smoothing and grid coupling, whereas voltage and current sensors deliver real-time feedback for closed-loop control.

The control algorithms were developed in MATLAB/Simulink and executed in real time through the dSPACE 1104 interface. For observation and validation purposes, a digital oscilloscope was employed to visualize current and voltage waveforms, while a power analyzer was utilized to measure key power quality indicators, including active power (P), reactive power (Q), THD, PF, displacement power factor ($cos\ (\Phi)$), and the reactive power ratio ($tan\ (\Phi)$). Table 5.1 summarizes the main components of the experimental setup and their respective functions.

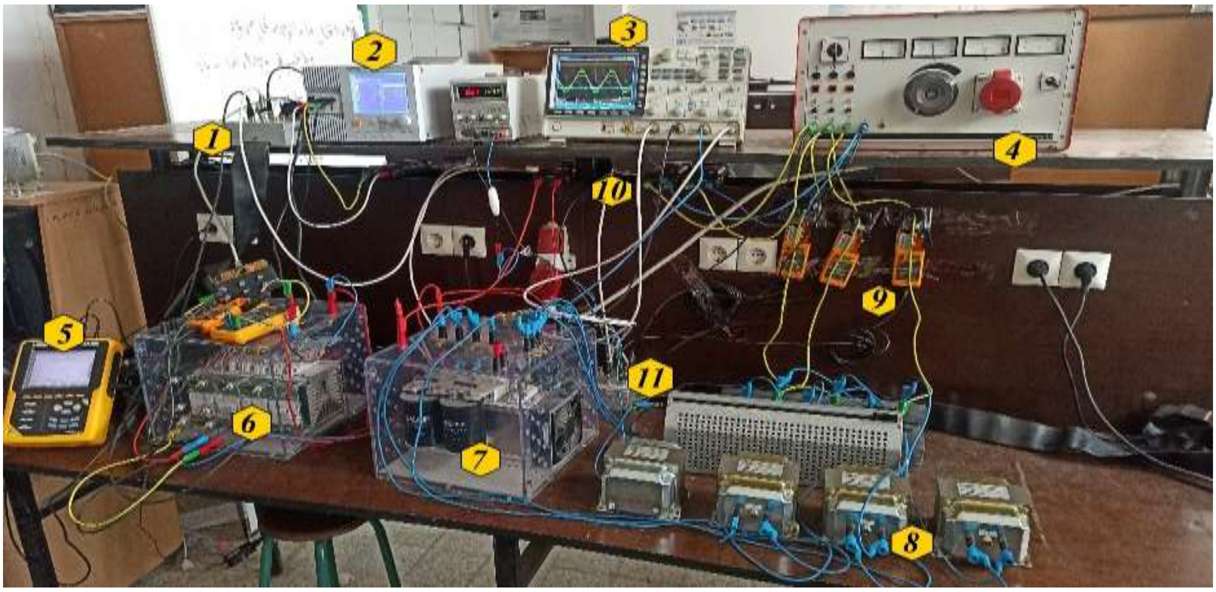

Figure 5.1: Experimental setting up

Table 5.1: List of devices and their functions

No	Component	Function
1	PV emulator	To emulate the electrical characteristics of a photovoltaic array under STCs and PSCs, allowing reproducible PV behavior in laboratory tests.
2	dSPACE 1104 (for PV system)	To execute the PV system's MPPT algorithms in real-time, converting analog-to-digital (ADC) and digital-to-analog (DAC) signals for control and measurement purposes.
3	Oscilloscope	To measures and displays instantaneous power, voltage, current, and duty cycle waveforms for real-time observation and validation of system behavior.
4	Three-phase voltage source	To provides a stable, low-voltage AC supply that emulates the electrical grid, enabling realistic testing of grid-connected operation.
5	Power analyzer	To measures electrical parameters such as P, Q, PF, and THD, *cos (Φ)*, *tan (Φ)*.
6	DC–DC converter	To converts DC power from the PV emulator to the DC link while implementing MPPT control to ensure maximum power extraction.
7	Three-phase voltage inverter	To converts DC power into AC and injects compensating currents into the grid to mitigate harmonics and improve power factor.
8	Filter inductances (L)	Smooth the inverter output current and provide coupling between the SAPF and the grid. They also help reduce harmonics and improve overall power quality.
9	Current sensors	To use to measure currents at key points (DC link, inverter, grid, load, and PV source) and send feedback to the dSPACE 1104 controller for real-time monitoring, precise power flow control, MPPT, and harmonic compensation.
10	Voltage sensors	To use to measure voltages at key points (PV terminals, DC link, inverter output, and grid) and provide feedback to the dSPACE 1104 controller for real-time voltage regulation, synchronization, and power quality analysis.
11	dSPACE 1104 (for SAPF)	To implements and executes the control algorithms of the SAPF in real time, ensuring precise current regulation and harmonic compensation.

5.3 Experimental setup and measurement instrumentation

This section presents the main components of the experimental setup used to validate the proposed system. Since the detailed modeling and theoretical explanations were provided in the previous chapters, the focus here is on a concise description of the essential hardware elements and their practical implementation in the laboratory. Each component of the setup is represented in two ways: its theoretical model (schematic diagram) and its practical realization (photograph). This dual representation highlights how the theoretical models developed in the earlier chapters are translated into real devices and integrated into the laboratory test bench. The overall configuration was carefully designed to reproduce realistic operating conditions of a GCPV-SAPF system.

5.3.1 PV emulator

PV generator is implemented using a programmable power supply (GWINSTEK-APS1102A), capable of accurately reproducing the nonlinear electrical characteristics of a PV array. This emulator can replicate both standard and dynamic irradiance profiles, allowing controlled and repeatable testing of various MPPT algorithms under STC and PSCs. The power supply's digital interface provides precise and stable PV current, PV voltage, and PV power readings, ensuring reliable assessment of system performance under diverse operating scenarios.

In this thesis, the conventional PV model was reformulated to express voltage as a function of current ($V_{pv} = f(I_{pv})$), aligning with the operating principle of voltage-source emulators such as the GWINSTEK-APS1102A, as detailed in Chapter 2. In traditional PV system modeling, an algebraic loop problem often arises due to the strong interdependence among voltage, current, and power, leading to iterative computation cycles that complicate the determination of the MPP. This challenge originates from the tightly coupled mathematical formulation of classical PV models. To overcome this limitation, a Lookup Table (LUT) method was adopted as an efficient and numerically stable alternative, enabling faster computation and improved convergence. The detailed modeling procedure and LUT-based implementation are presented in Chapter 2. These design strategies enable the PV emulator to accurately reproduce the dynamic behavior of real solar modules under varying operating conditions. Figure 5.2 illustrates both the schematic representation of the PV generator and the corresponding laboratory photograph of the emulator used during the experiments.

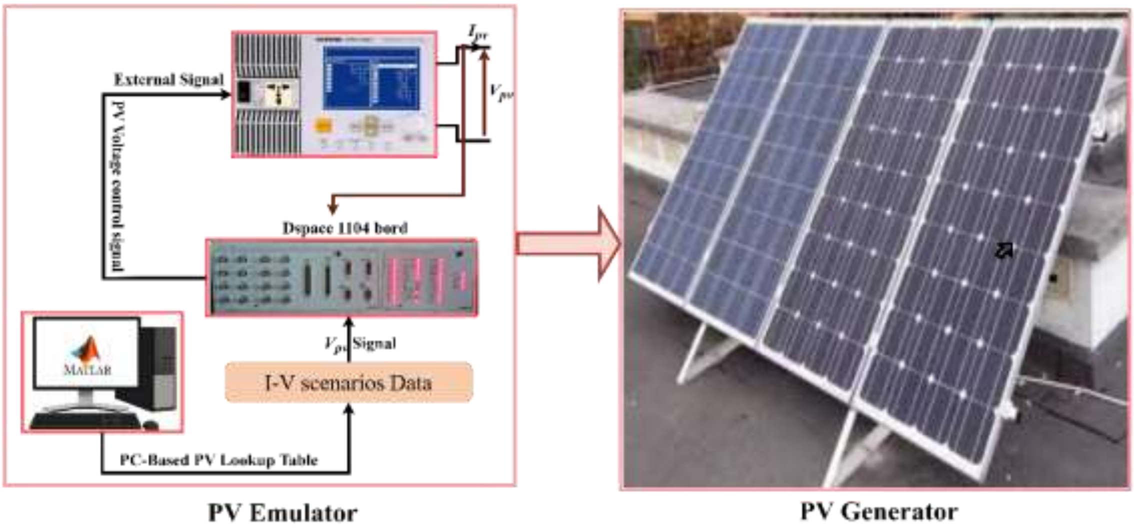

Figure 5.2: Schematic representation of the PV generator and the corresponding laboratory photograph of PV emulator used during the experiments

5.3.2 Three-phase voltage source

The three-phase voltage source provides a stable and balanced AC power supply that accurately emulates the behavior of the electrical grid [27]. It is utilized to evaluate the grid-connected operation of the system and to analyze the interaction between the SAPF and the electrical network under various load and compensation conditions. Figure 5.3 illustrates both the schematic diagram of the three-phase voltage source and its corresponding experimental setup in the laboratory.

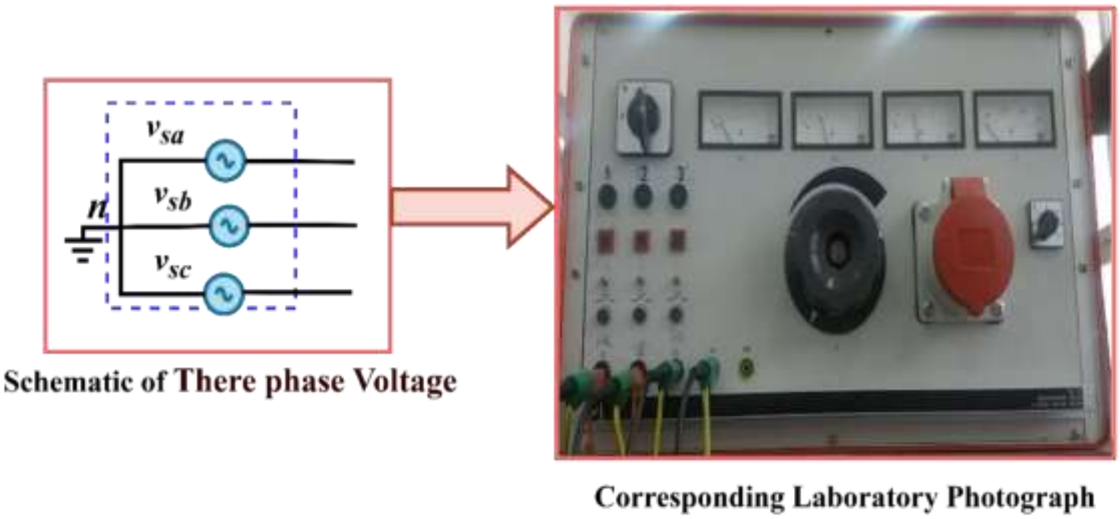

Figure 5.3: Schematic representation of the three-phase electrical network and the corresponding laboratory photograph

5.3.3 DC-DC Boost converter

A unidirectional DC-DC boost converter is employed to regulate the PV output voltage and ensure optimal power transfer to the C_{dc}, as described in Chapter 2. The converter parameters were carefully designed to satisfy the dynamic response requirements defined by the MPPT controller. It provides a stable DC output voltage and effectively decouples the PV source from the inverter stage, thereby enhancing system stability [1].

In the experimental implementation, the converter utilizes a single IGBT switch and a diode, both integrated within a universal SEMIKRON power module, in combination with an inductor and a capacitor [27]. Figure 5.4 presents both the schematic diagram and the photograph of the laboratory prototype of the DC–DC boost converter used in this study.

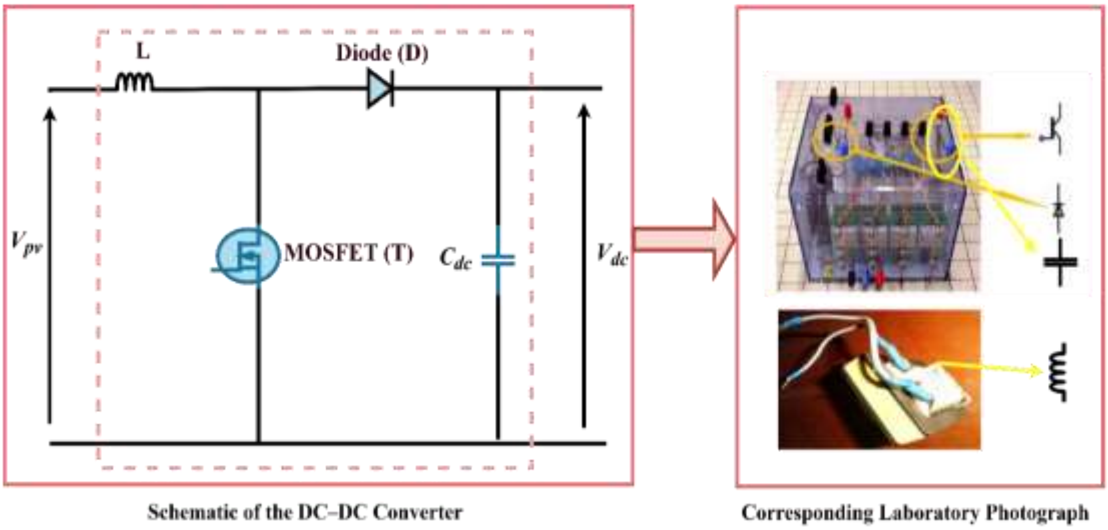

Figure 5.4: Schematic representation of the DC-DC converter and the corresponding laboratory photograph

5.3.4 Three-phase voltage source inverter (VSI)

The three-phase VSI operates as a SAPF, acting as a bidirectional current converter composed of six IGBT switches along with the associated filtering components. The inverter output stage incorporates three interface inductors designed to mitigate current harmonics and provide reactive power compensation during the injection of photovoltaic (PV) energy into the grid, as discussed in Chapter 2. The VSI is controlled using the advanced control and optimization strategies developed in this research and presented in Chapter 4. Figure 5.5

presents both the schematic diagram and the laboratory prototype of the three-phase VSI configuration implemented in this work.

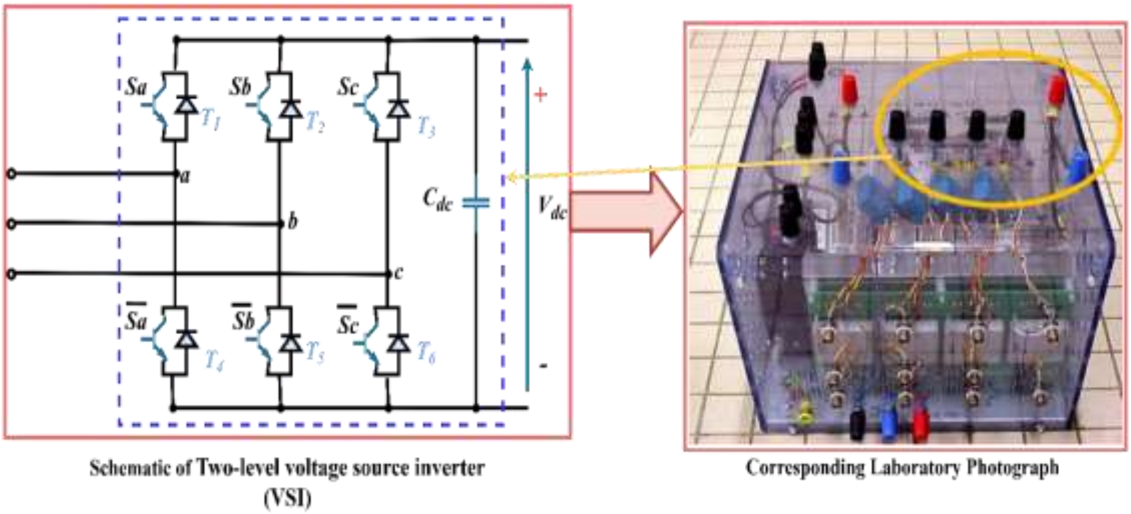

Figure 5.5: Schematic representation of the three-phase VSI and the corresponding laboratory photograph

5.3.5 dSPACE DS1104 control board

The dSPACE DS1104 control board serves as the central processing unit for real-time control and communication between the MATLAB/Simulink control models and the experimental hardware. It performs high-precision analog-to-digital (ADC) conversions to acquire external signals, such as voltage and current measurements, from system sensors. Based on these measurements, the board generates the required control and gating signals for DC–DC converter and VSI.

The control algorithms are implemented, compiled, and executed in real time via the MATLAB/Simulink interface, ensuring accurate PWM generation and precise synchronization with the power electronic stages. This configuration enables continuous monitoring, data acquisition, and online adjustment of control parameters during experimental validation. Figure 5.6 shows the laboratory photograph of the dSPACE DS1104 board integrated into the overall control and measurement setup.

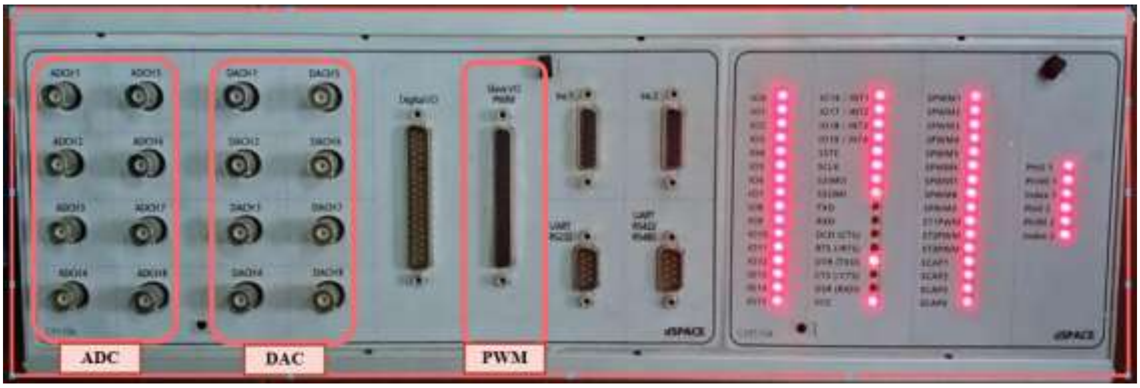

Figure 5.6: Laboratory image of the dSPACE DS1104 board integrated into the control and data acquisition system.

5.3.6 Nonlinear load configuration

To emulate distorted grid conditions, a nonlinear load is implemented using a diode bridge rectifier combined with resistive–inductive (R–L) components, which generate current harmonics representative of real industrial and commercial load behaviors. This configuration is essential for evaluating the performance of the SAPF in mitigating current harmonics and compensating for reactive power under realistic operating conditions [27].

In the experimental setup, a SEMIKRON universal converter is employed to realize the nonlinear load, ensuring flexibility and reproducibility of test scenarios.

Figure 5.7 illustrates both the schematic diagram and the laboratory photograph of the implemented nonlinear load configuration.

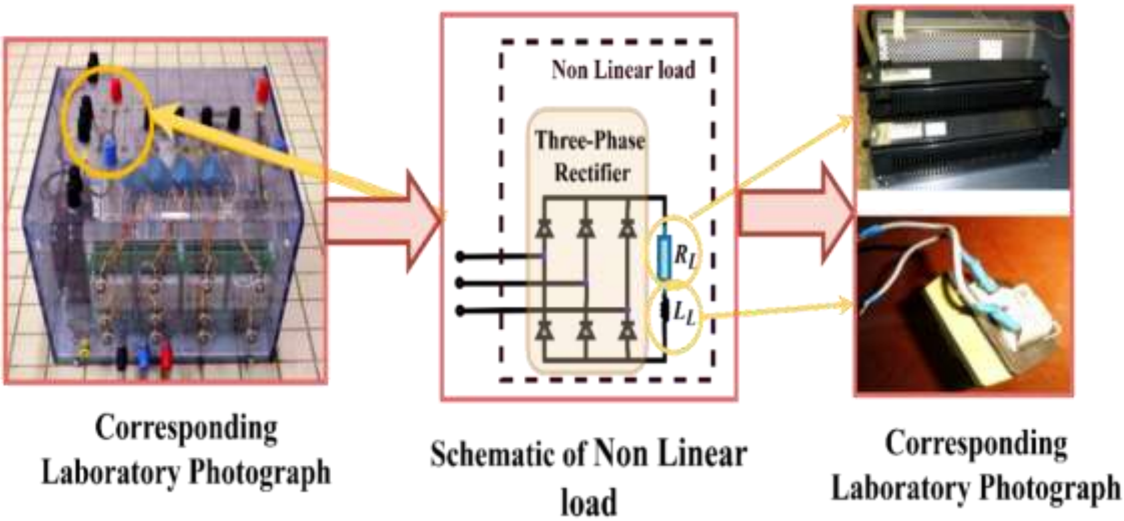

Figure 5.7: Schematic representation and laboratory photograph of the nonlinear load configuration.

5.3.7 Measurement and data acquisition system

Experimental measurements include the PV current (I_{pv}), PV voltage (V_{pv}), DC-link voltage (V_{dc}), inverter output current ($I_{fph\text{-}a,\,b,\,c}$), grid currents ($I_{ph\text{-}a,\,b,\,c}$), load current ($I_{Lph\text{-}a,\,b,\,c}$) and grid voltages ($V_{ph\text{-}a,\,b,\,c}$). These electrical quantities are measured using high-precision voltage and current sensors, as illustrated in Figures 5.8(a) and 5.8(b).

The system's transient and steady-state behaviors are recorded using a digital oscilloscope, shown in Figure 5.8(c), while a power analyzer is utilized to evaluate key power quality parameters such as THD, P, Q, PF, THD, *cos (Φ)*, *tan (Φ),* and overall system efficiency, as shown in Figure 5.8(d).

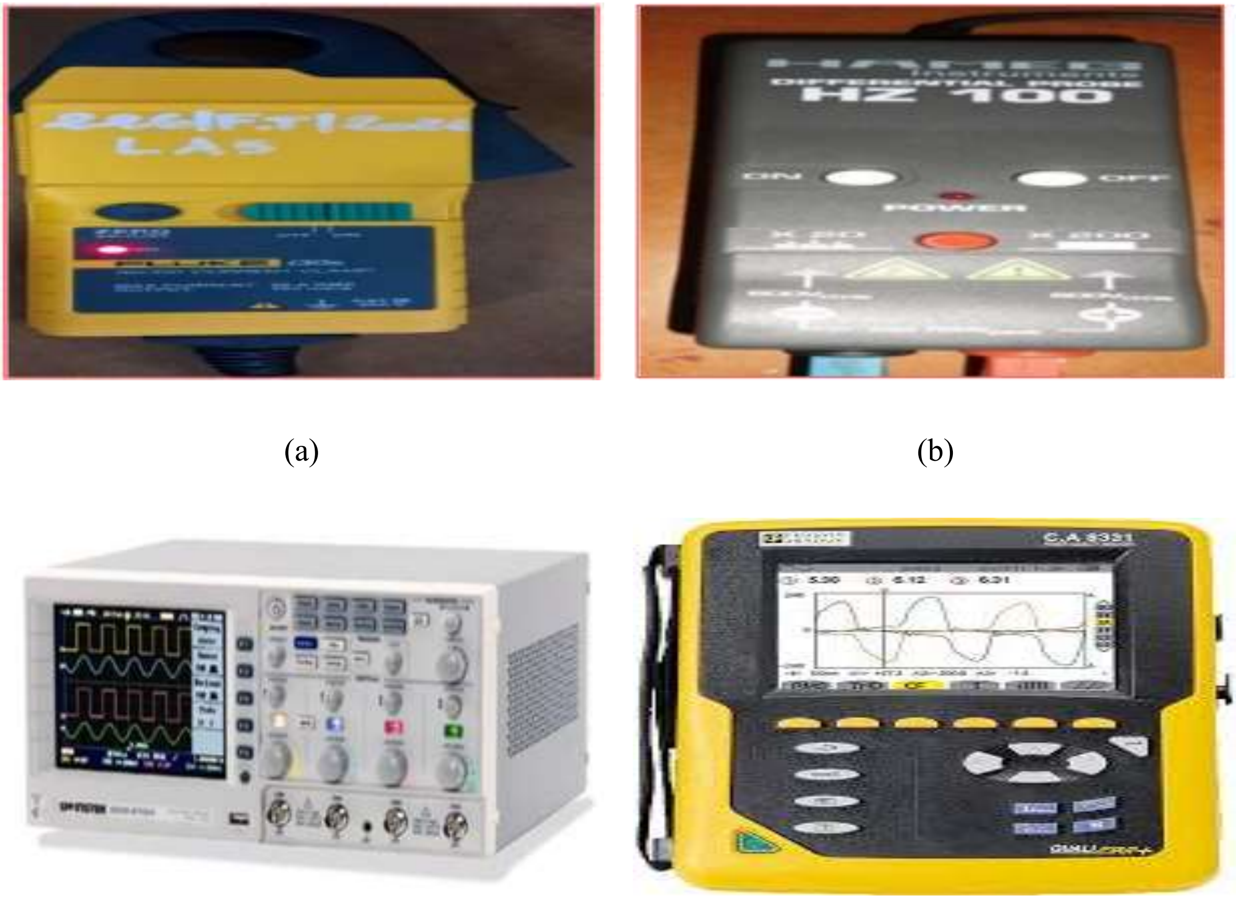

(a) (b)

(c) (d)

Figure 5.8: Photographs of the experimental measurement setup: a) current sensors, b) voltage sensors, c) digital oscilloscope, and d) Power analyzer

5.4 Advanced strategies for control and power maximization

Building upon the theoretical developments presented in Chapters 3 and 4, this section outlines the control and optimization strategies selected for the experimental implementation of the proposed GCPV-SAPF system. The objective is to experimentally validate, under real operating conditions, the effectiveness of the proposed algorithms. The focus of this thesis is placed exclusively on experimental results, as they provide a more practical assessment of system performance and implementation feasibility.

For SAPF subsystem, the P-DPC technique combined with a proposed FOPI-AW tuned using the ZOA algorithm, ensures robust DC-link voltage (V_{dc}) regulation, minimizes overshoot, and maintains dynamic stability under grid disturbances.

For PV subsystem, MOAs are employed in the MPPT process to extract the maximum available power from the PV array under varying environmental conditions. In this study, novel approaches such as the ZOA, and GWEO are proposed and comparatively evaluated against well-established techniques, including the WOA, PSO, GWO, and FPA.

Both subsystems are managed and synchronized through the dSPACE DS1104 control platform, which provides real-time data acquisition, signal processing, and coordinated control between the PV source and the SAPF. This architecture establishes a reliable foundation for validating the proposed control and optimization strategies within a unified experimental framework. Figure 5.9 illustrates the overall control algorithm of the integrated GCPV-SAPF system.

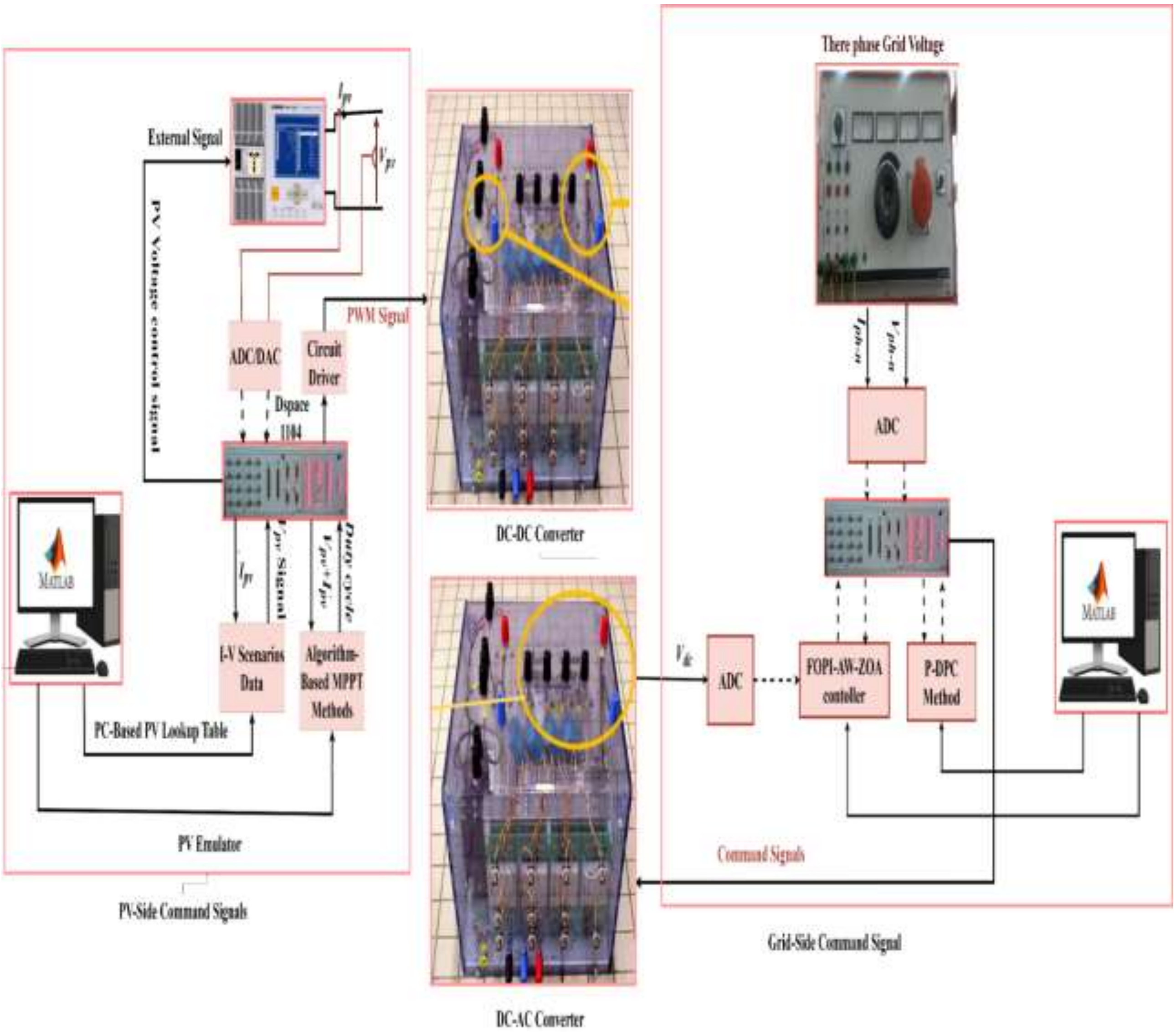

Figure 5.9: Overall control algorithm of the integrated GCPV-SAPF system

5.5 Implementation of the control system on dSPACE

The experimental implementation of the proposed control strategies was carried out using the dSPACE DS1104 real-time control platform. This system serves as the interface between the MATLAB/Simulink control models and the physical components of the GCPV-SAPF system test bench, enabling direct real-time execution of the control algorithms on the actual hardware.

The control tasks are divided between two dSPACE units: one dedicated to the Photovoltaic (PV) subsystem and the other to the SAPF. These two control units are electrically linked via the C_{dc}, ensuring coordinated energy exchange between PV source and grid. The DS1104 boards provide high-speed ADC and DAC channels for acquiring real-time voltage and current signals from the sensors, as well as generating PWM control signals for the IGBT converters.

All control algorithms, including the PDPC-FOPI-AW (ZOA-tuned) controller for SAPF and the metaheuristic MPPT algorithms (ZOA, GWEO, …etc.) for PV emulator, are implemented in MATLAB/Simulink and automatically compiled into the dSPACE environment using Real-Time Interface (RTI) blocks.

The Control Desk interface is used for online monitoring, parameter adjustment, and real-time visualization of system behavior, ensuring flexibility and reliability during experimental tests.

This architecture guarantees deterministic execution of the control loops with precise timing, thus ensuring the stability and accuracy of the entire GCPV-SAPF system during real operation.

5.6 Testing protocol

To validate the performance of the proposed control and optimization strategies, a systematic testing protocol was designed to evaluate both steady-state and dynamic responses of the integrated GCPV-SAPF under different operating conditions.

1. **System initialization:**

   During the system initialization phase, the dSPACE DS1104 platform is powered on, and all communication interfaces, including ADC, DAC, PWM channels, and sensor connections, are thoroughly checked. This ensures full synchronization, signal integrity, and accurate data transmission between the control hardware and the MATLAB/Simulink environment.

2. **Operating conditions:**

   Experimental tests are conducted under four main operating scenarios:

   - STC: Nominal solar irradiance of 1000 W/m² and ambient temperature of 25 °C.
   - PSC: Non-uniform irradiance patterns applied to evaluate the robustness and tracking capability of the MPPT algorithms.

- DSC: Time-varying irradiance profiles introduced to assess the transient response, adaptability, and dynamic performance of the proposed control and optimization strategies under rapidly changing environmental conditions.
- PSC–STC Transition: A transition test from PSC to STC, conducted to evaluate the dynamic response, convergence speed, and stability of the control and optimization strategies during sudden irradiance recovery.

3. **Performance evaluation:**

The following metrics are measured:

- DC-link voltage regulation (V_{dc} stability and overshoot percentage)
- THD of grid current
- PF and reactive power compensation
- MPPT tracking efficiency and tracking time
- Dynamic response to load and irradiance variations

4. **Data acquisition and analysis:**

Real-time electrical waveforms are acquired using a digital oscilloscope, whereas the power analyzer is employed to measure electrical quantities and power quality parameters. The acquired data are subsequently post-processed in MATLAB to compute key performance indicators, including THD, PF, V_{dc} regulation accuracy, tracking time, and MPPT efficiency. This analysis ensures a precise evaluation of the control system's accuracy, dynamic behavior, and robustness under diverse operating conditions.

This testing procedure provides a comprehensive validation of the proposed control architecture and confirms its suitability for GCPV-SAPF operation under realistic environmental variations.

Following the description of the experimental setup, measurement instrumentation, and testing methodology, the next section presents and discusses the experimental results obtained from the conducted tests. The experiments were carried out according to the established testing protocol and cover several scenarios, including STC, five distinct PSC patterns, DSC conditions, and PSC-STC transition tests. These scenarios were selected to rigorously evaluate the dynamic response, stability, and overall performance of the proposed control and optimization strategies under practical operating conditions.

5.7 Experimental results and discussions

This section presents and analyzes the experimental results obtained from the real-time implementation of the proposed GCPV-SAPF system. The objective is to validate the effectiveness of the developed control and optimization strategies under realistic operating conditions. The experiments were performed using the dSPACE DS1104 real-time control platform, which provided precise control, signal acquisition, and real-time monitoring of both the PV and SAPF subsystems.

Key performance indicators were analyzed, including V_{dc} regulation, current harmonic mitigation, reactive power compensation, and MPPT efficiency. Comparative analyses were carried out among the implemented control and optimization algorithms to highlight their advantages, dynamic behavior, and overall contribution to power quality improvement.

An analytical comparison was performed among the GWEO, ZOA, PSO, GWO, WOA, and FPA algorithms in terms of several performance indices:

- Tracking Time (T_T): to identify the algorithm with the fastest MPPT response;
- Generated PV Power: to evaluate the accuracy of MPP identification;
- Efficiency Ratio;
- Measured PV Current (I_{pv}); and
- Measured PV Voltage (V_{pv}).

These parameters were evaluated under STC, PSCs, and DSCs, while maintaining a constant temperature of 25°C. The comparison included five distinct PSC patterns, designated as PSC-1, PSC-2, PSC-3, PSC-4, and PSC-5, along with one STC case. Each condition corresponds to a unique GMPP distribution within the search space, providing a comprehensive and rigorous assessment of the proposed algorithm's tracking performance and adaptability under diverse irradiance profiles.

This detailed setup provides a robust framework for analyzing the PV array behavior and validating the MPPT algorithm under various PSC scenarios. It ensures the existence of both local and global maxima in the P-V curve, which is essential for evaluating the tracking capability, convergence speed, and robustness of the proposed optimization-based MPPT strategy [9,12].

Table 5.2 summarizes the electrical parameters of each curve. These values were experimentally determined by measuring the MPP coordinates (I_{mpp}, V_{mpp}, and P_{mpp}) during preliminary testing to ensure precision and reproducibility in subsequent comparative analyses.

To further validate the reliability and significance of the experimental findings, the reactive power compensation capability of the SAPF was also examined. The system's ability to inject active power into the grid while maintaining high power quality, characterized by a low THD and near-unity PF, was verified through detailed measurements. A comprehensive overview of the global system parameters implemented in the experimental prototype is provided in Table 5.3.

Table 5.2: Details of STC and PSCs Pattern

PSCs	Pattern (W/m^2)	T (°C)	Num of Peaks	$P_{mpp}(W)$	$V_{mpp}(V)$	$I_{mpp}(A)$
STCs	1000,1000,1000,1000, and 1000	25	1	292.47	45.33	6.5
PSC-1	800, 1000, 200, 400 and 700		5	133.2	28.52	4.67
PSC-2	100, 900, 800, 1000 and 400		5	151.1	28.033	5.39
PSC-3	1000, 950,850,900 and 800		5	254.2	48.34	5.259
PSC-4	400, 600, 800, 1000 and 900		5	120	30	4
PSC-5	800, 300, 200, 100, and 1000		5	100	19.3207	5.2

Table 5.3: Electrical parameters of experimental setup

Parameters	Values
PV array electrical parameters under STC	
I_{sc}	7.2 A
V_{oc}	53 V
I_{mpp}	6.5 A
V_{mpp}	45.33 V
P_{mpp}	292.47
L-BOOST	30 mH
Grid electrical parameters	
Grid RMS voltage ($V_{ph\text{-}n}$)	13 V
Grid frequency (F)	50 Hz
C_{dc}	2200 µF

R_L	5 Ω
L	8.5 mH
R_f	0.1 Ω
L_f	8.5 mH
T_s	47 µs
Switching frequency (f)	20 kHz
V_{dcref}	92V

5.7.1 SAPF performance verification

The initial experimental investigation aimed to assess the performance of the SAPF in mitigating harmonic distortions within the grid current. The VSI was controlled using P-DPC strategy combined with a FOPI-AW controller tuned by the ZOA, operating with a switching frequency (f) of 20 kHz and a sampling time of T_s=47µs.

The SAPF prototype employed a SEMIKRON universal inverter rated at 20 kVA, with a voltage capacity of 1200 V and a current limit of 50 A. This bidirectional inverter facilitated both current compensation and Q support in real time.

Figures 5.10 to 5.17 summarize the main experimental observations, including the source current (Is), source voltage (Vs), DC-link voltage (V_{dc}), filter current (I_f), load current (I_L), as well as the active power (P) and reactive (Q) power components recorded before and after SAPF activation.

Figure 5.10 displays the experimental current and voltage waveforms of the SAPF under several operating conditions, including (a) steady-state operation and (b) a zoomed view of the steady-state behavior. The steady-state response demonstrates stable and well-regulated system performance, where the Is exhibits a nearly sinusoidal waveform and remains properly synchronized with the Vs. The enlarged view further emphasizes the high quality of the waveforms and confirms the effectiveness of the SAPF in mitigating current harmonics under steady-state conditions.

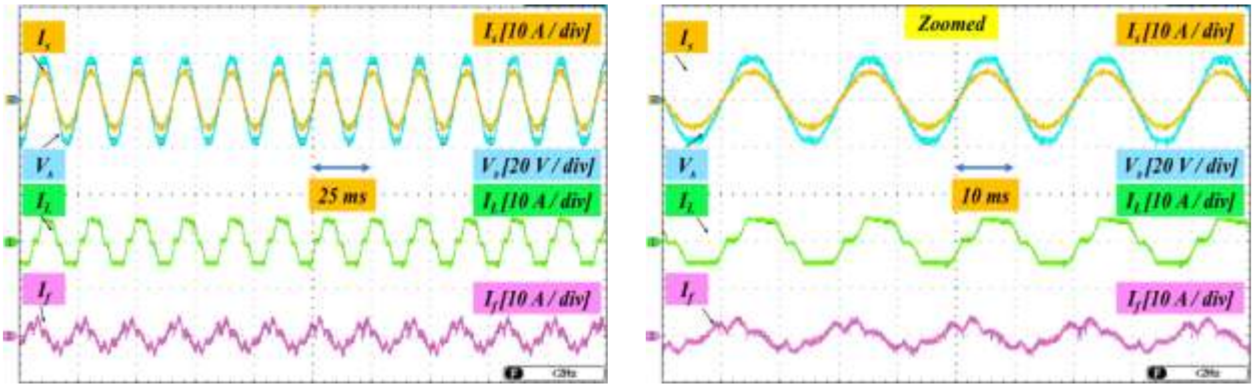

(a) (b)

Figure 5.10: Experimental waveforms of the SAPF before current compensation under steady-state conditions

Figure 5.11(a) presents the experimental voltage and current waveforms of the SAPF during load variation, including V_s, Is, I_L, and I_f. The results show that the SAPF rapidly adapts to changes in load conditions, maintaining good current quality and overall system stability. Figure 5.11(b) provides a zoomed-in view of the waveforms, highlighting the smooth dynamic response and confirming the effectiveness of the SAPF in regulating the source current during the transient interval.

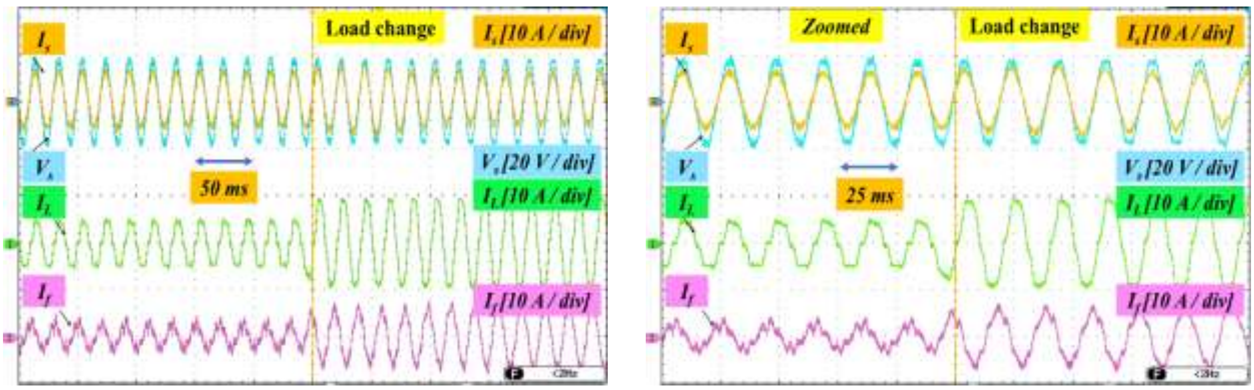

(c) (d)

Figure 5.11: Experimental waveforms of the SAPF before current compensation during load variation

Figure 5.12(a) presents the experimental P and Q as well as the V_{dc} profiles, illustrating the system behavior before and after SAPF activation. Prior to SAPF activation, the I_L exhibits significant distortion, reflected in higher Q and fluctuations in V_{dc}. Upon SAPF activation, the filter rapidly mitigates the harmonics, reduces the Q, and stabilizes the V_{dc}, confirming its effectiveness in improving power quality and ensuring reliable operation. Figure 5.12(b) provides a zoomed-in view of the same waveforms, highlighting the steady-state response of the SAPF and demonstrating smooth performance and precise regulation of power flow during the activation process.

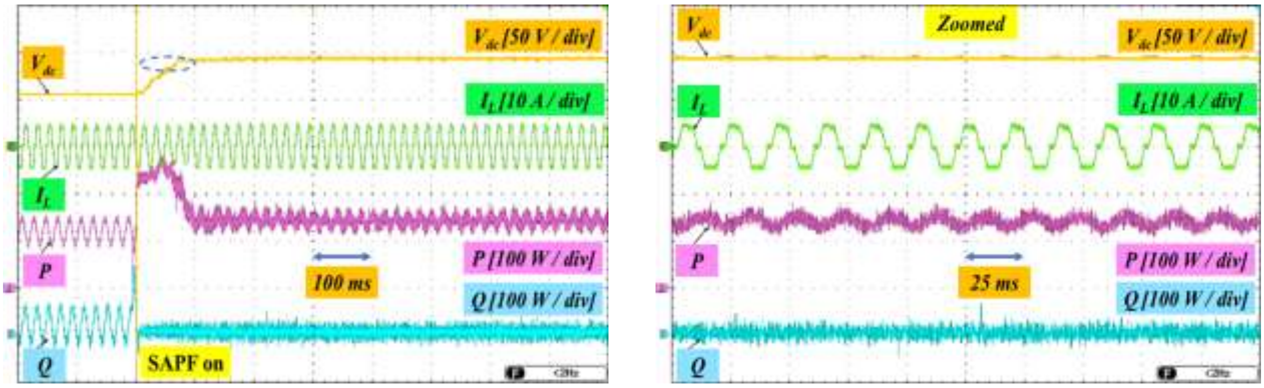

(a) (b)

Figure 5.12: Experimental waveforms of the SAPF before current compensation during filter current injection

Figures 5.13 and 5.14 examine the system behavior before SAPF operation. Figure 5.13(a–b) presents the RMS measurements of three-phase currents and voltages without compensation, showing distorted waveforms and slight current imbalance across the phases. Figure 5.14(a–c) shows the harmonic spectra of phases a, b, and c without SAPF, where each phase exhibits noticeable harmonic distortion. Figure 5.14(d) presents the combined three-phase I_s waveform, confirming overall non-sinusoidal and harmonically distorted current behavior due to the absence of filtering and compensation.

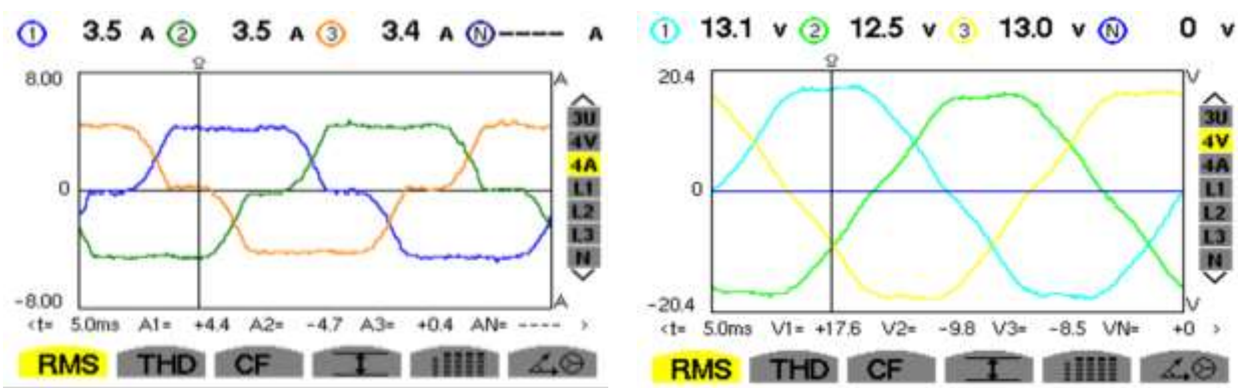

(a) (b)

Figure 5.13: RMS measurements of the three-phase system without SAPF operation

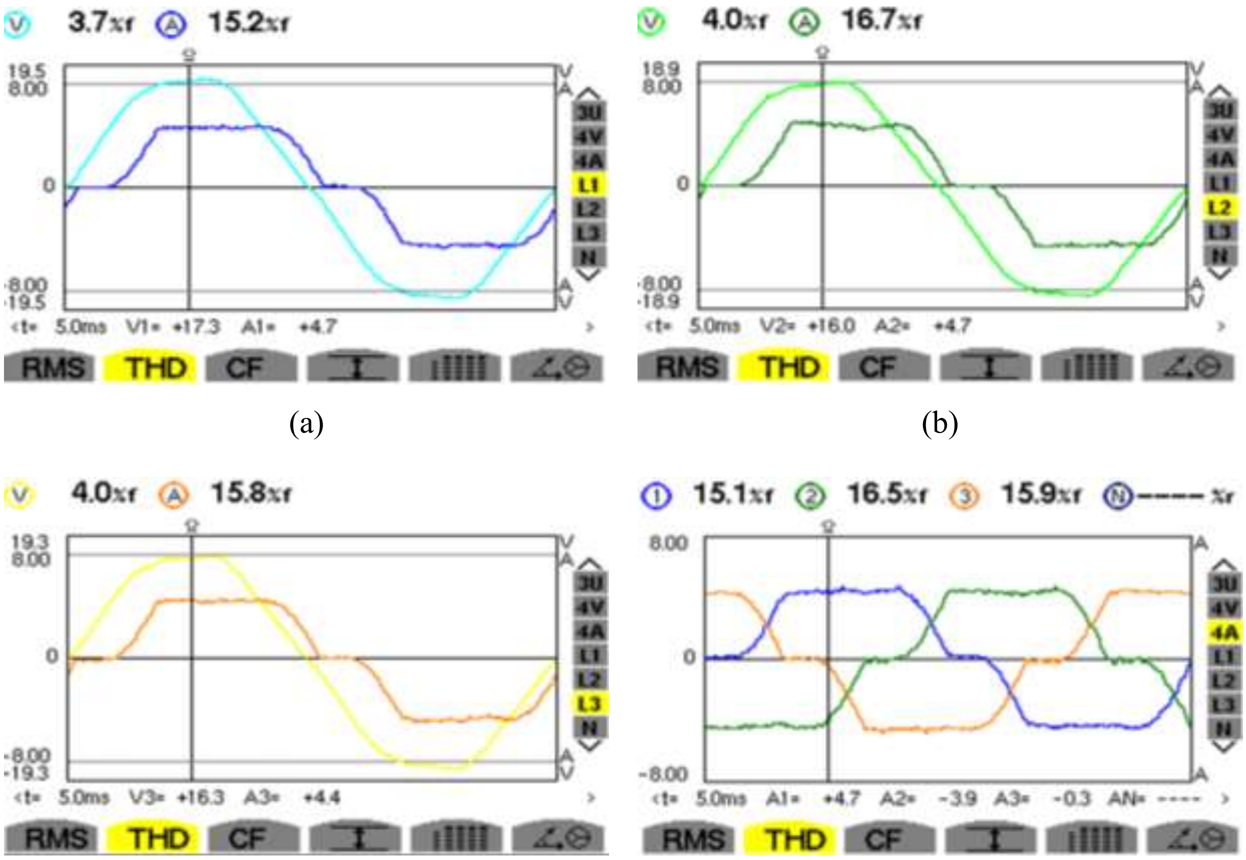

(a) (b)

(c) (d)

Figure 5.14: Harmonic distortion of the three-phase system without SAPF operation

Figure 5.15(a–d) presents the harmonic spectrum of phase a under load prior to SAPF activation at four zoom levels: full scale, 20%, 10%, and 5%. The full-scale view shows the dominant low-order harmonics, while the successive zooms reveal smaller medium- and high-order components. This detailed analysis highlights the overall harmonic distortion introduced by the nonlinear load, providing a clear baseline for assessing the SAPF's compensation performance.

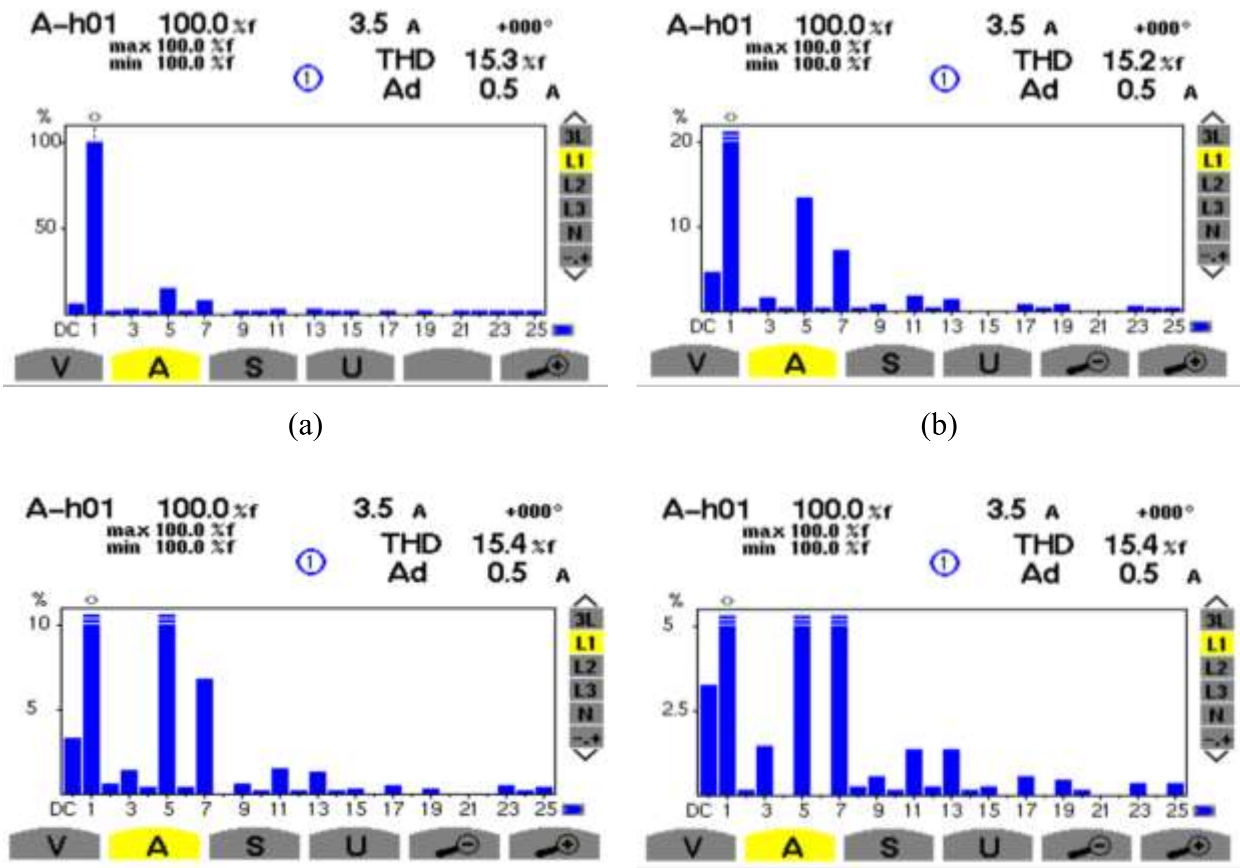

(a) (b) (c) (d)

Figure 5.15: Harmonic spectrum of the phase a system under different zoom levels before SAPF operation: a) full-scale view, b) zoomed to 20%, c) zoomed to 10%, and d) zoomed to 5%.

Figure 5.16(a-b) presents the three-phase power quality measurements before SAPF implementation. The waveforms indicate that the system supplies the load with P and Q components affected by harmonic distortion, resulting in non-ideal I_s. The power analyzer confirms that the PF is below unity and that deformation power is present, showing a clear need for SAPF to enhance power quality by reducing harmonics, compensating Q, and minimizing power deformation (D).

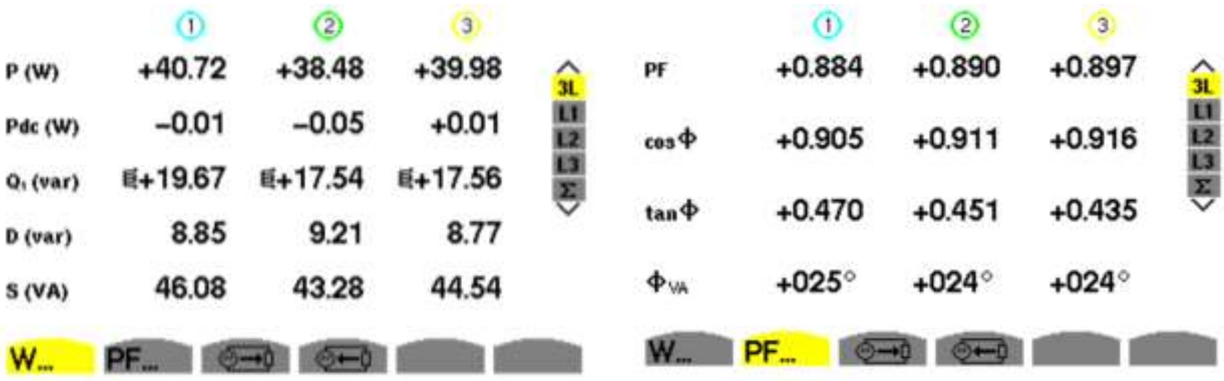

(a) (b)

Figure 5.16: Power analyzer measurement results of three-phase power quality parameters before SAPF implementation

Figure 5.17 illustrates the phase shift behavior of the three-phase system before SAPF activation. In Figure 5.17(a), the current waveforms exhibit phase displacement and distortion due to the presence of harmonic and reactive components. Figure 5.17(b) shows the corresponding three-phase voltages, which remain balanced but are not aligned in phase with the distorted *Is*. The figure confirms a non-ideal phase relationship between current and voltage, indicating the necessity of SAPF to correct phase alignment and improve overall power quality.

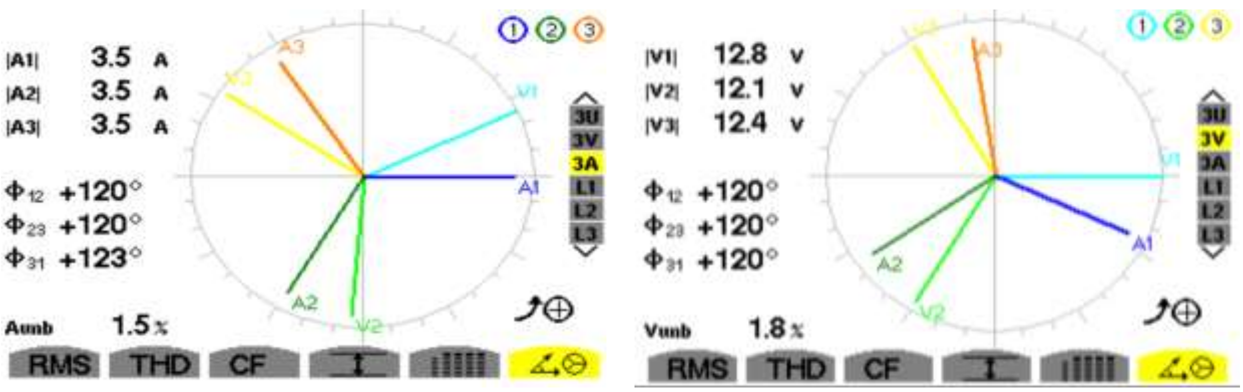

(a) (b)

Figure 5.17: Phase shift angle before activating the SAPF*:* a) current, b) voltage

Figures 5.18 to 5.21 present the present the system behavior after activating the SAPF, demonstrating its effectiveness in enhancing the power quality of the three-phase system. After the SAPF was engaged, the harmonic and phase characteristics of the system improved significantly.

Figure 5.18(a-d) illustrates the system performance after SAPF activation, where harmonic and phase characteristics show clear improvement. Figures 5.18(a-c) presents the THD of the compensated three-phase currents for phases a, b, and c, confirming a low distortion level and effective harmonic suppression. Figure 5.18(d) shows the combined compensated three-phase current waveform, where the currents appear balanced and nearly sinusoidal, demonstrating stable three-phase compensation and the SAPF's strong capability in harmonic mitigation.

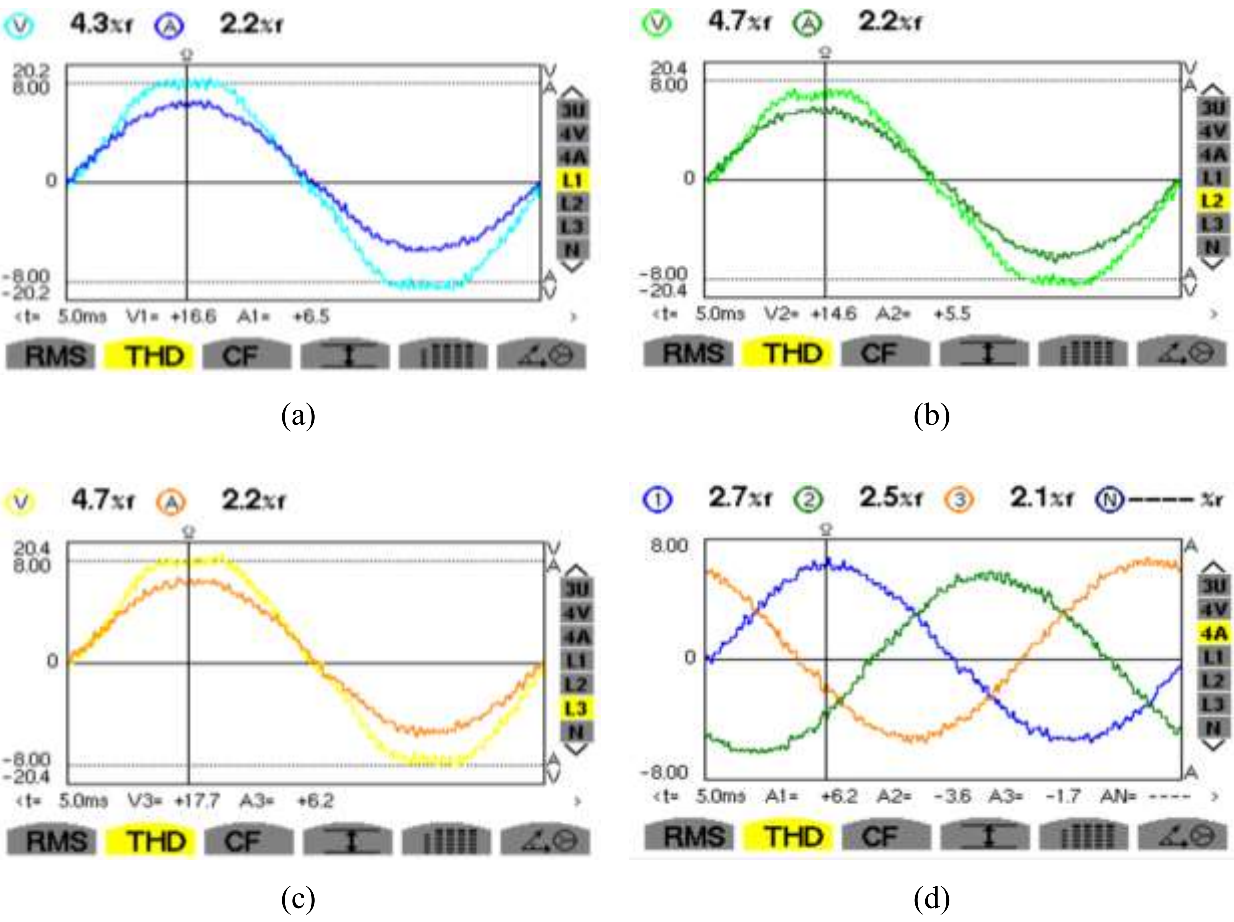

Figure 5.18: Harmonic distortion of the three-phase system after SAPF operation: a) phase a, b) phase b, c) phase c, and d) combined three-phase currents

Figure 5.19(a-c) presents the harmonic spectrum of the three-phase currents after SAPF operation. The harmonic components across phases a, b, and c were significantly reduced, confirming effective filtering performance.

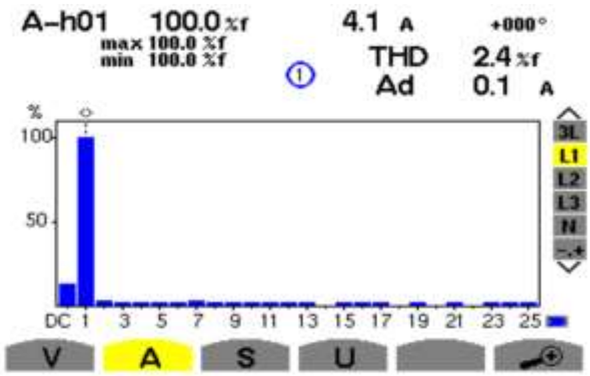

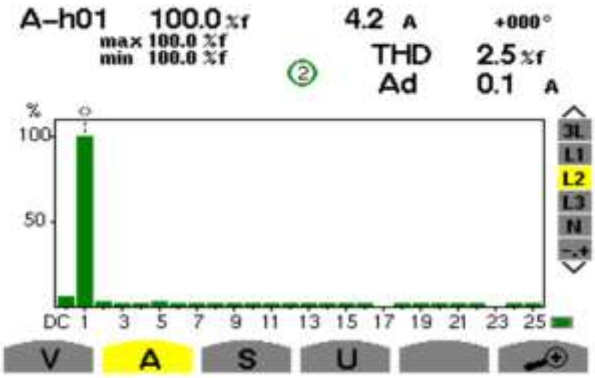

(a) (b)

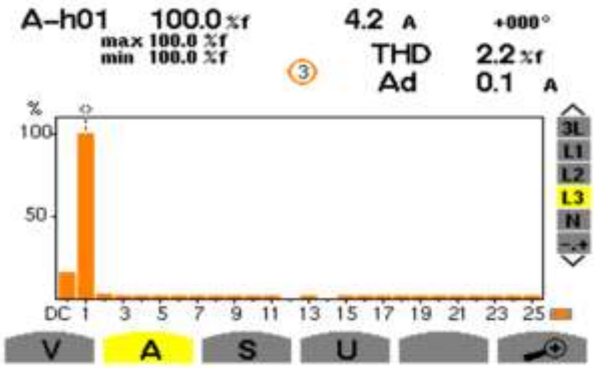

(c)

Figure 5.19: Harmonic spectrum of the three-phase system after SAPF operation: a) phase a, b) phase b, c) and phase c

Figure 5.20(a-b) shows the phase shift angle after SAPF activation. The current and voltage waveforms are nearly in phase, indicating a significant reduction in Q flow and a notable improvement in the overall PF.

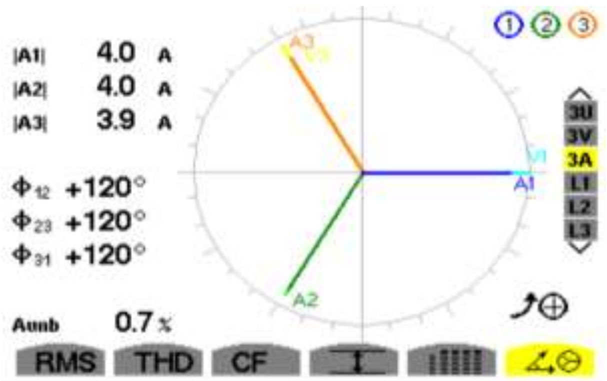

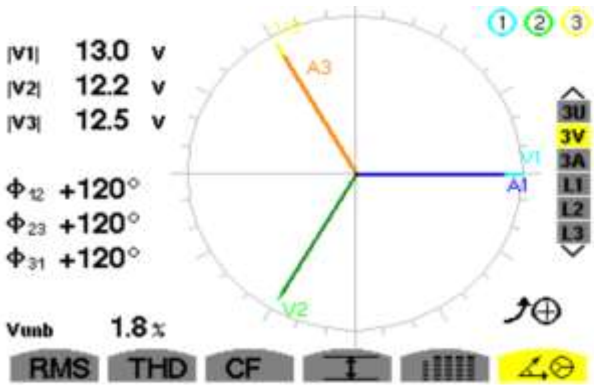

(a) (b)

Figure 5.20: Phase shift angle after activating the SAPF

Figure 5.21(a) presents the corresponding *P*, *Q*, *D*, and *S* powers measurements. The *Q* components are significantly reduced, and the power distribution among the three phases is nearly balanced. The total load power is approximately 150.57 W, confirming effective power quality improvement after SAPF operation. Figure 5.21(b) illustrates the power analyzer measurements of the PF–related parameters for the three phases after SAPF implementation. The results show that the PF of all phases is very close to unity, with *cos φ* values close to 1, indicating proper synchronization between voltage and current.

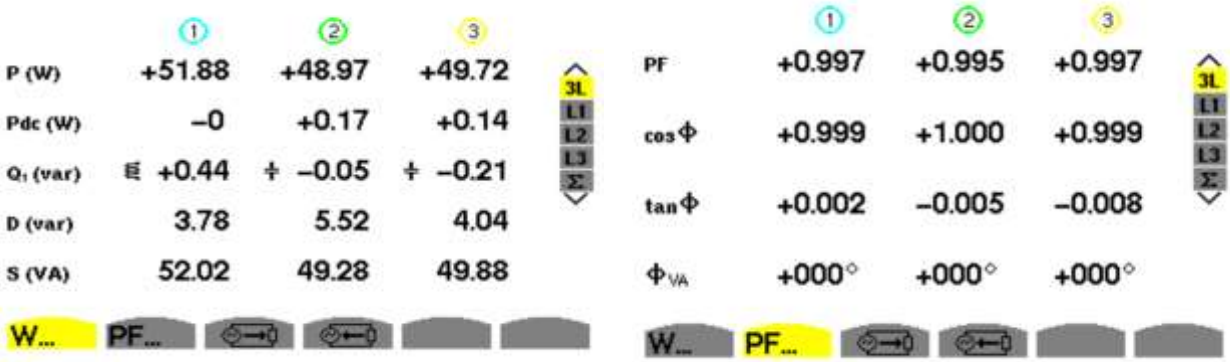

(a) (b)

Figure 5.21: Power analyzer measurement results of three-phase power quality parameters after SAPF implementation

5.7.2 Experimental results under STC of proposed methods

To establish a performance baseline, the proposed GCPV-SAPF was first tested under STC. In this scenario, all photovoltaic modules were uniformly illuminated with an irradiance of 1000 W/m² and maintained at a constant temperature of 25°C, as summarized in Table 5.2.

The objective of this test is to validate the effectiveness of the proposed MPPT and control strategies under ideal and stable operating conditions. The evaluation focuses on both power extraction efficiency and power quality enhancement provided by the SAPF through harmonic mitigation and reactive power compensation.

The experimental PV characteristics obtained under STC are illustrated in Figure 5.22. The red dot on PV curves denotes the MPP achieved by the proposed optimization algorithm, confirming its ability to accurately track the global optimum and maintain steady-state operation.

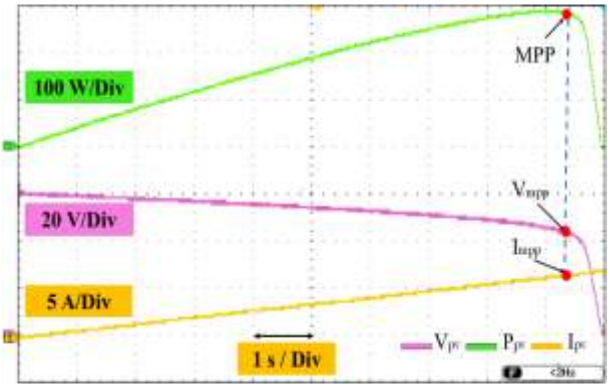

Figure 5.22: Experimental P–V and I–V curves of the PV array system under STCs

A uniform irradiance scenario was considered, in which all PV modules were subjected to a constant irradiance level of 1000 W/m², while the V_{dc} was set to its reference value. The experimental results obtained using the proposed GWEO and ZOA methods are presented in Figures 5.23 and 5.24. These figures illustrate the time-domain waveforms of the PV voltage (V_{pv}), PV current (I_{pv}), PV power (P_{pv}), and the duty cycle (D) of the DC–DC converter, as shown in Figures 5.23(a) and 5.24(a). Additionally, the corresponding V_{dc}, along with the active power (P) and reactive power (Q) exchanged with the grid, are depicted in Figures 5.23(b) and 5.24(b).

Under STC, the GWEO method achieved the fastest tracking performance, reaching the MPP within 0.9 s, with a MPP of 292.35 W, as shown in Figure 5.23(a). The tracking process exhibits a fast dynamic response and stable steady-state behavior, resulting in a high tracking efficiency (η) of 99.96%, calculated using Equation (5.1).

$$\eta = \frac{P_{pv-SteadyState}}{P_{\max Available}} \times 100 \tag{5.1}$$

Regarding grid interaction, the PV system supplies a three-phase load with a P demand of approximately 150.57 W. The surplus generated power, estimated at -97.38 W, is injected into the utility grid. The remaining power difference of approximately 44.4 W corresponds to inherent system losses, mainly attributed to inverter switching losses, resistive losses in the filter inductors, power electronic components, and measurement and control-related losses. Moreover, the grid-connected SAPF ensures effective Q compensation, maintaining the Q close to 0 VAR, as illustrated in Figure 5.23(b).

In comparison, the ZOA method exhibits a slower dynamic response, with a T_T =0.92 s, as depicted in Figure 5.24(a). It achieves a MPP of 290.55 W, which is slightly lower than the

MPP, and injects approximately P= -95.58 W into the grid, as shown in Figure 5.24(b). Despite its slower response, the ZOA method demonstrates satisfactory performance, achieving a η = 99.34%. The obtained results are summarized in Table 5.4.

The V_{dc} accurately tracks its reference value (V_{dcref}=92 V) with fast settling time and negligible deviation. The proposed FOPI-AW-ZOA controller ensures stable voltage regulation during both SAPF operation and PV power injection, demonstrating effective disturbance rejection and robust steady-state performance.

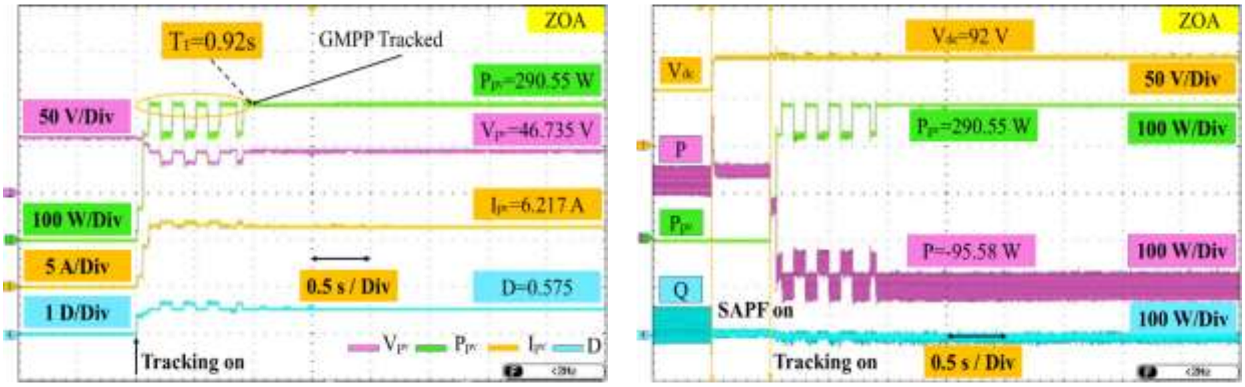

(a) (b)

Figure 5.23: Experimental results of the proposed ZOA method under STC

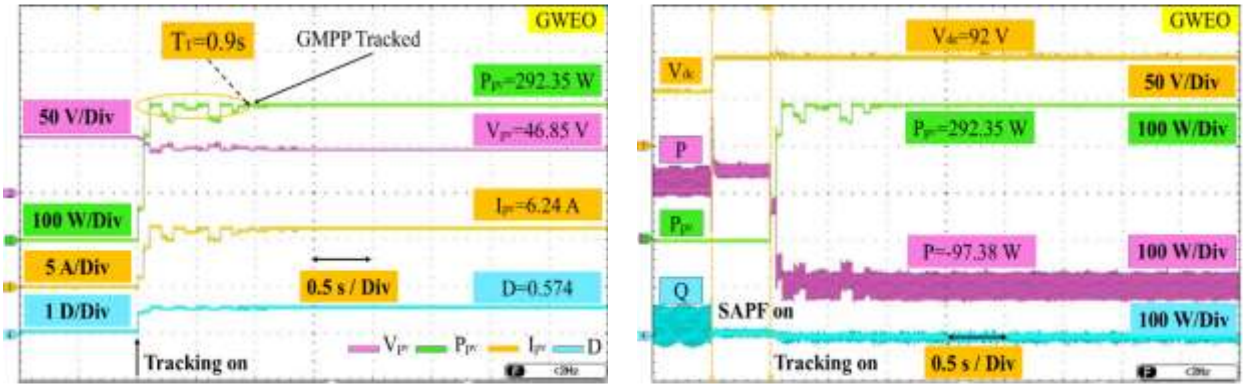

(a) (b)

Figure 5.24: Experimental results of the proposed GWEO method under STC

Table 5.4: Summarizing the experimental results of proposed methods ZOA and GWEO under STCs

MPPT	$V_{mpp}(V)$	$I_{mpp}(A)$	$P_{mpp}(W)$	$P_{\max}(W)$	P	P_{load}	Power loss	T_T (s)	η (%)
ZOA	46.735	6.217	290.55	292.47	-95.58	150.57	44.4	0.92	99.34
GWEO	46.85	6.24	292.35	292.47	-97.38			0.9	99.96

The results illustrated in Figure 5.25 present a detailed comparison of the main performance indicators, namely η and T_T, for the evaluated MPPT algorithms. The comparison demonstrates noticeable performance differences among the techniques and allows an objective assessment of the proposed GWEO and ZOA methods, highlighting their respective advantages and limitations in terms of convergence speed and energy extraction efficiency.

(a)

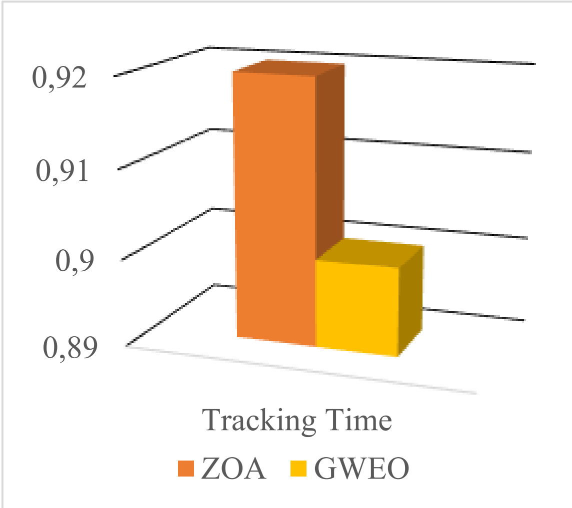

(b)

Figure 5.25: Comparative performance analysis of the proposed GWEO and ZOA techniques under STCs in terms of: a) η , and b) T_T

5.7.3 Experimental results under PSCs scenario of proposed methods

As mentioned earlier, an experimental setup was implemented to evaluate the effectiveness of the proposed GWEO and ZOA techniques in rapidly and accurately tracking the GMPP, thereby maximizing P injection into the grid. All key electrical parameters of the PV system and the grid, including P, Q, V_{dc}, P_{pv}, I_{pv}, V_{pv}, and D, were continuously monitored.

All experimental data, including numerical values of the key parameters, were obtained from the PV emulator and the control desk. The control desk provided comprehensive monitoring capabilities, enabling access to all relevant system measurements and reports. In addition, a power analyzer was used to measure electrical quantities in the grid and filter sections, such as P and Q, PF, and THD… etc.

The overall performance of the proposed methods was evaluated under various PSCs, each characterized by five distinct power peaks representing different levels of complexity and operational challenges, as illustrated in Figure 5.26. These complex PSCs present a significant challenge for MPPT algorithms, increasing the risk of convergence to suboptimal operating points. Testing the GWEO and ZOA techniques under these scenarios demonstrates their robustness, global tracking capability, and efficiency in handling highly nonlinear and challenging operating conditions. Five representative PSC cases were selected for detailed evaluation, as summarized in Table 5.2.

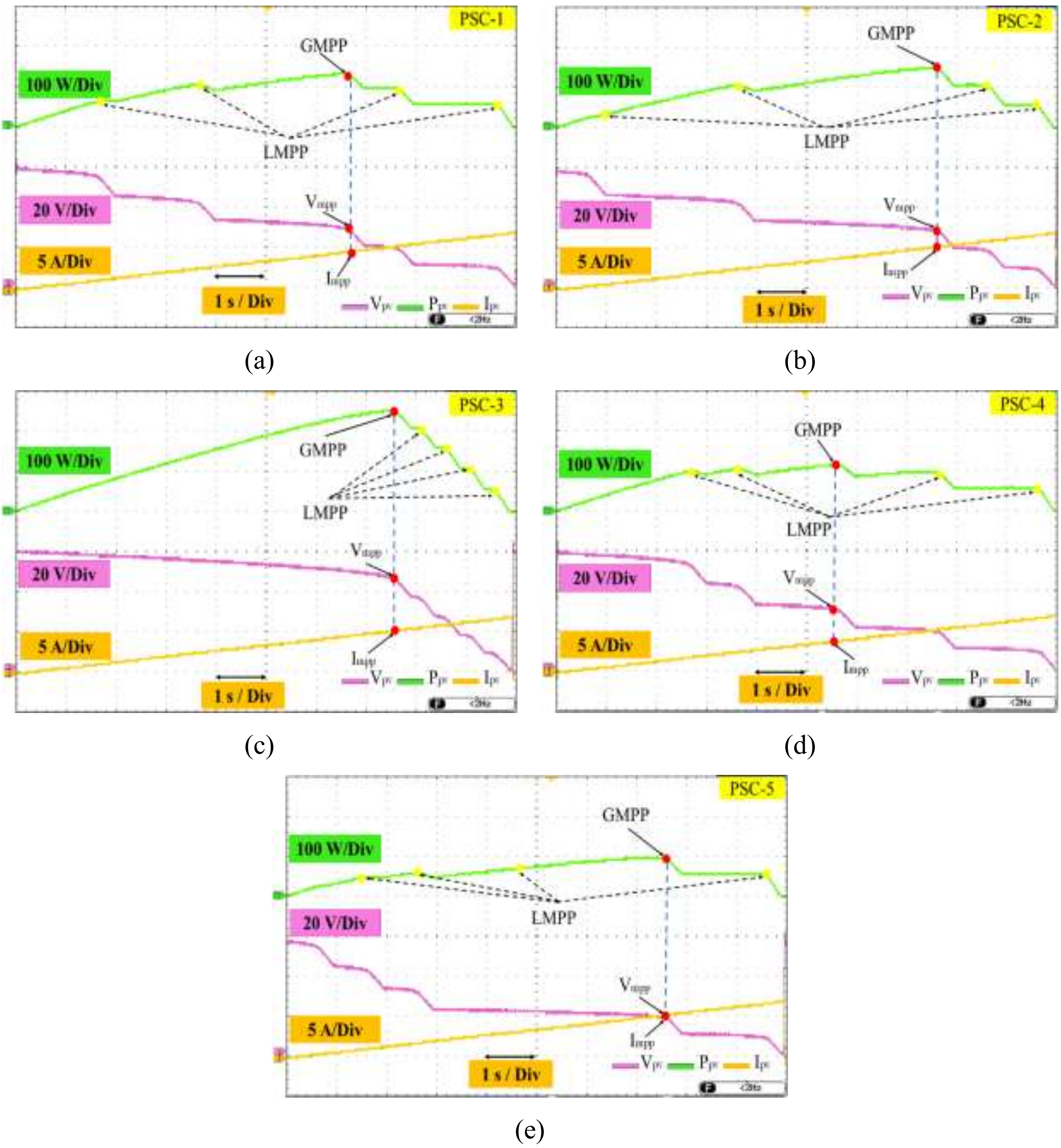

Figure 5.26: Experimental P–V and I–V curves of the PV array under five PSC scenarios: a) PSC-1, b) PSC-2, c) PSC-3, d) PSC-4, and e) PSC-5

In the first scenario (PSC-1), corresponding to different irradiance levels summarized in Table 5.2 and illustrated in Figure 5.26(a), the tracking performance of the proposed GWEO and ZOA techniques was evaluated. As shown in Figure 5.27(a) and (b), the GWEO method achieved the fastest T_T =1 s to reach the GMPP, delivering a GMPP of 133.17 W with an η =99.97%, as also shown in Figure 5.27(a). Under this operating condition, the PV system partially supplied the load demand. Since the total load requirement exceeded the available PV power, the remaining power deficit was supplied by the grid to ensure stable system operation, providing P = 33.79 W. The V_{dc} was well regulated around its V_{dcref}= 92 V, demonstrating stable operation of the power conversion stage without noticeable oscillations. Figures 5.27(b) confirm the stability of the grid-connected system, where Q remained close to 0 VAR, indicating effective power decoupling and proper synchronization with the grid.

Similarly, the ZOA technique exhibited competitive performance, achieving a T_T=1.05 s and delivering a peak power of approximately 133 W with an η =99.85%, as depicted in Figure 5.28(a). Under the same operating conditions, it injected P= 33.96 W into the grid, as illustrated in Figure 5.28(b). The V_{dc} accurately tracked its reference value (V_{dcref}=92 V) with fast settling time and negligible deviation under both SAPF activation and PV injection modes, demonstrating effective voltage regulation and robust dynamic behavior during GMPP tracking.

Overall, these results demonstrate the superior tracking speed, high efficiency, stable V_{dc} regulation, and excellent grid compatibility of the proposed GWEO and ZOA techniques under real-time PSC-1 scenarios.

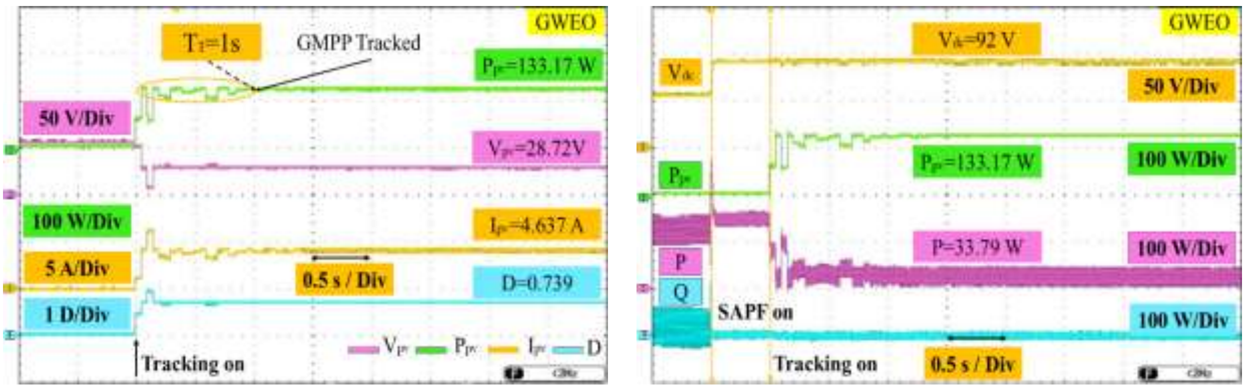

(a) (b)

Figure 5.27: Experimental results of the proposed GWEO method under PSC-1

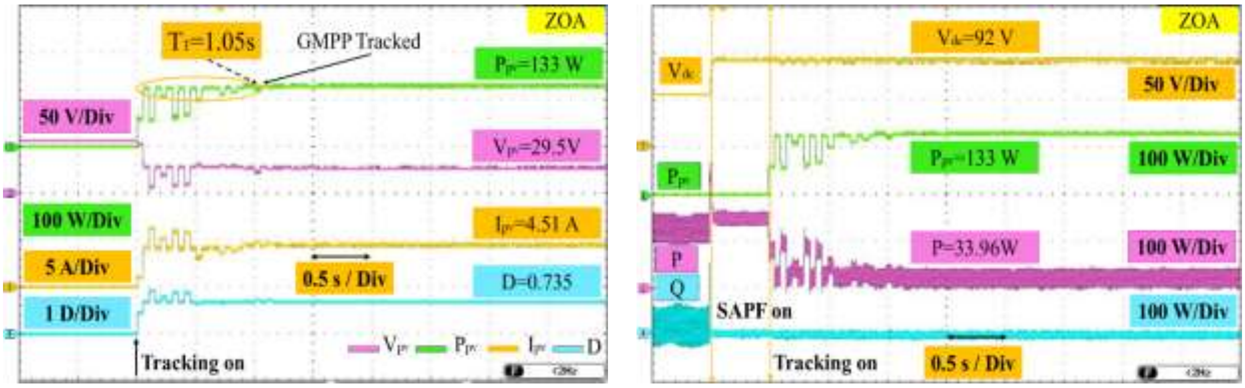

(a) (b)

Figure 5.28: Experimental results of the proposed ZOA method under PSC-1

In the second scenario (PSC-2), corresponding to the irradiance pattern summarized in Table 5.2 and illustrated in Figure 5.26(b), the PV array exhibited four LMPPs with a GMPP of 151.1 W. Under these more complex shading conditions, the tracking performance of the proposed GWEO and ZOA techniques was further evaluated. As shown in Figure 5.29(a), the GWEO method successfully tracked the GMPP within a T_T=1 s, delivering a GMPP of 150.98 W with a η = 99.92%.

Under this condition, the PV system was able to nearly satisfy the three-phase load demand. Since the generated PV power (150.98 W) was approximately equal to the load requirement (150.57 W), the load was almost entirely supplied by the PV system. As shown in Figure 5.29(b), the small power mismatch was mainly compensated by the grid, which supplied approximately P=11.91 W. The power loss of about 6.31 W is attributed to inherent system losses, including power conversion and filtering effects. Consequently, no significant surplus power was available for injection into the grid.

Similarly, the ZOA technique demonstrated competitive performance, achieving a T_T=1.1 s and delivering a peak power of approximately 151 W with a η=99.93%, as shown in Figure 5.30(a). Under the same operating conditions, the small power mismatch was compensated by the grid, which supplied approximately P=11.89 W, as illustrated in Figure 5.30(b).

Throughout this scenario, the V_{dc} remained tightly regulated around its reference value of 92 V during both SAPF operation and PV injection, indicating stable operation of the power conversion stage. Additionally, the Q exchanged with the grid remained close to zero, confirming proper grid synchronization and effective power management under PSC conditions.

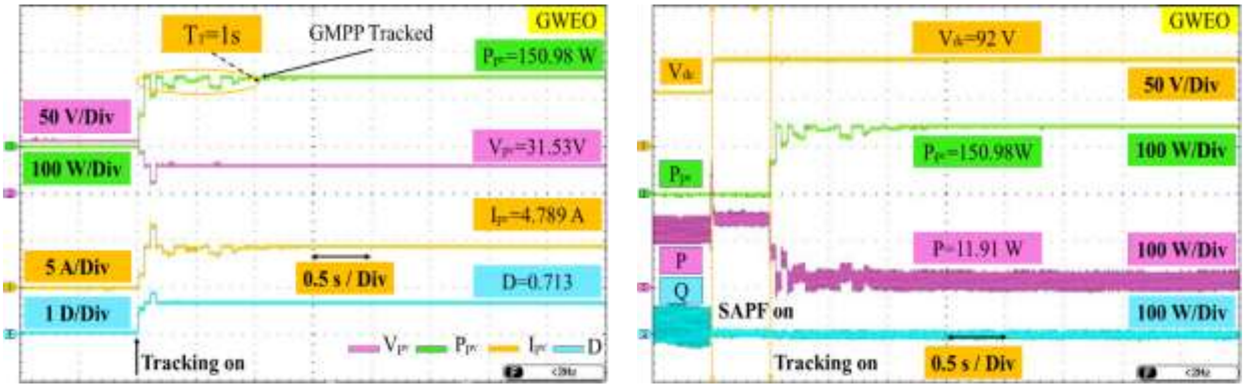

(a) (b)

Figure 5.29: Experimental results of the proposed GWEO method under PSC-2

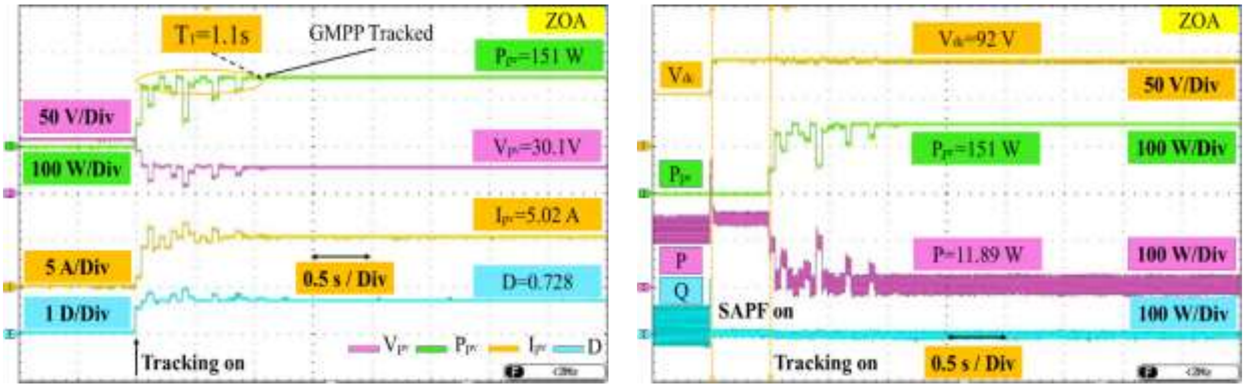

(a) (b)

Figure 5.30: Experimental results of the proposed ZOA method under PSC-2

In the third scenario (PSC 3), associated with the irradiance distribution presented in Table 5.2 and depicted in Figure 5.26(c), the PV array presents several local maxima, while the GMPP is positioned on the left side of the P–V curve. Under these conditions, the performance of the proposed GWEO and ZOA algorithms was examined in the presence of pronounced nonlinearity caused by partial shading.

As shown in Figure 5.31(a), the GWEO method successfully tracked the GMPP within a T_T = 1.05 s, delivering a GMPP of 253.79 W with a η=99.91%. In this scenario, the PV system was able to fully satisfy the load demand, and the excess generated power was injected into the grid. Specifically, injected approximately P=60.4 W into the grid, as illustrated in Figure 5.31(b). The difference between the generated PV power and the load demand is attributed to inherent system losses, including inverter switching losses, power conversion, filtering effects and measurement and control-related losses.

Similarly, the ZOA technique demonstrated effective tracking performance, achieving a faster T_T =0.7 s and delivering a peak power of 254 W with an η =100%, as depicted in Figure 5.32(a). Under the same operating conditions, injected approximately P=60.61 W into the grid, as depicted in Figure 5.32(b), confirming effective management of surplus power.

The V_{dc} remained stable around its reference value, while the Q exchanged with the grid stayed near was minimal, indicating stable converter operation and effective grid synchronization under these PSC-2.

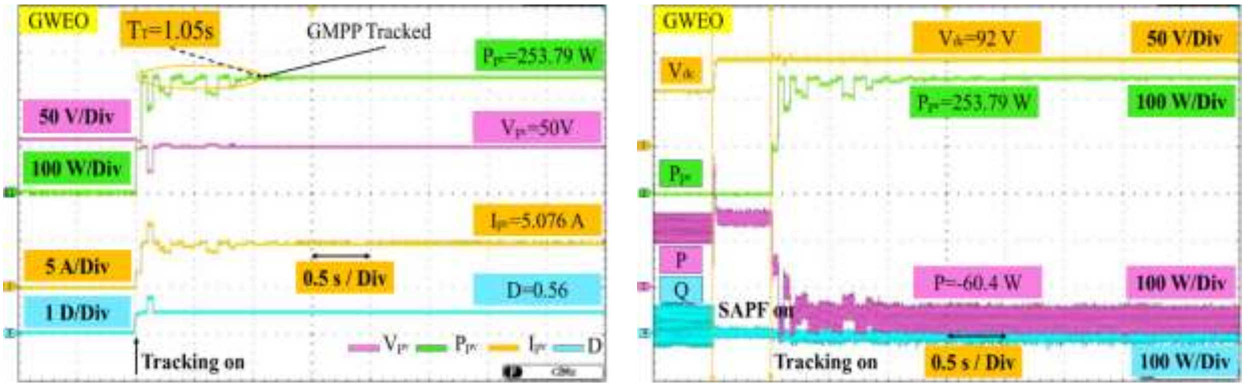

(a) (b)

Figure 5.31: Experimental results of the proposed GWEO method under PSC-3

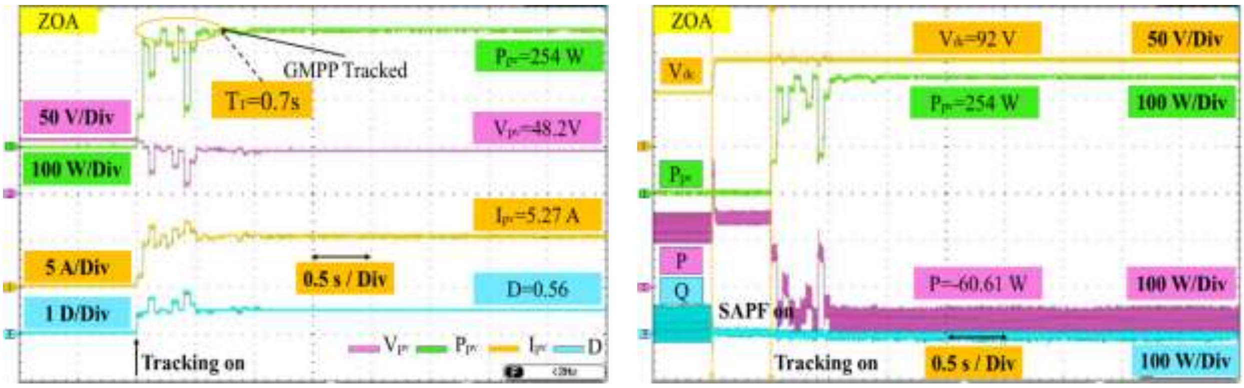

(a) (b)

Figure 5.32: Experimental results of the proposed ZOA method under PSC-3

In the fourth scenario (PSC-4), corresponding to the irradiance pattern summarized in Table 5.2 and illustrated in Figure 5.26(d), the tracking performance of the proposed GWEO and ZOA techniques was evaluated. In this scenario, the GMPP is located approximately midway along the PV curve, with a power level of 120 W.

As shown in Figure 5.33 (a), the GWEO method successfully converged to the GMPP within a T_T=0.85 s, achieving a η=100%. Under this operating condition, the PV system partially supplied the load demand, while the remaining P required by the load was supplied by the grid to maintain power balance. The grid supplied approximately P=27.7 W, as depicted in Figure 5.33 (b).

Similarly, the ZOA technique demonstrated reliable tracking performance, reaching the GMPP within 1 s and delivering a PV power of 119.92 W with an η=99.93%, as shown in Figure 5.34(a). Under the same operating conditions, the grid supplied approximately P=27.78 W to support the total load demand of 150.57 W, as shown in Figure 5.34(b).

The remaining small difference of about 2.79 W is attributed to inherent system losses, including power conversion and filtering effects. This ensured stable system operation under PSC-4.

During PSC-4, the V_{dc} remained close to its reference value, while the Q exchanged with the grid was minimal, indicating stable SAPF operation performance and efficient power management.

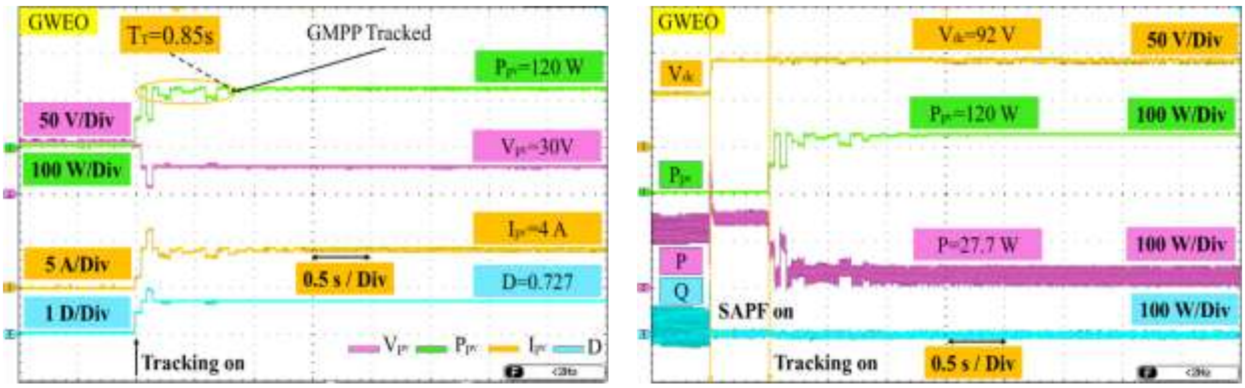

(a) (b)

Figure 5.33: Experimental results of the proposed GWEO method under PSC-4

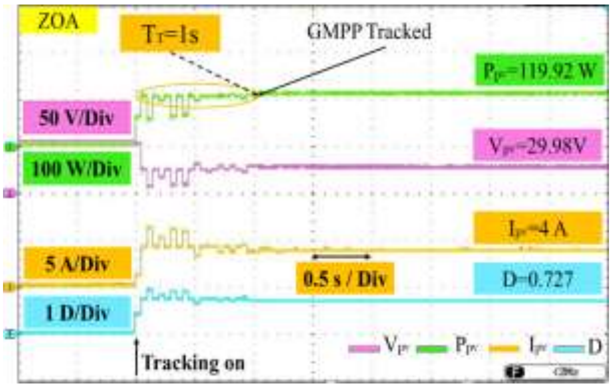

(a)

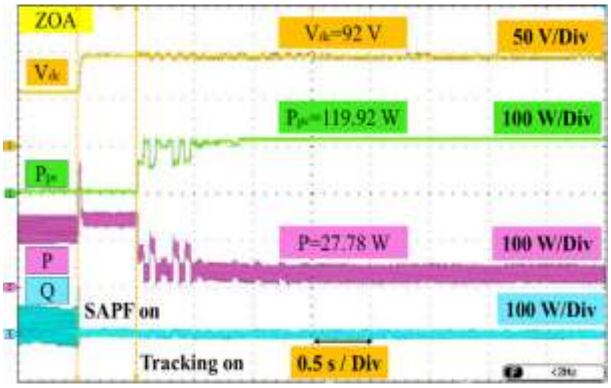

(b)

Figure 5.34: Experimental results of the proposed ZOA method under PSC-4

In the fifth PSC scenario (PSC-5), corresponding to the irradiance profile shown in Table 5.2 and Figure 5.26(f), the performance of the proposed GWEO and ZOA algorithms was assessed under severe shading conditions. Under these conditions, PV system deliver a GMPP=100 W.

As shown in Figure 5.35(a), the GWEO algorithm successfully tracked the GMPP within a T_T=1 s, achieving a η=100%. Since the available PV power was lower than the load demand, the PV system supplied only a portion of the load requirement, while the remaining P was drawn from the grid to maintain power balance. In this case, the grid supplied approximately P=63.62 W, as depicted in Figure 5.35(b). The observed power mismatch is mainly attributed to inherent system losses.

Similarly, the ZOA algorithm exhibited comparable tracking performance, converging to the GMPP within T_T=0.65 s and delivering a similar power level with a η=100%, as depicted in Figure 5.36(a). Under the same operating conditions, the grid supplied approximately P= 63.618 W, as shown in Figure 5.36(b). ensuring stable system operation under PSC-5.

Throughout PSC-5, the V_{dc} accurately tracked its reference, while the Q exchanged with the grid remained minimal. This demonstrates stable SAPF operation and effective PV injection, achieved by the proposed FOPI-AW-ZOA strategy even under severe partial shading conditions.

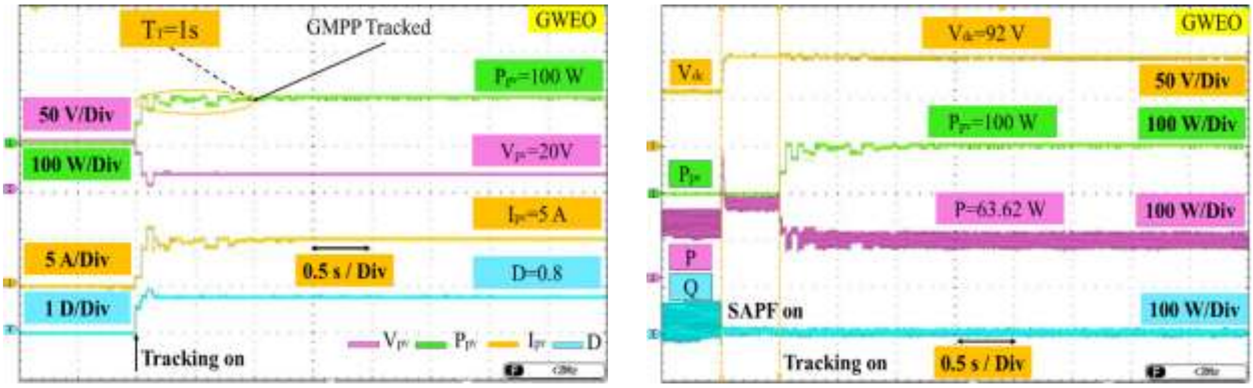

(a) (b)

Figure 5.35: Experimental results of the proposed GWEO method under PSC-5

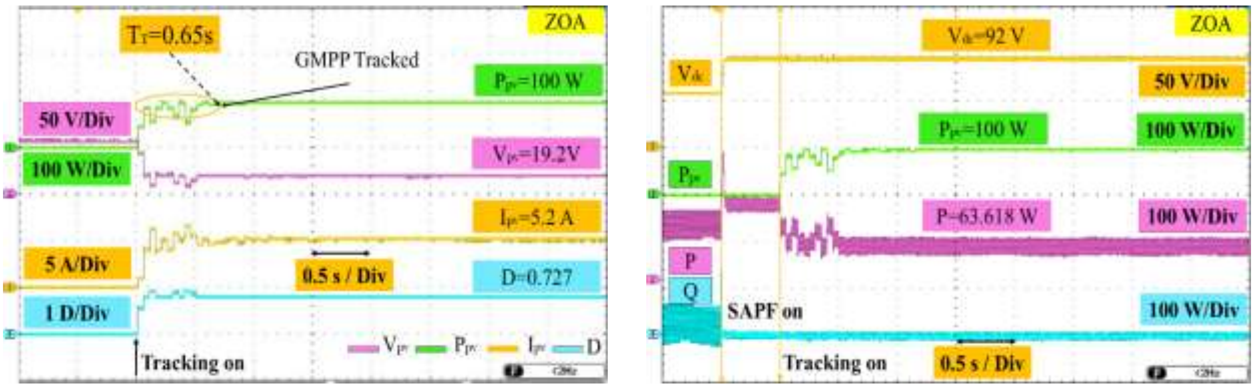

(a) (b)

Figure 5.36: Experimental results of the proposed ZOA method under PSC-5

All results obtained using the proposed GWEO and ZOA methods are summarized in the Table 5.5. The values of the PV system components listed in the Table 5.5 were obtained using PV emulator. The accompanying Figure 5.37 presents a representative example of the PV voltage, PV current, and PV power values. The ZOA algorithm was selected solely for illustrative purposes to demonstrate how the photovoltaic electrical quantities are evaluated and displayed. This example clarifies the procedure adopted to extract and visualize the PV parameters.

Furthermore, system variables can be monitored and recorded in real time via the Control Desk interface during the experimental operation. In addition, electrical quantities related to the SAPF, particularly power quality indicators, are measured using a power analyzer. The corresponding measurements and analyses will be presented and discussed in a subsequent section.

(a)

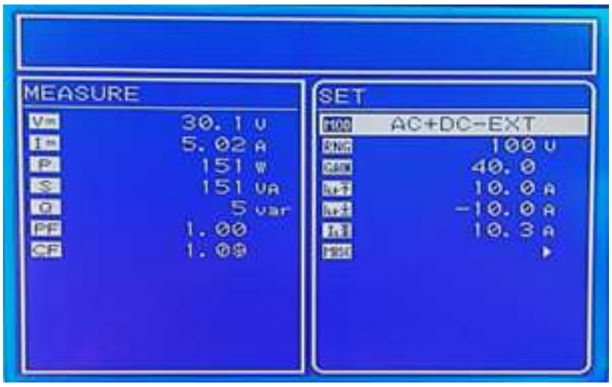

(b)

(c)

(d)

Figure 5.37: Maximum Power Level ($P_{mpp}(W)$), PV voltage ($V_{mpp}(V)$), and PV current ($I_{mpp}(A)$) on PV emulator screen of ZOA MPPT, a) PSC-1, b) PSC-2, c) PSC-3 and d) PSC-5

Table 5.5: Summarizing the experimental results of proposed methods ZOA and GWEO under PSCs

MPPT	PSCs	$V_{mpp}(V)$	$I_{mpp}(A)$	$P_{mpp}(W)$	$P_{\max}(W)$	P	P_{load}	Power loss	T_T (s)	η (%)
GWEO	PSC-1	28.27	4.637	133.17	133.2	33.79	150.57	16.39	1	99.98
	PSC-2	31.53	4.789	150.98	151.1	11.91		12.32	1	99.92
	PSC-3	50	5.076	253.79	254	-60.4		42.82	1.05	99.84
	PSC-4	30	4	120	120	27.7		2.87	0.85	100
	PSC-5	20	5	100	100	63.62		13.048	1	100
ZOA	PSC-1	29.5	4.51	133	133.2	33.96		16.39	1.05	99.85
	PSC-2	30.1	5.02	151	151.1	11.89		12.32	1.1	99.93
	PSC-3	48.2	5.27	254	254	-60.61		42.82	0.7	100
	PSC-4	29.98	4	119.92	120	27.78		2.87	1	99.93
	PSC-5	19.2	5.2	100	100	63.62		13.048	0.65	100

The results presented in Figure 5.38 provide a comprehensive comparative analysis of the key performance metrics, namely η and T_T, for the evaluated MPPT algorithms under PSCs.

As illustrated in Figure 5.38(a), both GWEO and ZOA exhibit high η across all PSCs (PSC-1 to PSC-5). However, the GWEO technique generally achieves slightly higher or comparable efficiency levels, indicating its strong capability to accurately track the GMPP and maximize energy extraction. Minor variations observed under certain PSCs reflect the sensitivity of the algorithms to shading patterns.

In terms of T_T, shown in Figure 5.38(b), noticeable differences can be observed between the two methods. The ZOA algorithm demonstrates faster convergence in several scenarios, highlighting its advantage in terms of rapid response and reduced tracking duration. On the other hand, GWEO maintains stable tracking performance with competitive convergence times, ensuring reliable operation without excessive delay.

Overall, this comparison highlights the trade-off between convergence speed and tracking accuracy. While ZOA offers faster tracking in some cases, GWEO provides superior or comparable efficiency, making both algorithms suitable for MPPT applications, depending on the priority between speed and energy harvesting performance.

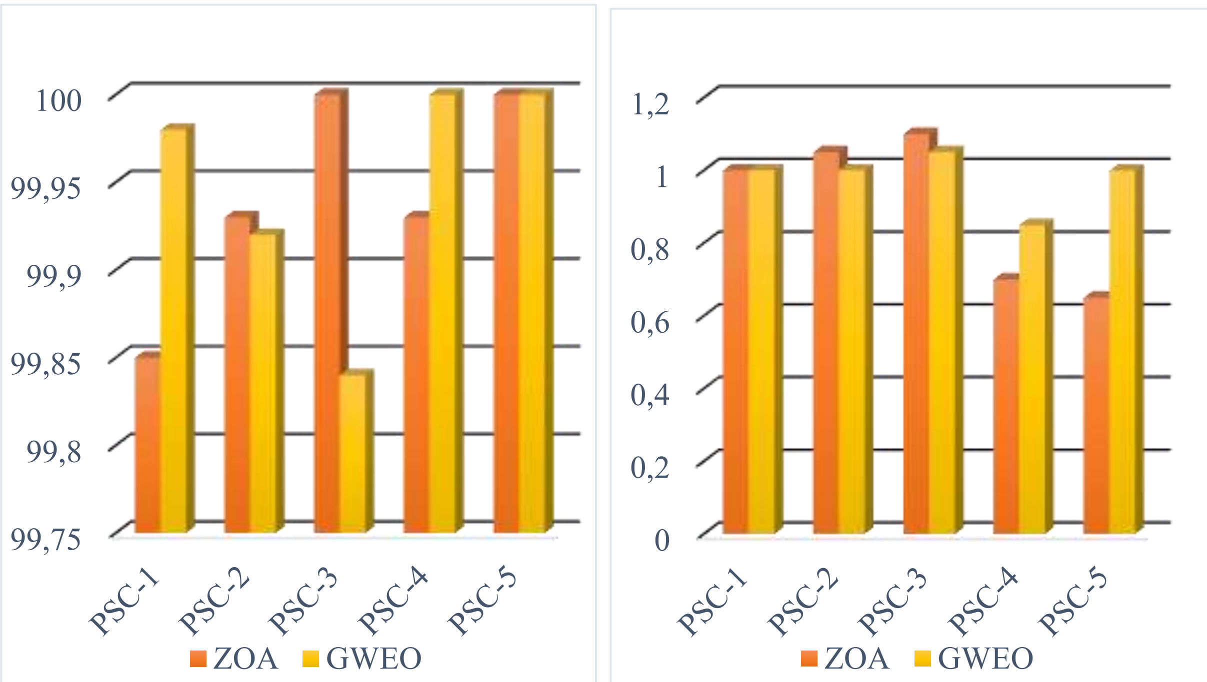

(a) (b)

Figure 5.38: Comparative performance analysis of the proposed GWEO and ZOA techniques under PSCs in terms of: a) η, and b) T_T

5.7.4 Experimental results under DSCs scenario of proposed methods

To further evaluate the robustness of the proposed GWEO and ZOA techniques under DSCs, additional experiments were conducted involving a transition between two PSC scenarios, namely PSC-3 and PSC-1, as illustrated in Figures 5.39 and 5.40. The shading pattern was intentionally changed after 6 s, allowing sufficient time to capture both the transient and steady-state responses of the algorithms in each scenario.

As shown in Figure 5.39(a) for the ZOA method, the algorithm successfully tracks the GMPP after the shading transition. The recorded T_T =0.95 s during the initial tracking phase and T_T=1.59 s following the re-initialization process, indicating fast convergence and effective adaptation to irradiance variations.

Similarly, Figure 5.40(a) demonstrates the performance of the GWEO technique under the same dynamic conditions. The GWEO algorithm also achieves accurate GMPP tracking, with a T_T =0.95 s during the first operating stage and a T_T =1.87 s after the shading change, confirming its robustness despite a slightly longer convergence time compared to ZOA.

From Figures 5.39(b) and 5.40(b), it can be observed that when the SAPF is activated, the V_{dc} remains well-regulated around 92 V, ensuring stable system operation. Furthermore, during PV injection, the V_{dc} stabilizes rapidly after activation, indicating a fast dynamic response and efficient energy regulation, even under changes in the irradiance pattern. In addition, the Q is effectively compensated and maintained close to minimum, while the P follows the available PV power, confirming proper grid interaction and power quality enhancement.

The experimental results confirm that both ZOA and GWEO algorithms can reliably track the GMPP under DSC conditions. ZOA provides faster convergence, while GWEO offers stable and accurate tracking, making both suitable for real-time GCPV applications.

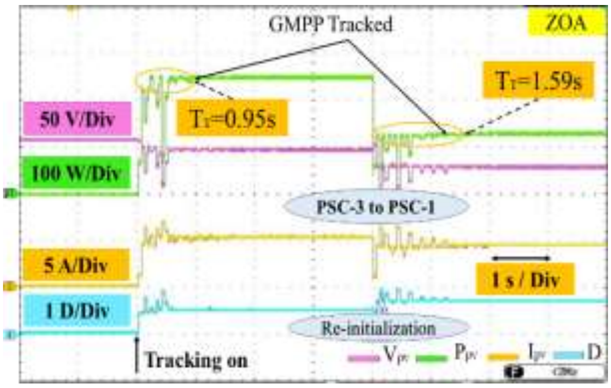

(a)

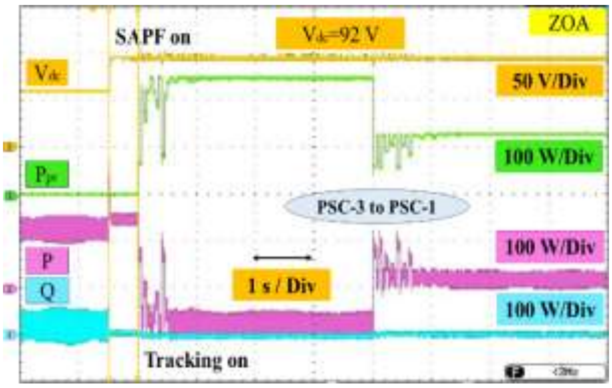

(b)

Figure 5.39: Experimental results of the proposed ZOA method under DSC

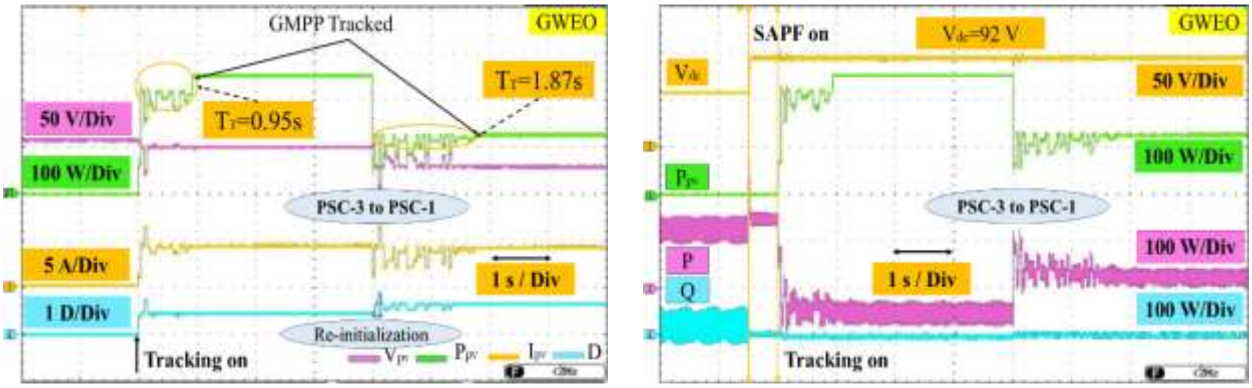

(a) (b)

Figure 5.40: Experimental results of the proposed GWEO method under DSC

5.7.5 Experimental evaluation of the proposed methods under PSC-STC transitions

To further assess the dynamic performance of the proposed GWEO and ZOA algorithms, additional experiments were carried out to investigate the system response during a transition from PSC-4 to STC, as illustrated in Figures 5.41 and 5.42. The irradiance profile was intentionally changed after a predefined time interval to allow observation of both the transient and steady-state behaviors of the MPPT techniques.

As shown in Figure 5.41(a), the ZOA algorithm successfully re-tracks the MPP following the transition from PSC-4 to STC. After re-initialization, the algorithm converges toward the new operating point with a recorded $T_T = 1.42$ s, demonstrating effective adaptation to sudden irradiance variations.

Similarly, Figure 5.42(a) presents the experimental response of the GWEO method under the same transition. The GWEO algorithm accurately identifies the MPP after the system returns to STC, achieving a tracking time of about $T_T = 0.76$ s, which is faster than that of ZOA. The tracking process remains stable and free of oscillations.

From Figures 5.41(b) and 5.42(b), it can be observed that once the SAPF is activated, the V_{dc} is well regulated around its reference value of 92 V, ensuring stable operation of the power conversion stage. In addition, the Q is effectively compensated and maintained close to minimum, while the P smoothly increases to its nominal value under STC, confirming proper grid synchronization and efficient power flow control.

Overall, these experimental results confirm that both ZOA and GWEO algorithms are capable of reliable and accurate GMPP tracking during a dynamic transition from PSC-4 to STC. While the GWEO method exhibits faster convergence, the ZOA approach maintains stable tracking performance, highlighting the robustness and real-time applicability of both techniques in grid-connected photovoltaic systems.

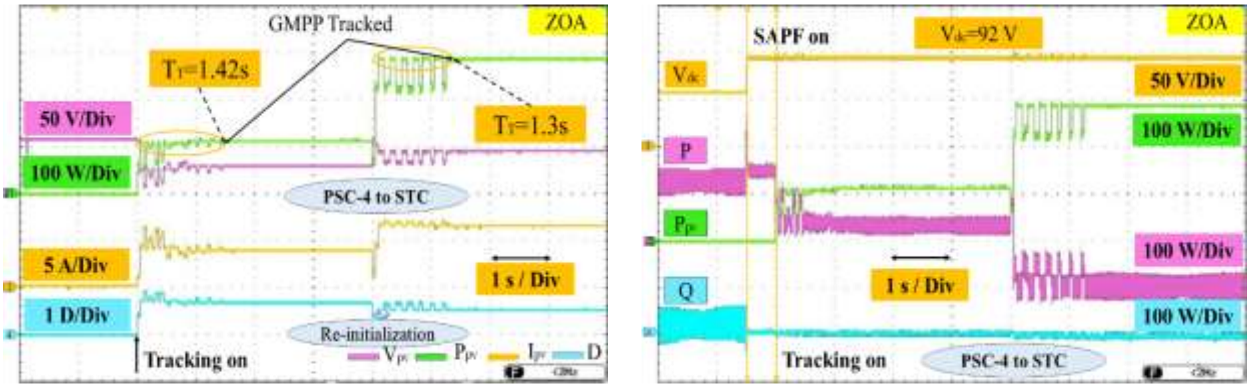

(a) (b)

Figure 5.41: Experimental results of the proposed ZOA method under PSC-4-STC transition

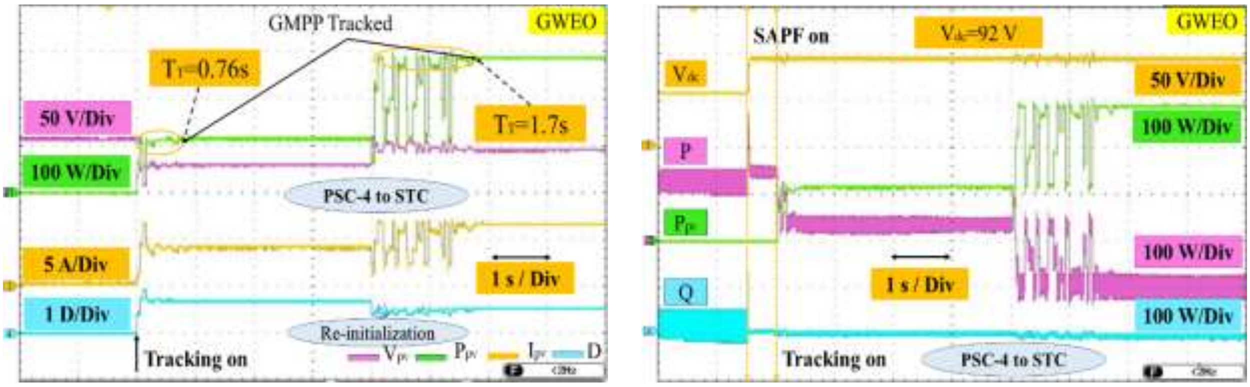

(a) (b)

Figure 5.42: Experimental results of the proposed GWEO method under PSC-4-STC transition

5.7.6 Comparative experimental results of MPPT algorithms under STC

MOAs play a vital role in accurately tracking the GMPP in GCPV-SQPF systems. To further validate the effectiveness of the proposed methods, a comparative experimental study was conducted under STC. The proposed algorithms were benchmarked against well-established MPPT techniques, including GWO, WOA, PSO, and FPA, under identical experimental conditions.

All algorithms were implemented using the same system parameters, control structure, and operating conditions to ensure a fair and consistent comparison. Figures 43–46 present the experimental results, illustrating the dynamic responses of each MPPT technique. In addition, all key electrical parameters of the PV system and the grid, including P, Q, V_{dc}, P_{pv}, I_{pv}, V_{pv}, and D, were continuously monitored, as previously described.

This comparative evaluation highlights the superior tracking MPP performance and operational stability of the proposed methods compared with conventional and state-of-the-art MPPT algorithms under STC.

Based on the experimental results presented in Figures 43–46, it can be observed that the GWO, WOA, PSO, and FPA algorithms are capable of tracking the MPP under STC. Under these conditions, the PV system generates sufficient power to fully satisfy the three-phase load demand, while the excess generated power is injected into the utility grid.

For the GWO method (Figure 5.43), the MPP is reached within a T_T =1.6 s, with a η =98.94%. After supplying the load, an excess P =-94.4 W is injected into the grid. At the same time, internal system power losses of about 44.4 W are observed.

In the case of the WOA algorithm (Figure 5.44), a T_T =1.75 s is achieved with a η =99.12%. Once the load is fully supplied, a surplus P= -94.8 W is injected into the grid, while comparable internal power losses are recorded, reflecting a slower stabilization of the optimization process.

As shown in Figure 5.45, the PSO algorithm achieves a fast tracking performance with a T_T = 1.1 s and a η =98.90%. Moreover, the surplus PV power is effectively injected into the grid, reaching approximately P=-94.25W, which confirms proper energy management and grid support under STC.

Finally, the FPA method (Figure 5.46) reaches the MPP in 1.9 s, with a η =98.99%. The surplus power injected into the grid is approximately P=-94.55 W.

It is worth noting that, in addition to the proposed methods, the comparative MPPT algorithms also ensure stable V_{dc} and maintain the Q exchanged with the grid close to minimum. This behavior is observed during both SAPF activation and PV injection modes. However, the superior stability, faster settling, and enhanced robustness of V_{dc} regulation are primarily attributed to the proposed P-DPC strategy combined with the optimized FOPI-AW-ZOA controller, which guarantees effective Q compensation and stable system operation under STC.

It should be noted that all quantitative results corresponding to the compared methods are comprehensively summarized and discussed in Table 5.6.

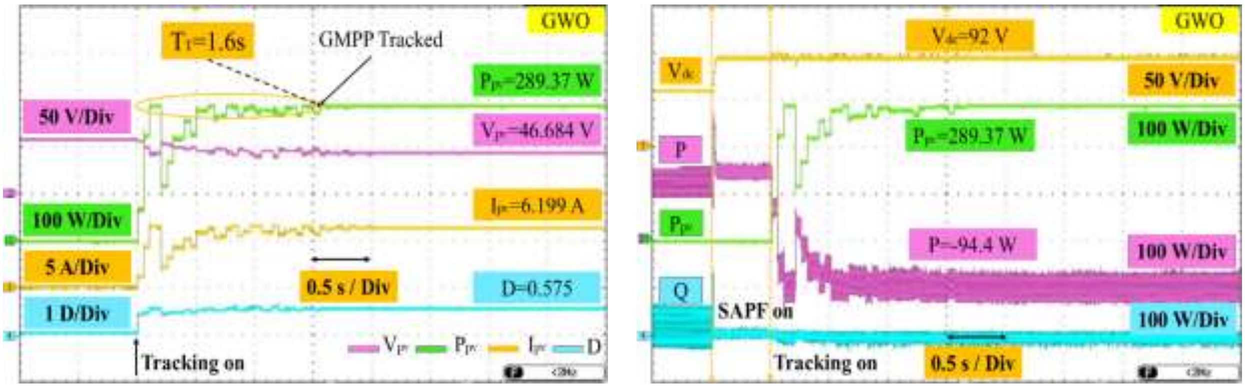

(a) (b)

Figure 5.43: Experimental results of the proposed GWO method under STC

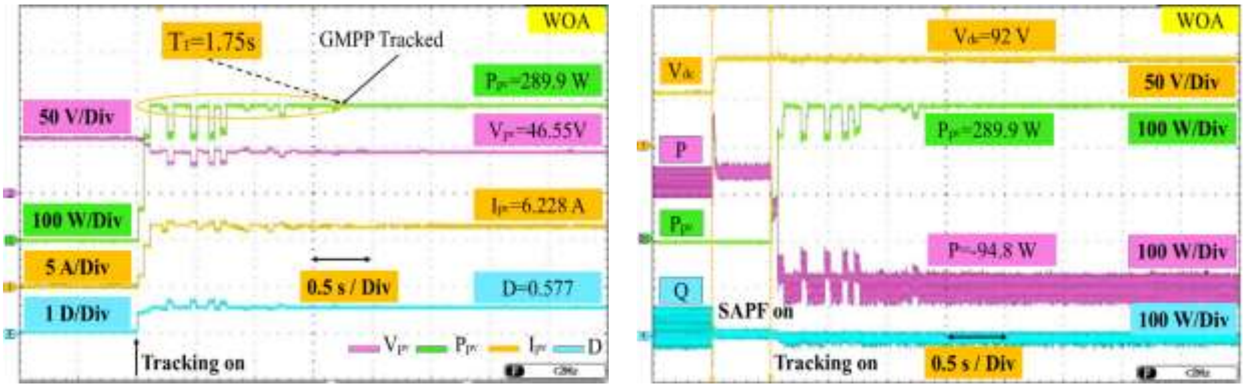

(a) (b)

Figure 5.44: Experimental results of the proposed WOA method under STC

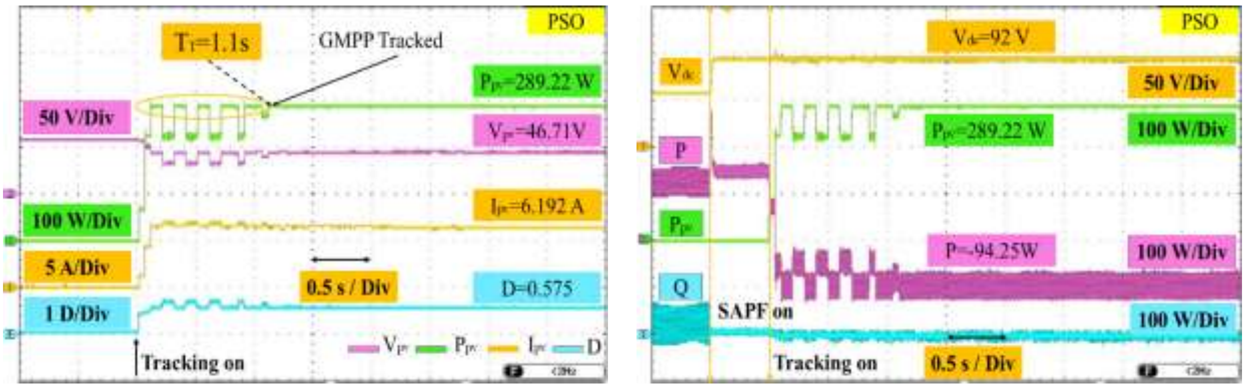

(a) (b)

Figure 5.45: Experimental results of the proposed PSO method under STC

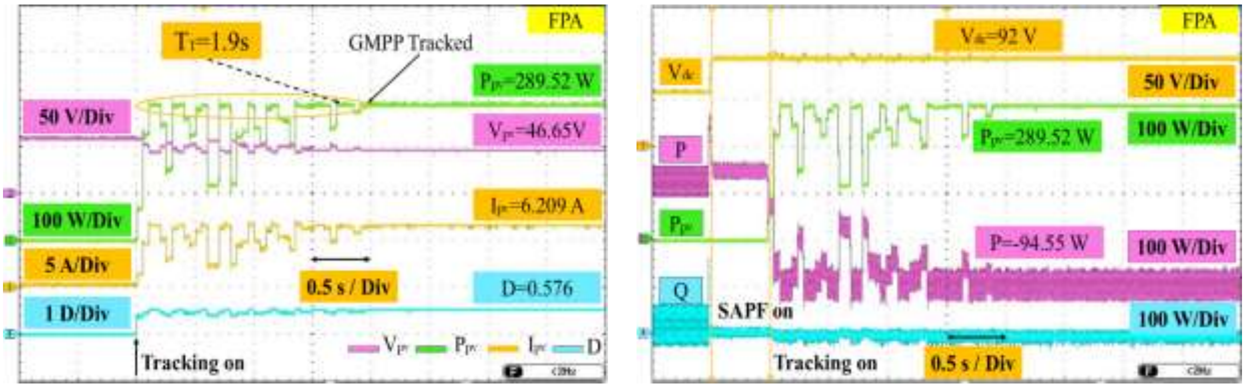

(a) (b)

Figure 5.46: Experimental results of the proposed FPA method under STC

Table 5.6. Comparative performance of MPPT algorithms under STC

MPPT	$V_{mpp}(V)$	$I_{mpp}(A)$	$P_{mpp}(W)$	$P_{\max}(W)$	P	P_{load}	Power loses	T_T (s)	η (%)
GWO	46.684	6.199	289.37		-94.4			1.6	98.94
WOA	46.55	6.228	289.9	292.47	-94.8	150.57	44.4	1.75	99.12
PSO	46.71	6.192	289.22		-94.25			1.1	98.90
FPA	46.65	6.209	289.52		-94.55			1.9	98.99

The results illustrated in Figure 5.47 present a comparative evaluation of the proposed and benchmark MPPT algorithms in terms of η and T_T.

As shown in Figure 5.47(a), the GWEO algorithm achieves the highest η among all compared methods, exceeding 99.96%, which highlights its strong capability to accurately locate the MPP. The ZOA and WOA techniques also demonstrate high efficiency levels, closely following GWEO. In contrast, GWO, PSO, and FPA exhibit slightly lower efficiencies, indicating comparatively reduced energy extraction performance under the same operating conditions.

Regarding T_T, depicted in Figure 5.47(b), noticeable differences are observed among the evaluated algorithms. The GWEO method achieves the shortest T_T, demonstrating the fastest convergence toward the GMPP. The ZOA and PSO algorithms present competitive response times, while WOA, GWO, and FPA require longer tracking durations, reflecting slower convergence behavior.

Overall, the bar-chart-based comparison confirms that GWEO offers the best compromise between high η and fast convergence speed. Although algorithms provide satisfactory performance, GWEO clearly outperforms the benchmark methods, emphasizing its effectiveness and suitability for real-time MPPT implementation in GCPV systems.

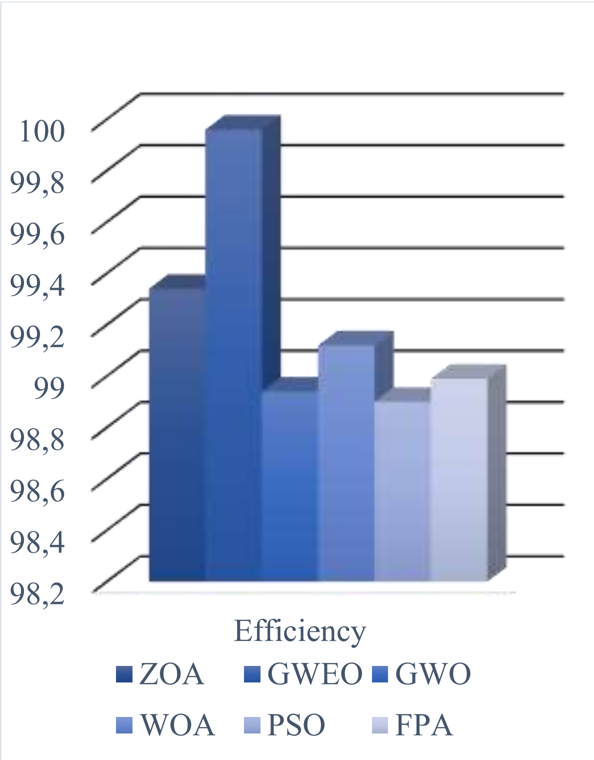

a)

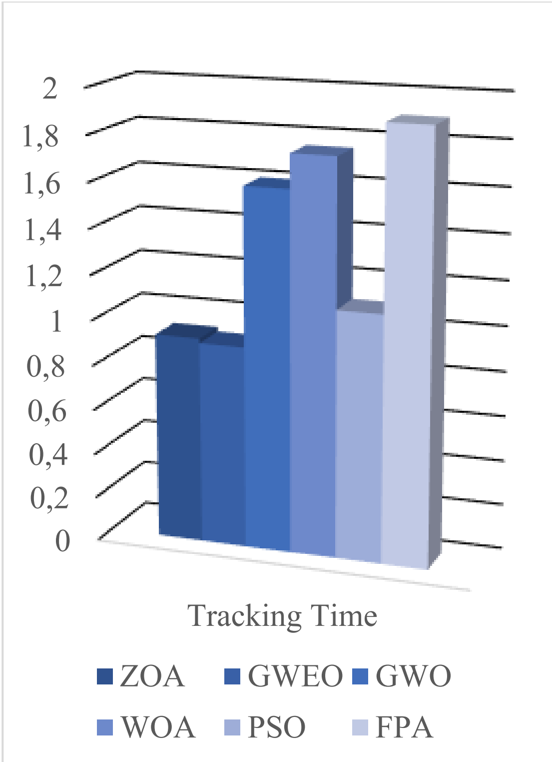

b)

Figure 5.47: Comparative performance analysis of MPPT algorithms under STCs in terms of: a) η , and b) T_T

5.7.7 Comparative experimental results of MPPT algorithms under PSC

Following the evaluation of the proposed MPPT strategies under PDCs, this section presents a comparative experimental analysis of conventional and state-of-the-art MPPT algorithms conducted under identical operating scenarios. The comparison focuses on the tracking performance and the extracted power during both SAPF activation and PV injection. To ensure a fair assessment, the same partial shading patterns are applied, and the dynamic responses of the different algorithms are examined sequentially under these conditions.

Under PSC-1, the available PV power at the GMPP (133.2 W) is lower than the three-phase load demand (150.57 W). As a result, the PV system cannot fully satisfy the load, and the remaining power deficit is supplied by the utility grid, with additional internal system losses. This operating behavior has already been discussed earlier.

For the GWO algorithm (Figure 5.48), the GMPP is tracked with a T_T =1.8 s and a η =99.60%. The extracted PV power reaches approximately 132.68 W, supplying part of the load demand, while the remaining load requirement is supported by the grid, with a P= 34.28 W.

The WOA method exhibits slightly improved dynamic performance (Figure 5.49), achieving a shorter T_T =1.325 s and a higher η=99.75%. The extracted PV power closely approaches the GMPP, reaching approximately 132.88 W, while the remaining demand is supplied by the grid with a P=34.14 W. These results indicate faster stabilization of the operating point compared to the GWO algorithm.

In the case of the PSO algorithm (Figure 5.50), the GMPP is reached in 1.65 s, with a η =99.52%. The extracted PV power amounts to approximately 132.56 W, which is slightly lower than that obtained using the GWO and WOA methods, while the grid supplies a P=34.403 W. Although PSO demonstrates acceptable tracking accuracy, its convergence speed remains inferior to that of WOA under PSC-1.

The FPA algorithm exhibits the weakest performance under this operating scenario (Figure 5.51). It records the longest T_T=1.95 s and the lowest η =97.22% among the compared methods. Consequently, the extracted PV power decreases to approximately 129.5 W, resulting in a P demand of about 37.46 W from the grid and increased reliance on grid support. This behavior reflects reduced optimization stability and inferior convergence characteristics under PSC-1.

Overall, the results indicate that although all the compared methods are capable of meeting the load demand under PSC-1. In contrast, the compared methods exhibit lower η and longer T_T, indicating inferior optimization performance under the same operating conditions. This behavior further highlights the superior performance of the proposed methods, as discussed previously.

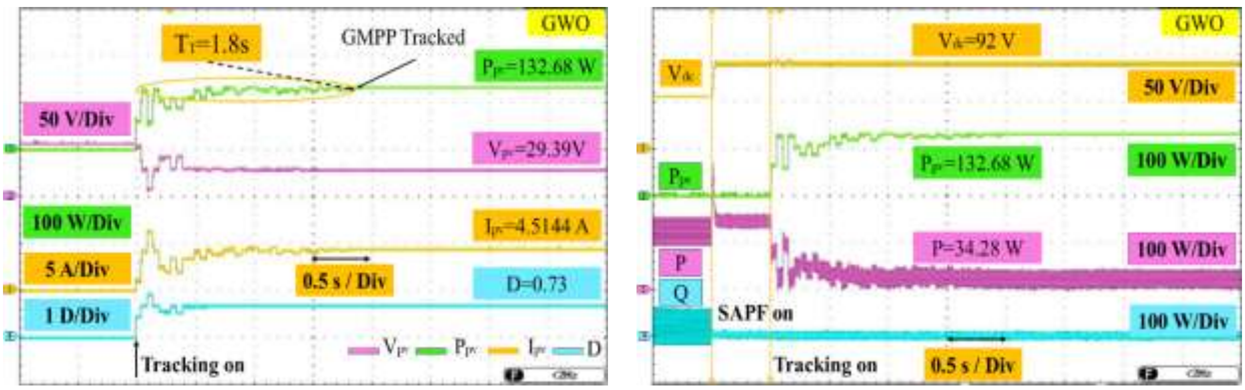

(a) (b)

Figure 5.48: Experimental results of the proposed GWO method under PSC-1

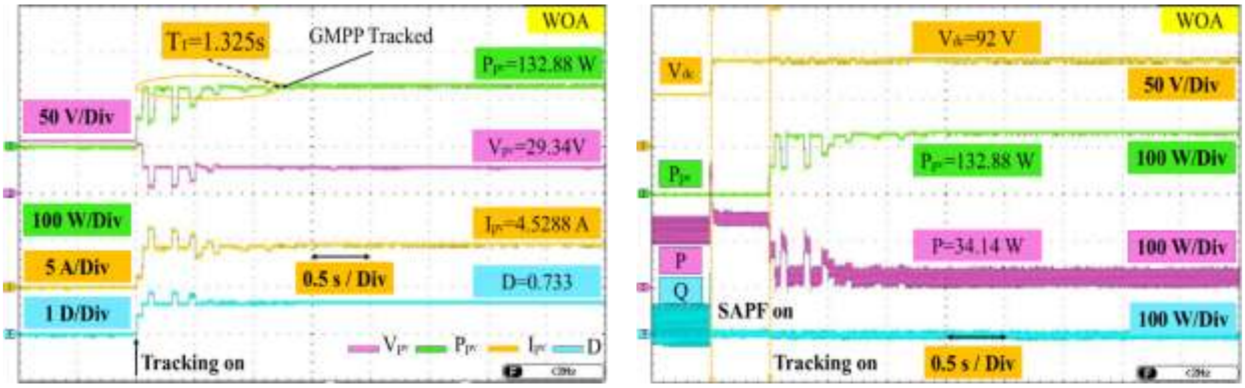

(a) (b)

Figure 5.49: Experimental results of the proposed WOA method under PSC-1

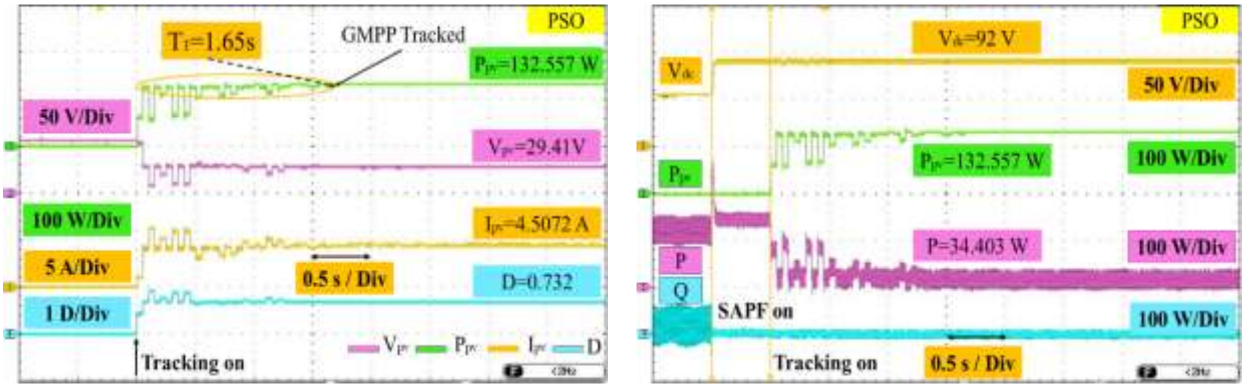

(a) (b)

Figure 5.50: Experimental results of the proposed PSO method under PSC-1

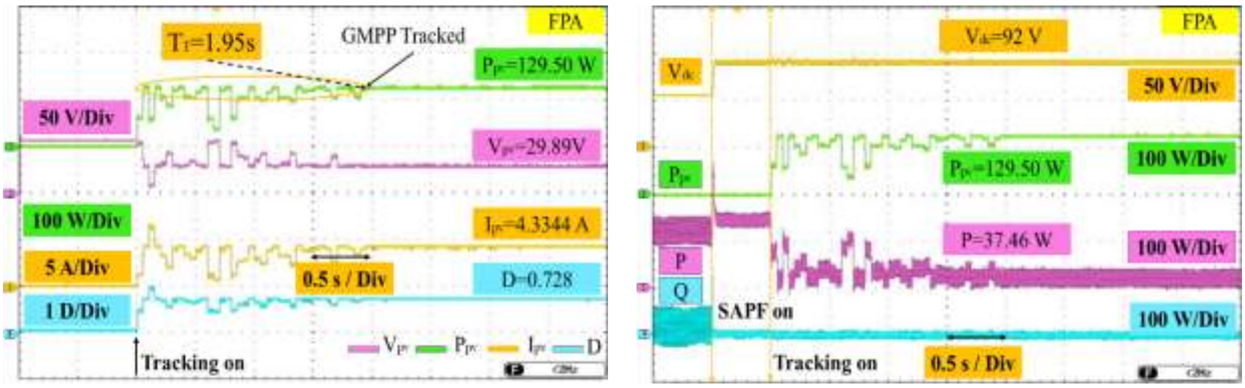

(a) (b)

Figure 5.51: Experimental results of the proposed FPA method under PSC-1

Under PSC-2, the PV system operates at a GMPP of approximately 151.1 W, which is very close to the three-phase load demand of 150.57 W. Consequently, the PV system is able to almost fully supply the load, with only a very small power mismatch attributed to inherent system losses, as previously mentioned.

For the GWO algorithm (Figure 5.52), the GMPP is reached within a T_T=1.8 s, achieving a η=99.34%. The extracted PV power is approximately 150.1 W, which nearly satisfies the load demand, while the grid supplies a P=12.79 W.

The WOA method exhibits improved performance (Figure 5.53), converging to the GMPP within T_T=1.25 s with a η=99.91%. The extracted PV power reaches 150.96 W, which closely matches the theoretical GMPP. The remaining load demand is supported by the grid with a P= 11.93 W, indicating efficient power sharing and stable system operation.

In the case of the PSO algorithm (Figure 5.54), the T_T =1.3 s, while η=96.65%. The extracted PV power is 148.65 W, which is noticeably lower than the GMPP. This deviation from the optimal operating point results in a higher P demand of 14.25 W from the grid, indicating less effective tracking performance and increased sensitivity to PSC-2.

In this scenario, the FPA algorithm demonstrates the poorest performance (Figure 5.55). It exhibits the longest T_T =1.95 s and achieves the lowest η=94.54%. The extracted PV power drops substantially to 142.86 W, resulting in a P = 20.03 W, which increases the mismatch with the load and raises internal system losses. This behavior underscores the limited robustness of the FPA algorithm under PSC-2. The remaining power mismatch is minimal and is mainly attributed to system losses, estimated at about 12.32 W. Overall, under PSC-2, GWO and WOA demonstrate superior tracking accuracy and stability, successfully extracting power very close to the GMPP and nearly satisfying the load demand. In contrast, PSO and FPA suffer from reduced efficiency and larger deviations from the optimal operating point, confirming the advantage of more robust optimization strategies under PSC-2.

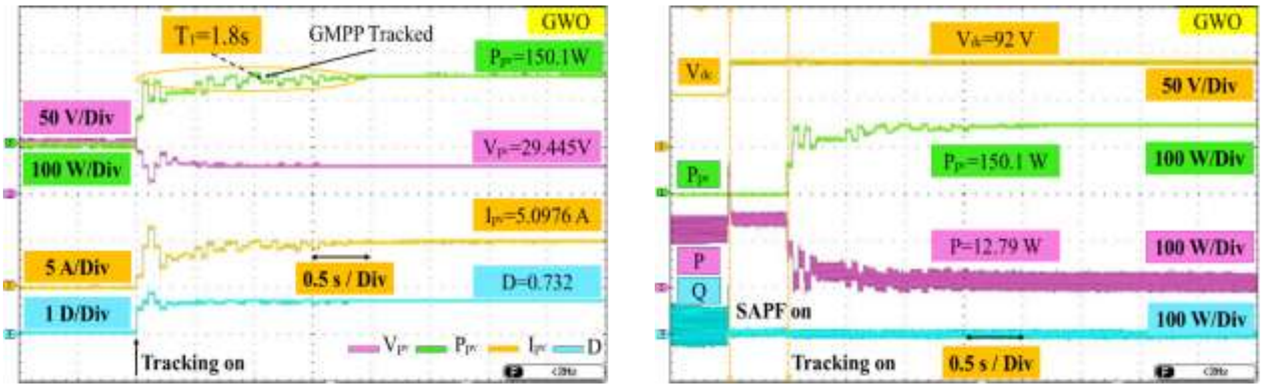

(a) (b)

Figure 5.52: Experimental results of the proposed GWO method under PSC-2

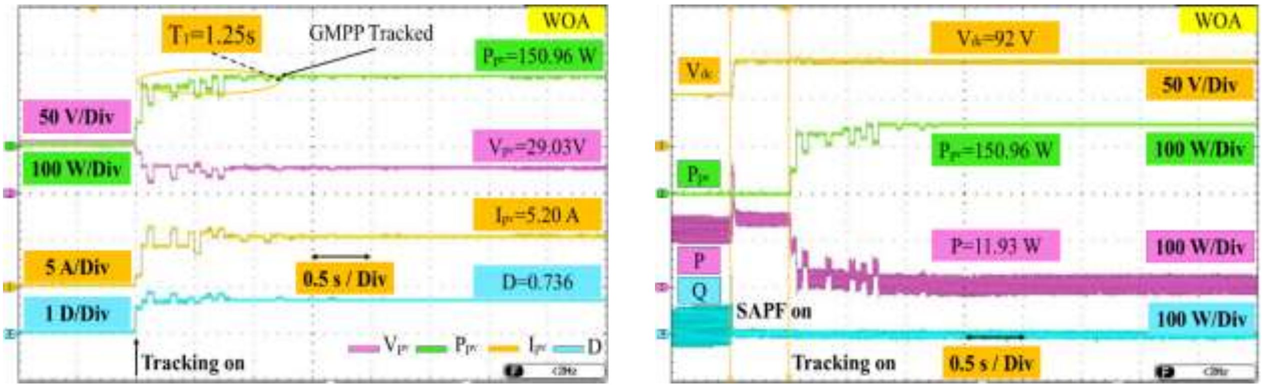

(a) (b)

Figure 5.53: Experimental results of the proposed WOA method under PSC-2

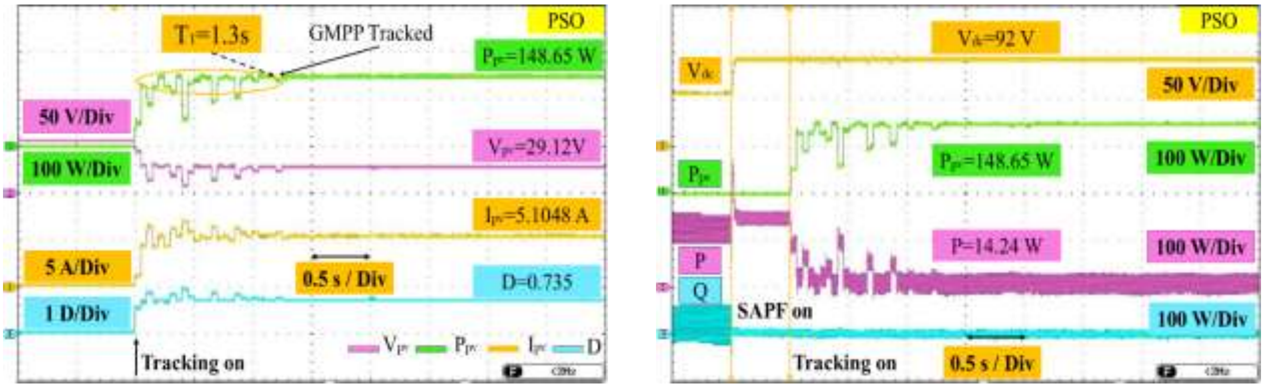

(a) (b)

Figure 5.54: Experimental results of the proposed PSO method under PSC-2

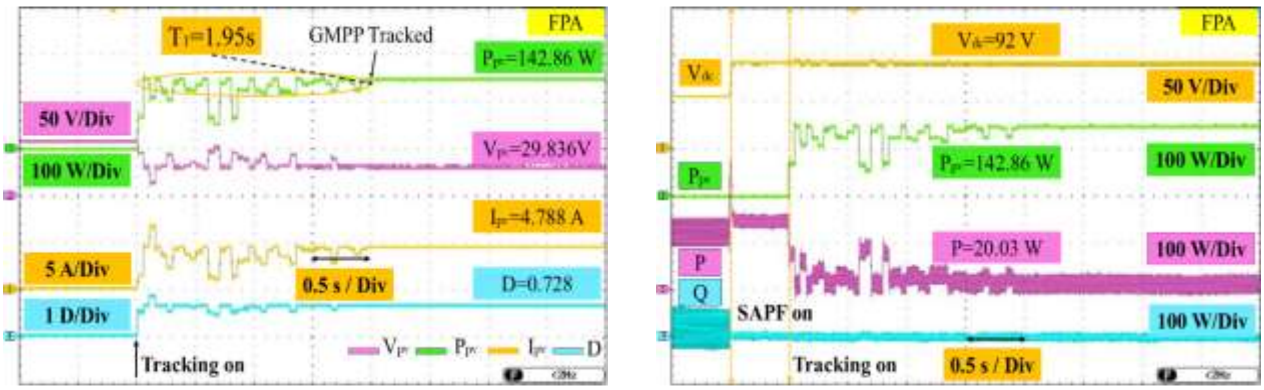

(a) (b)

Figure 5.55: Experimental results of the proposed FPA method under PSC-2

Under PSC-3, the PV system operates at a high GMPP of approximately 254.2 W, which is significantly higher than the load demand (150.57 W). Consequently, the PV array is capable of fully supplying the load, while the excess generated power is injected into the utility grid.

With the GWO algorithm (Figure 5.56), the PV system produces approximately 253 W, achieving a T_T=1.6 s and a η=99.60%. The system operates stably, delivering a noticeable surplus power to the grid (P= -59.61 W).

The WOA method achieves comparable performance (Figure 5.57), extracting around 251.24 W with a T_T =1.35 s and a η=98.91%. The system operates stably, delivering a noticeable surplus power to the grid (P=-57.849 W), although the extracted power is slightly lower than that of GWO.

For PSO (Figure 5.58), the extracted power decreases to approximately 249.82 W, with a T_T =1.3 s and a η=98.35%. The system exhibits larger oscillations around the optimal operating point, resulting in increased power deviation and slightly reduced efficiency under this complex shading condition, while delivering a noticeable surplus power to the grid of 56.43 W.

The FPA algorithm presents the weakest performance under PSC-3 (Figure 5.59). It records the longest T_T=1.95 s and the lowest η=96.61%, extracting only 245.4 W. This pronounced deviation from the GMPP leads to inefficient utilization of the available solar energy, with a surplus power of approximately $P = -52.01$ W injected into the grid.

In summary, under PSC-3, all comparative methods are capable of tracking the GMPP; however, GWO and WOA demonstrate superior robustness and accuracy, achieving higher extracted power and better efficiency. In contrast, PSO and FPA suffer from increased deviations and losses, highlighting their reduced effectiveness under complex partial shading conditions.

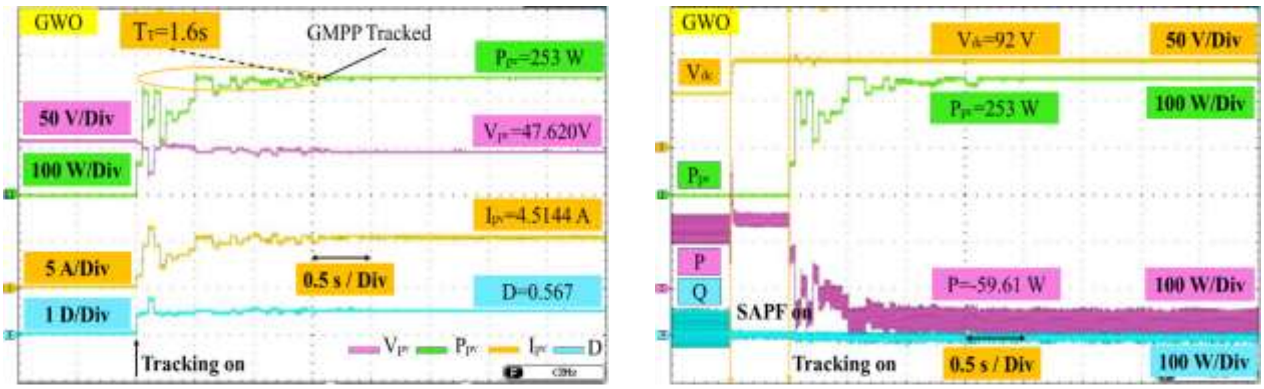

(a) (b)

Figure 5.56: Experimental results of the proposed GWO method under PSC-3

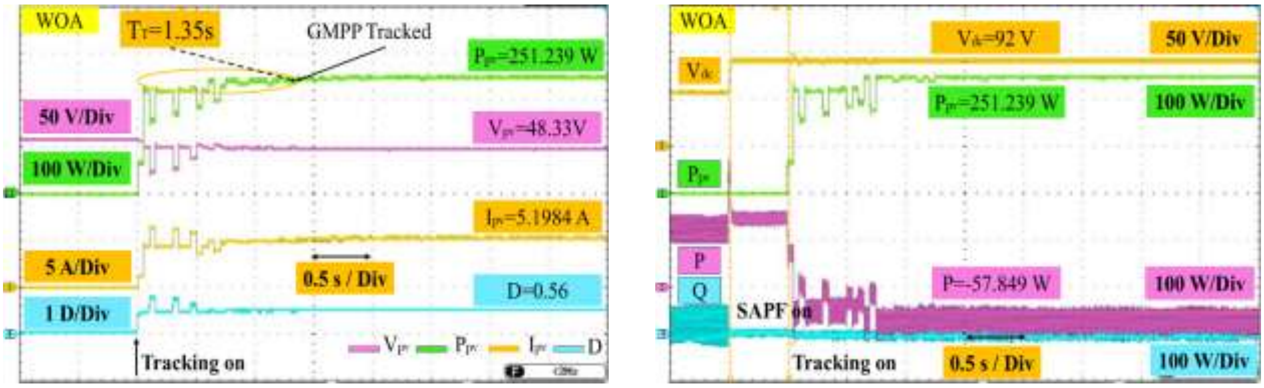

(a) (b)

Figure 5.57: Experimental results of the proposed WOA method under PSC-3

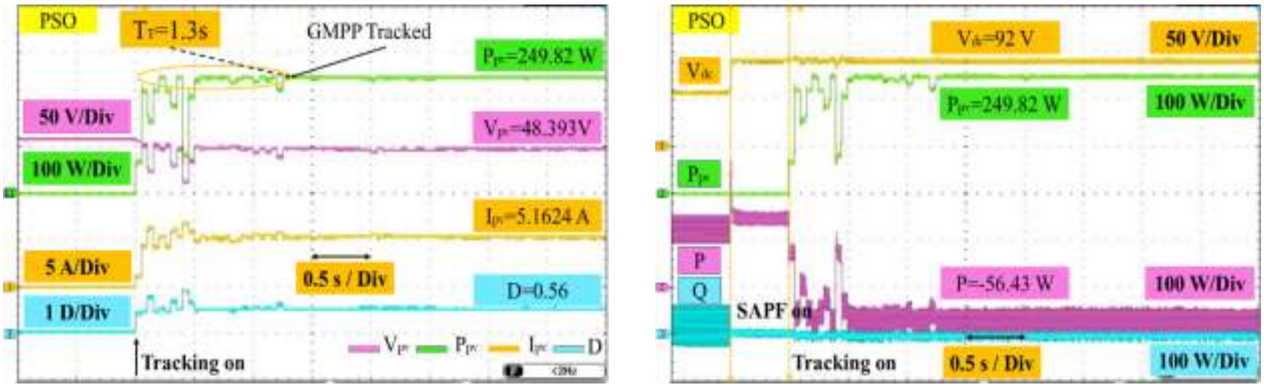

(a) (b)

Figure 5.58: Experimental results of the proposed PSO method under PSC-3

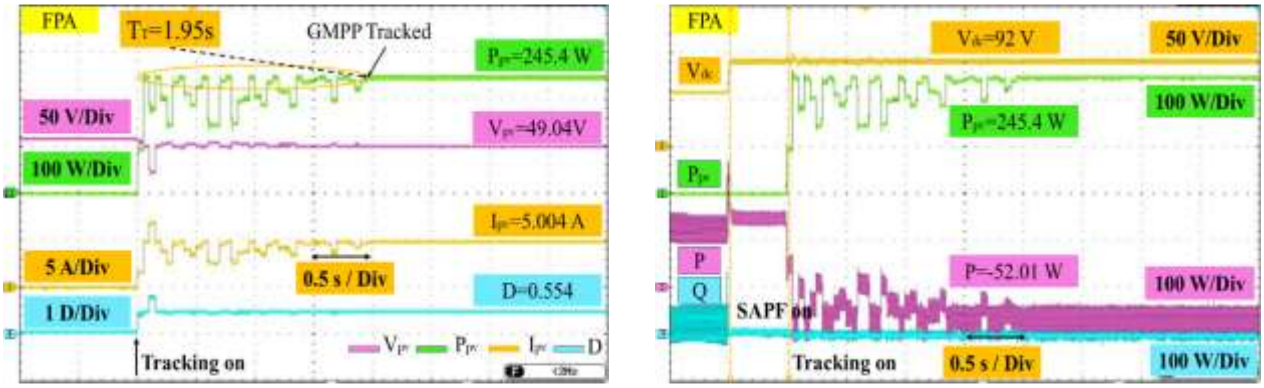

(a) (b)

Figure 5.59: Experimental results of the proposed FPA method under PSC-3

Under PSC-4, the PV system operates at a GMPP of approximately 120 W, which is lower than the load demand (150.57 W). Therefore, the PV array supplies only part of the required load power, while the remaining demand is covered by the utility grid.

For the GWO algorithm (Figure 5.60), the PV system provides 119.6 W and the grid contributes P=28.1 W under this shading scenario. However, since the P_{load} =150.57 W, the supplied power is still insufficient to fully meet the load. The T_T=1.1 s, with a high η = 99.80%, indicating good convergence and stable operation.

For the WOA algorithm (Figure 5.61), the PV system provides 117.71 W, and the grid supplies P=29.99 W under this shading scenario. However, with a P_{load} =150.57 W, the supplied power is still insufficient to fully meet the load. The T_T = 0.93 s, with a high η =99.69%, and the system exhibits a slightly faster dynamic response than GWO, despite the marginally lower PV.

For the PSO algorithm (Figure 5.62), the PV system delivers approximately 117.91 W, while the grid provides P=29.79 W under this shading scenario. With a P_{load} =150.57 W, the combined supply is still insufficient to fully meet the load. The T_T = 1.7 s, with a η =99.61%, and the slower convergence leads to noticeable oscillations during the transient phase.

The FPA algorithm extracts approximately 118.88 W with a T_T=1.5 s and a η =93.73%. The system draws P=28.82 W from the grid to partially meet the load, yet the total supply is still insufficient to fully satisfy the demand (Figure 5.63).

Overall, under PSC-4, all comparative algorithms are able to supply a significant portion of the load, but none fully meet the total demand due to the limited PV output. Tracking times and efficiencies vary among the methods, with minor differences in dynamic response and internal losses. The grid provides the remaining power to partially cover the deficit, highlighting the importance of hybrid operation under moderate PSC-4.

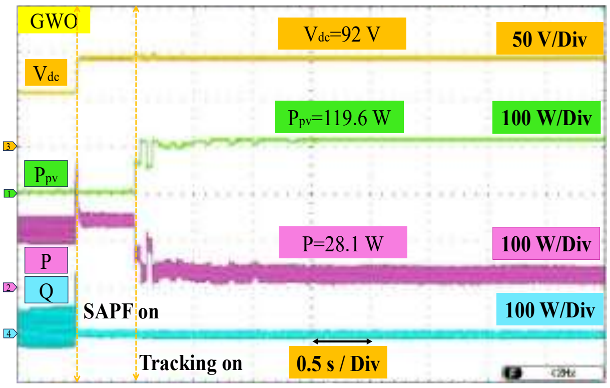

(a)

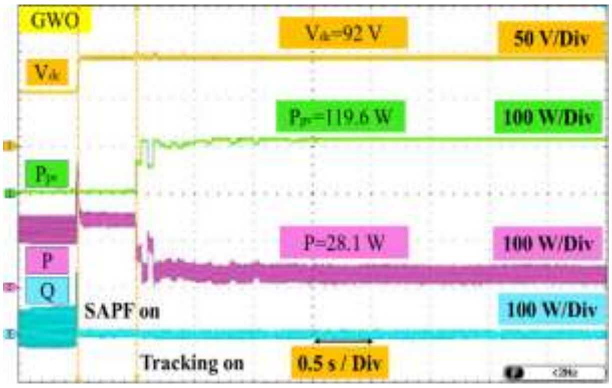

(b)

Figure 5.60: Experimental results of the proposed GWO method under PSC-4

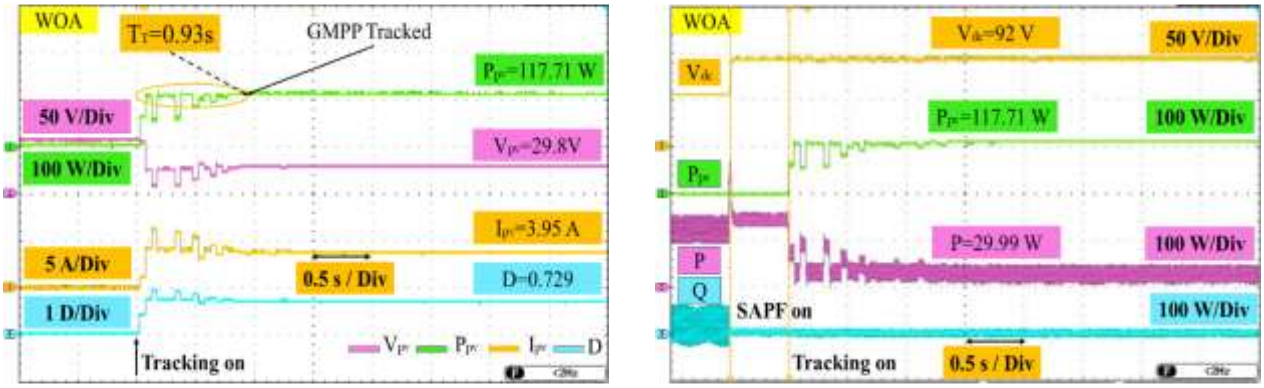

(a) (b)

Figure 5.61: Experimental results of the proposed WOA method under PSC-4

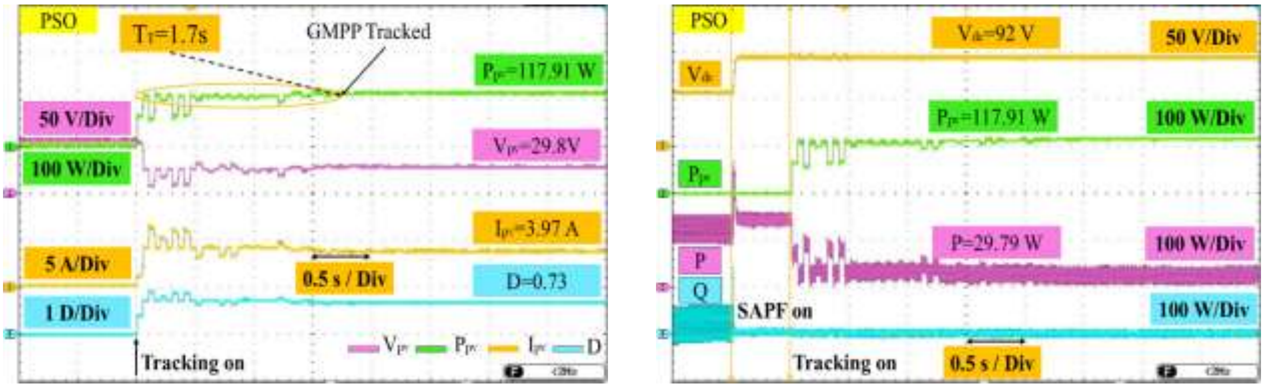

(a) (b)

Figure 5.62: Experimental results of the proposed PSO method under PSC-4

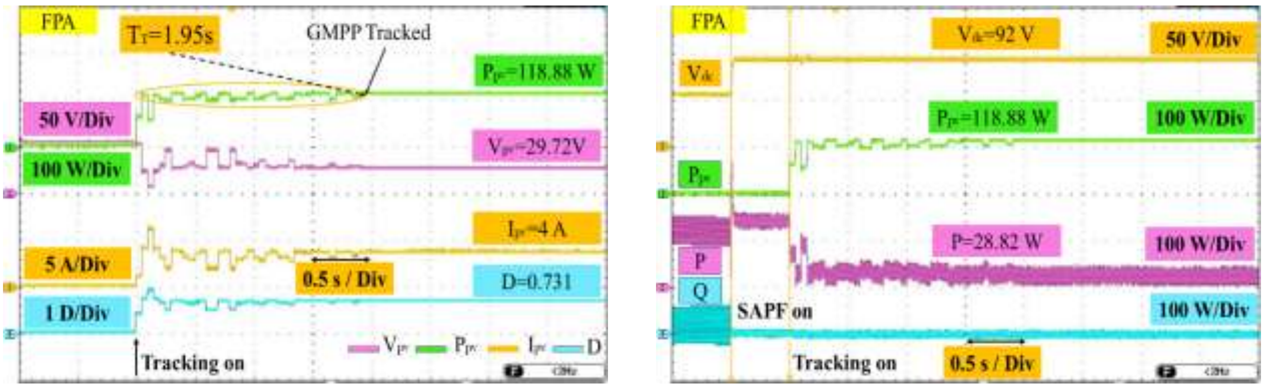

(a) (b)

Figure 5.63: Experimental results of the proposed FPA method under PSC-4

Under PSC-5, the PV array operates at a reduced GMPP of approximately 100 W, which is significantly lower than the load demand (150.57 W). Consequently, the PV system supplies only a portion of the P_{load}, while the remaining power deficit is provided by the utility grid.

For the GWO algorithm (Figure 5.64), the extracted PV power reaches approximately 98.60 W, with a T_T=1.8 s and a η=98.60%. Although the GMPP is correctly identified, the longer T_T indicates slower convergence under severe shading conditions. Consequently, the grid supplies a P=65.021 W to partially satisfy the load demand.

As illustrated in Figure 5.65, the WOA method extracts approximately 98.72 W, achieving a shorter T_T =1.3 s and a η=98.72%. This reflects improved dynamic performance compared to the GWO algorithm under the same operating condition. Consequently, the utility grid supplies an P= 64.898 W to compensate for the remaining power deficit.

As shown in Figure 5.66, the PSO algorithm extracts approximately 98.46 W, with a T_T=1.3 s and a η=98.46%. The utility grid supplies a P=65.158 W to compensate for the power deficit.

As illustrated in Figure 5.67, the FPA algorithm exhibits the poorest performance under PSC-5, extracting only 88.05 W with a long T_T=1.95 s and a significantly reduced η=88.05%. This behavior indicates that FPA struggles to achieve stable convergence under severe PSC, leading to substantial power losses. Consequently, the utility grid supplies a P= 75.57 W to compensate for the resulting power deficit.

All algorithms experience reduced PV power due to severe shading, requiring significant support from the utility grid. GWO and WOA maintain high efficiency and stable tracking, PSO shows minor deviations and higher losses, while FPA exhibits the poorest performance with slow convergence and substantial power losses.

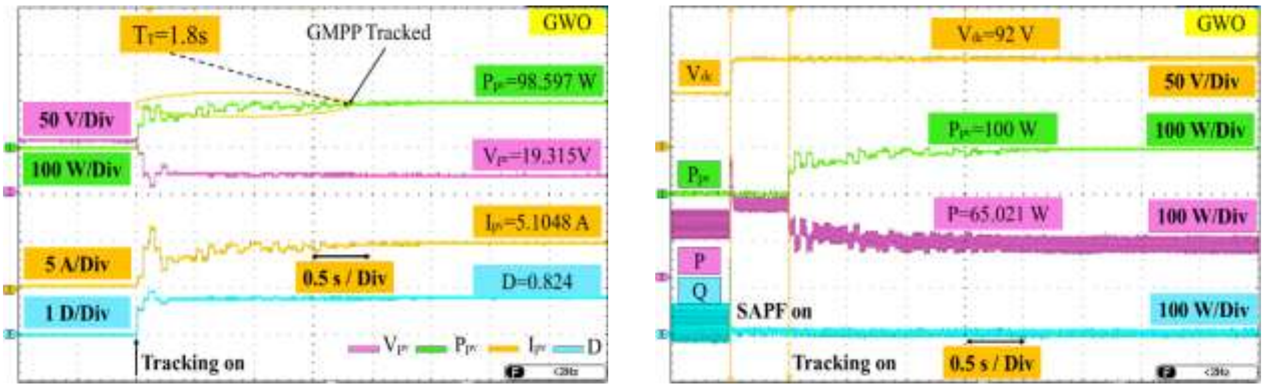

(a) (b)

Figure 5.64: Experimental results of the proposed GWO method under PSC-5

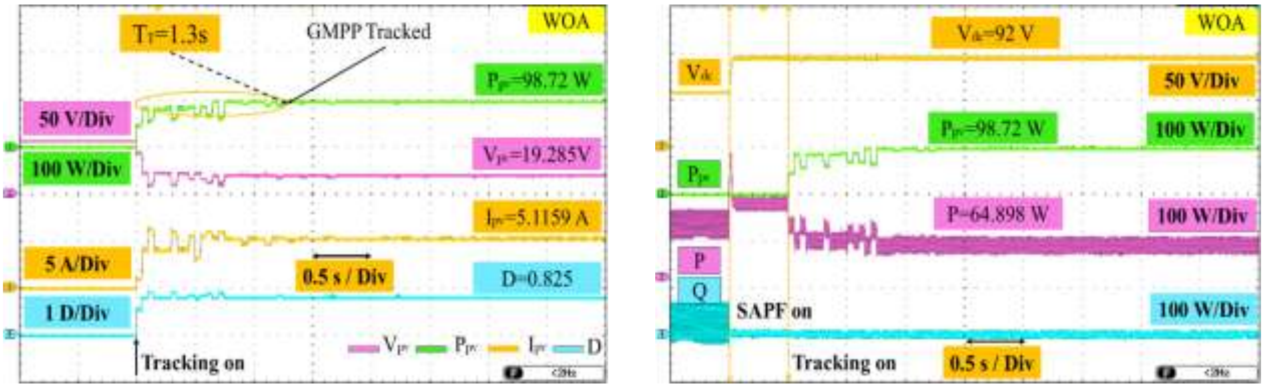

(a) (b)

Figure 5.65: Experimental results of the proposed WOA method under PSC-5

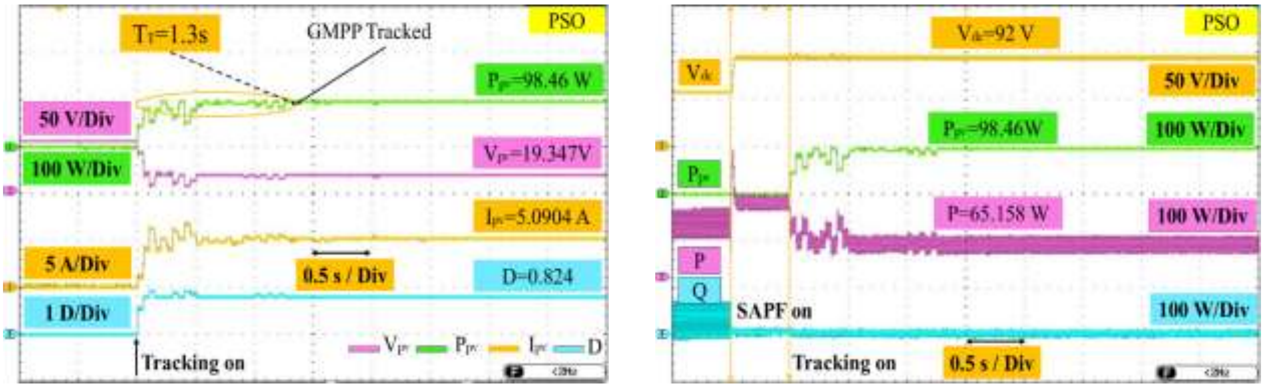

(a) (b)

Figure 5.66: Exprimental results of the proposed PSO method under PSC-5

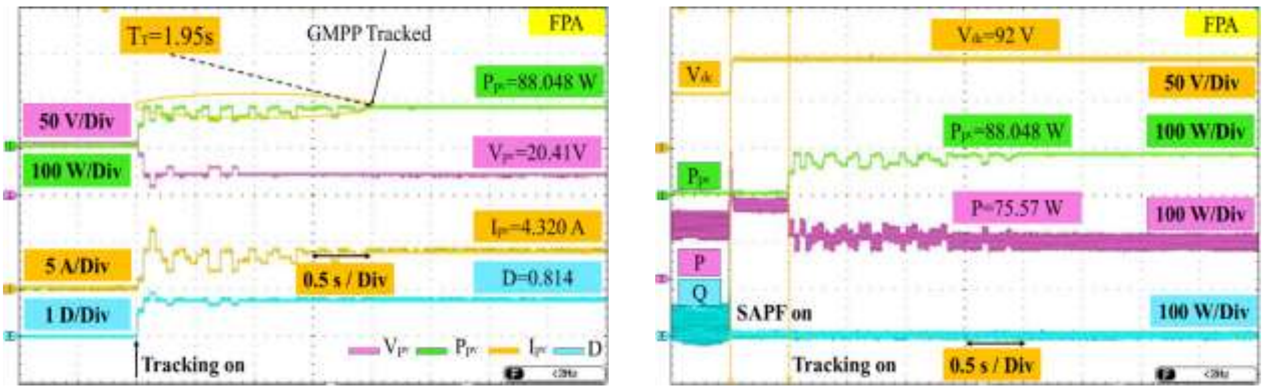

(a) (b)

Figure 5.67: Experimental results of the proposed FPA method under PSC-5

It is worth noting that the V_{dc} remains well-regulated for both the proposed and comparative MPPT methods, while the Q exchanged with the grid stays minimal. This behavior is mainly attributed to the adopted SAPF control strategy (P-DPC combined with the FOPI-AW-ZOA regulator), which is uniformly applied across all tested algorithms. Consequently, irrespective of the MPPT technique, the SAPF ensures effective V_{dc} regulation during both SAPF activation and PV injection, confirming the robustness and reliability of the proposed voltage control scheme under optimized operating conditions.

Moreover, power losses are observed under all optimized operating scenarios (PSC1-PSC5), consistent with the results obtained for the proposed methods. These losses are primarily associated with inverter switching losses, conduction losses in the filter inductors and power electronic components, as well as measurement and control-related losses inherent to real-time implementation. Table 5.7 presents a comparative evaluation of the conventional MPPT techniques (GWO, WOA, PSO, and FPA) under different PSCs (PSC-1 to PSC-5).

Table 5.7. Comparative Performance of Conventional MPPT Algorithms under PSCs (PSC-1 to PSC-5)

MPPT	PSCs	$V_{mpp}(V)$	$I_{mpp}(A)$	$P_{mpp}(W)$	$P_{\max}(W)$	P	Pload	Power Losses	T_T (s)	η (%)
GWO	PSC-1	29.390	4.5144	132.68	133.2	34.28	150.57	16.39	1.8	99.60
	PSC-2	29.445	5.0976	150.1	151.1	0.88		12.32	1.8	99.34
	PSC-3	47.620	5.3136	253	254.2	-59.61		42.82	1.6	99.60
	PSC-4	29.9	4	119.6	120	48.75		2.87	1.1	99.80
	PSC-5	19.315	5.1048	98.597	100	65.021		13.048	1.8	98.597
WOA	PSC-1	29.34	4.5288	132.88	133.2	34.14		16.39	1.325	99.75
	PSC-2	29.03	5.205	150.96	151.1	0.02		12.32	1.25	99.91
	PSC-3	48.33	5.1984	251.239	254.2	-57.849		42.82	1.35	98.91
	PSC-4	29.8	3.95	117.71	120	50.64		2.87	0.93	99.69
	PSC-5	19.285	5.1159	98.72	100	64.898		13.048	1.3	98.72
PSO	PSC-1	29.41	4.5072	132.557	133.2	34.403		16.39	1.65	99.52
	PSC-2	29.12	5.1048	148.65	151.1	2.33		12.32	1.3	96.65
	PSC-3	48.393	5.1624	249.82	254.2	-56.43		42.82	1.3	98.35
	PSC-4	29.8	3.97	119.91	120	48.44		2.87	1.7	99.61
	PSC-5	19.347	5.0904	98.46	100	65.158		13.048	1.3	98.46
FPA	PSC-1	29.89	4.3344	129.50	133.2	37.46		16.39	1.95	97.22
	PSC-2	29.836	4.788	142.86	151.1	8.12		12.32	1.95	94.54
	PSC-3	49.04	5.004	245.4	254.2	-52.01		42.82	1.95	96.61

PSC-4	29.72	4	118.88	120	49.47		2.87	1.5	93.73
PSC-5	20.41	4.320	88.048	100	75.57		13.048	1.95	88.048

Across all PSCs scenarios (PSC-1 to PSC-5), the performance of both the proposed algorithms (GWEO and ZOA) and the comparative MPPT methods (GWO, WOA, PSO, and FPA) was systematically evaluated. In all scenarios, the algorithms were able to track the GMPP; however, noticeable differences were observed in terms of T_T, extracted power, and η.

The proposed GWEO and ZOA algorithms consistently demonstrated superior performance under all PSCs, characterized by faster convergence, higher η, and smoother dynamic responses compared to the conventional methods. In contrast, the comparative algorithms exhibited slower convergence and larger oscillations during the tracking process, particularly under more complex shading patterns (PSC-3 to PSC-5), which resulted in increased transient behavior and reduced optimization stability.

Regarding power losses, it is observed that, for a given operating condition, the losses remain approximately similar across all algorithms within each scenario. This is because these losses are mainly inherent to the system itself, including inverter switching losses, filter losses, and power conversion inefficiencies, rather than being solely dependent on the MPPT technique. Nevertheless, algorithms with slower convergence and higher oscillations tend to aggravate these losses during transient periods.

Overall, these results confirm that while conventional MPPT algorithms are capable of GMPP tracking, the proposed GWEO and ZOA methods provide enhanced performance, improved stability, and more efficient energy management under all shading scenarios, supported by an effective control strategy for the GCPV system.

Figure 5.68 summarizes the performance of all MPPT algorithms in terms of η and T_T under PSCs. The proposed GWEO and ZOA consistently achieve higher η and faster convergence compared with the conventional methods. ZOA generally provides the shortest T_T, while GWEO maintains the highest and most stable efficiency. In contrast, GWO, WOA, PSO, and FPA exhibit slower convergence and increased performance variability under complex shading conditions. Overall, the proposed methods demonstrate superior robustness, accuracy, and dynamic response across all PSCs.

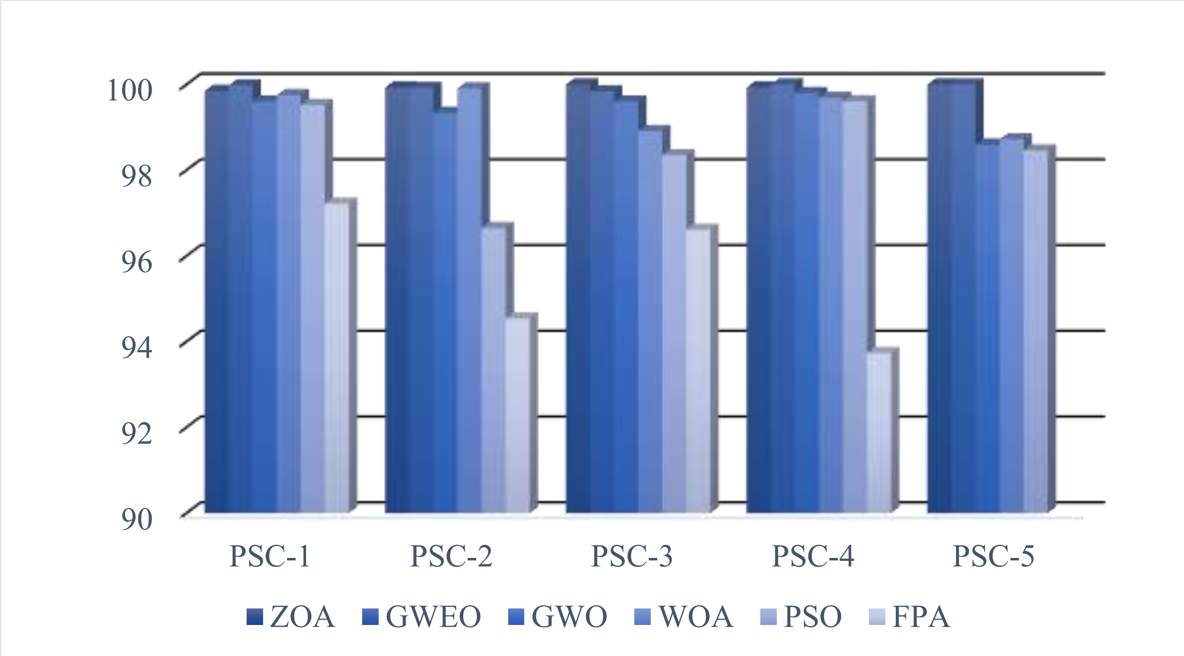

a)

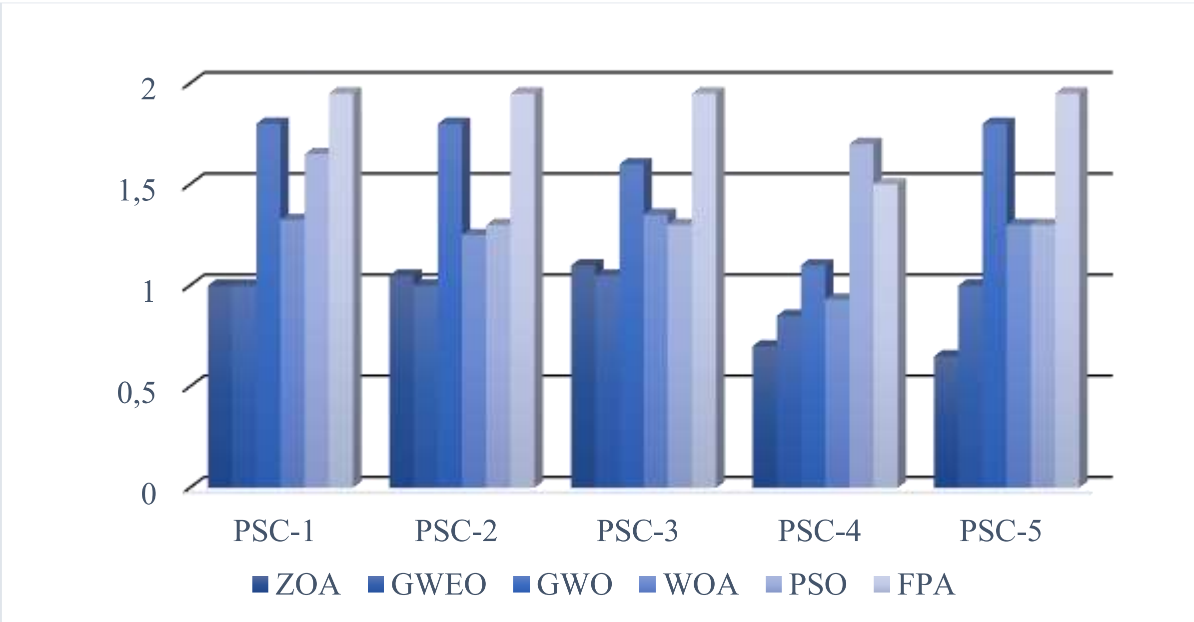

b)

Figure 5.68: Comparative performance analysis of the MPPT techniques under PSCs in terms of: a) η, and b) T_T

5.7.8 Comparative experimental results of MPPT algorithms under DSC

To further assess the robustness of the MPPT techniques, the proposed algorithms (GWEO and ZOA) and the comparative methods (GWO, WOA, PSO, and FPA) were evaluated under

DSC (Figure 5.69-5.72), where the operating point of the PV array changes abruptly due to transitions between different shading patterns. Such conditions impose severe constraints on MPPT controllers, requiring rapid reinitialization and accurate retracking of the new GMPP.

For the GWO algorithm (Figure 5.69), the results indicate that the GMPP is successfully tracked both before and after the shading transition. The recorded T_T= 1.6 s during the initial convergence phase. When the solar irradiance changes from PSC-3 to PSC-1, a recalibration process is triggered, resulting in noticeable transient fluctuations in the photovoltaic power and voltage. The new GMPP is reached within a T_T = 1.4 s. Although convergence is achieved, these transient oscillations reveal a moderate sensitivity of the GWO algorithm to rapid irradiance variations. The WOA algorithm (Figure 5.70) exhibits improved dynamic performance compared to the GWO algorithm. During the initial convergence phase, a T_T=1.3s is recorded. Following the shading transition, the WOA algorithm rapidly reinitializes and converges to the new GMPP within a T_T =1.58 s. Moreover, the fluctuations in the PV power are less pronounced, indicating enhanced stability and smoother convergence under dynamic operating conditions. In contrast, the PSO algorithm (Figure 5.71) exhibits slower dynamic behavior. During the initial convergence phase, a T_T =1.6 s is recorded. Following the transition from PSC-3 to PSC-1, pronounced oscillations appear in the PV power and voltage waveforms. Consequently, the algorithm requires a significantly longer time to stabilize at the new GMPP, with a T_T =2.6 s, indicating limited adaptability to DSCs. The FPA algorithm (Figure 5.72) shows the weakest performance under DSCs. During the irradiance transition, significant power fluctuations and prolonged oscillatory behavior are observed. The reinitialization process is slower, and convergence to the new GMPP is delayed compared to GWO and WOA. This behavior highlights reduced robustness of FPA under rapidly changing shading conditions and explains the higher energy losses observed during DSCs.

As illustrated in Figures 5.69–5.72(b), the activation of the SAPF ensures a stable V_{dc}, which is consistently regulated around its reference value of 92 V for all evaluated algorithms. Moreover, the Q is effectively compensated and maintained close to minimum, while the P accurately follows the available PV generation. These results confirm proper grid interaction, effective power quality enhancement, and reliable operation of the system regardless of the MPPT technique employed.

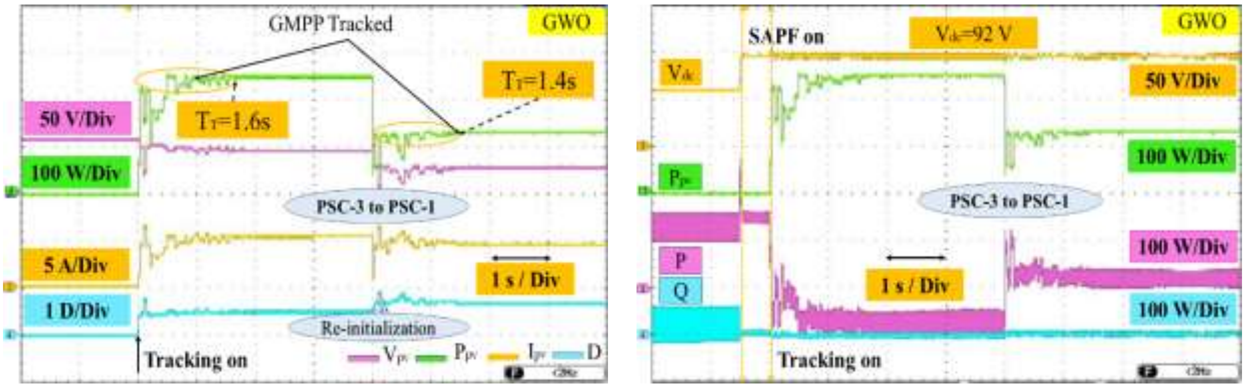

(a) (b)

Figure 5.69: Experimental results of the proposed GWO method under DSC

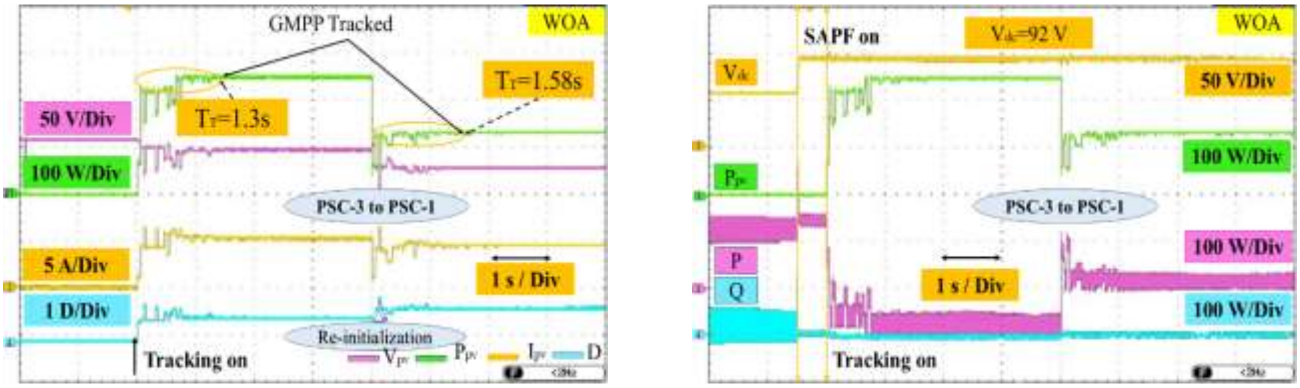

(a) (b)

Figure 5.70: Experimental results of the proposed WOA method under DSC

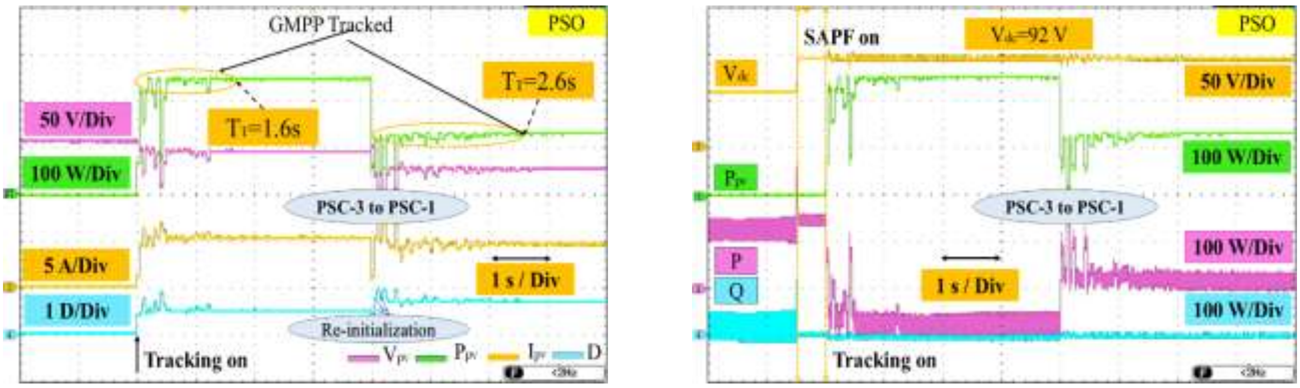

(a) (b)

Figure 5.71: Experimental results of the proposed PSO method under DSC

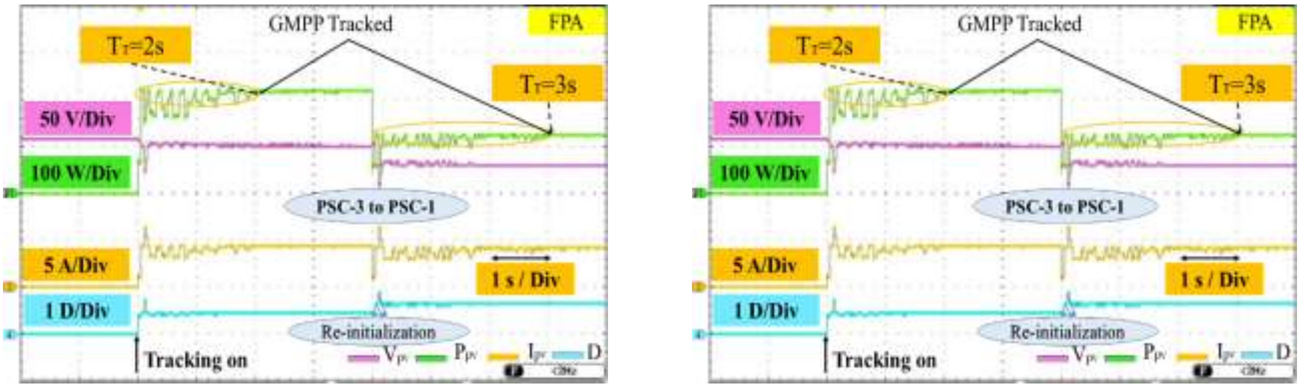

(a) (b)

Figure 5.72: Experimental results of the proposed FPA method under DSC

In summary, all comparative MPPT algorithms are capable of tracking the GMPP under DSCs; however, their dynamic performance differs significantly. WOA exhibits the fastest convergence and lowest oscillations, followed by GWO, while PSO and FPA suffer from slower convergence and higher transient power fluctuations. These differences result in increased energy losses during dynamic operation for PSO and FPA.

In contrast, the proposed methods (GWEO and ZOA), as discussed previously, demonstrate superior dynamic behavior, characterized by faster tracking, reduced oscillations, lower losses, and more stable P regulation. This confirms their suitability for real-time PV applications subject to rapid and unpredictable shading variations.

5.7.9 Comparative experimental results of MPPT algorithms under PSC-STC transition

During the dynamic shading transition from PSC-4 to STC, the behavior of the comparative MPPT algorithms (GWO, WOA, PSO, and FPA) was experimentally evaluated, as illustrated in Figures 5.73–5.76. This transition represents a severe operating condition, since the PV array abruptly shifts from a multi-peak P–V characteristic to a single-peak profile under STC, requiring rapid re-tracking and stable power regulation. For the GWO method (Figure 5.73), the algorithm successfully retracks the new global peak power point following the PSC-4 to STC transition. After reconvergence, it reaches the new operating point with a T_T= 1.6 s, demonstrating acceptable adaptability to sudden changes in solar irradiance. However, noticeable fluctuations in the PV power are observed during the transition interval, indicating moderate dynamic stability. In the case of the WOA algorithm (Figure 5.74), a slightly faster dynamic response than GWO is achieved; nevertheless, transient power oscillations still occur immediately after the irradiance transition, reflecting limited damping capability under abrupt operating changes. For the PSO algorithm (Figure 5.75), the dynamic response is characterized by a relatively fast initial convergence; however, more pronounced oscillations in PV power are observed compared to GWO and WOA. This oscillatory behavior during the transition leads to increased power losses and reduced energy utilization. The FPA algorithm (Figure 5.76) exhibits the weakest dynamic performance among the comparative methods. Significant power oscillations and a longer settling time are observed following the PSC-4 to STC transition, resulting in considerable energy losses and reduced tracking effectiveness.

For all comparative algorithms, the V_{dc} remains well-regulated around its reference value, confirming that the observed performance degradation is primarily related to MPPT dynamic behavior rather than limitations of the voltage control loop.

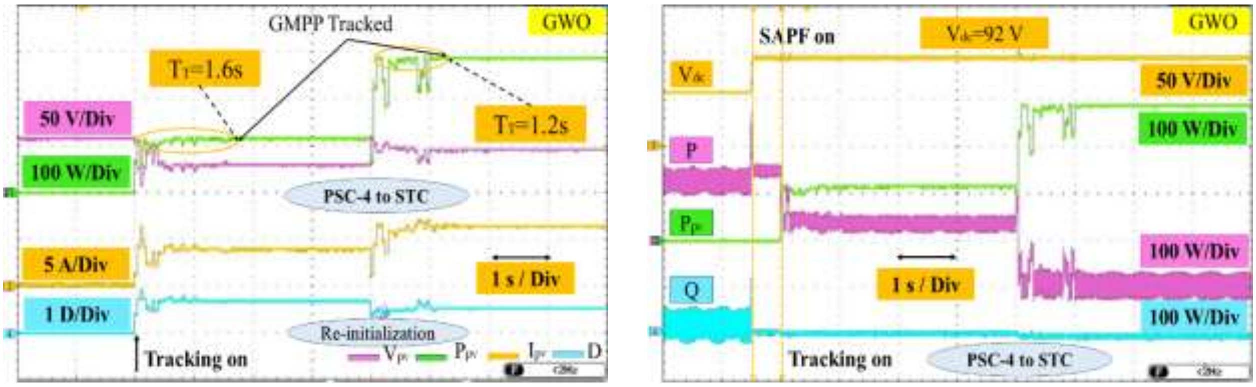

(a) (b)

Figure 5.73: Experimental results of the proposed GWO method under PSC-4-STC transition

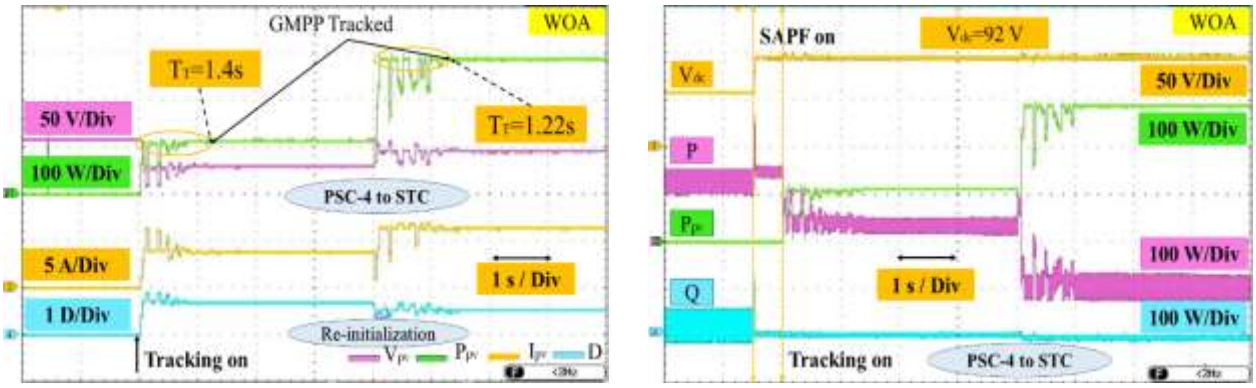

(a) (b)

Figure 5.74: Experimental results of the proposed WOA method under PSC-4-STC transition

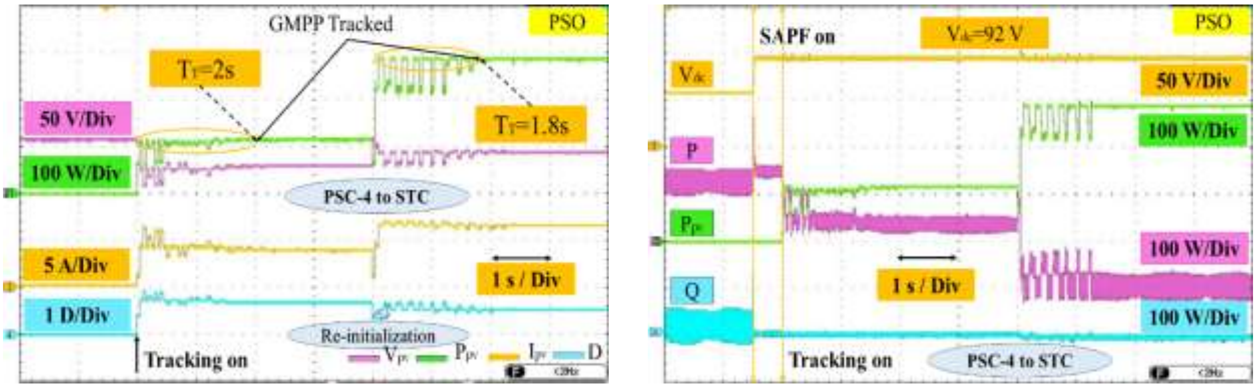

(a) (b)

Figure 5.75: Experimental results of the proposed PSO method under PSC-4-STC transition

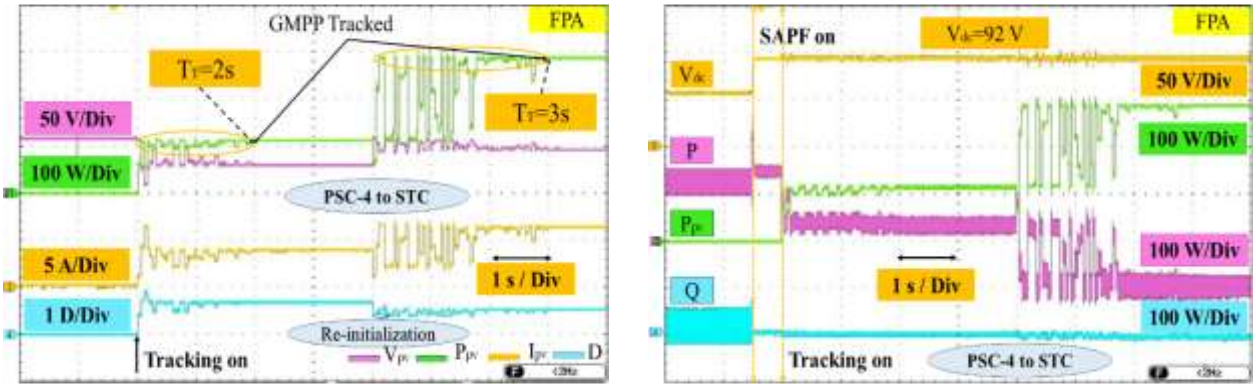

(a) (b)

Figure 5.76: Experimental results of the proposed FPA method under PSC-4-STC transition

Under PSC-4 to STC dynamic conditions, all comparative MPPT algorithms are capable of retracking the new operating point after the irradiance transition. Some methods exhibit faster initial tracking, while others require a longer re-tracking duration but eventually converge to the GMPP with acceptable power levels. The proposed GWEO and ZOA strategies show a more regular dynamic response, characterized by smoother convergence and reduced oscillations during the transition. Although comparable algorithms can achieve similar steady-state performance, the proposed methods provide improved stability and robustness under abrupt irradiance changes, which is advantageous for practical MPPT operation.

5.8 Experimental analysis of SAPF operation during PV injection under STC and PSCs

In this section, the performance of the SAPF is evaluated under steady-state operating conditions during PV injection. The main objective is to assess the effectiveness of the SAPF in enhancing power quality by mitigating current harmonics, compensating *Q*, and improving the overall PF. The SAPF is controlled using a P-DPC strategy, while V_{dc} regulation is ensured by a FOPI-AW controller optimally tuned using ZOA.

Since the proposed and comparative control strategies exhibit very similar performance trends under steady-state conditions, a detailed algorithm-by-algorithm analysis is not required. Therefore, for clarity and conciseness, a single representative control strategy GWEO method, is selected for in-depth analysis.

The system's performance, including the source current (I_s), load current (I_L), filter current (I_f), and grid voltage (V_s), is analyzed during PV injection and under load variation conditions. Key parameters, including P, Q, THD, and PF, are evaluated using a power analyzer. This comprehensive evaluation provides clear insight into the steady-state performance of the SAPF and forms the basis for the interpretation of the experimental results presented in the subsequent figures.

The system behavior before SAPF and during SAPF operation before PV injection has been thoroughly discussed in previous sections, where the detrimental effects of nonlinear loads, such as current distortion, increased Q, and reduced PF, were clearly identified. Consequently, this section focuses exclusively on the PV injection stage, assessing the SAPF performance under both STC and PSC conditions.

5.8.1 Experimental analysis of SAPF operation during PV injection under STC

Figure 5.77(a) illustrates the steady-state operation of the SAPF under STC during PV injection. The source current (I_s) remains sinusoidal and synchronized with the grid voltage (V_s). Due to the surplus power generated by the PV system, this excess energy is injected into the grid, causing the fundamental component of I_s to become phase-opposed to the load current (I_L). This behavior confirms correct inverse current injection and effective PV injection through the SAPF. The zoomed view in Figure 5.77(b) further highlights the high waveform quality and accurate phase alignment, indicating effective harmonic mitigation and controlled power exchange with the grid. Figure 5.78 presents the system response under load variation during PV injection, showing that the SAPF rapidly adapts the I_s to the new load conditions, thereby preserving current quality and ensuring stable operation with a fast transient response.

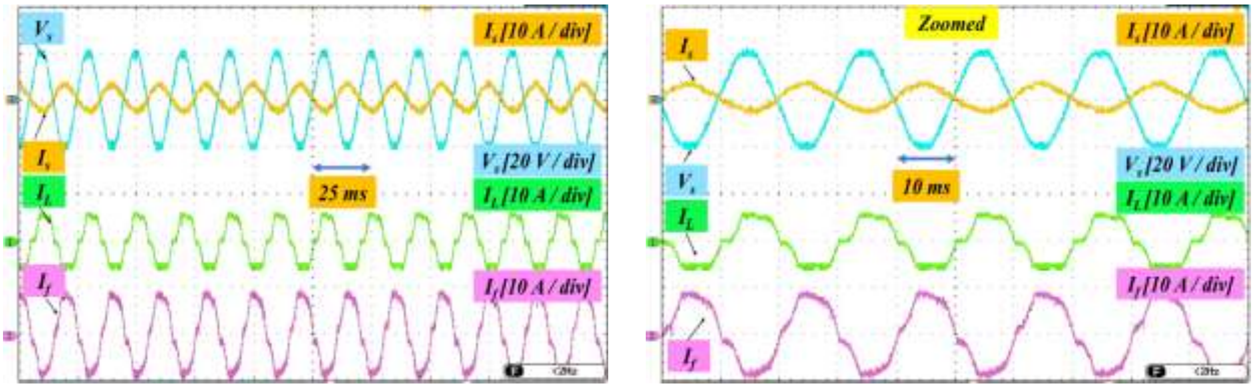

(a) (b)

Figure 5.77: Experimental waveforms of the GCPV–SAPF under STC during steady-state operation

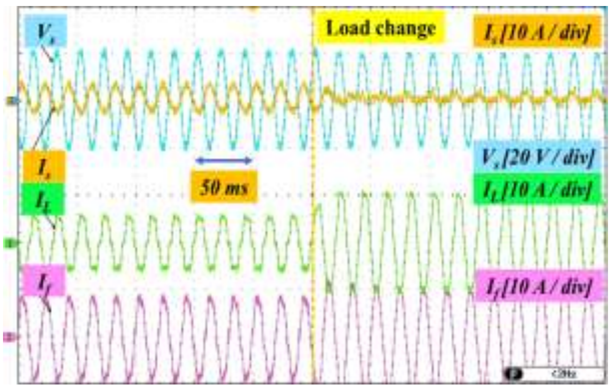

Figure 5.78: Experimental waveforms of the GCPV–SAPF system under STC during load variation

Figure 5.79(a) illustrates the harmonic performance of the I_s for Phase a under STC with PV power injection. The measured THD=9.4% confirms effective harmonic attenuation. Figure 5.79(b) shows that this harmonic mitigation is consistent across all three phases (I_s-a, b, and c), maintaining a THD =10.5% and demonstrating balanced, reliable operation.

These results confirm that, under steady-state conditions with PV injection, the SAPF ensures effective harmonic attenuation, proper power flow, and stable I_s behavior.

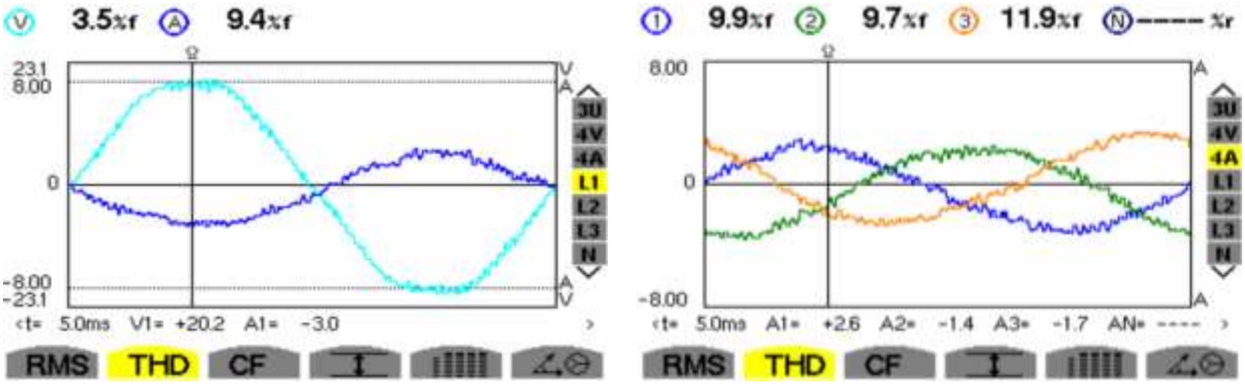

(a) (b)

Figure 5.79: Harmonic distortion of the GCPV–SAPF system under STC

In Figure 5.80(a), the three vectors represent the SAPF injected compensating currents for the three phases. Each current vector is approximately 180° opposite to its corresponding load harmonic current, illustrating the intended inverse current injection, which enables harmonic cancellation and reactive power compensation. In Figure 5.80(b), the three vectors represent the three-phase supply voltages, spaced at 120° apart, confirming a balanced voltage system. The compensated source current vectors (shown close to the voltage directions) are nearly in phase with the supply voltages, indicating successful reactive power regulation and power factor improvement toward unity.

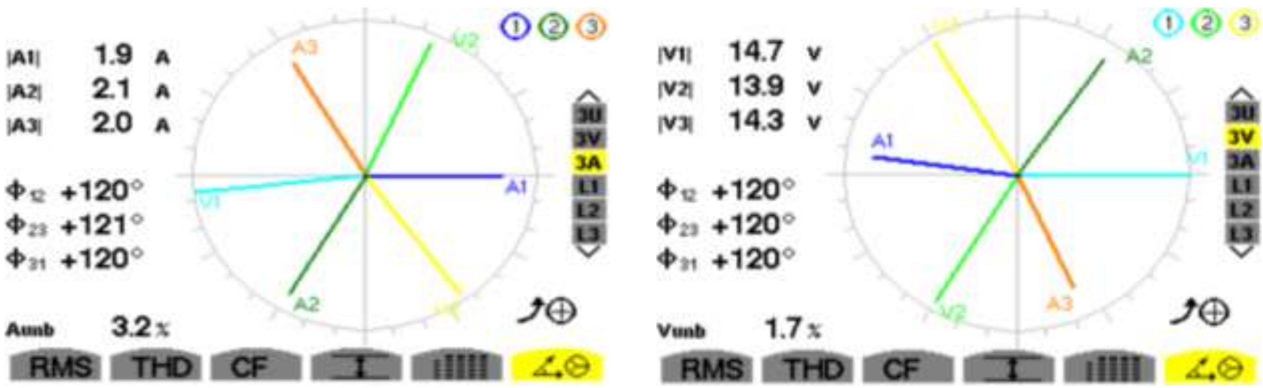

(a) (b)

Figure 5.80: Phase shift angle between the GCPV–SAPF system and supply voltage under STCs

Figure 5.81(a) presents the real-time power measurements of the GCPV-SAPF system under STC, as reported by the power analyzer. In this operating condition, the PV array generates surplus useful power that is injected into the grid, where the P delivered to the grid reaches approximately P=-97.38 W. Meanwhile, the SAPF effectively compensates the Q component, reducing power quality distortions and validating proper power flow regulation and harmonic mitigation during steady-state compensation. Figure 5.81(b) presents the corresponding power quality indicators under STC, including PF, *cos φ*, and *tan φ*. The results indicate nearly balanced P sharing among the three phases and a negligible Q demand. A PF ≈ -0.91 is consistently maintained across all phases, confirming effective Q compensation and reliable harmonic mitigation with minimal harmonic influence on the power measurements.

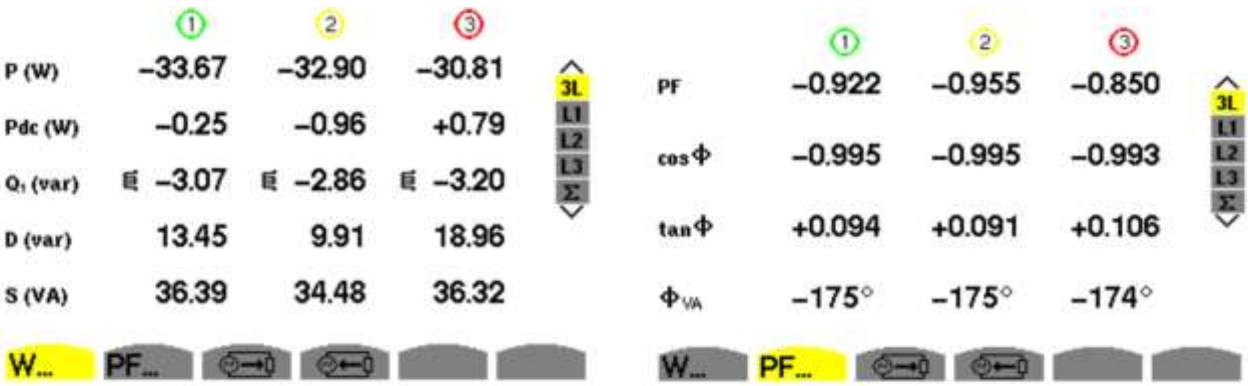

(a) (b)

Figure 5.81. Power analyzer measurement results of three-phase power quality parameters under STC

Overall, the experimental results under STC confirm that the SAPF effectively mitigates current harmonics, enhances PF, and ensures stable dynamic performance, demonstrating its suitability for practical PQ improvement applications.

5.8.2 Experimental analysis of SAPF operation during PV injection under PSC

Under PSC-1, Figure 5.82(a) illustrates the experimental waveforms of the V_s, I_s, I_f, and I_L under PSC-1 during steady-state operation. Due to partial shading, the I_s remains sinusoidal and synchronized with the V_s, and is close to minimum because the load is mainly supplied by the PV system. Figure 5.82(b) provides a zoomed view, highlighting the steady-state behavior of the currents and confirming the waveform characteristics under PSC-1.

Figure 5.83(a) shows the system response to load changes, demonstrating that the I_s slightly varies according to the new load and shading conditions, while the PV system and grid maintain continuous load supply. Figure 5.83(b) presents a zoomed view, highlighting the system's response to load variations under PSC-1.

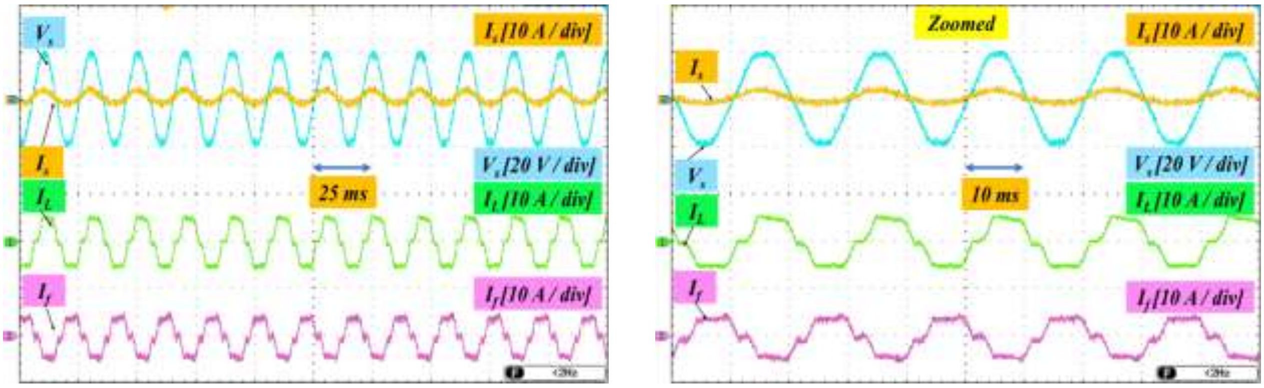

(a) (b)

Figure 5.82: Experimental waveforms of the GCPV–SAPF under PSC-1 during steady-state operation

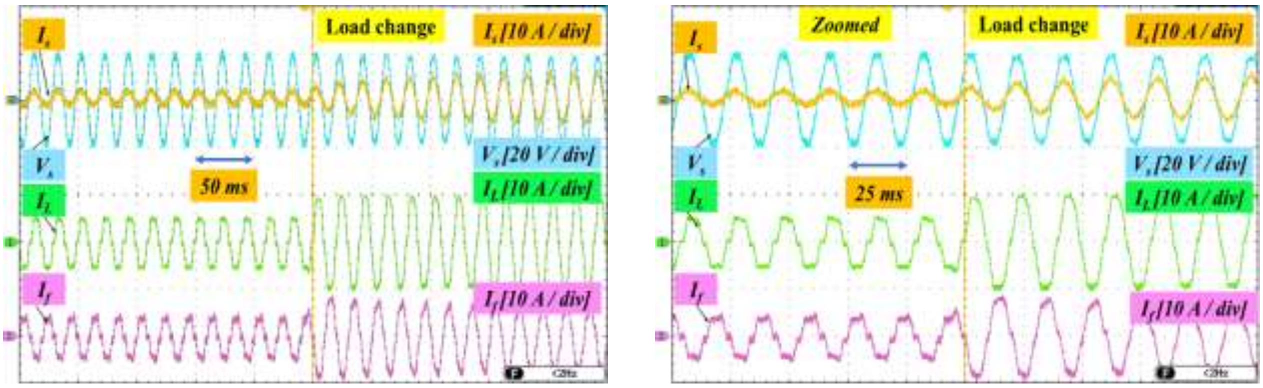

(a) (b)

Figure 5.83: Experimental waveforms of the GCPV–SAPF system under PSC-1 during load variation

Figure 5.84(a) shows the harmonic distortion of the I_s in phase a under PSC-1 operating conditions. Since the PV system supplies most of the load, the I_s remains very low, and the distorted load current is mainly drawn from the PV. As a result, the THD =14.5% due to the small magnitude of the I_s. Figure 5.84(b) confirms that the THD behavior is similar across the three I_s (a, b, and c) under PSC-1.

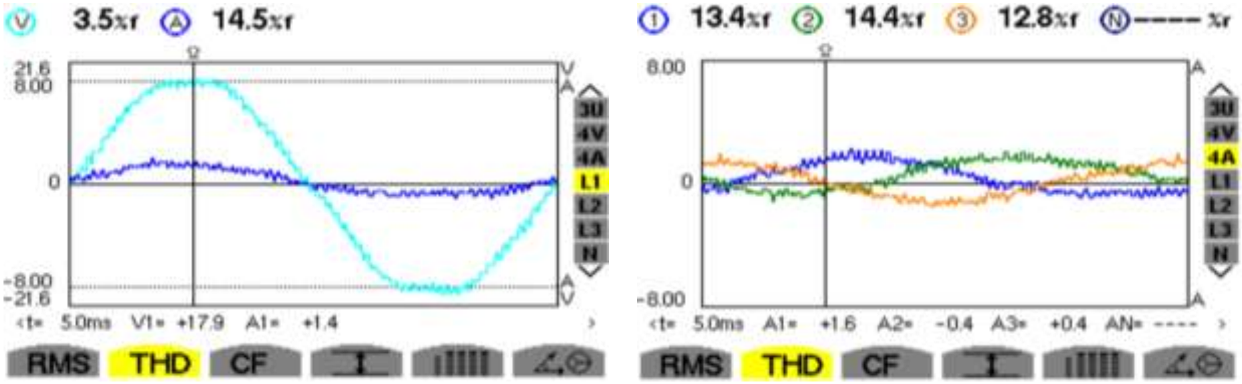

(a) (b)

Figure 5.84: Harmonic distortion of the GCPV–SAPF system under PSC-1

Figure 5.85(a) illustrates the instantaneous power measurements of the GCPV-SAPF system under PSC-1, as recorded by the power analyzer. The measured values include *P*, *Q*, *S*, and *D*. In this scenario, the PV array supplies most of the load, while the grid provides only a small portion.

Figure 5.85(b) presents the corresponding power quality parameters, including PF ≈ 0.646, and cos φ ≈ 0.986. The relatively low PF is primarily due to the combination of the limited grid contribution and the moderate *D*, which increases the *S* relative to the *P*. Despite the low PF, the three-phase *P* and *Q* distribution remains nearly balanced, and the voltage-current phase relationship is preserved, indicating stable operation of the system under PSC-1.

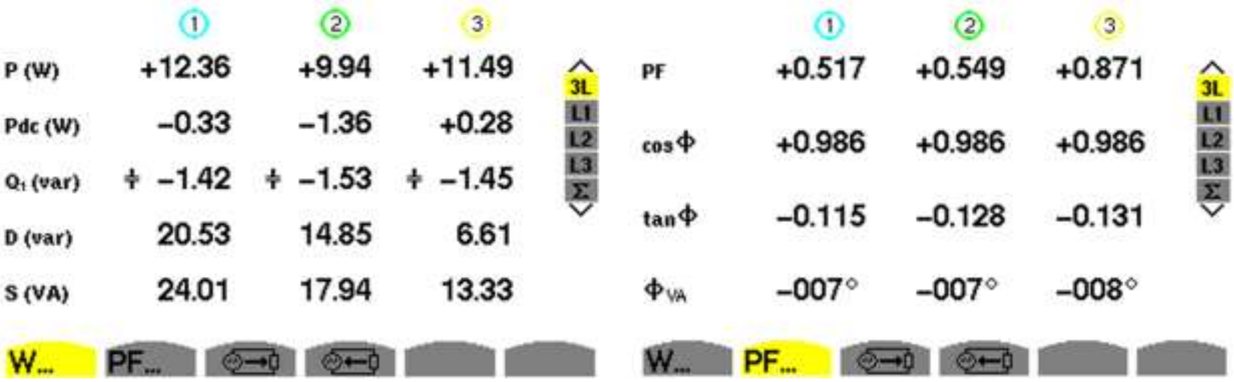

(a) (b)

Figure 5.85: Power analyzer measurement results of three-phase power quality parameters under PSC-1

Under PSC-2, Figure 5.86(a) presents the experimental waveforms during steady-state operation. Despite partial shading, the PV system supplies most of the load demand. Consequently, the grid I_s remains very small, indicating that only a limited amount of power is drawn from the grid. Figure 5.86(b) provides a zoomed-in view highlighting the steady-state behavior and confirming that the PV system covers most of the load demand, with minimal contribution from the grid. Figure 5.87(a) shows the system response to a load change under PSC-2. When the load increases beyond the PV generation capability, the grid supplies the additional required current, while the PV system continues to operate at its maximum available power. This demonstrates proper power sharing between the PV system and the grid. Figure 5.87(b) illustrates a zoomed-in view, highlighting the slight increase in I_s and the stable dynamic response of the system during the load transition.

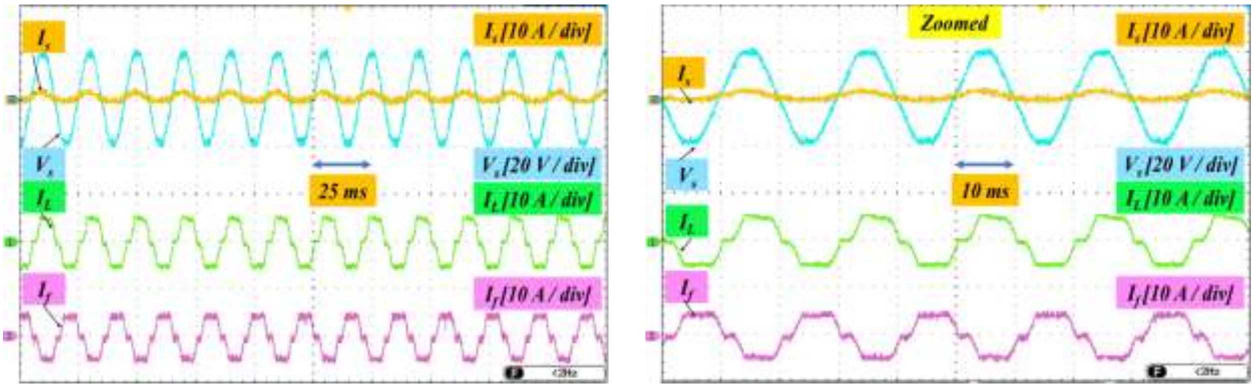

(a) (b)

Figure 5.86: Experimental waveforms of the GCPV-SAPF system under PSC-2 during steady-state operation

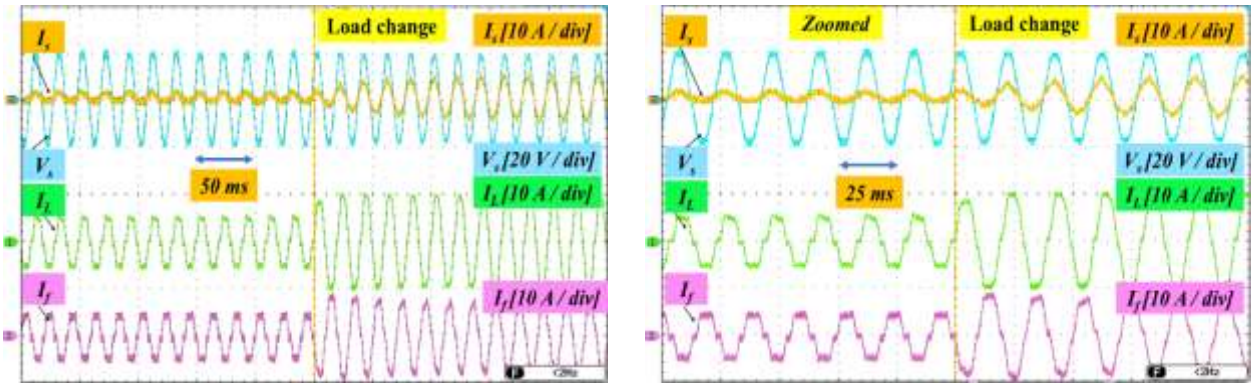

(a) (b)

Figure 5.87: Experimental waveforms of the GCPV-SAPF system under PSC-2 during load change

Figure 5.88(a) shows the harmonic distortion of the I_s in phase a under PSC-2 operating conditions. Since the PV system supplies nearly all of the load demand, the grid I_s is almost zero, indicating that the grid contribution is minimal. The I_L is therefore mainly supplied by the

PV-side inverter. As a result, the THD reaches approximately 23.5%, which is mainly due to the very low magnitude of the I_s rather than to ineffective harmonic compensation. Figure 5.88(b) shows that a similar THD behavior is observed for all three phases (a, b, and c) under PSC-2 conditions. It should be noted that when the I_s magnitude is very small, the THD value tends to increase, since the relative contribution of harmonic components becomes more significant, even though the grid contribution to the load remains minimal.

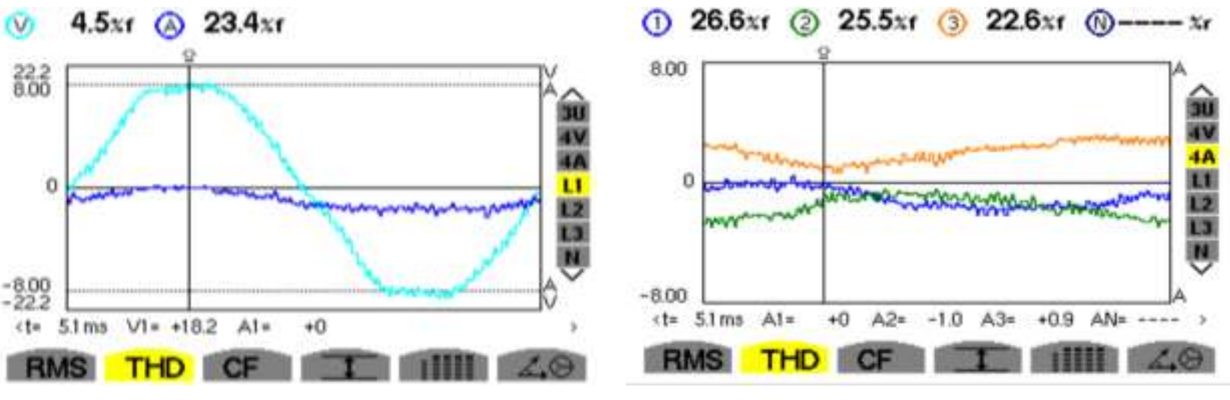

(a) (b)

Figure 5.88: Harmonic distortion of the GCPV-SAPF system under PSC-2

Figure 5.89(a) presents the power quality parameters of the three-phase system under PSC-2, reporting a P=0.864 and $cos\ \varphi$ = 0.992, which confirm operation close to unity PF with effective Q regulation. Figure 5.89(b) shows the P distribution across the phases under the same conditions. The measured P=11.91 W in Phase a, while phases b and c show 0 W, indicating that active power delivery occurs only in phase a under PSC-2. In this case, the PV power is approximately equal to the load demand, and the grid contribution remains nearly zero, confirming continuous and stable load supply under PSC-2.

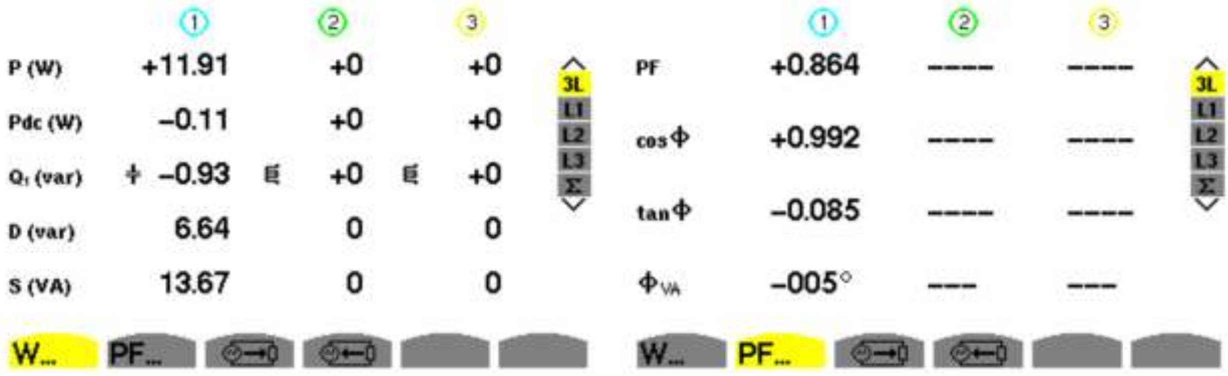

(a) (b)

Figure 5.89: Power analyzer measurement results of three-phase power quality parameters under PSC-2.

Under PSC-3, Figure 5.90(a) presents the steady-state performance of the GCPV–SAPF system. In this operating condition, the PV system, through the grid-side inverter, supplies the entire load demand, and the surplus P is exported to the utility grid. The I_s remains sinusoidal and synchronized with the grid voltage; however, its direction is reversed with respect to the defined grid-to-load reference, indicating P injection into the grid. This confirms the correct power-flow direction and stable interaction between the PV system and the utility network.

The enlarged view in Figure 5.90(b) further emphasizes the steady-state behavior, highlighting the sinusoidal waveform and precise phase alignment of the source current with the grid voltage despite the reversed direction. Figure 5.91(a) illustrates the system response to load variations under PSC-3. When the load changes, the I_s adapts smoothly to maintain the power balance among PV generation, load demand, and the power exported to the grid. The waveform remains stable and sinusoidal during the transient period, demonstrating the robustness of the system. Figure 5.91(b) provides a zoomed-in view, emphasizing the rapid adjustment of the source current and the overall stability of the GCPV–SAPF system during load transitions.

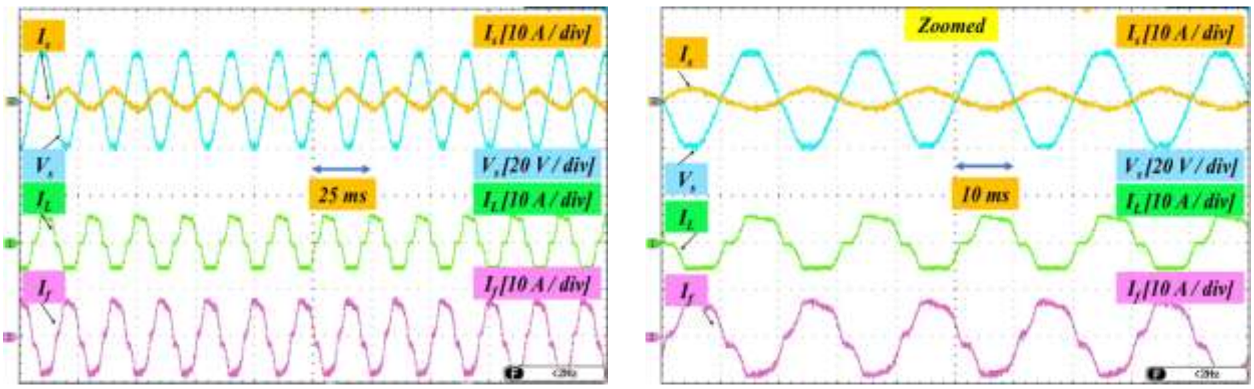

(a) (b)

Figure 5.90: Experimental waveforms of the GCPV-SAPF system under PSC-3 during steady-state operation

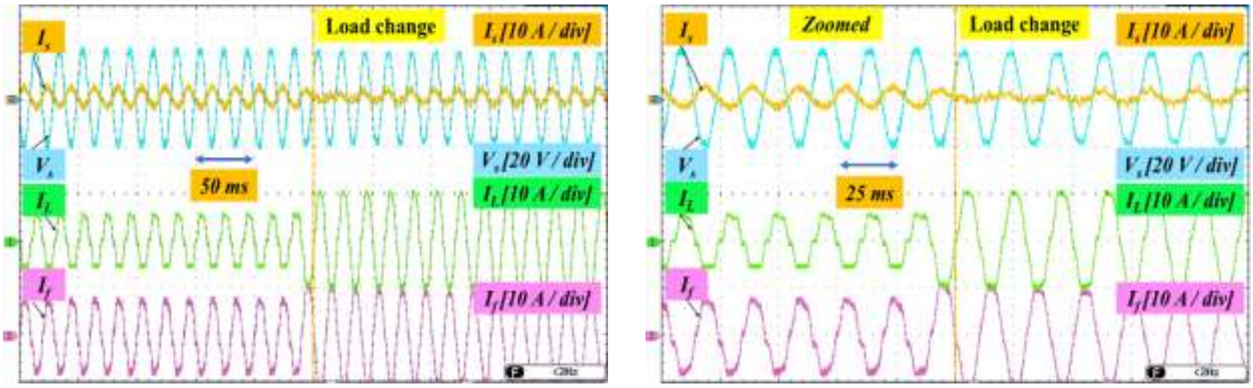

(a) (b)

Figure 5.91: Experimental waveforms of the GCPV-SAPF system under PSC-3 during load change

Figure 5.92(a) shows the harmonic distortion of the I_s in phase a under PSC-3. In this scenario, the PV system, through the grid-side inverter, supplies most of the load demand, and the surplus active power is exported to the utility grid. As a result, the I_s is small in magnitude and flows in the opposite direction relative to the I_L, reflecting power export to the grid. The THD reaches approximately THD=14.5%, which is primarily due to the low magnitude of I_s rather than poor harmonic compensation. Figure 5.92(b) shows that the THD behavior is similar across all three phases (a, b, and c), with a THD =14.8%. This indicates a consistent harmonic profile among the three-phase I_s and confirms stable current quality at the PCC under PSC-3 steady-state conditions.

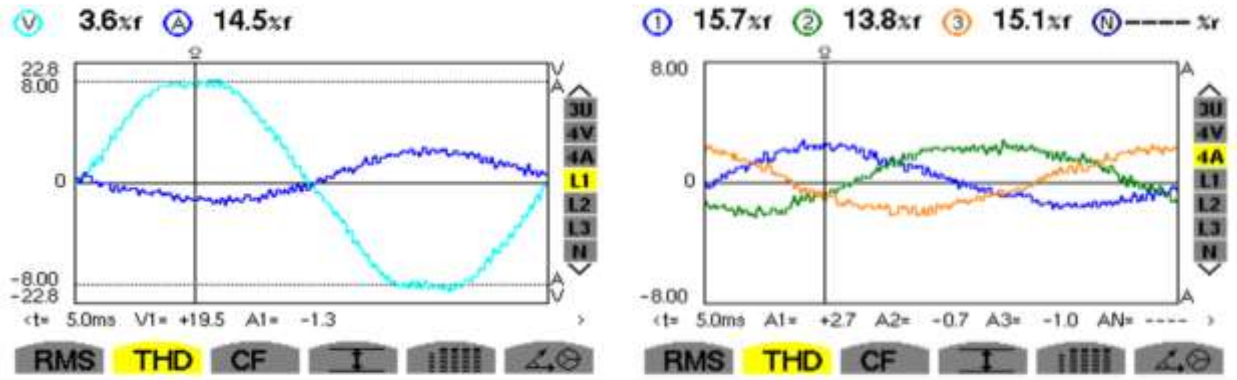

(a) (b)

Figure 5.92: Harmonic distortion of the GCPV– SAPF compensating currents under PSC-3

Figure 5.93(a) presents the real-time power measurements of the GCPV–SAPF system under PSC-3. In this scenario, the PV system, through its grid-connected inverter, delivers most of the load demand, with a surplus P = -60.4 W injected into the utility grid.

Figure 5.93(b) shows the corresponding power quality indicators, including a PF ≈ -0.944 and cos φ ≈ 0.988. The negative PF indicates that *P* is being exported from the PV system to the grid. The results also demonstrate a nearly balanced distribution of active power among the three phases and minimal *Q*, reflecting the efficient operation of the PV system and stable power export under PSC-3 conditions.

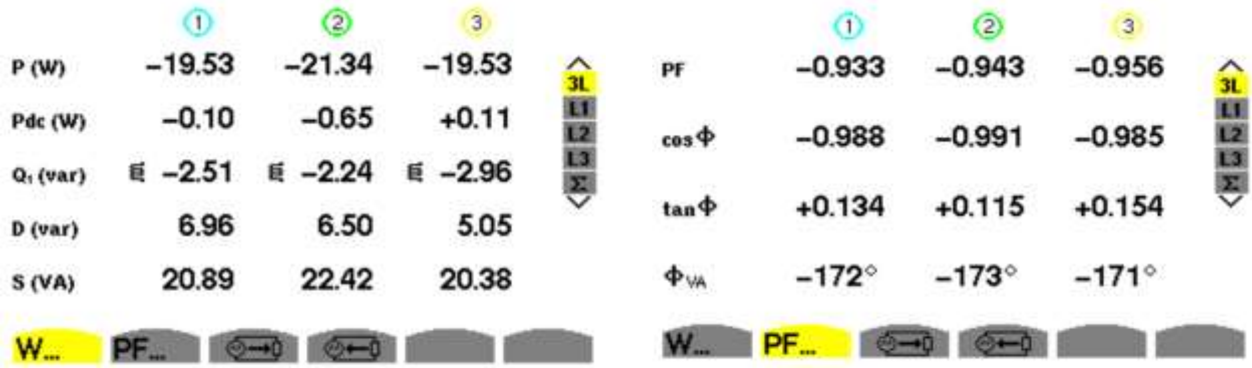

(a) (b)

Figure 5.93: Power analyzer measurement results of three-phase power quality parameters under PSC-3.

Under PSC-4, Figure 5.94(a) illustrates the steady-state waveforms under PSC-4 conditions. In this scenario, the PV array is unable to fully supply the load, so the grid provides the missing power; however, the load is still not completely met. The I_s flows in the same direction as the V_s to compensate for the deficit in PV generation. The waveform remains sinusoidal, indicating stable operation despite the insufficient PV power.

Figure 5.94(b) presents a zoomed-in view of the waveforms under steady-state conditions, highlighting the fine details of the I_s and I_L. Figure 5.95(a) shows the system response to a load change under PSC-4 conditions. When the load varies, the I_s adjusts smoothly to maintain the power balance between PV generation, load demand, and the grid contribution. The waveform remains sinusoidal and stable, confirming that the grid reliably supports the load during dynamic conditions. Figure 5.95(b) provides a zoomed-in view of the waveforms during the load change, emphasizing the smooth adjustment of the I_s and the stability of the system under transient conditions.

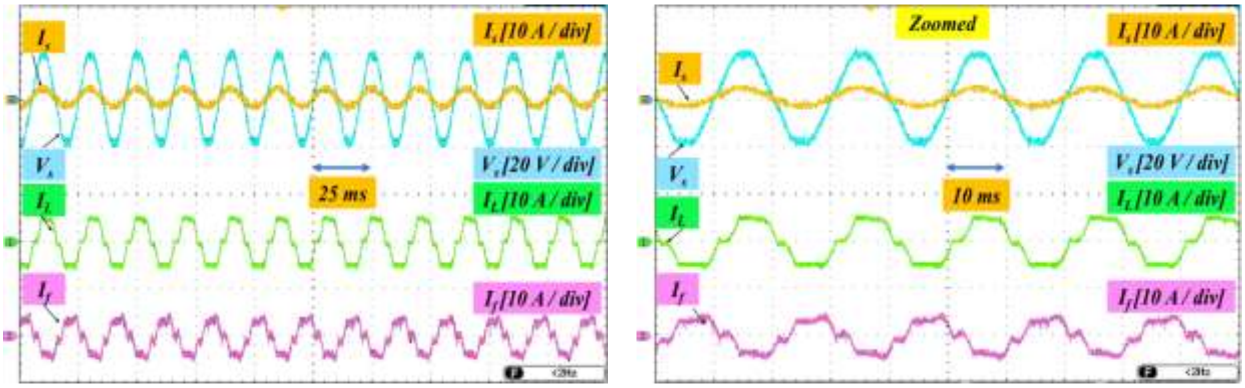

(a) (b)

Figure 5.94: Experimental waveforms of the GCPV-SAPF system under PSC-4 during steady-state operation

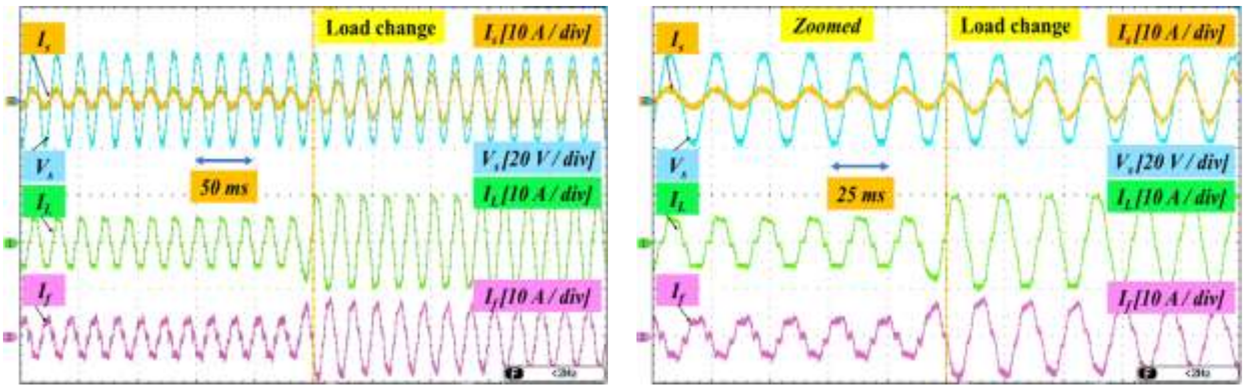

(a) (b)

Figure 5.95: Experimental waveforms of the GCPV-SAPF system under PSC-4 during load change

Figure 5.96(a) presents the harmonic distortion of the I_s in phase a under PSC-4 conditions. As the PV system is unable to fully supply the load, the grid provides the missing P, and the I_s flows in the same direction as the grid voltage. The current magnitude is relatively low, resulting in a THD =11.6%.

Figure 5.96(b) shows the THD behavior for all three phases (a, b, and c). The three-phase I_s remained well-balanced, and the waveforms are sinusoidal and stable. The relatively higher THD is attributed to the low magnitude of the I_s, which amplifies the relative impact of harmonic components. These results confirm that the system maintains acceptable current quality under PSC-4, despite the insufficient PV generation.

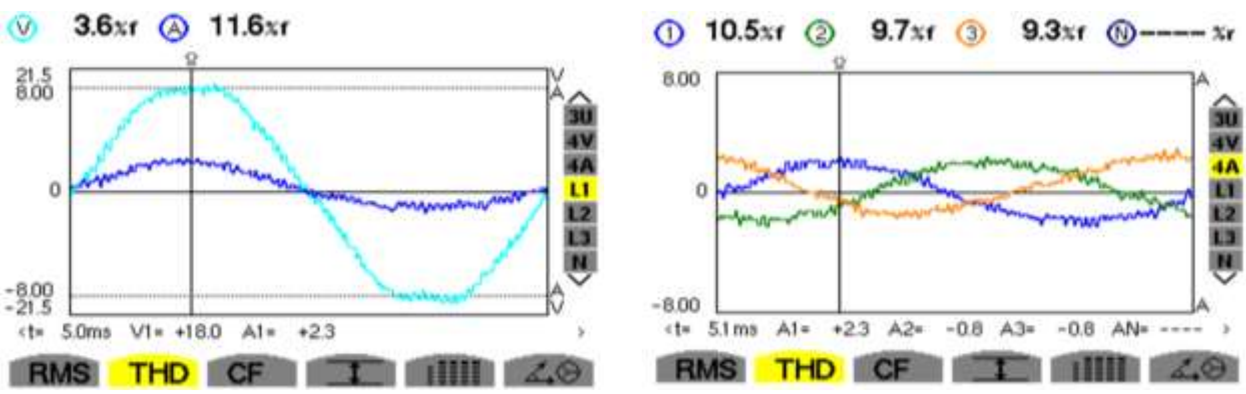

(a) (b)

Figure 5.96: Harmonic distortion of the GCPV-SAPF system under PSC-4

Figure 5.97 presents the power analyzer measurements of the three-phase power quality parameters under PSC-4. In this scenario, the PV system cannot fully supply the load, and the grid provides the missing power. The measured three-phase P =27.7 W, Q= -5.01 W, PF = 0.535, the $cos\ \varphi$ = 0.966, and D = 62.58 VAR. The relatively low PF is primarily due to the combined effects of the limited Q and the moderate D, which increase the S relative to the P. Despite the low current, the three-phase P and Q distribution remains nearly balanced, and the voltage-current phase relationship is preserved, indicating stable system operation under PSC-4, even in the presence of moderate harmonic distortion.

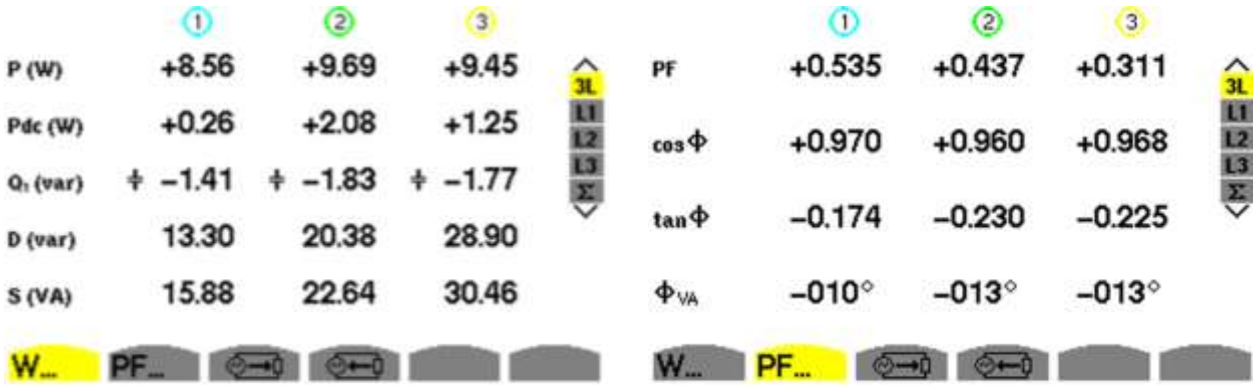

(a) (b)

Figure 5.97. Power analyzer measurement results of three-phase power quality parameters under PSC-4

Under PSC-5, Figure 5.98(a) illustrates the steady-state waveforms under PSC-5. In this scenario, the photovoltaic array supplies only a portion of the load (approximately 100 W out of a total load of 150.57 W), while the remaining power is provided by the utility grid. The source current flows in the same direction as the grid voltage to compensate for the deficit in

PV generation. Despite the partial supply from PV, the waveform remains sinusoidal and well-aligned with the grid voltage, indicating stable operation.

Figure 5.98(b) presents a zoomed-in view of the source current waveform, emphasizing the precise tracking of load requirements and the stable steady-state behavior under PSC-5. Figure 5.99(a) depicts the system response to load variations under PSC-5. When the load changes, the source current adapts smoothly to maintain the power balance between PV generation, grid contribution, and load demand. The waveform remains stable and sinusoidal, demonstrating the robustness of the system during transient conditions. Figure 5.99(b) provides a zoomed-in view, highlighting the rapid adjustment of the source current and confirming the reliability of the grid support in meeting the load deficit during dynamic operation.

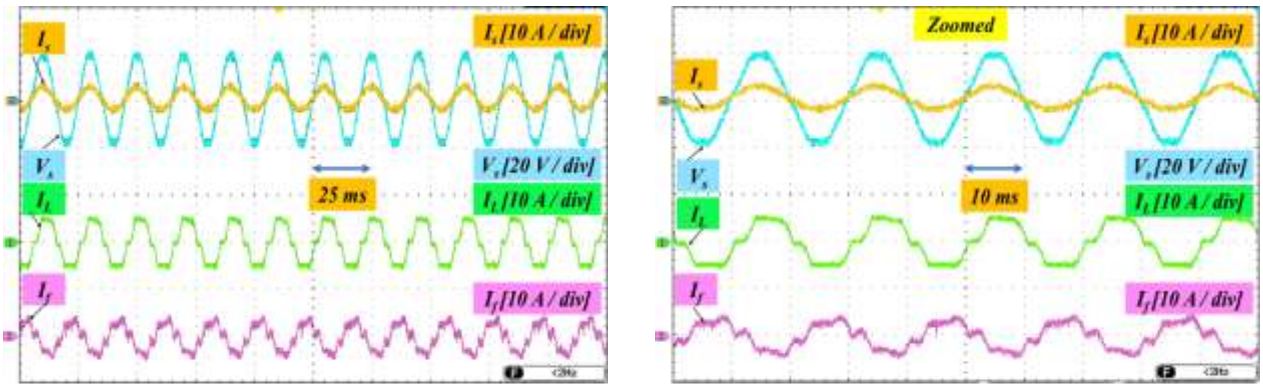

(a) (b)

Figure 5.98: Experimental waveforms of the GCPV-SAPF system under PSC-5 during steady-state operation

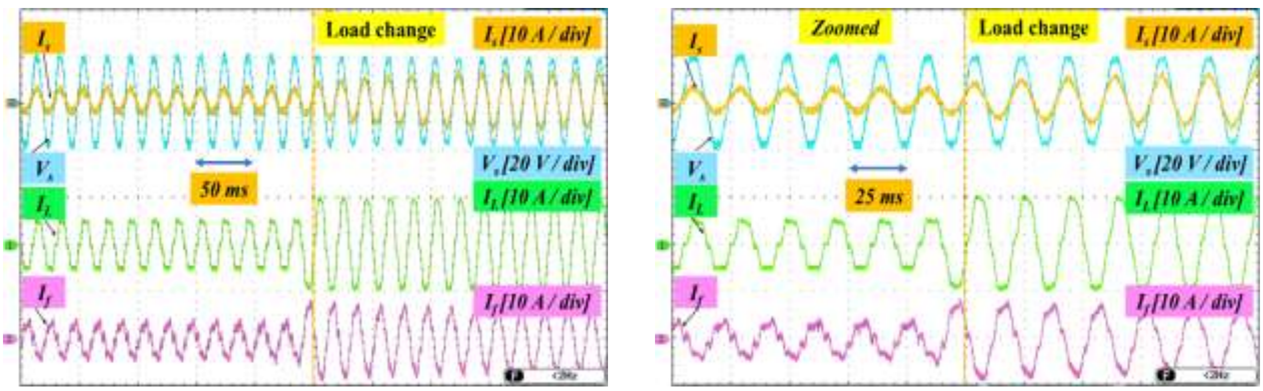

(a) (b)

Figure 5.99: Experimental waveforms of the GCPV-SAPF system under PSC-5 during load change

Figure 5.100(a) illustrates the harmonic distortion of the I_s in phase a under PSC-5 conditions, where the THD = 7.9%. Despite the PV array supplying only a portion of the load, the SAPF and grid support maintain a relatively low distortion level, ensuring good current waveform quality. Figure 5.100(b) shows the THD behavior across all three phases (a, b, and c), indicating that harmonic mitigation is consistent and three-phase operation remains balanced. The results confirm that the SAPF effectively manages harmonic content even when the I_s increases to compensate for the PV deficit, preserving sinusoidal waveforms and overall system stability under partial shading and low PV generation conditions.

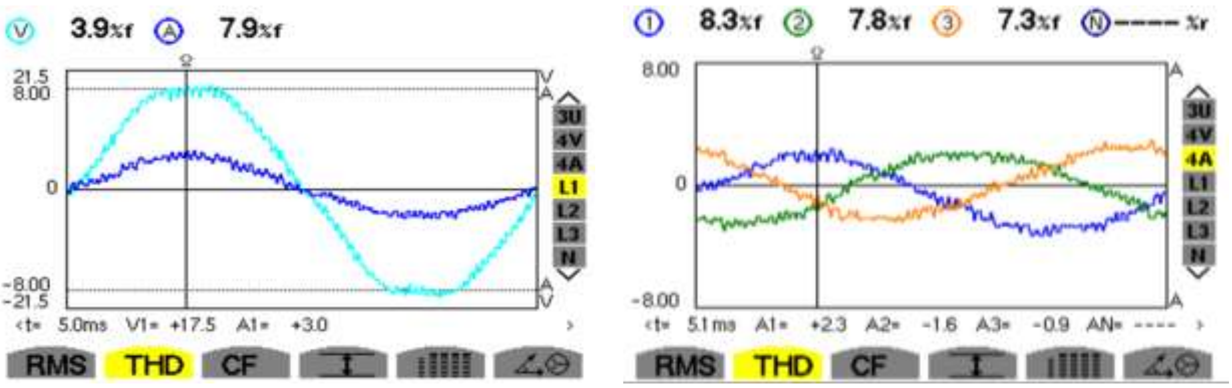

(a) (b)

Figure 5.100: Harmonic distortion of the GCPV-SAPF system under PSC-5

Figure 5.101 (power analyzer measurements) presents the three-phase PQ parameters under PSC-5. The measured P = 63.62 W, Q = -4.35 VAR, D =12.58 VAR, PF ≈ 0.996, and $cos\ \varphi$ ≈ 0.979. The slightly reduced PF is primarily influenced by the D and the relative contribution of the I_s. The three-phase P distribution remains nearly balanced, and the voltage-current phase relationship is well-maintained, confirming stable and reliable system operation.

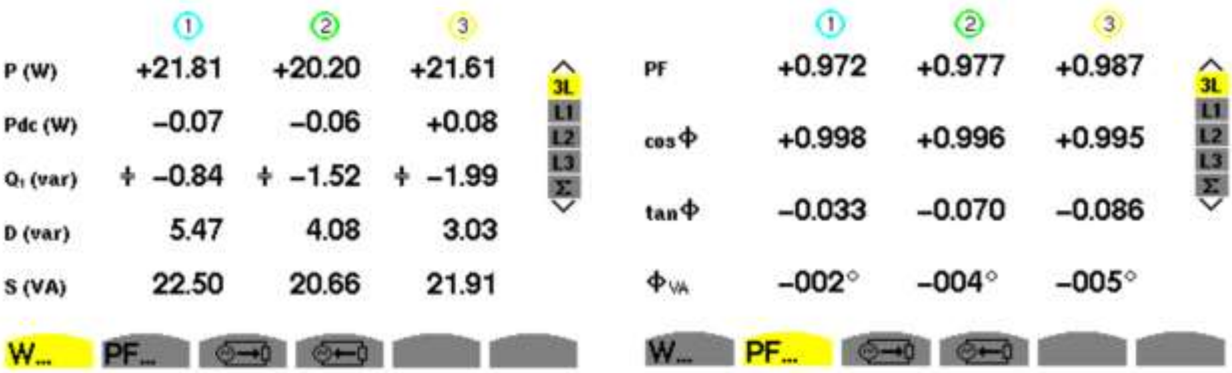

(a) (b)

Figure 5.101: Power analyzer measurement results of three-phase power quality parameters under PSC-5

The experimental investigations conducted under various PSC scenarios clearly demonstrate the robust and reliable performance of the GCPV–SAPF system. The studied operating conditions include cases where the PV array is unable to fully supply the load, conditions where PV generation closely matches the load demand, scenarios in which the PV system supplies the load with surplus power injected into the utility grid, and cases where the PV system supplies the load while still requiring partial support from the grid. Together, these scenarios encompass all practically possible operating modes of GCPV-SAPF systems under partial shading.

Across all scenarios, the SAPF effectively mitigates current harmonics, maintains nearly sinusoidal I_s waveforms, and ensures balanced three-phase operation at the PCC. The experimental results confirm that the SAPF control strategy adapts efficiently to variations in irradiance, operating mode transitions, and load changes, without compromising system stability or overall power quality.

It is observed that under certain operating conditions, particularly when the I_s magnitude is very low or approaches zero, the measured THD of I_s increases. This increase in THD does not indicate poor filtering performance; rather, it results from the low fundamental current magnitude, where even small residual harmonic components become significant in relative terms. Under these conditions, the S increases due to the relatively larger contribution of the D, which in turn affects the measured PF. Despite this, the Q remains negligible, and the voltage-current phase angle cosine remains close to unity, confirming that system operation and harmonic mitigation remain effective.

Furthermore, dynamic tests involving load variations and operating condition transitions demonstrate the fast transient response of the SAPF. The system rapidly restores steady-state operation following disturbances, ensuring continuous harmonic mitigation, stable power exchange, and reliable power quality enhancement under all examined PSC scenarios.

5.9 Practical limitations and challenges

Although the proposed optimization algorithms and the overall GCPV–SAPF system demonstrated successful operation under STC, PSC, DSC, and during transitions from PSC to STC, achieving these results required overcoming significant practical limitations and experimental constraints.

One of the major challenges was related to the measurement system and sensing equipment. Several sensors operated using battery power, and variations in battery charge directly affected measurement accuracy and computational results. This limitation influenced the reliability of measured quantities such as active power, reactive power, power factor, and THD, thereby impacting system evaluation.

Another critical limitation was the restricted computational capability of the available DSPACE units. Two dSPACE devices, one from 2008 and the other from 2011, were used for real-time control and signal processing. Their limited performance resulted in slower computations, constraining the real-time implementation of the algorithms and affecting dynamic system performance.

Furthermore, energy losses were observed during system operation due to the integration of additional hardware components. The equipment was also sensitive to temperature variations, as thermal effects impacted the performance and reliability of power electronic devices, sensors, and measurement accuracy, particularly during prolonged operation.

Furthermore, thermal effects significantly influenced the system. The equipment's performance and the accuracy of power electronic devices and sensors were affected by temperature variations during prolonged operation. In addition, the resistances of the coils (bobines) contributed to variations in current measurements and affected system behavior, requiring careful consideration during experiments.

Despite these constraints, the system achieved stable operation and satisfactory performance, highlighting the robustness of the proposed optimization and control strategies under realistic experimental conditions. These limitations emphasize the need for improved sensing devices, higher-performance dSPACE platforms, enhanced thermal management, and controlled laboratory environments, which will be addressed in future work.

5.10 Conclusion

This chapter presented the experimental validation of the proposed GCPV-SAPF system, focusing on the implementation and performance evaluation of the developed control and optimization strategies under real operating conditions. The experiments were carried out using the dSPACE DS1104 real-time control platform, which provided a reliable interface for signal acquisition, control execution, and data analysis. Through this setup, the feasibility and robustness of the predictive control and metaheuristic-based optimization techniques were verified.

The obtained experimental results have successfully confirmed the accuracy and effectiveness of the proposed control architecture. The PDPC combined with the FOPI-AW controller tuned by the ZOA algorithm demonstrated excellent performance in maintaining V_{dc} stability, minimizing overshoot, and ensuring smooth dynamic response even under grid disturbances and varying irradiance levels. The integration of anti-windup compensation further enhanced the system's robustness and stability.

For the PV subsystem, the proposed MPPT algorithms, namely, the ZOA, and GWEO, exhibited superior performance compared to conventional methods such as PSO, GWO, WOA, and FPA. Experimental results under STC, PSCs, and DSC revealed that the proposed methods achieved faster convergence toward the GMPP with reduced oscillations, higher tracking efficiency, and improved steady-state accuracy. The GWEO-based MPPT, in particular, provided a balanced trade-off between convergence speed and precision, proving to be the most effective algorithm for real-time operation.

Additionally, the SAPF subsystem efficiently compensated reactive power, reduced THD in grid current to levels compliant with IEEE-519 standards, and maintained unity power factor operation during all test scenarios. This confirmed the capability of the system to inject active power into the grid while simultaneously improving power quality.

Overall, the experimental results demonstrate the practicality and high performance of the proposed GCPV-SAPF system. The combination of advanced predictive control, fractional-order regulation, and intelligent metaheuristic optimization ensures optimal energy utilization and enhanced power quality in grid-connected renewable energy systems.

The findings of this chapter validate the theoretical based studies presented in the previous chapters and provide strong evidence of the proposed system's potential for real-world applications

General Conclusion

This thesis focused on the experimental study of GCPV-SAPF system and the development of advanced strategies for improving their performance through optimization algorithms and control techniques. The primary objective was to maximize energy extraction and enhance power quality under varying environmental conditions, including STC and PSC.

Several metaheuristic and hybrid optimization algorithms were independently applied, including the ZOA, GWEO, and the hybrid GWO-PSO. Experimental results demonstrated that these proposed algorithms outperform conventional optimization methods in terms of convergence speed, energy yield, and robustness under different operating conditions.

In parallel, a P-DPC with FOPI-AW tuning, adjusted using the ZOA, was implemented for the shunt active power filter. This control approach effectively reduced current harmonics and improved reactive power compensation, resulting in higher system stability and enhanced power quality.

The findings of this work confirm that combining advanced optimization algorithms with precise control of SAPF provides an effective and reliable solution for improving both energy efficiency and power quality in real GCPV–SAPF systems. Furthermore, this study provides a strong foundation for future applications in larger systems or more complex networks, with the potential to develop more adaptive and dynamic control and optimization strategies to maximize the benefits of renewable energy integration.

Recommendations for future work:

1. Conduct experimental studies on larger photovoltaic systems to evaluate the impact of system scale on algorithm performance and control effectiveness.
2. Develop adaptive real-time optimization algorithms to handle rapid environmental changes more efficiently.
3. Integrate energy storage systems and evaluate combined control strategies to further enhance grid stability and energy management.
4. Implement additional renewable energy sources, such as wind turbines, into the DC bus of shunt active power filters.

5. Test and evaluate new power converter topologies, such as the Z-source inverter, for enhanced system performance.

[1] A. Kihal, “Approche avancée pour l’optimisation d’une installation photovoltaïque interconnectée au réseau,” PhD Thesis, 2019. Accessed: Nov. 15, 2025. [Online]. Available: http://dspace.univ-setif.dz:8888/jspui/handle/123456789/3511

[2] M. E. Amran and M. N. Muhtazaruddin, “Renewable energy optimization review: variables towards competitive advantage in green building development,” *Progress in Energy and Environment*, pp. 1–15, 2019.

[3] K. T. Swetha and B. V. Reddy, “An effective dual-objective optimization to enhance power generation in a two-stage grid-tied PV system under partial shading conditions,” *Energy*, vol. 305, p. 132259, 2024.

[4] D. R. Mani, S. Muthu, and K. Kasilingam, “Enhanced power quality and efficient photovoltaic integration with a PV-based unified power quality conditioner using optimized MPPT technique,” *Electr Eng*, vol. 107, no. 2, pp. 2015–2036, Feb. 2025, doi: 10.1007/s00202-024-02627-x.

[5] A.Tiwari and R. Agarwal, “A comparative analysis of PI & FLC based grid connected PV system with power backup to improve power quality,” *Engineering Research Express*, vol. 4, no. 4, p. 045010, 2022.

[6] M. Obi and R. Bass, “Trends and challenges of grid-connected photovoltaic systems–A review,” *Renewable and Sustainable Energy Reviews*, vol. 58, pp. 1082–1094, 2016.

[7] F. Abdelmalek, H. Afghoul, F. Krim, D. E. Zabia, T. L. Belahcene, and S. A. Krim, “Comparison between MPPTs for PV systems using P&O and Grey Wolf controllers,” in *2023 International Conference on Advances in Electronics, Control and Communication Systems (ICAECCS)*, IEEE, 2023, pp. 1–5.

[8] F. Abdelmalek *et al.*, “Experimental validation of effective zebra optimization algorithm-based MPPT under partial shading conditions in photovoltaic systems,” *Scientific Reports*, vol. 14, no. 1, p. 26047, 2024.

[9] T. Toumi, A. Allali, A. Meftouhi, O. Abdelkhalek, A. Benabdelkader, and M. Denai, “Robust control of series active power filters for power quality enhancement in distribution grids: Simulation and experimental validation,” *ISA transactions*, vol. 107, pp. 350–359, 2020.

[10] H. Afghoul, F. Krim, D. Chikouche, and A. Beddar, “Robust switched fractional controller for performance improvement of single phase active power filter under unbalanced conditions,” *Front. Energy*, vol. 10, no. 2, pp. 203–212, June 2016, doi: 10.1007/s11708-015-0381-7.

[11] S. Ouchen, M. Benbouzid, F. Blaabjerg, A. Betka, and H. Steinhart, “Direct power control of shunt active power filter using space vector modulation based on supertwisting sliding mode control,” *IEEE Journal of Emerging and Selected Topics in Power Electronics*, vol. 9, no. 3, pp. 3243–3253, 2020.

[12] F. Abdelmalek, H. Afghoul, F. Krim, M. Bajaj, and V. Blazek, “Experimental validation of novel hybrid grey Wolf equilibrium optimization for MPPT to improve the efficiency of solar photovoltaic system,” *Results in Engineering*, vol. 25, p. 103831, 2025.

[13] H. Afghoul, F. Krim, D. Chikouche, and A. Beddar, “Design and real time implementation of fuzzy switched controller for single phase active power filter,” *ISA transactions*, vol. 58, pp. 614–621, 2015.

[14] B. Boukezata, “Etude et commande d’une chaine de conversion d’énergie d’un système solaire photovoltaïque,” PhD Thesis, 2018. Accessed: Nov. 15, 2025. [Online]. Available: http://dspace.univ-setif.dz:8888/jspui/handle/123456789/1555

[15] S. Chtita, A. Derouich, S. Motahhir, A.E. Ghzizal, A new MPPT design using arithmetic optimization algorithm for PV energy storage systems operating under partial shading conditions, *Energy Convers. Manag.* 289 (2023) 117197.

[16] A. Laib, “Commande robuste de systèmes photovoltaïques interconnectés au réseau avec convertisseurs multi niveaux,” PhD Thesis, 2019. Accessed: Nov. 15, 2025. [Online]. Available: http://dspace.univ-setif.dz:8888/jspui/handle/123456789/3235

[17] A. Jäger-Waldau, “Snapshot of photovoltaics-March 2025,” *EPJ Photovoltaics*, vol. 16, p. 22, 2025.

[18] B. Talbi, “Contribution à l’Amélioration de la Commande d’un Système de Pompage Photovoltaïque,” PhD Thesis, 2018. Accessed: Nov. 15, 2025. [Online]. Available: http://dspace.univ-setif.dz:8888/jspui/handle/123456789/3011

[19] S. Kouro, J. I. Leon, D. Vinnikov, and L. G. Franquelo, “Grid-connected photovoltaic systems: An overview of recent research and emerging PV converter technology,” *IEEE Industrial Electronics Magazine*, vol. 9, no. 1, pp. 47–61, 2015.

[20] A. Anzalchi and A. Sarwat, “Overview of technical specifications for grid-connected photovoltaic systems,” *Energy conversion and management*, vol. 152, pp. 312–327, 2017.

[21] S. Ouchen, “Contribution a la commande directe de puissance dediee au filtrage actif, associe a une source photovoltaïque,” PhD Thesis, Université Mohamed Khider-Biskra, 2017. Accessed: Nov. 15, 2025. [Online]. Available: http://thesis.univ-biskra.dz/id/eprint/2967

[22] S. Ahmed, A. Ali, J. A. Ansari, S. A. Qadir, and L. Kumar, “A Comprehensive Review of Solar Photovoltaic Systems: Scope, Technologies, Applications, Progress, Challenges and Recommendations,” *IEEE Access*, 2025, Accessed: Nov. 15, 2025. [Online]. Available: https://ieeexplore.ieee.org/abstract/document/10955279/

[23] A. Chaoui, “Filtrage actif triphasé pour charges non linéaires,” PhD Thesis, 2018. Accessed: Nov. 15, 2025. [Online]. Available: http://dspace.univ-setif.dz:8888/jspui/handle/123456789/2409

[24] S. Deshpande and N. R. Bhasme, “A review of topologies of inverter for grid connected PV systems,” *2017 Innovations in Power and Advanced Computing Technologies (i-PACT)*, pp. 1–6, 2017.

[25] V. Boddapati and S. A. Daniel, “Performance analysis and investigations of grid-connected Solar Power Park in Kurnool, South India,” *Energy for sustainable development*, vol. 55, pp. 161–169, 2020.

[26] A. Hamza, “Approche avancée du filtrage actif et du contrôle de puissances dans les installations photovoltaïques interconnectées au réseau,” PhD Thesis, Université de M’sila, Département Electronique, 2016. Accessed: Nov. 15, 2025. [Online]. Available: https://www.ccdz.cerist.dz/admin/notice.php?id=00000000000000706418000826

[27] J. C. Das, *Power system harmonics and passive filter designs*. John Wiley & Sons, 2015.

[28] I. F II, “IEEE recommended practices and requirements for harmonic control in electrical power systems,” *New York, NY, USA*, pp. 1–1, 1993.

[29] A. K. Panda and S. Mikkili, *Power quality issues: current harmonics*. CRC press, 2015.

[30] S. Gallardo-Saavedra and B. Karlsson, “Simulation, validation and analysis of shading effects on a PV system,” *Solar Energy*, vol. 170, pp. 828–839, 2018.

[31] Dhaouadi Guiza, « Contribution à l'Etude et commande d'un système Photovoltaïque. Université 20 Aout 1955 – SKIKDA », Thèse Doctorat en Sciences, 2019.

[32] M. Dhimish, “Assessing MPPT techniques on hot-spotted and partially shaded photovoltaic modules: Comprehensive review based on experimental data,” *IEEE Transactions on Electron Devices*, vol. 66, no. 3, pp. 1132–1144, 2019.

[33] S. N. Deshkar, S. B. Dhale, J. S. Mukherjee, T. S. Babu, and N. Rajasekar, "Solar PV array reconfiguration under partial shading conditions for maximum power extraction using genetic algorithm," *Renewable and Sustainable Energy Reviews*, vol. 43, pp. 102–110, 2015.

[34] M. Dhimish and A. M. Tyrrell, "Power loss and hotspot analysis for photovoltaic modules affected by potential induced degradation," *npj Materials Degradation*, vol. 6, no. 1, p. 11, 2022.

[35] H. L. D. Ha, L. Gopal, C. W. R. Chiong, F. H. Juwono, and K. H. Law, "A novel Artificial Location Selection Optimization for Global Maximum Power Point Tracking under Partial Shading Conditions," *Energy Conversion and Management*, vol. 304, p. 118218, 2024.

[36] Refaat, A.-E. Khalifa, M. M. Elsakka, Y. Elhenawy, A. Kalas, and M. H. Elfar, "A novel metaheuristic MPPT technique based on enhanced autonomous group Particle Swarm Optimization Algorithm to track the GMPP under partial shading conditions-Experimental validation," *Energy Conversion and Management*, vol. 287, p. 117124, 2023.

[37] R. Bisht and A. Sikander, "A novel hybrid architecture for MPPT of PV array under partial shading conditions," *Soft Computing*, vol. 28, no. 2, pp. 1351–1365, 2024.

[38] S.A. Krim, F. Krim, H. Afghoul, F. Abdelmalek, An improved perturb and observe MPPT for photovoltaic systems using fuzzy step size, *WSEAS Trans. Power Syst.* 19 (2024) 105–114.

[39] N. Hadjidj, M. Benbrahim, D. Ounnas, L.H. Mouss, Analysis and design of modified incremental conductance-based MPPT algorithm for photovoltaic system, *J. Renew. Energ.* 25 (2) (2022) 187–198.

[40] V. Jately, B. Azzopardi, J. Joshi, A. Sharma, S. Arora, Experimental analysis of hill-climbing MPPT algorithms under low irradiance levels, *Renew. Sustain. Energy Rev.* 150 (2021) 111467.

[41] N. Mwine, H. Han, H. Liu, H. Wang, X. Zheng, L. Fei, A novel neural network based MPPT method under partial shading conditions, in: *Proc. 2023 Panda Forum on Power and Energy (PandaFPE)*, IEEE, 2023, pp. 1057–1062.

[42] G. Dileep, S.N. Singh, Application of soft computing techniques for maximum power point tracking of SPV system, *Sol. Energy* 141 (2017) 182–202.

[43] D.E. Zabia, H. Afghoul, O. Kraa, Y. Himeur, H.S. Ramadan, I. Genc, A.I. Idriss, S. Miniaoui, S. Atalla, W. Mansoor, Experimental validation of a novel hybrid equilibrium slime mould optimization for solar photovoltaic system, *Heliyon* (2024).

[44] S. Chtita, A. Derouich, S. Motahhir, A.E. Ghzizal, A new MPPT design using arithmetic optimization algorithm for PV energy storage systems operating under partial shading conditions, *Energy Convers. Manag.* 289 (2023) 117197.

[45] M.J. Alshareef, An effective falcon optimization algorithm based MPPT under partial shaded photovoltaic systems, *IEEE Access* 10 (2022) 131345–131360.

[46] I. Sajid, A. Sarwar, M. Tariq, F.I. Bakhsh, S. Ahmad, A.S.N. Mohamed, Archimedes optimization algorithm (AOA)-based global maximum power point tracking for a photovoltaic system under partial and complex shading conditions, *Energy* 283 (2023) 129169.

[47] E. Trojovská, M. Dehghani, and P. Trojovskỳ, “Zebra optimization algorithm: A new bio-inspired optimization algorithm for solving optimization algorithm,” *IEEE Access*, vol. 10, pp. 49445–49473, 2022.

[48] S. Mirjalili, S. M. Mirjalili, and A. Lewis, “Grey wolf optimizer Advances in Engineering Software. 69 46–61.” 2014.

[49] S. Mohanty, B. Subudhi, and P. K. Ray, “A new MPPT design using grey wolf optimization technique for photovoltaic system under partial shading conditions,” *IEEE Transactions on Sustainable Energy*, vol. 7, no. 1, pp. 181–188, 2015.

[50] H. Gundogdu, A. Demirci, S. M. Tercan, and U. Cali, “A novel improved grey wolf algorithm based global maximum power point tracker method considering partial shading,” *IEEE Access*, 2024, Accessed: Jun. 25, 2024. [Online]. Available: https://ieeexplore.ieee.org/abstract/document/10381715/

[51] A. Faramarzi, M. Heidarinejad, B. Stephens, and S. Mirjalili, “Equilibrium optimizer: A novel optimization algorithm,” *Knowledge-based systems*, vol. 191, p. 105190, 2020.

[52] H. Rezk, M. Aly, and A. Fathy, “A novel strategy based on recent equilibrium optimizer to enhance the performance of PEM fuel cell system through optimized fuzzy logic MPPT,” *Energy*, vol. 234, p. 121267, 2021.

[53] W. Liu, Z. Ding, H. Zhang, and M. Zhu, “Multiobjective Optimal Power Flow for Distribution Networks Utilizing a Novel Heuristic Algorithm—Grey Wolf Equilibrium

Optimizer,” *IEEE Systems Journal*, 2024, Accessed: Aug. 31, 2024. [Online]. Available: https://ieeexplore.ieee.org/abstract/document/10419145/

[54] E. W. Mukti, A. Risdiyanto, A. A. Kristi, and R. Darussalam, “Particle Swarm Optimization (PSO) based Photovoltaic MPPT Algorithm under the Partial Shading Condition,” *Jurnal Elektronika dan Telekomunikasi*, vol. 23, no. 2, pp. 99–107, 2023.

[55] K. Ishaque, Z. Salam, M. Amjad, and S. Mekhilef, “An improved particle swarm optimization (PSO)–based MPPT for PV with reduced steady-state oscillation,” *IEEE transactions on Power Electronics*, vol. 27, no. 8, pp. 3627–3638, 2012.

[56] F. Abdelmalek, H. Afghoul, F. Krim, D. E. Zabia, O. Kraa, and S. A. Krim, “A New Hybrid Algorithm for Power Optimization in Shaded Photovoltaic Systems”, Accessed: Oct. 06, 2025. [Online].

[57] S. Chtita *et al.*, “A novel hybrid GWO–PSO-based maximum power point tracking for photovoltaic systems operating under partial shading conditions”, *Scientific Reports*, vol. 12, no. 1, p. 10637, 2022.

[58] M. M. A. Awan and T. Mahmood, “Optimization of maximum power point tracking flower pollination algorithm for a standalone solar photovoltaic system,” *Mehran University Research Journal of Engineering & Technology*, vol. 39, no. 2, pp. 267–278, 2020.

[59] B. Kumar and A. Kumar, “A Novel Adaptive Flower Pollination Algorithm for Maximum Power Tracking of Photovoltaic Systems Under Dynamic Shading Conditions,” *Iran J Sci Technol Trans Electr Eng*, vol. 48, no. 2, pp. 859–875, Jun. 2024, doi: 10.1007/s40998-024-00696-z.

[60] N. Kumar, I. Hussain, B. Singh, and B. K. Panigrahi, “MPPT in dynamic condition of partially shaded PV system by using WODE technique,” *IEEE transactions on sustainable energy*, vol. 8, no. 3, pp. 1204–1214, 2017.

[61] D.E. Zabia, H. Afghoul, and O. Kraa “Maximum Power Point Tracking of a Photovoltaic System Under Partial Shading Condition Using Whale Optimization Algorithm,” *Artificial Intelligence and Heuristics for Smart Energy Efficiency in Smart Cities*, pp. 121–132, 2021.

[62] T. Noguchi, et al, “Direct power control of PWM converter without power-source voltage sensors”. IEEE transactions on industry applications, 1998. **34**(3): p. 473-479.

[63] B. Essoussi, et al, “Power Quality Improvement using a New DPC Switching Table for a Three-Phase SAPF”. International Journal of Robotics and Control Systems, 2023. **3**(3): p. 510-529.

[64] Y. Bekakra, L. Zellouma, and O. Malik, “Improved predictive direct power control of shunt active power filter using GWO and ALO–Simulation and experimental study”. Ain Shams Engineering Journal, 2021. **12**(4): p. 3859-3877.

[65] A. BEDDAR and I. ABADLIA, “Development and Performance Evaluation of a Hybrid Fractional Order Proportional Integral Controller for Grid-Connected Inverters,” 2024, Accessed: Apr. 23, 2025. [Online]. Available: https://www.researchsquare.com/article/rs-4449405/latest

[66] K. Mishra, S. R. Das, P. K. Ray, R. K. Mallick, A. Mohanty, and D. K. Mishra, “PSO-GWO optimized fractional order PID based hybrid shunt active power filter for power quality improvements,” *IEEE Access*, vol. 8, pp. 74497–74512, 2020.

[67] H. S. Ramadan, “Optimal fractional order PI control applicability for enhanced dynamic behavior of on-grid solar PV systems,” *International Journal of Hydrogen Energy*, vol. 42, no. 7, pp. 4017–4031, 2017.

[68] M. M. Mahmoud *et al.*, “Application of whale optimization algorithm based FOPI controllers for STATCOM and UPQC to mitigate harmonics and voltage instability in modern distribution power grids,” *Axioms*, vol. 12, no. 5, p. 420, 2023.

[69] H. Ramezanian, S. Balochian, and A. Zare, “Design of Optimal Fractional-Order PID Controllers Using Particle Swarm Optimization Algorithm for Automatic Voltage Regulator (AVR) System,” *J Control Autom Electr Syst*, vol. 24, no. 5, pp. 601–611, Oct. 2013, doi: 10.1007/s40313-013-0057-7.

[70] E. Trojovská, M. Dehghani, and P. Trojovskỳ, “Zebra optimization algorithm: A new bio-inspired optimization algorithm for solving optimization algorithm,” *IEEE Access*, vol. 10, pp. 49445–49473, 2022.

[71] K. Diethelm, N.J. Ford, and A.D. Freed, “A predictor–corrector approach for the numerical solution of fractional differential equations,” Nonlin. Dynam., Vol. 29, pp. 3–22, 2002.

[72] C. Hwang, J.-F. Leu, and S.-Y. Tsay, “A note on time-domain simulation of feedback fractional-order systems,” *IEEE Transactions on Automatic Control*, vol. 47, no. 4, pp. 625–631, 2002.

[73] T. Poinot and J.-C. Trigeassou, “A method for modelling and simulation of fractional systems,” *Signal processing*, vol. 83, no. 11, pp. 2319–2333, 2003.

[74] A. Oustaloup, B. Mathieu, and P. Lanusse, “The CRONE control of resonant plants: application to a flexible transmission,” *European Journal of control*, vol. 1, no. 2, pp. 113–121, 1995.

Our Publication and Communication

Publication

- **F. Abdelmalek** et al., “Experimental validation of effective zebra optimization algorithm-based MPPT under partial shading conditions in photovoltaic systems,” Sci. Rep., vol. 14, no. 1, p. 26047, Oct. 2024, doi: 10.1038/s41598-024-77488-2.
- **F. Abdelmalek**, H. Afghoul, F. Krim, M. Bajaj, and V. Blazek, “Experimental validation of novel hybrid Grey Wolf Equilibrium Optimization for MPPT to improve the efficiency of solar photovoltaic system,” Results Eng., vol. 25, p. 103831, Mar. 2025, doi: 10.1016/j.rineng.2024.103831.
- **F. Abdelmalek** et al., “A New Hybrid Algorithm for Power Optimization in Shaded Photovoltaic Systems,” Electroteh. Electron. Autom., vol. 73, no. 3, pp. 45–52, Sep. 2025, doi: 10.46904/eea.25.73.3.1108006.
- A.E. Boukhdenna, H. Afghoul, D. E. Zabia, **F. Abdelmalek** et **al**., “Enhancing power quality of pv grid-connected system through mantis shrimp optimization algorithm for optimal Dc bus voltage control,” Sci. Rep., vol. 16, no. 1, p. 2370, Jan. 2026, doi: 10.1038/s41598-025-32058-y.
- M. Khitas, H. Afghoul, **F. Abdelmalek**, D. E. Zabia, and L. Ziet, “Design and Experimental Validation of a Hybrid GWO-PSO Tuned PI Controller for Predictive Direct Power Control in SAPF,” J. Eur. Systèmes Autom., vol. 58, no. 5, pp. 963–974, May 2025, doi: 10.18280/jesa.580510.
- **F. Abdelmalek** *et al.*, “Design of a Novel Hybrid Grey Wolf Equilibrium Optimizer for MPPT to Enhance the Efficiency of Solar Photovoltaic Systems,” *JOURNAL OF RENEWABLE ENERGY SYSTEMS AND MANAGEMENT*, vol. 1, no. 1, pp. 40–48, 2025.
- S.A. Krim, F. Krim, H. Afghoul and **F. Abdelmalek**, "An Enhanced Perturb and Observerve MPPT for Photovoltaic Systems Based on Fuzzy Step," Journal Européen des Systèmes Automatisés, vol. 57, no. 2, pp. 363-372, 2024.

Communication

- **F. Abdelmalek** et al., “Experimental Implementation of Direct Power Control for a SAPF with a PI Controller Tuned Using Grey Wolf Optimization,” in 2024 International Conference on Advances in Electrical and Communication Technologies (ICAECOT), Setif, Algeria: IEEE, Oct. 2024, pp. 1–6. doi: 10.1109/ICAECOT62402.2024.10828779.
- **F. Abdelmalek**, H. Afghoul, F. Krim, D. E. Zabia, T. L. Belahcene, and S. A. Krim, “Comparison between MPPTs for PV systems using P&O and Grey Wolf controllers,” in 2023 International Conference on Advances in Electronics, Control and Communication Systems (ICAECCS), BLIDA, Algeria: IEEE, Mar. 2023, pp. 1–5. doi: 10.1109/ICAECCS56710.2023.10104731.
- **F. Abdelmalek**, H. Afghoul, F. Krim, D. E. Zabia, T. L. Belahcene, and S. A. Krim, “A Shunt Active Power Filter’s Pi and Fuzzy DPC Control Comparison,” AIJR Abstracts, pp. 80–81, 2024
- T. L. Belahcene, H. Afghoul, O. Kraa, D. E. Zabia, **F. Abdelmalek**, and B. M. Nassim Bouzidi, “Enhancing Active Harmonic Compensator by Using Fuzzy-PI Controller,” in 2024 2nd International Conference on Electrical Engineering and Automatic Control (ICEEAC), Setif, Algeria: IEEE, May 2024, pp. 1–5. doi: 10.1109/ICEEAC61226.2024.10576307.
- T. L. Belahcene, O. Kraa, H. Afghoul, D. E. Zabia, B. Med Nassim Bouzidi, and **F. Abdelmalek**, “Maximum power point tracking based on metaheuristic algorithms of Partially Shaded solar photovoltaic system,” in 2024 8th International Conference on Image and Signal Processing and their Applications (ISPA), Biskra, Algeria: IEEE, Apr. 2024, pp. 1–6. doi: 10.1109/ISPA59904.2024.10536735.
- S. A. Krim, H. Afghoul, F. Krim, **F. Abdelmalek**, D. E. Zabia, and T. Lamdjed Belahcene, “Enhancement of Z-Source Inverter Controller for Improvement of Grid-tied PV systems,” in 2023 IEEE International Conference on Advanced Systems and Emergent Technologies (IC_ASET), Hammamet, Tunisia: IEEE, Apr. 2023, pp. 1–5. doi: 10.1109/IC_ASET58101.2023.10151231.
- A. E. Boukhedenna, H. Afghoul, D. E. Zabia, B. M. N. Bouzidi, **F. Abdelmalek**, and L. Ouchen, “Experimental Test Bench for Power Quality Enhancement Using Direct Current Control Based on Fuzzy PI Controller,” in 2024 1st International Conference

on Electrical, Computer, Telecommunication and Energy Technologies (ECTE-Tech), Oum El Bouaghi, Algeria: IEEE, Dec. 2024, pp. 1–6. doi: 10.1109/ECTE-Tech62477.2024.10850963.

- S. A. Krim, F. Krim, H. Afghoul, H. Bey, and **F. Abdelmalek**, “Topologies, Control Algorithms and Applications of Bidirectional DC-DC Converters,” in 2024 International Conference on Advances in Electrical and Communication Technologies (ICAECOT), Setif, Algeria: IEEE, Oct. 2024, pp. 1–9. doi: 10.1109/ICAECOT62402.2024.10994890.
- M. N. Bouzidi et **al**., “Experimental Test Bench for Direct Current Control Strategy in a Three-Phase Shunt Active Power Filter Based on IP Controller,” in 2024 2nd International Conference on Electrical Engineering and Automatic Control (ICEEAC), Setif, Algeria: IEEE, May 2024, pp. 1–6. doi: 10.1109/ICEEAC61226.2024.10576320.
- D. E. Zabia, O. Kraa, H. Afghoul, T. L. Belahcene, S. A. Krim, and **F. Abdelmalek**, “Finite Control Set-Model Predictive Control for Grid connected Shunt Active Power Filter,” in 2023 International Conference on Advances in Electronics, Control and Communication Systems (ICAECCS), BLIDA, Algeria: IEEE, Mar. 2023, pp. 1–5. doi: 10.1109/ICAECCS56710.2023.10105128.

Abstract:

Integrating photovoltaic (PV) systems into today's power grids brings about a number of practical challenges, especially when it comes to maintaining good energy efficiency and consistent power quality. This thesis proposes and experimentally investigates advanced optimization and control strategies to boost the overall performance of GCPV-SAPF systems. Different metaheuristic and hybrid-based optimization approaches, among which the ZOA, GWEO, and hybrid GWO-PSO, were independently applied to maximize power extraction through MPPT. Their experimental performance was systematically compared with widely recognized metaheuristic algorithms, including GWO, PSO, WOA, and FPA, considering convergence speed, energy yield, and robustness under different levels of solar irradiance and PSCs. In parallel, a P-DPC with FOPI-AW tuning, as determined by ZOA, was implemented for the SAPF, effectively mitigating grid current harmonics and enhancing reactive power compensation. Experimental results demonstrate that the proposed optimization algorithms achieve superior MPPT performance, while the ZOA-tuned FOPI-AW controller ensures enhanced power quality and system stability. The results demonstrate that the proposed methods are practically applicable, reliable, and robust, offering practical solutions for increasing energy efficiency and maintaining high power quality in real grid-connected photovoltaic systems.

Keywords: Maximum Power Point Tracking (MPPT), Metaheuristic Optimization Algorithms (MOAs), Photovoltaic (PV) systems, Power Quality (PQ), Predictive-Direct Power Controller (P-DPC), Shunt Active Power Filter (SAPF).

Résumé :

L'intégration des systèmes photovoltaïques (PV) dans les réseaux électriques modernes pose des défis importants en termes d'efficacité énergétique et de qualité de l'énergie. Cette thèse propose et étudie expérimentalement des stratégies avancées d'optimisation et de contrôle visant à améliorer les performances des systèmes PV connectés au réseau, intégrant des FAP. Plusieurs algorithmes d'optimisation métaheuristiques et hybrides, ZOA, GWEO, et GWO-PSO, ont été appliqués de manière indépendante pour maximiser l'extraction de puissance via le MPPT. Leurs performances expérimentales ont été systématiquement comparées avec des algorithmes métaheuristiques conventionnels, incluant GWO, PSO, WOA et FPA, En prenant en considération la vitesse de convergence, du rendement énergétique et de la robustesse sous différentes conditions d'irradiation et d'ombre partielle. Parallèlement, un P-DPC avec régulation FOPI, réglé par ZOA, a été mis en œuvre pour le FAP, permettant de réduire efficacement les harmoniques du courant du réseau et d'améliorer la compensation de puissance réactive. Les résultats expérimentaux démontrent que les algorithmes d'optimisation proposés atteignent des performances supérieures de MPPT, tandis que le contrôleur FOPI réglé par ZOA garantit une meilleure qualité de l'énergie et la stabilité du système. Ces résultats confirment l'applicabilité pratique, la fiabilité et la robustesse des méthodes proposées, offrant des solutions efficaces pour améliorer l'efficacité énergétique et maintenir une haute qualité de l'énergie dans les systèmes photovoltaïques connectés au réseau.

Mots-clés : Algorithmes d'optimisation métaheuristiques (MOAs), Contrôleur prédictif à puissance directe (P-DPC), Filtre Actif Parallèle (FAP), Qualité de l'énergie (PQ), Systèmes photovoltaïques (PV), Suivi du point de puissance maximale (MPPT).

ملخص:

إنّ دمج الأنظمة الكهروضوئية (PV) في شبكات الكهرباء الحديثة يطرح تحديات كبيرة من حيث كفاءة الطاقة وجودتها. تقترح هذه الأطروحة وتدرس بشكل تجريبي استراتيجيات متقدمة للضبط والتحسين بهدف رفع أداء الأنظمة الكهروضوئية المرتبطة بالشبكة، مع دمج مرشحات القدرة الفعّالة (FAP) .وقد تم تطبيق عدة خوارزميات تحسين ميتاوريستيكية وهجينة، مثل ZOA، GWEO، GWO-PSO، بشكل مستقل لتعظيم استخلاص القدرة عبر تقنية MPPT. وتمت مقارنة أدائها تجريبياً مع خوارزميات ميتاوريستيكية تقليدية تشمل GWO، PSO، WOA، وFPA، مع الأخذ في الاعتبار سرعة التقارب، وكفاءة الطاقة، والقدرة على التحمل تحت مختلف ظروف الإشعاع والظلال الجزئية. وبالتوازي مع ذلك، جرى تنفيذ التحكم المباشر في القدرة التنبؤية (P-DPC) باستخدام منظم FOPI مضبوط بواسطة ZOA لتشغيل مرشح القدرة الفعّال، مما مكّن من تقليل التوافقيات في تيار الشبكة وتحسين تعويض القدرة غير الفعّالة. تُظهر النتائج التجريبية أن خوارزميات التحسين المقترحة تحقق أداءً متفوّقاً في تتبع نقطة القدرة العظمى MPPT ، في حين يضمن المنظم FOPI المضبوط بواسطة ZOA جودة طاقة أفضل واستقراراً أعلى للنظام. تؤكد هذه النتائج القابلية العملية والموثوقية والصلابة للطرق المقترحة، باعتبارها حلولاً فعّالة لتحسين كفاءة الطاقة والحفاظ على جودة طاقة عالية في الأنظمة الكهروضوئية المرتبطة بالشبكة.

الكلمات المفتاحية: خوارزميات التحسين الميتاوريستيكية(MOAs) ، التحكم التنبؤي بالقدرة المباشرة(P-DPC) ، المرشح النشط المتوازي(FAP) ، جودة الطاقة(PQ) ، الأنظمة الكهروضوئية(PV) ، تتبع نقطة القدرة العظمى(MPPT) .